DISS. ETH NO. 25372

Semiconductor Disk Lasers for Optical Frequency Comb Applications

A thesis submitted to attain the degree of

DOCTOR OF SCIENCES of ETH ZURICH

(Dr. sc. ETH Zurich)

presented by

Dominik Waldburger

MSc ETH Physics, ETH Zurich

born on 08.05.1990

citizen of Teufen (AR)

accepted on the recommendation of

Prof. Dr. Ursula Keller, examiner
Prof. Dr. Mircea Guina, co-examiner

2018

„Être fort pour être utile.“

— Georges Hébert, *Méthode Naturelle*

Contents

List of Figures

List of Tables

List of Symbols and Acronyms

Symbols

$\tilde{A}(\omega)$	pulse envelope in the frequency domain.
$A(t)$	pulse envelope in the time domain.
A_{pump}	fraction of absorbed power.
α	linewidth enhancement factor.
α_a	linewidth enhancement factor of the absorber.
α_g	linewidth enhancement factor of the gain.
$N(z,t)$	charge-carrier density.
$Q(t)$	absorber charge-carrier density.
$G(t)$	gain charge-carrier density.
ΔE	energy difference between sub-bands.
ΔR	absorber modulation depth.
ΔR_{ns}	nonsaturable losses.
$E^{\pm}(z,t)$	electric field amplitude.
$A(t)$	electric field at the out-coupling mirror.
$\tilde{E}(\omega)$	electric field in the frequency domain.
$E(t)$	electric field in the time domain.
E_0	average carrier energy.
E_{F}	Fermi energy.
η	optical-to-optical efficiency.
η_{calc}	calculated optical-to-optical efficiency.
F_{p}	pulse fluence.
F_0	fluence at maximum reflectivity.
F_2	two-photon absorption coefficient.

$\mathcal{F}$	Fourier transformation.
f_{CEO}	carrier-envelope offset frequency.
f_{rep}	pulse repetition rate.
g	gain per unit lenght.
g_{ss}	small signal gain.
γ	gain bandwidth.
γ_Q	absorber recovery rate.
γ_G	gain recovery rate.
Γ_{abs}	absorption rate.
Γ_{gain}	stimulated emission coefficient.
J_G	pump current.
J_Q	unsaturated absorption.
K	ratio between the fluence on the SESAM and the fluence on the gain chip.
k_B	Boltzmann constant.
κ	intensity losses per round trip.
λ	wavelength.
L_{CAVITY}	length of total cavity.
$L_{\text{OC-VECSEL}}$	length between the output coupler and VECSEL chip.
$L_{\text{VECSEL-SESAM}}$	length between the VECSEL chip and SESAM.
N	number of measurements.
N	carrier density.
n	refractive index.
N_{spont}	carriers recombined via spontaneous emission.
N_{stim}	carriers recombined via stimulated emission.
N_1	carrier density (interaction region).
N_{10}	maximum value of N_1.
N'_{10}	thermal equilibrium value of N_1.
N_2	carrier density (reservoir).
N_{20}	maximum value of N_2.
N_{abs}	carrier density (absorber).
ν_0	nominal frequency.
$\nu(t)$	instantaneous frequency.
ω	angular frequency.
ω_0	carrier angular frequency.
$\Phi(t)$	phase deviation.
Q_{def}	quantum defect.

R	radius of curvature.
r_s	ratio between the gain and absorber differential.
sech^2	squared hyperbolic secant.
τ	measurement interval.
τ_0	shortest measurement interval.
τ_0	time of interaction with gain chip.
τ_1	time delay between output coupler and VECSEL.
τ_2	time delay between VECSEL and SESAM.
τ_{abs}	SESAM recovery time.
τ_{c}	carrier capture time.
τ_{intra}	intraband time constant.
τ_{life}	spontaneous recombination time constant.
τ_{p}	pulse duration.
τ_{pulse}	pulse duration.
τ_{sep}	pulse separation.
T	temperature.
T	cold-cavity round trip time.
T	transmission.
T_{r}	cavity roundtrip time.
v_g	group velocity.
$x(t)$	time-error function.

Acronyms

AC	autocorrelation.
ADEV	Allan deviation.
AFM	atomic force microscope.
AlAs	aluminium arsenide.
AlGaAs	aluminium gallium arsenide.
AOM	acousto-optic modulator.
AR	anti-reflection.
BPF	optical band-pass filter.
BRF	birefringent filter.
BS	beams splitter.
$CaCO_3$	calcium carbonate.
CEO	carrier envelope-offset.
CMOS	complementary metal-oxide-semiconductor.
CPM	colliding pulse modelocking.
CVD	chemical vapour deposition.
cw	continous wave.
dBc	decibels relative to the carrier.
DBR	distributed Bragg reflector.
DFG	difference frequency generation.
DOS	density of states.
DPSSL	diode pumped solid-state laser.
DUT	device under test.
FC	fiber coupling.
FROG	frequency-resolved optical gating.
FS	fused silica.
FWHM	full width at half maximum.
GaAs	gallium arsenide.
GDD	group delay dispersion.
GVD	group velocity dispersion.
HS	heatsink.
IBS	ion beam sputtering.
InAs	indium arsenide.
InGaAs	indium gallium arsenide.
IR	infrared.
laser	light amplification by stimulated emission of radiation.
LBO	lithium triborate.
lidar	light detection and ranging.

LIGO	laser interferometer gravitational-wave observatory.
M^2	M square value.
MBE	molecular beam epitaxy.
MDEV	modified Allan deviance.
MECSEL	membrane external-cavity surface-emitting laser.
MIXSEL	modelocked integrated external-cavity surface-emitting laser.
ML	modelocking.
ML	monolayer.
MOVPE	metalorganic vapour phase epitaxy.
MSA	microwave spectrum analyzer.
Nd:YAG	neodymium-doped:yttrium-aluminum-garnet.
OC	output coupler.
OFC	optical frequency comb.
OPSL	optically pump semiconductor laser.
PBS	polarizing beam splitter.
PCF	photonic-crystal fiber.
PD	photodetector.
PECVD	plasma-enhanced chemical vapor deposition.
PI	proportional–integral.
PL	photoluminescence.
PLL	phase-locked loop.
PPLN	periodically poled lithium niobate.
PSD	power spectral density.
QD	quantum dot.
QW	quantum well.
RBW	resolution bandwidth.
RE	rate equation.
ROC	radius of curvature.
SC	strain compensation.
SC	supercontinuum.
SCG	supercontinuum generation.
SDL	semiconductor disk laser.
SESAM	semiconductor saturable absorber mirror.
SHG	second harmonic generation.
Si_3N_4	silicon nitride.
SiC	silicon carbide.
SiO_2	silicon oxide.
SiO_xN_y	silicon oxide/nirtide.
SiO_x	silicon oxide.

SK	Stranski–Krastanov.
SML	sub-monolayer.
SNR	signal-to-noise ratio.
SSA	signal source analyzer.
SVEA	slowly varying envelope approximation.
Ta_2O_5	tantalum pentoxide.
Ti:sapphire	titanium-sapphire.
TM	transverse magnetic.
TOD	third order dispersion.
TPA	two photon absorption.
UHFLI	digital ultra-high lock-in amplifier.
UV	ultraviolet.
V-to-A	voltage to current.
VCSEL	vertical cavity surface-emitting laser.
VECSEL	vertical external-cavity surface-emitting laser.
VHG	volume holographic grating.
XUV	extreme ultraviolet.
Yb	ytterbium.
Yb:CALGO	Yb^{3+}:$CaGdAlO_4$.
Yb:YAG	ytterbium-doped yttrium aluminum garnet.
ZDW	zero-dispersion wavelength.
ZnSe	zinc selenide.

Publications

Parts of this doctoral thesis are published in the following journal papers and conference proceedings.

Journal Papers

1. A. Jallageas, J. Nürnberg, C. G. E. Alfieri, D. Waldburger, S. M. Link, F. Emaury, J. Morel, U. Keller, "Wavelength calibration of high performance spectrometers using a fully stabilized semiconductor disk laser comb", in preparation (2018)

2. C. G. E. Alfieri, D. Waldburger, J. Nürnberg, M. Golling, U. Keller, "Sub-150-fs pulses from a broadband MIXSEL", submitted to Opt. Lett. (2018)

3. J. Nürnberg, C. G. E. Alfieri, Z. Chen, D. Waldburger, N. Picqué, U. Keller, "An unstabilized femtosecond semiconductor laser for dual-comb spectroscopy of acetylene", submitted to Opt. Express (2018)

4. D. Waldburger, A. S. Mayer, C. G. E. Alfieri, J. Nürnberg, A. R. Johnson, X. Ji, A. Klenner, Y. Okawachi, M. Lipson, A. L. Gaeta, U. Keller, "Tightly locked optical frequency comb from a semiconductor disk laser", submitted to Optica (2018)

5. C. G. E. Alfieri, D. Waldburger, J. Nürnberg, M. Golling, L. C. Jaurigue, K. Lüdge, U. Keller, "Mode-locking Instabilities for High-Gain Semiconductor Disk Lasers Based on Active Submonolayer Quantum Dots", Phys. Rev. Applied 10 (2018), 044015

6. D. Waldburger, C. G. E. Alfieri, S. M. Link, S. Meinecke, L. C. Jaurigue, K. Lüdge, U. Keller, "Multipulse instabilities of a femtosecond SESAM-modelocked VECSEL", Opt. Express 26 (2018), 21872–21886

7. C. G. E. Alfieri, D. Waldburger, M. Golling, U. Keller, "High-power Sub-300-Femtosecond Quantum Dot Semiconductor Disk Lasers", IEEE Photon. Technol. Lett. 30 (2018), 525–528

8. N. Jornod, K. Gürel, V. J. Wittwer, P. Brochard, S. Hakobyan, S. Schilt, D. Waldburger, U. Keller, T. Südmeyer, "Carrier-envelope offset frequency stabilization of a gigahertz semiconductor disk laser", Optica 4 (2017), 1482–1487

9. S. M. Link, D. Waldburger, C. G. E. Alfieri, M. Golling, U. Keller, "Coherent beam combining and noise analysis of a colliding pulse modelocked VECSEL", Opt. Express 25 (2017), 19281–19290

10. N. Jornod, V. J. Wittwer, C. Kränkel, D. Waldburger, U. Keller, T. Südmeyer, T. Calmano, "High-power amplification of a femtosecond vertical external-cavity surface-emitting laser in an Yb:YAG waveguide", Opt. Express 25 (2017), 16527–16533

11. F. F. Voigt, F. Emaury, P. Bethge, D. Waldburger, S. M. Link, S. Carta, A. van der Bourg, F. Helmchen, U. Keller, "Multiphoton in vivo imaging with a femtosecond semiconductor disk laser", Biomed. Opt. Express 8 (2017), 3213–3231

12. S. M. Link, D. J. H. C. Maas, D. Waldburger, U. Keller, "Dual-comb spectroscopy of water vapor with a free-running semiconductor disk laser", Science 356 (2017), 1164–1168

13. C. G. E. Alfieri, D. Waldburger, S. M. Link, E. Gini, M. Golling, G. Eisenstein, U. Keller, "Optical efficiency and gain dynamics of modelocked semiconductor disk lasers", Opt. Express 25 (2017), 6402–6420

14. D. Waldburger, S. M. Link, M. Mangold, C. G. E. Alfieri, E. Gini, M. Golling, B. W. Tilma, U. Keller, "High-power 100 fs semiconductor disk lasers", Optica 3 (2016), 844–852

15. P. Brochard, N. Jornod, S. Schilt, V. J. Wittwer, S. Hakobyan, D. Waldburger, S. M. Link, C. G. E. Alfieri, M. Golling, L. Devenoges, J. Morel, U. Keller, T. Südmeyer, "First investigation of the noise and modulation properties of the carrier-envelope offset in a modelocked semiconductor laser", Opt. Lett. 41 (2016), 3165–3168

16. B. W. Tilma, M. Mangold, C. A. Zaugg, S. M. Link, D. Waldburger, A. Klenner, A. S. Mayer, E. Gini, M. Golling, U. Keller, "Recent advances in ultrafast semiconductor disk lasers", Light Sci. Appl. 4 (2015), e310, **invited**

Conference Papers

1. D. Waldburger, A. S. Mayer, C. G. E. Alfieri, J. Nürnberg, A. R. Johnson, X. Ji, A. Klenner, Y. Okawachi, M. Lipson, A. L. Gaeta, U. Keller, "Silicon nitride waveguide enables self-referenced frequency comb from a semiconductor disk laser", in Advanced Photonics Congress (APC), Zürich, Switzerland (2018), talk

2. J. Nürnberg, C. G. E. Alfieri, Z. Chen, D. Waldburger, M. Golling, N. Picqué, U. Keller, "Dual-Comb Spectroscopy with one unstabilized semiconductor laser", in Advanced Photonics Congress (APC), Zürich, Switzerland (2018), **invited talk**

3. J. Nürnberg, C. G. E. Alfieri, D. Waldburger, M. Golling, U. Keller, "Pushing integrated semiconductor disk lasers towards 100-fs pulses", in Advanced Photonics Congress (APC), Zürich, Switzerland (2018), talk

4. C. G. E. Alfieri, D. Waldburger, J. Nürnberg, M. Golling, U. Keller, "Quantum Dot Semiconductor Disk Lasers: Record Performance Depending on Growth Techniques", in Advanced Photonics Congress (APC), Zürich, Switzerland (2018), talk

5. D. Waldburger, A. S. Mayer, C. G. E. Alfieri, J. Nürnberg, A. R. Johnson, X. Ji, A. Klenner, Y. Okawachi, M. Lipson, A. L. Gaeta, U. Keller, "Fully Stabilized Optical Frequency Comb from a Semiconductor Disk Laser", in Conference on Lasers and Electro-Optics (CLEO), San Jose, United States (2018), **upgrade to invited talk**

6. C. G. E. Alfieri, D. Waldburger, J. Nürnberg, M. Golling, U. Keller, "Ultrafast Quantum Dot VECSELs: Record Performance Depending on Growth Techniques", in Conference on Lasers and Electro-Optics (CLEO), San Jose, United States (2018), talk

7. A. Jallageas, J. Nürnberg, C. G. E. Alfieri, D. Waldburger, S. M. Link, F. Emaury, J. Morel, U. Keller, "Wavelength calibration of high-performance spectrometers with a stabilized optical comb from an ultrafast semiconductor disk laser", in Conference on Lasers and Electro-Optics (CLEO), San Jose, United States (2018), talk

8. J. Nürnberg, C. G. E. Alfieri, Z. Chen, D. Waldburger, M. Golling, N. Picqué, U. Keller, "Free-running, Femtosecond Dual-Comb MIXSEL for Spectroscopy of Acetylene", in Conference on Lasers and Electro-Optics (CLEO), San Jose, United States (2018), poster

9. D. Waldburger, A. S. Mayer, C. G. E. Alfieri, A. R. Johnson, X. Ji, A. Klenner, Y. Okawachi, M. Lipson, A. L. Gaeta, U. Keller, "Octave-spanning supercontinuum generated in silicon nitride waveguide directly from a SESAM-modelocked VECSEL", in SPIE Photonics West - LASE, San Francisco, United States (2018), **invited talk**

10. D. Waldburger, S. M. Link, C. G. E. Alfieri, M. Golling, U. Keller, "Coherent beam combining of a colliding pulse modelocked VECSEL", in SPIE Photonics West - LASE, San Francisco, United States (2018), talk

11. C. G. E. Alfieri, D. Waldburger, J. Nürnberg, M. Golling, U. Keller, "Sub-300-fs semiconductor disk laser based on active quantum dots", SPIE Photonics West - LASE (2018), **invited talk**

12. J. Nürnberg, C. G. E. Alfieri, S. M. Link, D. Waldburger, M. Golling, U. Keller, "Femtosecond dual-comb MIXSEL at 1030 nm", SPIE Photonics West - LASE (2018), talk

13. F. Emaury, F. F. Voigt, P. Bethge, D. Waldburger, S. M. Link, S. Carta, A. van der Bourg, F. Helmchen, U. Keller, "Femtosecond semiconductor disk lasers: a promising tool for the future of multiphoton imaging", SPIE Photonics West - BIOS (2018), poster

14. D. Waldburger, A. S. Mayer, C. G. E. Alfieri, A. R. Johnson, X. Ji, A. Klenner, Y. Okawachi, M. Lipson, A. L. Gaeta, U. Keller, "Self-referenced CEO Frequency Detection of a Semiconductor Disk Laser using a Silicon NitrideWaveguide", in Advanced Solid State Lasers (ASSL), Nagoya, Japan (2017), **post-deadline talk**

15. D. Waldburger, S. M. Link, D. J. Maas, U. Keller, "Free-Running Dual-comb MIXSEL used for Dual-Comb Spectroscopy", in Advanced Solid State Lasers (ASSL), Nagoya, Japan (2017), talk

16. D. Waldburger, S. M. Link, C. G. Alfieri, M. Golling, U. Keller, "Coherent Beam Combining of a Colliding Pulse Modelocked VECSEL", in Advanced Solid State Lasers (ASSL), Nagoya, Japan (2017), talk

17. N. Jornod, K. Gürel, V. J. Wittwer, P. Brochard, S. Hakobyan, S. Schilt, D. Waldburger, U. Keller, T. Südmeyer, "Carrier-envelope offset frequency stabilization of a mode-locked semiconductor laser", in Advanced Solid State Lasers (ASSL), Nagoya, Japan (2017), talk

18. D. J. H. C. Maas, S. M. Link, D. Waldburger, U. Keller, "Dual-Comb Spectroscopy with a Semiconductor Disk Laser", in IEEE Sensors, Glasgow, Scotland (2017), talk

19. D. Waldburger, C. G. E. Alfieri, S. M. Link, E. Gini, M. Golling, U. Keller, "High-Power Semiconductor Disk Lasers with Record-Short Pulse Durations", in European Conference on Lasers and Electro-Optics (CLEO-ECBO), Munich, Germany (2017), talk

20. C. G. E. Alfieri, D. Waldburger, S. M. Link, M. Golling, U. Keller, "Ultrafast dynamics of semiconductor disk lasers", in European Conference on Lasers and Electro-Optics (CLEO-ECBO), Munich, Germany (2017), talk

21. F. Emaury, F. F. Voigt, P. Bethge, D. Waldburger, S. M. Link, S. Carta, A. van der Bourg, F. Helmchen, U. Keller, "Multiphoton microscopy in every lab: the promise of ultrafast semiconductor disk lasers", in European Conference on Lasers and Electro-Optics (CLEO-ECBO), Munich, Germany (2017), talk

22. N. Jornod, K. Gürel, V. J. Wittwer, P. Brochard, S. Hakobyan, S. Schilt, D. Waldburger, U. Keller, T. Südmeyer, "Towards Self-Referencing of a VECSEL Frequency Comb", in European Conference on Lasers and Electro-Optics (CLEO-ECBO), Munich, Germany (2017), talk

23. S. M. Link, D. J. H. C. Maas, D. Waldburger, U. Keller, "Gas Spectroscopy with a Free-Running Dual-Comb Semiconductor Disk Laser", in European Conference on Lasers and Electro-Optics (CLEO-ECBO), (2017), talk

24. S. M. Link, D. J. Maas, D. Waldburger, C. G. Alfieri, M. Golling, F. Emaury, U. Keller, "Gas Spectroscopy with a Dual-Comb Semiconductor Disk Laser", in Conference on Lasers and Electro-Optics (CLEO), San Jose, United States (2017), talk

25. F. Emaury, F. F. Voigt, P. Bethge, D. Waldburger, S. M. Link, S. Carta, F. Helmchen, U. Keller, "Ultrafast semiconductor disk lasers for in vivo multiphoton imaging", in Conference on Lasers and Electro-Optics (CLEO), San Jose, United States (2017), talk

26. C. Alfieri, D. Waldburger, S. M. Link, M. Golling, U. Keller, "Carrier Dynamics of Ultrafast Semiconductor Disk Lasers", in Conference on Lasers and Electro-Optics (CLEO), San Jose, United States (2017), poster

27. F. F. Voigt, F. Emaury, P. Bethge, D. Waldburger, S. M. Link, S. Carta, A. v. d. Bourg, F. Helmchen, U. Keller, ""In vivo multiphoton imaging using ultrafast semiconductor disk lasers", in Focus on Microscopy (FoM), Bordeaux, France (2017), poster

28. D. Waldburger, C. G. E. Alfieri, S. M. Link, E. Gini, M. Golling, U. Keller, "Gigahertz 100-fs semiconductor disk lasers", in Compound Semiconductor Week (CSW), Berlin, Germany (2017), talk

29. C. G. E. Alfieri, D. Waldburger, M. Golling, U. Keller, "High-power sub 200-fs semiconductor disk laser based on quantum dots layers", in Compound Semiconductor Week (CSW), Berlin, Germany (2017), talk

30. D. Waldburger, S. M. Link, C. G. E. Alfieri, M. Golling, U. Keller, "High-power 100-fs SESAM-modelocked VESCEL", in SPIE Photonics West - LASE, San Francisco, United States (2017), **invited talk**

31. S. M. Link, D. Waldburger, C. G. E. Alfieri, M. Golling, U. Keller, "Stabilized dual-comb MIXSEL", in SPIE Photonics West - LASE, San Francisco, United States (2017), **invited talk**

32. C. G. E. Alfieri, D. Waldburger, S. M. Link, M. Golling, U. Keller, "Optical efficiency and gain dynamics of ultrafast semiconductor disk lasers", in SPIE Photonics West - LASE, San Francisco, United States (2017), **invited talk**

33. D. Waldburger, S. M. Link, C. G. Alfieri, M. Golling, U. Keller, "High-power 100-fs SESAM-modelocked VECSEL", in Advanced Solid State Lasers (ASSL), Boston, United States (2016), talk

34. S. M. Link, D. Waldburger, C. G. Alfieri, M. Golling, U. Keller, "Stabilized Microwave Frequency Comb from a Dual-Comb Modelocked Semiconductor Disk Laser", in Advanced Solid State Lasers (ASSL), Boston, United States (2016), talk

35. N. Jornod, P. Brochard, V. Wittwer, S. Schilt, S. Hakobyan, D. Waldburger, S. M. Link, C. Alfieri, M. Golling, L. Devenoges, J. Morel, U. Keller, T. Sudmeyer,

"First Investigation of the Noise and Modulation Properties of the Carrier Envelope Offset Frequency in a Semiconductor Modelocked Laser", in Conference on Lasers and Electro-Optics (CLEO), San Jose, United States (2016), talk

36. S. M. Link, C. G. Alfieri, D. Waldburger, M. Golling, A. Klenner, U. Keller, "Saturable Absorber Decouples Noise Stabilization in Dual-Comb Modelocked Lasers", in Conference on Lasers and Electro-Optics (CLEO), San Jose, United States (2016), talk

37. C. G. E. Alfieri, A. Diebold, M. Kopp, D. Waldburger, M. Mangold, F. Emaury, C. J. Saraceno, E. Gini, U. Keller, "SESAMs for high-power lasers", in Conference on Lasers and Electro-Optics (CLEO), San Jose, United States (2016), talk

38. M. Golling, C. G. E. Alfieri, D. Waldburger, S. M. Link, E. Gini, U. Keller, "Progress in MBE and MOVPE semiconductor disk laser growth", in German MBE-Workshop, Garching, Germany (2016), talk

39. P. Brochard, N. Jornod, V. J. Wittwer, S. Schilt, D. Waldburger, S. M. Link, C. Alfieri, M. Golling, L. Devenoges, J. Morel, U. Keller, T. Südmeyer, "Carrier-envelope offset characterization in a semiconductor modelocked laser without f-to-2f interferometry", in 30^{th} European Frequency and Time Forum (EFTF), York, United Kingdom (2016), talk

40. S. M. Link, D. Waldburger, C. G. E. Alfieri, M. Golling, U. Keller, "Stabilized dual-comb modelocked semiconductor disk laser", in 7^{th} EPS-QEOD Europhoton Conference (Europhoton), Vienna, Austria (2016), **post-deadline talk**

41. S. M. Link, D. Waldburger, C. G. E. Alfieri, M. Golling, E. Gini, U. Keller, "Record-short pulses from semiconductor disk lasers", in 7^{th} EPS-QEOD Europhoton Conference (Europhoton), Vienna, Austria (2016), talk

42. D. Waldburger, S. M. Link, C. G. E. Alfieri, M. Golling, U. Keller, "Multi-pulse behavior of a high-power sub-100-fs SESAM-modelocked VECSEL", in 7^{th} EPS-QEOD Europhoton Conference (Europhoton), Vienna, Austria (2016), poster

43. D. Waldburger, C. G. E. Alfieri, S. M. Link, E. Gini, M. Golling, M. Mangold, B. W. Tilma, U. Keller, "Pulse shortening of an ultrafast VECSEL", in SPIE Photonics West - LASE, San Francisco, United States (2016), talk

44. C. G. E. Alfieri, D. Waldburger, S. M. Link, E. Gini, M. Golling, B. W. Tilma, M. Mangold, K. Ursula, "Recent progress in high power ultrafast MIXSELs", in SPIE Photonics West - LASE, San Francisco, United States (2016), talk

45. A. Klenner, M. Mangold, A. S. Mayer, A. R. Johson, D. Waldburger, S. M. Link, M. Golling, E. Gini, B. W. Tilma, K. Luke, M. R. E. Lamont, Y. Okawachi, M. Lipson, A. L. Gaeta, U. Keller, "Gigahertz Laser Frequency Combs", in Australia and New Zealand Conference on Optics and Photonics (ANZCOP), Adelaide, South Australia (2015), talk

46. C. Alfieri, D. Waldburger, S. M. Link, E. Gini, M. Mangold, B. Tilma, M. Golling, U. Keller, "Recent Progress in High-Power Femtosecond Semiconductor Disk Lasers", in Advanced Solid State Lasers (ASSL), Berlin, Germany (2015), talk

47. M. Mangold, D. Waldburger, S. M. Link, M. Golling, E. Gini, B. W. Tilma, U. Keller, "High-Power Sub-300-fs Semiconductor Disk Lasers", in European Conference on Lasers and Electro-Optics (CLEO-ECBO), Munich, Germany (2015), **upgrade to invited talk**

48. D. Waldburger, M. Mangold, S. M. Link, M. Golling, E. Gini, B. W. Tilma, U. Keller, "Sub-300-femtosecond semiconductor disk lasers", in Conference on Lasers and Electro-Optics (CLEO), San Jose, United States (2015), talk

49. M. Golling, M. Mangold, C. A. Zaugg, S. M. Link, D. Waldburger, C. G. E. Alfieri, B. W. Tilma, U. Keller, "MBE growth of semiconductor disk laser for repetition rate scaling from 5 to 100 GHz", in 18^{th} European Molecular Beam Epitaxy Workshop (EUROMBE), Canazei, Italy (2015), talk

Abstract

Short pulse lasers can be used not only for applications relying on their enormous pulse peak power, such as material processing or driving of non-linear processes. A rising field of application takes advantage of the frequency properties of such modelocked lasers. The frequency spectrum of the regular pulse train emitted by these lasers consist of equidistant delta-like peaks. This so called optical frequency comb (OFC) can be seen as a ruler in the frequency domain, which allows to measure optical frequencies with a very high accuracy. In 2005 the pioneering work of Roy J. Glauber, John L. Hall, and Theodor W. Hänsch let to the Nobel prize in Physics "*for their contributions to the development of laser-based precision spectroscopy, including the optical frequency comb technique*". By now, optical frequencies can be measured with relative uncertainties down to 10^{-19}. It has been demonstrated that an optical clock based on strontium atoms can keep second-precision even after 15 billion years of time measurement, a period longer than the estimated age of the universe.

OFCs revolutionized frequency metrology. They allow to exactly measure optical frequencies, to transfer optical purity from one wavelength to another, or they can be used for the generation of ultra-low noise microwave frequencies. Furthermore, two OFCs with different comb tooth spacings can be used for nearly instantaneous dual-comb spectroscopy, asynchronous optical sampling, or precise distant ranging. Simple, compact, and cost-efficient laser sources are required to bring these application from the laboratory to the field environment.

For this purpose, semiconductor lasers represent an ideal technology in terms of miniaturization and prize. We are developing semiconductor disk lasers (SDLs) also known as optically pump semiconductor lasers (OPSLs), which combine the benefits of a semiconductor gain material with the advantages of diode-pumped thin-disk laser. Emission wavelengths inaccessible for solid-state laser can be reached by semiconductor band gap engineering and further expanded by efficient intracavtiy wavelength conversion. They convert spacially multimode pump light from cheap commercial diode lasers in a fundamental transverse mode beam. The thin-disk geometry enables excellent heat extraction and allows for mode-size power scalability. Passively modelocked with a semiconductor saturable absorber mirror (SESAM), they provide a compact ultrafast laser source with pulse duration as short as 100 femtosecond (1 fs = 10^{-15} s). In contrast to SESAM-modelocked solid-state laser, the short carrier lifetime and large gain-cross section of SDLs prevents the build-up of Q-switching instabilities. In particular, we are working with vertical external-cavity surface-emitting lasers (VECSELs) and modelocked integrated external-cavity surface-emitting lasers (MIXSELs). The MIXSEL directly integrates the absorber of a SESAM in the gain chip of a VECSEL. Fundamental modelocking with gigahertz repetition rates can be achieved with their simple and compact laser cavities.

The first goal of this doctoral thesis is to scale the performance of ultrafast SDLs both shortening the pulse duration and increasing the average output power. We present a gigahertz SESAM-modelocked VECSEL with pulses as short as 100 fs with kilowatt pulse peak power, making SDLs attractive for many different applications. During my doctoral studies, SDLs designed and produced in our group successfully expand their application range. They are used for high-power amplification in ytterbium-doped yttrium aluminum garnet (Yb:YAG) waveguides, for in-vivo multiphoton microscopy of mice brains, and for wavelength calibration of high-performance spectrometers. Our ultimate goal is to stabilize the OFC of these lasers in a self-referenced way for frequency metrology applications. We succeeded in the stabilization of the OFC without additional pulse amplification or compression, which was possible by using efficient supercontinuum generation (SCG) in a customized silicon nitride

(Si_3N_4) waveguide. This result marks a significant technological step towards compactness of reliable low-noise OFCs based on SDLs.

A different approach with distinctive aims by the dual-comb MIXSEL. This technology was developed in our group and produces two OFCs with different comb spacings from one single cavity. The mutual coherence between the two OFCs is sufficient to perform free-running dual-comb spectroscopy. After the first demonstration of a free-running dual-comb spectroscopy measurement of water vapor with a picosecond dual-comb MIXSEL, the technology is transferred to a femtosecond dual-comb MIXSEL with a more than ten-fold increased spectral bandwidth. With this new dual-comb MIXSEL, we could reconstruct the transmittance spectrum of acetylene in the near infrared (IR) in free-running operation.

Kurzfassung

Laser mit kurzen Pulsen sind nicht nur gefragt wegen ihrer hohen Pulsspitzenleistungen, welche Anwendung in der Materialbearbeitung finden oder für nichtlineare Effekte benutzt werden. Sondern auch wegen der spektralen Eigenschaften dieser modengekoppelten Laser, welche einen neuen aufstrebenden Bereich der optischen Frequenzmessung ermöglichten. Das Frequenzspektrum des Pulszuges eines solchen Lasers besteht aus äquidistanten scharfen Linien. Dieser sogenannte optische Frequenzkamm (genannt OFC für "optical frequency comb") kann wie ein optisches Lineal für hochgenaue Frequenzmessungen benützt werden. "*Für ihre wegweisenden Beiträge zur Entwicklung von laserbasierten Präzisionsspektroskopie einschliesslich der optischen Frequenzkammtechnik*" wurden Roy J. Glauber, John L. Hall und Theodor W. Hänsch im Jahr 2005 mit dem Nobelpreis in Physik geehrt. Mittlerweile sind optische Frequenzmessungen mit relativen Unsicherheiten von bis zu 10^{-19} möglich. Dies ermöglicht optische Gitteruhren mit Strontiumatomen, welche nur eine Sekunde falsch gehen über einen Zeitraum von 15 Milliarden Jahre, eine Zeitspanne länger als das geschätzte Alter des Universums.

Optische Frequenzkämme revolutionierten die Frequenzmetrologie. Sie ermöglichen die präzise Messung von optischen Frequenzen, den Transfer von optischen Signalen von einer Wellenlänge zu einer anderen oder die Generierung von ultrastabilen Mikrowellenfrequenzen. Des Weiteren können zwei optische Frequenzkämme mit unterschiedlichen Kammlinienabständen kombiniert werden für nahezu augenblickliche Doppelkamm-

Spektroskopie, für ungleichzeitiges optisches Sampling oder für präzise Distanzmessungen. Um diese Anwendungen nicht nur in der Forschung, sondern auch im Alltag zu ermöglichen, benötigt es einfache, kompakte und erschwingliche Laserquellen.

Diesbezüglich bieten Halbleiterlaser eine ideale Technologie hinsichtlich Miniaturisierung und Preis. Wir entwickeln Halbleiterscheibenlaser (abgekürzt SDL für "semiconductor disk laser"), auch optisch gepumpte Halbleiterlaser genannt (kurz OPSL für "optically pump semiconductor laser"), welche die Vorteile des Halbleiterverstärkungsmaterials mit den Vorzügen von dioden-gepumpten Scheibenlasern kombinieren. Emissionswellenlängen unerreichbar für Festkörperlaser können mit Abstimmung der Bandlückenenergie im Halbleitermaterial erreicht werden und überdies mit effizienter intrakavitären Frequenzumwandlung erweitert werden. SDLs wandeln Licht mit höheren transversalen Moden von preiswerten kommerziellen Pumpdiodenlasern in einen Laserstrahl mit beugungsbegrenzte Strahlqualtität um. Die Scheibengeometrie erlaubt eine effiziente Kühlung und ein Skalieren der Leistung durch Vergrössern der räumlichen Lasermode. Passives Modenkoppeln mit einem sättigbaren Halbleiterabsorberspiegel (abgekürzt SESAM für "semiconductor saturable absorber mirror") ermöglich die Erzeugung von ultrakurzen Pulsen mit Pulsdauren von bis zu 100 Femtosekunden (1 fs = 10^{-15} s). Im Gegensatz zum SESAM-modengekoppelten Festkörperlaser sind SDL nicht anfällig für Güteschaltungsinstabilitäten, weil sie eine kurze Ladungsträgerlebenszeit und einen grossen Verstärkungsquerschnitt aufweisen. Im Speziellen arbeiten wir mit oberflächenemittierende Halbleiterlaser mit externem Resonator (abgekürzt VECSEL für "vertical external-cavity surface-emitting laser") und einem noch kompakteren Laser, bei dem der sättigbare Absorber eines SESAMs direkt in die Schichtstruktur eines VECSELs integriert ist (gennant MIXSEL für "modelocked integrated external-cavity surface-emitting laser"). Mit der Hilfe dieser einfachen und kompakten Resonatoren können sehr hohe Pulsewiederholungsraten im Gagahertzbereich erreicht werden mit sauberem fundamentalem Modenkoppeln.

Das erste Ziel dieser Doktorarbeit umfasst die Verbesserung von SDLs, wobei die Pulsdauer reduziert und die Ausgangsleitung erhöht werden soll. Wir präsentierten einen SESAM-modengekoppelten VECSEL mit Pul-

sen so kurz wie 100 fs und einer Pulsspitzenleistung von einem Kilowatt, dies macht diese Laser interessant für eine Vielzahl von Anwendungen. Die während meines Doktoratsstudiums entwickelten und produzierten SDLs öffnen die Tür für vielen neuen Anwendungen. Die SDLs wurden unter anderm benutzt für die Verstärkung in Ytterbium-dotierten Yttrium-Aluminium-Granat (Yb:YAG) Wellenleitern mit hohen Leistungen, für die Mehrphotonenmikroskopie eines Gehirns einer lebenden Maus und für die Wellenlängenkalibierung eines hoch-präzisen optischen Spektrometers. Unser Hauptziel ist die selbst-referenzierte Stabilisierung des OFCs dieser Laser für Frequenzmetrologieanwendungen. Schlussendlich ist es uns gelungen den OFC zu stabilisieren, ohne zusätzlich die Pulse zu verstärken oder zu komprimieren. Diese wurde ermöglicht durch die effiziente Erzeugung eines Superkontinuums mit der Hilfe eines speziell angepassten Siliziumnitrid (Si_3N_4) Wellenleiters. Dieses Resultat markiert einen bedeutenden technologischen Fortschritt der Kompaktheit von zuverlässigen rauscharmen OFCs basiert auf SDLs.

Ein anderen Ansatz nimmt der in unserer Gruppe entwickelte Doppelkamm-MIXSEL. Der Doppelkamm-MIXSEL erzeugt zwei OFCs mit unterschiedlichen Linienabständen in dem gleichen Laserresonator. Die gegenseitige Kohärenz der beiden OFCs erlaubt Doppelkamm-Spektroskopie ohne zusätzliche Stabilisierung. Nach der ersten Demonstration einer Doppelkamm-Spektroskopiemessung von Wasserdampf mit einem Picosekunden-Doppelkamm-MIXSEL, wurde ein Doppelkamm-MIXSEL mit Femtosekundenpulsen und einem mehr als zehnfach breitern optischen Spektrum entwickelt. Dieser Femtosekunden-Doppelkamm-MIXSEL wurde dann benützt um das Transmissionsspektrum von Acetylen im Infraroten zu messen ohne dass der Laser stabilisiert werden musste.

Chapter 1

Introduction

Without laser (which stands for light amplification by stimulated emission of radiation) [1], our world would not be as it is. They are used in countless commercial, science, medical, industrial, and military applications. In many homes there are CD/DVD/Blu-Ray players, proximity sensors, optical smoke detectors, and high-speed telecommunication over glass fibers. Lasers are also used in many domains of science such as spectroscopy, light detection and ranging (lidar) for geology and seismology. Even the detection of gravitational waves would not have been possible without the laser interferometer gravitational-wave observatory (LIGO) [2]. Medical applications include eye surgery, tattoo removal, or cancer treatment. In industry, lasers are used for welding, cutting, and hardening of metal. But also the military sector is interested to use lasers as energy weapons, missile defense, and ranging instruments. New rising applications are among others: laser lighting such as laser based video projectors or car headlights, extreme ultraviolet (XUV) lithography, and quantum computing with trapped ions.

Ultrafast lasers with pulse duration in the picosecond (1 ps = 10^{-12} s) or even femtosecond (1 fs = 10^{-15} s) expand the possible application even further. They increase the speed and precision of micro-machining and enable the processing of glass. The short and intensive laser pulses are used in routine medical interventions in ophthalmology, stomatology, and dermatology. The pulse duration reaches timescales of fundamental atomic and molecular processes leading to ground-breaking research in various

scientific fields. Attosecond science studies chemical processes and electron dynamics on an attosecond (1 as = 10^{-18} s) time scale [3], nonlinear microscopy can resolve structures below the diffraction limit [4], and ultrafast lasers can be even used to remotely inspect the surface of planets [5]. The scientific community recognized the revolutionary impact of laser-based innovations and discoveries and awarded them recently with three Nobel prices in Chemistry 1999 [6], in Physic in 2005 [7], and in Chemistry 2014 [8].

Cutting-egde scientific experiments use in general ytterbium (Yb)-doped fiber and solid-state lasers or ultrafast lasers based on titanium-sapphire (Ti:sapphire), which represent complex, expensive and volume-demanding solutions. For this reason, the application-oriented industrial world looks with ever increasing interest at flexible and compact laser sources with a high degree of integration and large-scale production potential. Semiconductor lasers, thanks to a natural inclination to coast-effectiveness and mass fabrication, are the most representative example of today's broad dissemination of lasers. They are the leading technology in fiber communication, consumer electronics (laser pointers, etc.) and they are the the base of the face recognition system in the iPhone X.

Edge-emitter

The first semiconductor diode laser was demonstrated in 1962 [9]. The semiconductor material has a high gain cross-section providing sufficient optical gain with small devices. By engineering of the semiconductor bang-gap energy, the laser emission can be achieved from the blue to the mid-infrared (IR) and wafer-scale fabrication reduces the price in mass production. Semiconductor diode lasers are typically edge-emitting (Fig. 1.1) with a laser cavity along the plane of the wafer. They are usually electrically pumped and can be stacked for high-power operation. Edge emitters are widely used in industry, but they have the drawback of strongly diverging beams.

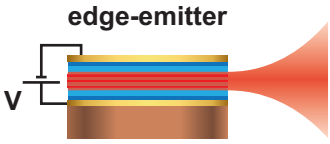

Figure 1.1: Schematic of an electrically pumped edge-emitting semiconductor lasers.

VCSEL

For applications requiring high brightness and good beam quality, a vertical cavity surface-emitting laser (VCSEL) can be used [10]. As the name suggests, a VCSEL adopts a vertical cavity scheme where the laser is emitted at the surface of the wafer (Fig. 1.2). The cavity is formed by a monolithic Fabry-Pérot resonator with a highly reflective bottom mirror and a partially reflective top mirror. The active region in between is electrically pumped. The world-wide optical telecommunication and the face recognition in the iPhone X are based on VCSELs. However their average output power is limited to few milliwatts per device.

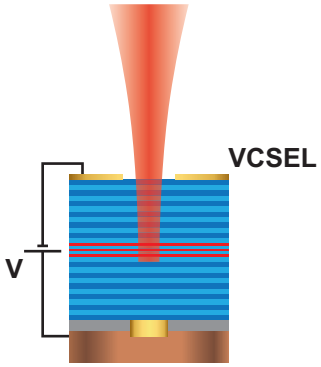

Figure 1.2: Schematic of an electrically pumped vertical cavity surface-emitting laser.

VECSEL

The vertical external-cavity surface-emitting laser (VECSEL) [11, 12], or more generally called semiconductor disk laser (SDL), is similar to the VCSEL except for the partially reflective top mirror which is replaced with an external output coupler (OC) (Fig. 1.3). It combines the key advantages of semiconductor lasers and the ones of thin-disk solid state lasers [13]. VECSELs can also be optically pumped with cheap commercial transversal multimode pump diodes. The VECSEL is an efficient brightness converter

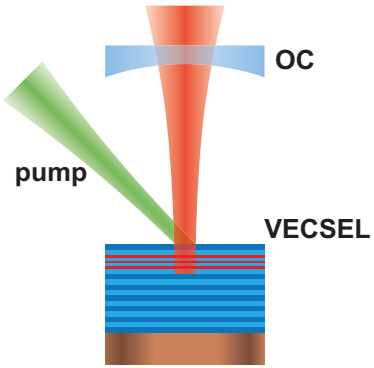

Figure 1.3: Schematic of an optically pumped vertical external-cavity surface-emitting laser.

and reached average output powers up to 106 W (in multimode operation) [14]. The VECSEL benefits from the thin disk geometry (sub-10-µm thickness) which results in a quasi one-dimensional heat-flow for efficient cooling and allows for power scaling by simply increasing the mode size area.The external air cavity offers space for additional intracavity elements such as etalons and birefringence filters for narrow wavelength operation or nonlinear crystals for efficient intracavity wavelength conversion from the ultraviolet (UV) to the mid-IR. These continous wave (cw) VECSELs are used as lighting or pumping sources, for medical application, or to trap ions for quantum computing. A comprehensive overview of recent cw VECSELs is given by the review paper by Guina *et al.* [15].

SESAM-modelocked VECSEL

For modelocked operation, the cavity mirror is extended with a semiconductor saturable absorber mirror (SESAM) [16]. Fundamental modelocking is typically achieved in simple V-shaped cavity (Fig. 1.4). They usually operate at gigahertz repetition rate - a regime where ultrafast solid-state and fiber lasers find problematic challenges with geometrical and Q-switching limitations [17, 18]. The short carrier lifetime of few hundreds of picoseconds [19] and the large gain-cross section of SDLs prevents the build-up of Q-switching instabilities [20].

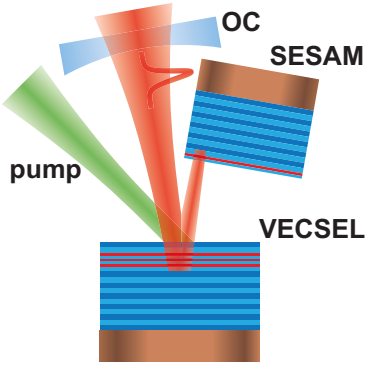

Figure 1.4: Schematic of an optically pumped SESAM-modelocked VECSEL with a typical V-shaped cavity.

Since the first demonstration of a SESAM-modelocked VECSEL in 2000 [21], the performance of ultrafast SDLs has been constantly improved. Pulses as short as 100 fs [22, 23] (see section 2.1 and 3.5) and pulse peak power up to 6.3 kW [24] have been shown. Even though there are few commercial ultrafast laser based on SESAM-modelocked VECSEL, further research on this technology is required to enable a commercial breakthrough. A comprehen-

sive overview of ultrafast SDLs is given by the following review papers [25, 26, 27, 28, 15].

MIXSEL

Even more compact is the modelocked integrated external-cavity surface-emitting laser (MIXSEL) [29, 30] which combines the saturable absorber of a SESAM and the gain structure of a VECSEL in a single epitaxial structure. Consequently, fundamental modelocking can be achieved in a straight laser cavity (Fig. 1.5). The simple arrangement of the laser cavity allows for high pulse repetition rate up to 100 GHz [31]. The performances of the MIXSELs approaches the results obtained with SESAM-modelocked VECSELs with average output power up to 6.4 W [32] and 139 fs pulse durations (see section 3.3). By inserting a birefringent crystal inside the cavity, the MIXSEL can be converted in a dual-comb MIXSEL [33, 34, 35], which produces two modelocked lasers with slightly different pulse repetition rates from the same laser cavity. The dual-comb MIXSEL enables free-running dual-comb spectroscopy (see chapter 5).

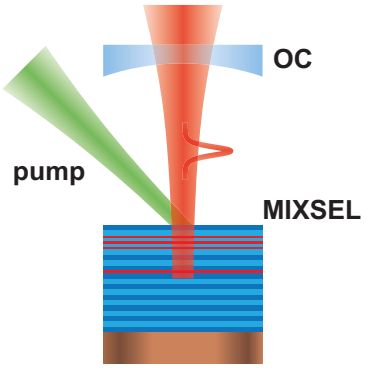

Figure 1.5: Schematic of an optically pumped MIXSEL.

Optical frequency comb

Ultrafast lasers are not only interesting for their short pulses in the time domain but also for their spectral features in the frequency domain. To form a pulse in the time domain, a spectrum made up of several frequencies is required, as described by the fundamental principle of the Fourier transform $\mathcal{F}$. The electric field (given by the real part of the complex formulation $E(t)$) of a pulse can be described by the product of a complex exponential with a temporal envelope function $A(t)$ (e.g. a Gaussian or hyperbolic secant shape) by $E(t) = A(t) \cdot e^{i\omega_0 t}$ with the carrier angular

frequency being ω_0. The corresponding frequency spectrum is given by the Fourier transform:

$$\mathcal{F}[E(t)] = \tilde{E}(\omega) = \tilde{A}(\Delta\omega = \omega - \omega_0), \tag{1.1}$$

with $\tilde{A}(\omega) = \mathcal{F}[A(t)]$. A modelocked laser with a pulse repetition rate f_{rep} can be described by an infinite train of pulses spaced by the roundtrip time $T_{\mathrm{r}} = 1/f_{\mathrm{rep}}$:

$$\begin{aligned} E(t) =& \sum_n A(t - n \cdot T_{\mathrm{r}}) \cdot e^{i\omega_0(t - n\cdot T_{\mathrm{r}})} \cdot e^{2\pi i f_{\mathrm{CEO}} n T_{\mathrm{r}}} \\ =& A(t) \cdot e^{i\omega_0 t} * \sum_n \delta\left(t - n \cdot T_{\mathrm{r}}\right) \cdot e^{2\pi i f_{\mathrm{CEO}} t}, \end{aligned} \tag{1.2}$$

where the carrier envelope-offset (CEO) frequency f_{CEO} describes an additional pulse-to-pulse phase shift of the carrier wave underneath the pulse envelope $A(t)$. The corresponding optical spectrum consists of equidistant sharp delta peaks separated by f_{rep} underneath the spectral pulse envelope $\tilde{A}(\omega)$ with a zero-offset given by f_{CEO}:

$$\tilde{E}(\omega) = \tilde{A}(\Delta\omega) \cdot \sum_n \delta\left(\omega - 2\pi\left(n \cdot f_{\mathrm{rep}} + f_{\mathrm{CEO}}\right)\right). \tag{1.3}$$

In analogy to a hair comb, these spectra are called optical frequency combs (OFCs) (Fig. 1.6). They can be used as an optical ruler to measure optical frequency (at hundreds of terahertz) with a very high precision. The beat note of the unknown frequency with the OFC (in the megahertz

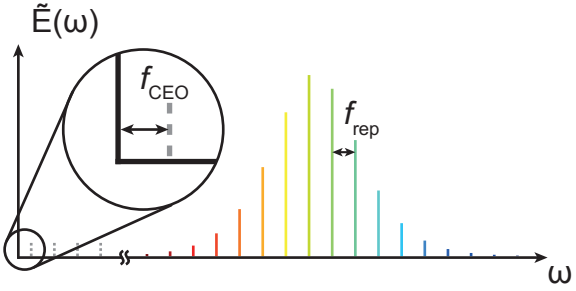

Figure 1.6: Optical frequency comb. A spectrum with equidistant spaced delta-like lines. The spacing of the lines is given by the pulse repetition rate (f_{rep}) and the offset to zero defines the carrier-envelope offset frequency (f_{CEO}).

regime) can be detected with standard electronics and describes the frequency difference of the unknown frequency and the nearest comb line. Knowing the beat note, f_{rep}, f_{CEO} and the number n of the nearest comb line, the unknown frequency is exactly defined. OFCs revolutionized frequency metrology and the pioneering of Roy J. Glauber, John L. Hall and Theodor W. Hänsch was awarded with the Nobel price in Physics in 2005 [7].

Many frequency metrology applications require the OFC to be fully stabilized, which means that both the pulse repetition rate f_{rep} and the CEO frequency f_{CEO} have to be stabilized. The pulse repetition rate can be directly detected and is straight forward to stabilized by for example varying the cavity length. The CEO frequency poses a more severe challenge, as it can be detected only indirectly. One way the f_{CEO} can be detected in a self-referenced amnner is f-to-2f interferometry [36]. The f-to-2f interferometry requires an octave-spanning spectrum, also called supercontinuum (SC). Consequently, modelocked lasers, which typically have optical spectra significantly narrower than one octave, have to be spectrally broadened in nonlinear media to reach an octave-spanning SC. The spectral broadening can take place for example in photonic-crystal fibers (PCFs) or silicon nitride (Si_3N_4) waveguides (see chapter 4). They require typically pulse duration of 100 fs or below with kilowatts of pulse peak power [37] for coherent octave-spanning supercontinuum generation (SCG). Once f_{CEO} is detected, it is typically stabilized by varying the power of the pump laser.

Outline of the thesis

The goal of this doctoral thesis is to scale the performance of ultrafast SDLs. We want to shorten the pulse pulse duration and to increase the average output power to enable new applications of these lasers, with the ultimate goal in mind, to fully stabilize the OFC without the need for external pulse amplification or compression.

Chapter 2 addresses the epitaxial optimization of the VECSEL gain structure which lead to the high-power 100 fs semiconductor disk lasers described in section 2.1. At the moment this gain structure produces the

shortest fundamental modelocked pulses of any SDLs.

To further scale the performance, we investigated the current limitations in chapter 3. In section 3.1, we study the multipulse instabilities arising at hight pump powers, which limit the average output power in fundamental modelocking. In section 3.2, we investigate a new laser cavity design which allows for colliding pulse modelocking (CPM). We show that the two output beams can be coherently combined for a resulting four-time increased power in comparison with a single beam. In section 3.3, we present a record short pulse MIXSEL. The MIXSEL was grown by molecular beam epitaxy (MBE) instead of metalorganic vapour phase epitaxy (MOVPE) as the VECSEL presented in chapter 2. One key aspect for the better performance is the increased thermal conductivity of the epitaxial structures grown by our MBE university machine compared to the MOVPE machine. The thermal conductivity is measured with a thermal camera in a setup described in details in section 3.4. VECSELs also benefit from the growth on the MBE machine. In modelocked operation, an MBE VECSEL produced 100-fs pulses with an increased average output power of 150 mW and a pulse peak power of 1.16 kW shown in section 3.5. In section 3.6, we take a closer look at the optical efficiency of SDLs. Semiconductor gain media based on quantum dots (QDs) promise a longer carrier life time compared to quantum wells (QWs) which is expected to significantly increase the optical-to-optical efficiency of SDLs. We investigate two types of QDs one grown by the Stranski–Krastanov (SK) technique and one by the sub-monolayer (SML) technique. It emerges that SK QDs enable more efficient sub-300-fs modelocked operation (section 3.7) while SML QDs are better suited for cw operation (section 3.8).

In chapter 4, we describe how we were able to fully stabilize the OFC of an ultrafast SDL in a self-referenced way without external pulse amplification or compression by combining major advances in two fields: the development of the ultrafast 100 fs SESAM-modelocked VECSEL with 1-kilowatt pulse peak power (section 3.5) and a customized Si_3N_4 waveguide for efficient SCG even with small pulse energies, provided by the groups of Prof. Alexander L. Gaeta and Prof. Michal Lipson from Columbia University.

Last but not least, we demonstrate the potential of the dual-comb MIXSEL by performing free-running dual-comb spectroscopy of water vapor (section 5.1). With the new MIXSEL presented in section 3.3, the dual-comb MIXSEL was pushed from tens of picoseconds to femtosecond operation with a more than ten-fold increase of the optical bandwidth. A fundamental aspect of this result is the good thermal conductivity of the MIXSEL chip which reduced the thermal cross talk between the two laser spots of the dual-comb MIXSEL. The upgraded version of the dual-comb MIXSEL is then used to measure the transmittance spectrum in the near-IR of an acetylene-filled gas cell in free-running operation (section 5.2).

The main results of chapters 2 to 5 are presented in journal publications. The text and figures are printed as published, only the format of the text, the numbering and the size of the figures and tables were adapted to the style of this thesis. All papers are reprinted with permission. The copyright of the original publications are held by the respective copyright holders.

Chapter 2

Ultrafast VECSEL

In this chapter, we describe the epitaxial optimization of the VECSEL gain structure which lead to the high-power 100 fs semiconductor disk lasers. At the moment this gain structure produces the shortest fundamental modelocked pulses of any SDLs. The transform-limited optical spectrum could in principle support pulses as short as 65 fs. The optical properties of the VECSEL gain chip are characterized and the modelocking results could be reproduced with our pulse formation simulation. The details are presented in the following journal publication:

Title: "High-power 100 fs semiconductor disk lasers", [23]
Journal: *Optica*
doi: 10.1364/OPTICA.3.000844

2.1 High-power 100 fs semiconductor disk lasers

Dominik Waldburger,[1] *Sandro M. Link,*[1] *Mario Mangold,*[1] *Cesare G. E. Alfieri,*[1] *Emilio Gini,*[2] *Matthias Golling,*[1] *Bauke W. Tilma,*[1] *and Ursula Keller*[1]

[1]Department of Physics, Institute for Quantum Electronics, ETH Zürich, 8093 Zürich, Switzerland

[2]FIRST Center for Micro- and Nanoscience, ETH Zürich, 8093 Zürich, Switzerland

Optically pumped passively modelocked semiconductor disk lasers (SDLs) provide superior performance in average output power, a broad range of operation wavelengths, and reduced complexity. Here, we present record performance with high average power and pulse durations as short as 100 fs with a semiconductor saturable absorber mirror (SESAM) modelocked vertical external-cavity surface-emitting laser (VECSEL) at a center wavelength of 1034 nm. A comprehensive pulse characterization confirms fundamental modelocking with a close to transform-limited output pulse of 128 fs and with negatively chirped output pulses as short as 107 fs, which are externally compressed to 96 fs with a single path through a 2-mm-thick ZnSe plate. For the "96 fs result" the pulse repetition rate is 1.6 GHz, the average output power is 100 mW, and the pulse peak power is 560 W. The transform-limited optical spectrum could in principle support pulses as short as 65 fs with higher order dispersion compensation. We measured the most relevant spectral and nonlinear VECSEL and SESAM parameters and used them as input parameters for our pulse formation simulations. These simulations agree well with our experimental results and provide an outlook for further performance scaling of ultrafast SDL technology.

2.1.1 Introduction

Passive modelocking of optically pumped semiconductor disk laser (SDL) [1] using semiconductor saturable absorber mirrors (SESAMs) [2] has demonstrated impressive progress during the past 10 years, as reviewed recently [3]. The optically pumped vertical external-cavity surface-

emitting laser (VECSEL) [4] was the first laser in the family of semiconductor disk lasers to demonstrate significant power scaling by superior heat removal in a thin disk geometry. The optically pumped VECSEL is an efficient mode converter that uses low-coherent high-power diode pump arrays and benefits from semiconductor bandgap engineering to support emission wavelengths ranging from UV to mid-IR (i.e., 391 nm up to 5.3 μm) [5,6]. The highest continous wave (cw) output power is ≈20 W in a Gaussian mode profile [7-9] and 106 W in multimode operation [10] at an emission wavelength around ≈1 μm using InGaAs quantum well gain on GaAs/AlGaAs Bragg reflectors. Here, we present record power performance with SESAM-modelocked VECSELs generating pulse durations in the 100 fs regime (Fig. 2.1).

We have observed a strong tradeoff between short pulse durations and average power or pulse peak power (Fig. 2.1). Fundamental physical processes, such as non-equilibrium kinetic hole burning [12], can partially explain this, but the full complex interplay between the gain and absorber dynamics in these high-Q SDLs are not yet fully understood. To date, the shortest pulses have been 107 fs, but with only 3 mW of average output power [13] and 60 fs in a pulse train within a picosecond pulse envelope [14]. The highest pulse peak power of up to 4.35 kW was obtained with significantly longer pulses of 400 fs duration [15].

Peak power scaling by reducing the pulse repetition rate has been successfully demonstrated with diode-pumped solid-state lasers [16]. This approach is less attractive for diode-pumped semiconductor lasers because the highly inverted quantum well gain has a lifetime of only a few hundred picoseconds, which currently limits the pulse repetition rate of quantum well VECSELs to above 100 MHz without the use of a more elaborated multi-gain-pass cavity [17,18]. Quantum dot gain SDLs [19-21] have a longer upper-state lifetime and may offer better performance in the future.

Many applications greatly benefit from a combination of femtosecond pulses with high pulse peak power to drive nonlinear optical processes, such as two-photon absorption for multiphoton microscopy [22] or supercontinuum generation for frequency comb applications [23-25]. The standard method to detect and stabilize the carrier envelope-offset (CEO)

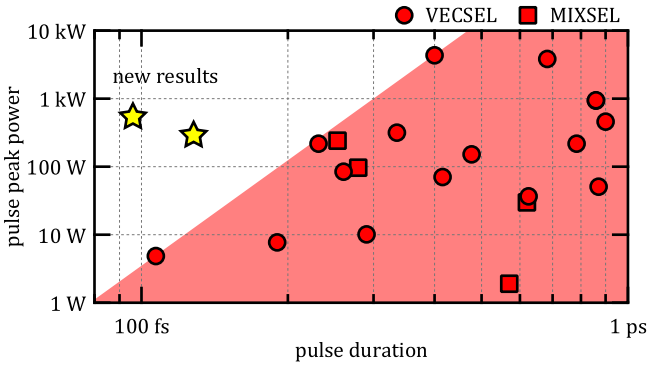

Figure 2.1: Overview of the pulse peak power versus pulse duration of the state-of-the-art femtosecond SDLs operating at a center wavelength around 1 µm using InGaAs gain layers [3,11]. The yellow stars indicate the two new milestone results presented in this paper.

frequency in a self-referencing scheme is based on f-to-$2f$ interferometry [26], for which a coherent octave-spanning spectrum is required. Typically the combination of sub-100-fs pulses with kilowatt pulse peak power was required for coherent supercontinuum generation in photonic crystal fibers [27], but supercontinuum generation in silicon nitride waveguides strongly reduces this requirement [28].

The limited upper-state lifetime of semiconductor lasers makes them ideally suited for gigahertz pulse repetition rates and the high gain cross-section eliminates Q-switching instabilities, typically a challenge with SESAM-modelocked diode-pumped ion-doped solid-state lasers [29,30]. The gigahertz repetition rate can be beneficial for frequency comb applications, since the comb lines have a larger frequency spacing with more power per mode and therefore provide a better signal-to-noise ratio (SNR). Additional benefits are a faster data acquisition or a faster data transmission in telecommunication applications [31]. To date, ultrafast SDLs have been demonstrated up to 100 GHz [32].

Here, we present two new milestone results for femtosecond ultrafast SDLs (shown in yellow in Fig. 2.1). First, our “128 fs result” with a pulse duration of 128 fs, a pulse repetition rate of 1.8 GHz, an average power of 80 mW, and, therefore, a pulse peak power of 303 W, slightly improved compared to [33]. Second, we present our “96 fs result” with a pulse

duration of 96 fs, a pulse repetition rate of 1.6 GHz, an average power of 100 mW, and, therefore, a pulse peak power of 560 W. These are, to the best of our knowledge, the shortest pulses of a fundamental modelocked SDL. To achieve pulse duration of 96 fs, the slightly negatively chirped 107 fs output pulses have been compressed with a single path through a 2-mm-thick zinc selenide plate.

We used a newly optimized VECSEL structure following the guidelines based on numerical pulse formation simulations [34]. This VECSEL structure has a larger gain saturation fluence and a slightly positive but flat group delay dispersion (GDD) over a larger gain bandwidth. In addition, a fast SESAM with a low saturation fluence was required. In a similar approach Head et al. [35] presented preliminary results of a high-power sub-200-fs VECSEL. We did not include this result in our overview graph because the VECSEL chip got damaged before fundamental modelocking was confirmed. Higher average power can easily be obtained with multiple pulses per cavity round-trip.

We measured most laser and absorber parameters (Table 2.1) [36,37], which were used as input parameters for our numerical pulse formation simulation and obtained a good agreement. This allows us to give an outlook for further performance scaling at the end of this paper.

2.1.2 Laser design

The laser cavity is arranged in a simple V-shaped cavity where the output coupler and the SESAM form the end mirrors, and the VECSEL chip is used as a folding mirror, as shown in Fig. 2.2. For the "96 fs result" [Fig. 2.2(a)], we changed the V-shaped cavity such that we more strongly saturate the absorber (i.e., beam radius in the gain estimated from ABCD-matrix calculations is increased from 186 to 192 μm, and in the absorber the beam radius is decreased from 100 to 83 μm; Table 2.1) and obtained more balanced cavity legs L_1 and L_2 (Fig. 2.2), which is clearly preferred for better gain recovery. In addition, for the "96 fs result", we inserted a 1-mm-thick fused silica Brewster plate (Infrasil 302, 300 wedged; wzw-optic AG) between the VECSEL and the SESAM for more stable operation in linear polarization and shorter pulses. The wedged plate strongly reduces etalon effects and introduces additional positive dispersion inside the cav-

ity. The VECSEL is pumped under an angle of 45° with a 35 W, 808 nm spatial multimode diode laser (LIMO; Lissotschenko Mikrooptik GmbH), with an elliptical shaped beam such that on the VECSEL chip surface the pump beam is circular with a radius of 177 µm. For the "96 fs result" we used a pump power of 21 W and for the "128 fs result" we used 18.1 W. The VECSEL and the SESAM are temperature stabilized with water-cooled Peltier elements to 1°C (-10°C) and 37°C (24°C), respectively for the "96 fs result" ("128 fs result").

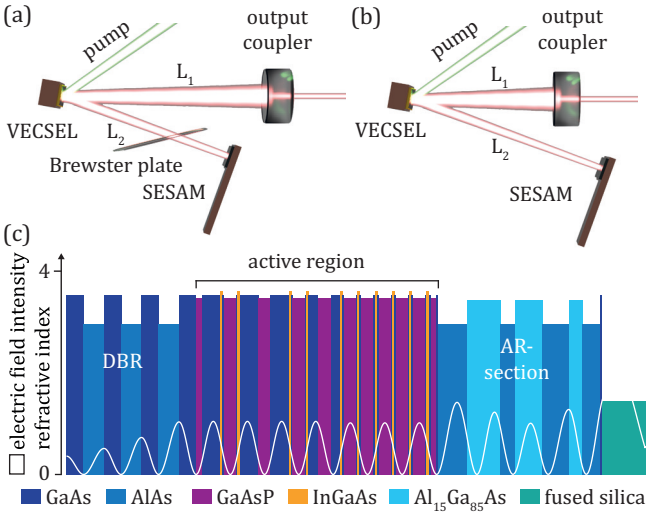

Figure 2.2: V-shaped cavity design with SESAM and output coupler as end mirrors and the VECSEL gain chip as a folding mirror. The output coupler has a 0.9% transmission and a radius of curvature of 100 mm. The folding angle is 20°. The 1-mm-thick fused silica Brewster plate was only used for the "96 fs result." (a) Cavity for the "96 fs result": $L_1 = 4.8$ cm and $L_2 = 4.2$ cm. (b) Cavity for the "128 fs result": $L_1 = 3.4$ cm and $L_2 = 4.8$ cm. (c) VECSEL layer stack, with a distributed Bragg reflector (DBR), a strain-compensated active region with 10 InGaAs quantum wells, and a multi-purpose AR section. The center laser wavelength is designed to be 1030 nm, and the white curve indicates the corresponding standing electric field intensity (normalized to 4 outside the structure).

A. VECSEL

The VECSEL structure was grown on a metalorganic vapour phase epitaxy (MOVPE) machine. For flip-chip bonding, the structure was grown in reversed order on a 600-μm-thick, (100)-oriented GaAs substrate. The structure is divided into a DBR, an active region, and a multipurpose antireflection (AR) top coating, as shown in Fig. 2.2(c). The active region is grown at a lower substrate temperature of 660°C, while the DBR and the AR top coating are grown at 750°C.

The DBR consists of 23.5 pairs of GaAs/AlAs quarter-wave layers, which balances the tradeoff between sufficient DBR reflectivity and high thermal conductivity to the underlying heat spreader. The center wavelength is designed to be at 1030 nm.

The active region contains five pairs of strain-compensated InGaAs quantum wells. The compressively strained, 8.8-nm-thick $In_{0.193}Ga_{0.807}As$ quantum wells are embedded in GaAs and compensated by 54 nm tensile strained $GaAs_{0.933}P_{0.067}$ layers. The quantum well pairs are separated by 64 nm and are placed symmetrically around the node or the anti-node of the standing electric field intensity. The spacing is optimized to obtain a low and spectrally flat field intensity enhancement factor of 0.52 [Fig. 2.3(a)]. The field intensity enhancement factor is defined as the field intensity inside the quantum wells averaged over all quantum wells and is normalized to the incoming field intensity (i.e., a 100% reflector results in a field intensity of 4) [38]. The spectrally flat field intensity enhancement avoids structural gain bandwidth restrictions, and the lower field intensity enhancement is expected to increase the gain saturation fluence at the expense of available gain. The pump absorbing GaAs layers become thicker with increasing penetration of the pump light [Fig. 2.2(c)], and the AR coating is designed for no absorption. The AR section consists of 3.5 pairs of $Al_{0.15}Ga_{0.85}As$/AlAs followed by a fused SiO_xN_y dielectric layer and is optimized for a reduced pump reflectivity, a broadband flat GDD, and a close to zero but positive GDD.

The semiconductor structure is cleaved in 4.5 mm⋄4.5 mm pieces and is then flip-chip bonded onto a 1-mm-thick chemical vapor deposited diamond heat spreader with a high thermal conductivity exceeding 2000 W m^{-1} K^{-1} [39]. After soldering and wet etching, the final SiO_xN_y

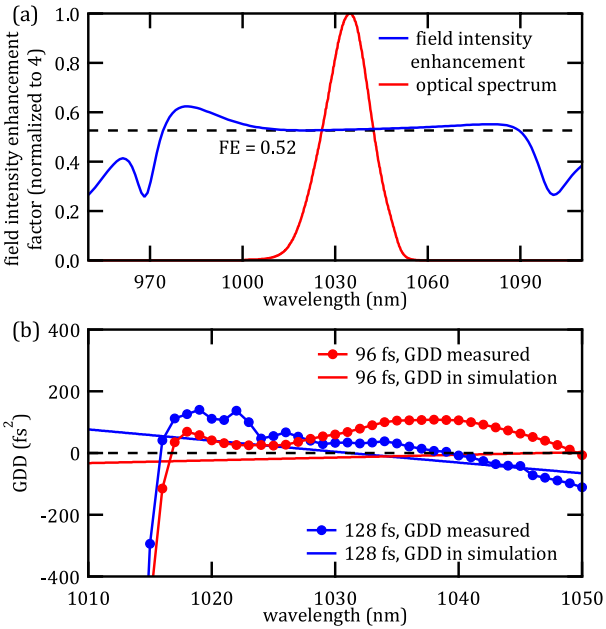

Figure 2.3: (a) Average field intensity in the gain quantum wells of the VECSEL (blue) normalized to the incoming field intensity (i.e., a 100% reflector results in a field intensity of 4) and the measured optical spectrum (red). (b) Measured GDD of the "unpumped" VECSEL structure at normal incidence and at room temperature (circles). For simulation of the modelocking results, we used the dispersion (both second and third order) as an adjustable parameter (Table 2.1). The dispersion explaining our pulse durations is shown for the "128 fs result" (blue line) and the "96 fs result" (red line).

layer is deposited using plasma-enhanced chemical vapor deposition (PECVD; Oxford Instruments).

The two modelocking results have been achieved with chips from different processing runs resulting in different SiO_xN_y layer thicknesses and so different GDD. The GDD of the VECSELs is measured at 20°C without optical pumping [40]. The measured GDD curves [Fig. 2.3(b)] are not flat but have in comparison to prior results [23] a much smaller deviation of ± 100 fs^2. The drop in GDD at 1015 nm is due to the absorption of the quantum wells. The nonuniform PECVD deposition allows us to further optimize the GDD by scanning the position on the processed chip.

Table 2.1: Complete list of input parameters used for the pulse formation simulation. (All non-italic parameters have been directly measured. If different, we show the parameters for the two modelocking results as follows: 96 fs input parameter/128 fs input parameter.)

Cavity		**VECSEL**		**SESAM**	
Output coupler	0.9%	Saturation fluence	40 μJ/cm^2	Saturation fluence	4.33 / 5.4 μJ/cm^2
Other losses	0.8%	*Recovery time*	3 ns	Fast recovery time	560 fs
Repetition rate	1.63 / 1.81 GHz	*Linewidth enhancement factor*	3	Slow recovery time	5.5 ps
Center wavelength	1034 / 1033 nm	Small signal gain	2.9%	Amplitude of slow component	0.25
Round-trip GDD	-12 / 12 fs^2	Gain FWHM	50 nm	*Linewidth enhancement factor*	2
Round-trip TOD	-500 / 620 fs^2	*Beam radius*	192 /185 μm	Modulation depth	2.03 / 1.37 %
				Beam radius	83 / 100 μm

B. SESAM

The SESAM was grown on a molecular beam epitaxy (MBE) machine. A single InGaAs quantum well absorber is grown on top of a 30 pair GaAs/AlAs DBR. To achieve a fast recovery time, the absorber is grown at a low temperature of 260°C and is embedded in AlAs barriers. The field intensity enhancement factor of the antiresonant structure can be engineered by PECVD deposition of a SiN_x top coating. An increased field intensity enhancement gives rise to a lower saturation fluence and an increased modulation depth [38]. For the "96 fs result", we reduced the mode size for a stronger saturation and increased the modulation depth with a higher temperature (i.e., moving from a heat-sink temperature of 24°C to 37°C). All SESAM parameters are summarized in Table 2.1.

2.1.3 Modelocking result

A careful and extended pulse characterization has to be performed to prove clean and stable fundamental modelocking. An incomplete or limited characterization may incorrectly suggest fundamental modelocking and may result in much higher average output powers [11]. In the following, the two modelocking results are presented. For the "96 fs result", the initially negatively chirped 107 fs output pulses are externally compressed by a single path through a 2-mm-thick zinc selenide plate (Eksma Optics) introducing a positive GDD of $\approx$1350 fs^2.

The detailed pulse characterization is summarized in Figs. 2.4 and 2.5. The pulse duration is measured with a home-built second harmonic generation (SHG) frequency-resolved optical gating (FROG) apparatus. The measured SHG-FROG spectrogram is reconstructed with a grid size of 512 by 512 points [Fig. 2.5(a)] and 1024 by 1024 points [Fig. 2.5(a)]. The retrieved pulse durations agree well with a more standard SHG-based autocorrelator (FR-103MN; Femtochrome Research, Inc.). The intensity autocorrelations are in excellent agreement with a $sech^2$ pulse shape [Figs. 2.4(d) and 2.5(d)], and long-span autocorrelation scans show no additional side pulses or pedestals [inset in Figs. 2.4(d) and 2.5(d)]. Figure 2.5(d) shows the autocorrelation of both the 107 fs output pulses and the compressed 96 fs pulses. The following pulse characterizations are

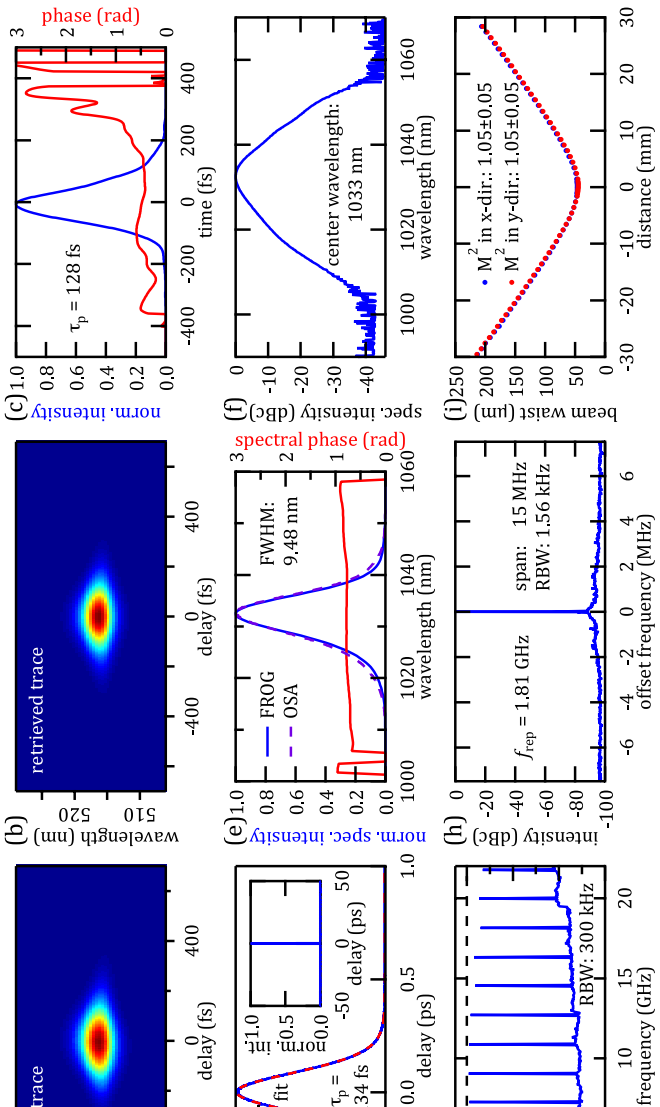

Figure 2.4: "128 fs result": modelocking characterization of the 128 fs pulses at 80 mW average output power, a peak power of 303 W, and a pulse repetition rate of 1.81 GHz. (a) Measured SHG-FROG spectrogram. (b) Retrieved FROG spectrogram (error: 0.0019). (c) Retrieved temporal intensity profile and temporal phase. (d) Intensity autocorrelation with corresponding sech^2 fit (inset: long-span autocorrelation without any satellite pulses).(e) Retrieved spectrum and spectral phase overlaid with the measured optical spectrum with a FWHM bandwidth of 9.48 nm. The time-bandwidth product is 1.09 times the ideal value for a sech^2 pulse shape, i.e., very close to perfect bandwidth-limited pulse duration. (f) Optical spectrum in logarithmic scale centered around 1033 nm, measured with a RBW of 0.1 nm. (g) Long-span microwave spectrum with a RBW of 300 kHz. (h) 15 MHz microwave spectrum at 1.81 GHz, measured with a RBW of 1.56 kHz. (i) Gaussian beam profile confirmed with a measured $M^2 < 1.05 \pm 0.05$ in two orthogonal directions.

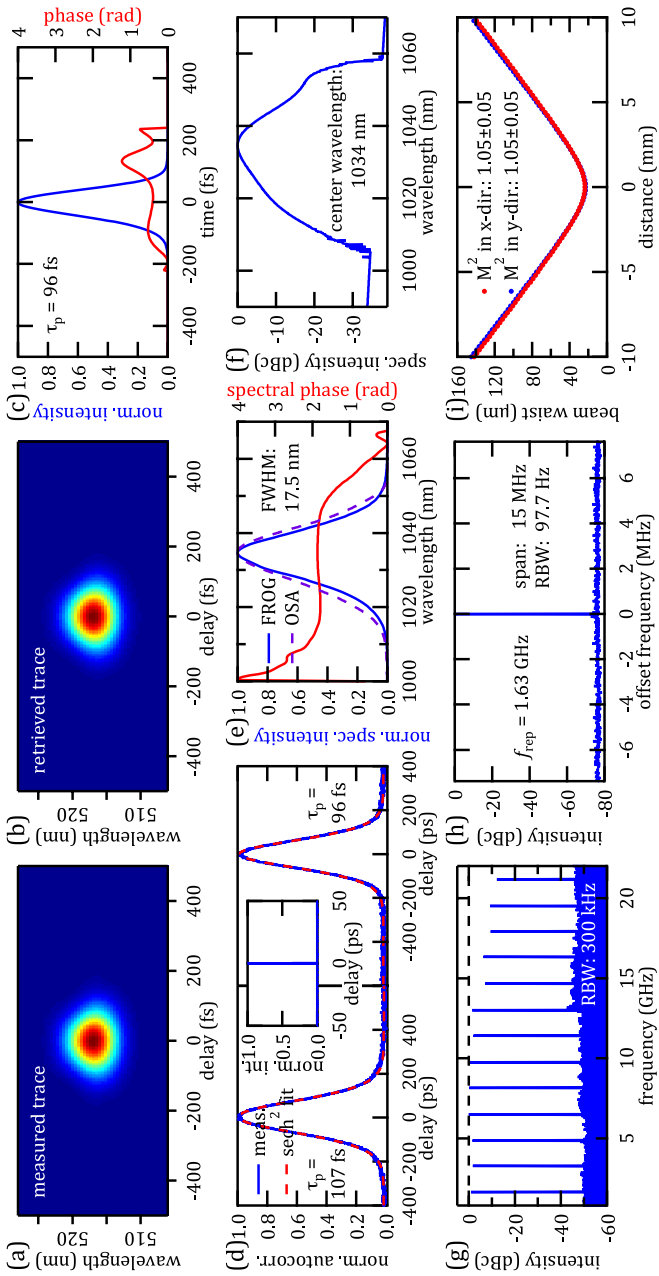

Figure 2.5: "96 fs result": modelocking characterization of the 96-fs pulses at 100 mW average output power, a peak power of 560 W and a pulse repetition rate of 1.63 GHz. (a) Measured SHG-FROG spectrogram. (b) Retrieved FROG spectrogram (error: 0.0004). (c) Retrieved temporal intensity profile and temporal phase. (d) Intensity autocorrelations with corresponding sech^2 fits of the 107 fs and 96 fs pulses (inset: long-span autocorrelation without any satellite pulses). (e) Retrieved spectrum and spectral phase overlaid with the measured optical spectrum with a FWHM bandwidth of 17.5 nm. The time-bandwidth product is 1.47 times the ideal value for a sech^2 pulse shape, i.e., with better dispersion compensation, we could obtain even shorter pulses.(f) Optical spectrum in logarithmic scale centered around 1034 nm, measured with a RBW of 0.1 nm. (g) Long-span microwave spectrum with a RBW of 300 kHz. (h) 15 MHz microwave spectrum at 1.63 GHz, measured with a RBW of 97.7 Hz. (i) Gaussian beam profile confirmed with a measured $M^2 < 1.05 \pm 0.05$ in two orthogonal directions.

identical for the 107 fs and the 96 fs pulses. The smooth modelocked spectrum overlaps with the retrieved FROG spectrum [Figs. 2.4(e) and 2.5(e)] and is free of cw breakthroughs, further shown in a logarithmic scale in Figs. 2.4(f) and 2.5(f). The "128 fs result" is close to transform-limited with a spectral bandwidth of 9.48 nm corresponding to a time-bandwidth product of 0.345, being 1.09 times the value for a sech^2 pulse shape. The 17.5 nm broad spectrum of the "96 fs result" corresponds to a time-bandwidth product of 0.472, i.e., 1.47 times the ideal value for a sech^2 pulse shape, and better external pulse compression could potentially support pulses as short as 65 fs.

The temporal laser intensity is measured with a fast photo-diode (New Focus, Model 1454), amplified with a broadband and low noise preamplifier (Agilent 87405C) and detected with a microwave spectrum analyzer (Agilent 8565EC, HP 8592L). As discussed in [11], we show two microwave spectra in Figs. 2.4(g) and 2.5(g) and Figs. 2.4(g) and 2.5(g) to further confirm clean fundamental modelocking.

Figures 2.4(g) and 2.5(g) show a scan with high resolution bandwidth (RBW) of 300 kHz from DC to 22 GHz with a high SNR of $\approx$50 dB. All higher harmonics of the repetition rate exist and are constant, apart from a small drop in intensity of the higher harmonics due to the limited bandwidth of the 18 GHz preamplifier. Figures 2.4(h) and 2.5(h) zoom into the first harmonic with a higher RBW over an offset frequency span of $\pm$7.5 MHz using a highly linear photodiode (DSC30S-HLPD; Discovery Semiconductors, Inc.) and a signal source analyzer (Agilent E5052B). Even with the high SNR of $\approx$80 dB ($\approx$90 dB), no line broadening and no additional side peaks become visible. Excellent beam quality was confirmed with measured M^2 values of less than 1.05 $\pm$0.05 in two orthogonal directions [Figs. 2.4(g) and 2.5(g)].

2.1.4 Gain characterization

Here we present both a spectrally resolved measurement of the small signal gain and a measurement of the gain saturation as described by Mangold et al. [37].

A. Spectral gain measurements

For the spectral gain characterization, we measured the spectrally resolved small signal reflectivity of a diode-pumped VECSEL. The probe laser is a tunable cw Ti:sapphire laser that is focused tightly to obtain a sub-20-μm diameter beam waist on the surface of the VECSEL chip. The VECSEL is optically pumped by a cw 808 nm multimode diode laser (Lumics) with an elliptical 122 μm × 172 μm full width at half maximum (FWHM) spot. The average pump intensity I_p of the probe spot can be varied from 0 to 57 kW/cm^2. Without any pump power, the VECSEL absorbs the probe laser for photon energies exceeding the bandgap energy [Fig. 2.6(a)]. With a pump intensity of approximately 10 kW/cm^2, the laser is pumped into transparency. For increasing pump power, the small signal gain increases, the spectrum becomes broader, and the peak wavelength experiences a redshift due to the elevated temperature in the gain quantum wells.

A shift in the peak wavelength is also visible in Fig. 2.6(b), which shows the small signal gain for different heat-sink temperatures at a constant pump intensity of 57 kW/cm^2. By lowering the heat-sink temperature, the small signal gain increases slightly, and the peak wavelength experiences a blueshift in the range of 0.32 nm/K, in agreement with the intrinsic temperature dependence of the InGaAs quantum well gain [1]. The maximum small signal gain of 3.17% is achieved at 57 kW/cm^2 pump in-tensity and a heat-sink temperature of -5°C. The small signal gain is lower than the values measured in [37], which can be explained by the reduced field intensity enhancement factor.

The VECSEL chip is heated by the absorbed pump light from the front side and cooled from the backside, creating a temperature gradient normal to the chip surface. This temperature gradient in the active region leads to different temperatures of the individual quantum wells, which shifts the corresponding emission wavelength and thereby broadens the overall accessible macroscopic gain. This effect becomes even stronger with increased pump intensities and reduced heat-sink temperatures. The short wavelength limit of the gain shown in Fig. 2.6, is defined by the reflectivity bandwidth of the underlying AlAs/GaAs DBR (full bandwidth of about 110 nm), resulting in a gain bandwidth of approximately 50-57 nm. This

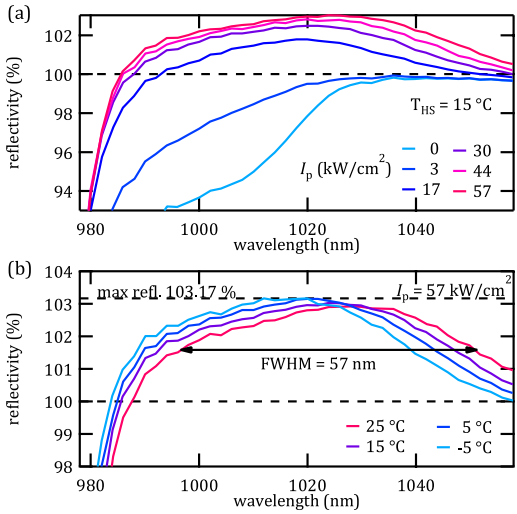

Figure 2.6: Spectral gain measurements. (a) Spectrally resolved reflectivity for different pump intensities at a constant heat-sink temperature of 15°C. (b) Spectrally resolved reflectivity for different heat-sink temperatures at a constant pump intensity of $I_p = 57$ kW/cm^2.

corresponds to a small signal gain, which is 2-3 times broader than the quantum well photo-luminescence measured by Wang et al. [7].

B. Gain saturation measurements

For the gain saturation characterization, we measured the fluence-dependent reflectivity of the diode-pumped VECSEL. The probe laser is a tunable modelocked Ti:sapphire laser generating 140 fs pulses. The probe light is focused to a 29.6 μm diameter spot. The pump arrangement is the same as the one used for the spectral gain measurement, resulting in a maximum pump intensity of 46.5 kW/cm^2. The dependence of the reflectivity on the probe fluence is measured for different probe wavelengths, pump fluences, and heat-sink temperatures. The probe fluence is varied over 3 orders of magnitude up to 1200 μJ/cm^2 for probing wavelengths of 1010, 1020, 1030, and 1040 nm. The pump intensity is varied between 0 and 46.5 kW/cm^2, while the heat-sink temperature is kept at -5°C, 5°C, 15°C, or 25°C.

The nonlinear reflectivity [Fig. 2.7(a)] is analyzed with a macroscopic

model for the gain saturation analogous to the saturable absorption of a SESAM. The characteristic parameters are the small signal reflectivity, the gain saturation fluence, the nonsaturable losses, and the induced absorption. The detailed description of the model can be found in [37].

To study the measured gain saturation parameters, the concept of the equivalent wavelength is introduced, which allows for a matching of measurement series taken at different probing wavelengths and temperatures. As visible in Fig. 2.6(b), the quantum well emission is blueshifted by approximately 3.2 nm for a heat-sink temperature reduction of 10°C. To account for this blueshift, the probing wavelength of 1030 nm at a heat-sink temperature of 15°C corresponds to an equivalent probing wavelength of 1033.2 nm at a heat-sink temperature of 25°C, for example. Following this concept, the equivalent probing wavelength is calculated for all temperatures lower than 25°C.

The saturation fluence varies between 30 and 50 $\mu J/cm^2$ and has a slight dip around 1030 nm [Fig. 2.7(b)]. The saturation fluence is comparable to that reported in [37], although the saturation fluence is expected to scale inversely proportional to the field intensity enhancement factor, and, therefore, we have expected higher saturation fluences. Figure 2.7(c) shows the small signal reflectivity of the probing pulse with an 11 nm wide spectrum analogous to the reflectivity spectrum [Fig. 2.6(b)] of a single frequency cw probe. The small signal reflectivity has a maximum around 1030 nm and is slightly reduced for lower heat-sink temperatures. The induced absorption shows a weak temperature dependence and has a maximum of 17.6 mJ/cm^2 at a probing wavelength of 1030 nm, as shown in Fig. 2.7(d).

2.1.5 Pulse formation simulation

We used our pulse formation simulations as described in [34]. This simulation is based on macroscopic input parameters summarized in Table 2.1. We used the same linewidth enhancement factors, the same additional cavity losses, and the same gain recovery time as discussed before in [34]. The input parameters of the VECSEL gain chip are chosen in the middle of the measured range of 50-57 nm (FWHM) for the gain bandwidth, 30-50 $\mu J/cm^2$ for the gain saturation fluence, and 2.5%-3.17% for the small sig-

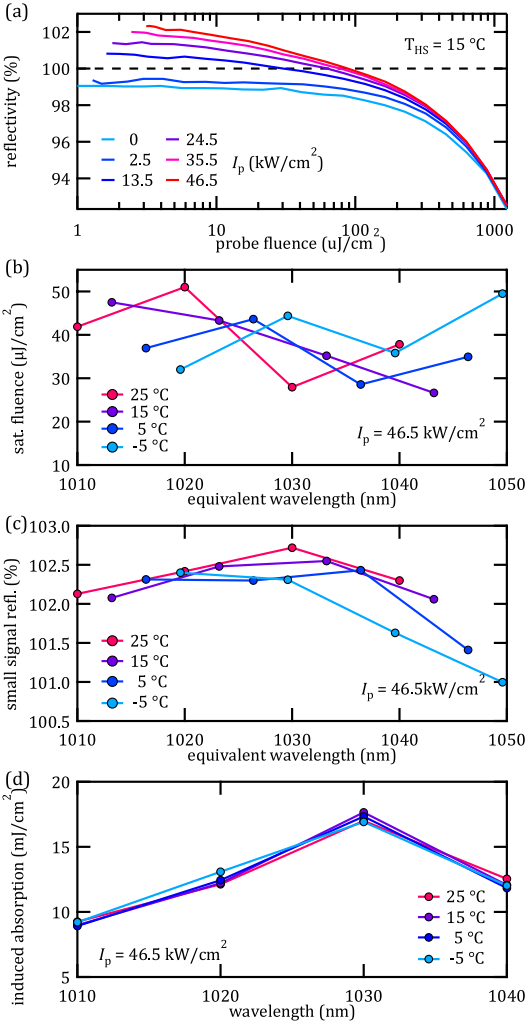

Figure 2.7: Gain saturation measurements. (a) Fluence-dependent reflectivity for different pump intensities at a heat-sink temperature of 15°C. (b) Saturation fluence as a function of heat-sink temperature and equivalent wavelength. (c) Small signal reflectivity as a function of heat-sink temperature and equivalent wavelength. The equivalent wavelength accounts for the temperature-induced wavelength shift of the gain peak wavelength for matching of measurement series. See text for a more detailed definition of equivalent wavelength. (d) Induced absorption as a function of wavelength and heat-sink temperature.

nal gain. More elaborated simulations starting from the fully microscopic many-body theory by Kilen et al. [41] indicated the limitations of macroscopic models for pulse durations below some hundreds of femtoseconds. Nevertheless, so far our macroscopic models have shown good agreement with our experimental results.

Our simulation shows that the combination of the gain bandwidth [Fig. 2.6(b)] and the gain saturation fluence [Fig. 2.7(b)] defines a range of stable modelocking configurations and, so, the minimum possible pulse duration. As expected, the small signal gain [Fig. 2.6(b)] and the losses mainly determine the output power. The values for dispersion per cavity round-trip used for the simulation are not straightforward because, for example, the dispersion of the VECSEL [Fig. 2.3(b)] was not measured under lasing operation. Furthermore, the modelocking simulations are very sensitive to dispersion, with increasing sensitivity for increasing gain bandwidth. The cavity round-trip dispersion fitting the "96 fs result" is -12 fs^2 of GDD and -500 fs^3 of third order dispersion (TOD), and these values are 12 fs^2 of GDD and 620 fs^3 of TOD for the "128 fs result." These dispersion values are shown in Fig. 2.3(b) and are in reasonable agreement with the dispersion of the VECSEL, which is expected to give the main contribution.

The pulse formation simulation for the "128 fs input parameters" (Table 2.1, Fig. 2.8) not only agrees with the pulse duration of 128 fs, but also with the spectral bandwidth of 9.5 nm (measured 9.48 nm) and the average output power of 78 mW (measured 80 mW). The 96 fs input parameters (Table 2.1) with the dispersion adapted to fit the compressed 96 fs pulses (Table 2.1: -12 fs^2 and -500 fs^3) results in negatively chirped 130 fs output pulses (i.e., not the measured 107 fs), which can be compressed with 1350 fs^2 positive GDD to 96 fs, a spectral bandwidth of 17.5 nm, and an average output power of 104 mW. With a slightly different cavity round-trip GDD of -4 fs^2 and TOD of -600 fs^3, we can fit the 107 fs output pulses: the simulation results in negatively chirped 108 fs output pulses, which can be compressed with 1350 fs^2 positive GDD to 86 fs (i.e., not the measured 96 fs), a spectral bandwidth of 17.4 nm, and an average output power of 100 mW (measured: 107 fs, 96 fs, 17.5 nm, 100 mW). Higher order dispersion of the zinc selenide (ZnSe) plate has not been taken into

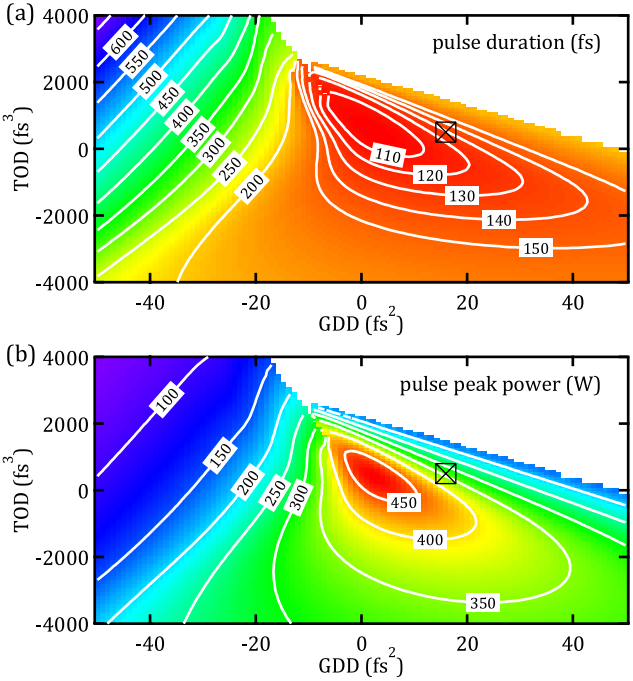

Figure 2.8: Numerical pulse formation simulations using the 128 fs input parameters from Table 2.1. Cavity round-trip dispersion management for both (a) a shorter pulse duration and (b) a higher peak power as functions of second-order dispersion (i.e., GDD) and TOD is shown. The best performance is obtained in the red shaded area, and the "128 fs result" is marked with a black cross.

account. The agreement is no longer perfect, but the simulation confirms the 100 fs pulse duration with initially negatively chirped output pulses. At this point, we did not include the nonlinear induced absorption in the SESAM and VECSEL even though this becomes more important with shorter pulses.

Using the 128 fs input parameters (Table 2.1), we further explored the sensitivity of the cavity round-trip dispersion taking into account both the second-order dispersion (GDD) and the TOD. Different values of TOD are applied in addition to the GDD, centered around the lasing frequency (Fig. 2.8), with the cross indicating the dispersion values used for fitting the "128 fs result." The shortest pulses (101 fs) are achieved with 2 fs^2

GDD and 560 fs^3 TOD. The highest pulse peak power is 480 W and is obtained with 3 fs^2 GDD and 400 fs^3 TOD. Similar sensitivity is observed with the 96 fs input parameters, but is not shown here.

2.1.6 Performance scaling

From our simulations as presented in Section 2.1.5 we can conclude that the shortest pulse duration is mainly determined by the gain bandwidth, the gain saturation fluence, and the second- and third-order dispersion of the VECSEL. Figure 2.8 summarizes the general sensitivity on second- and third-order dispersion for both shorter pulse durations [red area in Fig. 2.8(a)] and higher pulse peak powers [red area in Fig. 2.8(b)]. Slightly positive TOD is needed for the shortest pulses. Too much positive TOD, however, causes instabilities, while negative TOD results in stable modelocking with slowly increasing pulse duration and decreasing peak power (Fig. 2.8). Negative GDD should be avoided, as the pulse duration increases rapidly into the picosecond regime, while for positive GDD, the pulse duration increases more slowly. Thus dispersion management becomes even more critical for broadband gain. Most recently, this has also been confirmed by Head et al. [35]. Control of the GDD and TOD of a VECSEL is challenging, as they are very sensitive to growth and fabrication uncertainties. Even growth errors in the 1% range can significantly change the wavelength-dependent dispersion. The simulation and the modelocking results confirm that a VECSEL gain bandwidth of 50-57 nm (FWHM) is sufficient for the generation of sub-100-fs pulses.

In the future we will focus our efforts toward even higher average output power and higher optical-to-optical efficiency of sub-100-fs SESAM modelocked VECSELs. The optimized broadband gain has been the key enabler for these new milestone results and has been achieved with flat field intensity enhancement, broadband dispersion control, and high-quality epitaxial growth. Higher gain saturation fluence would further increase the output power and simultaneously shorten the pulse duration. The measured saturation fluences [Fig. 2.7(b)] have been lower than expected in comparison to [37] with the corresponding field intensity enhancement factors taken into account. However, we changed the lasing wavelength (1030 nm instead of 960 nm) and the epitaxial growth (MOVPE

instead of MBE), which makes a direct comparison more difficult.

2.1.7 Conclusion

In conclusion, we have presented a significant improvement of SESAM modelocked VECSELs with both shorter pulse durations and higher average power with 96 fs pulses and 560 W pulse peak power. We performed a detailed characterization of both the VECSEL and the SESAM parameters, which were used as input parameters in our simulations (Table 2.1). We obtained good agreement between experiment and theory. Both second- and third-order dispersion management is required for short pulse durations and transform-limited pulses. The "128 fs result" is very close to transform limited with a time-bandwidth product of 1.09 times the ideal value. The 96 fs pulses were obtained by additional external dispersion compensation with a single path through a 2-mm-thick zinc selenide plate and are still not transform limited, with a time-bandwidth product of 1.47 times the ideal value of a sech^2 pulse shape. The bandwidth could in principle support transform-limited pulses as short as 65 fs. We have explained the sensitivity and importance of dispersion management and outlined design guidelines for future improvements in output power. With these record modelocking results, we have demonstrated that high-power 100 fs pulses are possible from optically pumped ultrafast VECSELs. This performance will enable octave-spanning supercontinuum generation without any additional external pulse amplifications based on recent progress with Si_3N_4 waveguides [27,28] for supercontinuum generation.

Funding. Swiss Confederation Program Nano-Tera.ch.

Acknowledgement We thank the technology and clean-room facility FIRST of ETH Zürich for advanced micro- and nanotechnology. This work was financed by the Swiss Confederation Program Nano-Tera.ch, which was scientifically evaluated by the Swiss National Science Foundation (SNSF).

2.1.8 References

1. U. Keller and A. C. Tropper, "Passively modelocked surface-emitting semiconductor lasers," Phys. Rep. 429, 67-120 (2006).
2. U. Keller, K. J. Weingarten, F. X. Kärtner, D. Kopf, B. Braun, I. D. Jung, R. Fluck, C. Hönninger, N. Matuschek, and J. Aus der Au, "Semiconductor saturable absorber mirrors (SESAMs) for femtosecond to nanosecond pulse generation in solid-state lasers," IEEE J. Sel. Top. Quantum Electron. 2, 435-453 (1996).
3. B. W. Tilma, M. Mangold, C. A. Zaugg, S. M. Link, D. Waldburger, A. Klenner, A. S. Mayer, E. Gini, M. Golling, and U. Keller, "Recent advances in ultrafast semiconductor disk lasers," Light Sci. Appl. 4, e310 (2015).
4. M. Kuznetsov, F. Hakimi, R. Sprague, and A. Mooradian, "High-power (>0.5-W CW) diode-pumped vertical-external-cavity surface-emitting semiconductor lasers with circular TEM00 beams," IEEE Photon. Technol. Lett. 9, 1063-1065 (1997).
5. S. H. Park, J. Kim, H. Jeon, T. Sakong, S. N. Lee, S. Chae, Y. Park, C. H. Jeong, G. Y. Yeom, and Y. H. Cho, "Room-temperature GaN vertical-cavity surface-emitting laser operation in an extended cavity scheme," Appl. Phys. Lett. 83, 2121–2123 (2003).
6. M. Rahim, M. Arnold, F. Felder, K. Behfar, and H. Zogg, "Midinfrared lead-chalcogenide vertical external cavity surface emitting laser with 5 μm wavelength," Appl. Phys. Lett. 91, 151102 (2007).
7. T. L. Wang, Y. Kaneda, J. M. Yarborough, J. Hader, J. V. Moloney, A. Chernikov, S. Chatterjee, S. W. Koch, B. Kunert, and W. Stolz, "High-power optically pumped semiconductor laser at 1040 nm," IEEE Photon. Technol. Lett. 22, 661-663 (2010).
8. B. Rudin, A. Rutz, M. Hoffmann, D. J. H. C. Maas, A.-R. Bellancourt, E. Gini, T. Südmeyer, and U. Keller, "Highly efficient optically pumped vertical emitting semiconductor laser with more than 20 W average output power in a fundamental transverse mode," Opt. Lett. 33, 2719-2721 (2008).
9. A. Laurain, C. Mart, J. Hader, J. V. Moloney, B. Kunert, and W. Stolz, "15 W single frequency optically pumped semiconductor laser with sub-megahertz linewidth," IEEE Photon. Technol. Lett. 26, 131-133 (2014).
10. B. Heinen, T. L. Wang, M. Sparenberg, A. Weber, B. Kunert, J. Hader, S. W. Koch, J. V. Moloney, M. Koch, and W. Stolz, "106 W continuous-wave output power from vertical-external-cavity surface-emitting laser," Electron. Lett. 48, 516-517 (2012).

11. M. Mangold, M. Golling, E. Gini, B. W. Tilma, and U. Keller, "Sub-300-femtosecond operation from a MIXSEL," Opt. Express 23, 22043-22059 (2015).
12. I. Kilen, J. Hader, J. V. Moloney, and S. W. Koch, "Ultrafast nonequilibrium carrier dynamics in semiconductor laser mode locking," Optica 1, 192-197 (2014).
13. P. Klopp, U. Griebner, M. Zorn, and M. Weyers, "Pulse repetition rate up to 92 GHz or pulse duration shorter than 110 fs from a mode-locked semiconductor disk laser," Appl. Phys. Lett. 98, 071103 (2011).
14. A. H. Quarterman, K. G. Wilcox, V. Apostolopoulos, Z. Mihoubi, S. P. Elsmere, I. Farrer, D. A. Ritchie, and A. Tropper, "A passively mode-locked external-cavity semiconductor laser emitting 60-fs pulses," Nat. Photonics 3, 729-731 (2009).
15. K. G. Wilcox, A. C. Tropper, H. E. Beere, D. A. Ritchie, B. Kunert, B. Heinen, and W. Stolz, "4.35 kW peak power femtosecond pulse mode-locked VECSEL for supercontinuum generation," Opt. Express 21, 1599-1605 (2013).
16. C. J. Saraceno, F. Emaury, C. Schriber, M. Hoffmann, M. Golling, T. Südmeyer, and U. Keller, "Ultrafast thin-disk laser with 80 µJ pulse energy and 242 W of average power," Opt. Lett. 39,9-12 (2014).
17. C. A. Zaugg, A. Klenner, O. D. Sieber, M. Golling, B. W. Tilma, and U. Keller, "Sub-100 MHz passively modelocked VECSEL," in Conference on Lasers and Electro Optics (CLEO) (Optical Society of America, 2013), paper CW1G.6.
18. M. Butkus, E. A. Viktorov, T. Erneux, C. J. Hamilton, G. Maker, G. P. A. Malcolm, and E. U. Rafailov, "85.7 MHz repetition rate mode-locked semiconductor disk laser: fundamental and soliton bound states," Opt. Express 21, 25526-25531 (2013).
19. M. Hoffmann, Y. Barbarin, D. J. H. C. Maas, M. Golling, I. L. Krestnikov, S. S. Mikhrin, A. R. Kovsh, T. Südmeyer, and U. Keller, "Modelocked quantum dot vertical external cavity surface emitting laser," Appl. Phys. B 93, 733-736 (2008).
20. M. Hoffmann, O. D. Sieber, V. J. Wittwer, I. L. Krestnikov, D. A. Livshits, Y. Barbarin, T. Südmeyer, and U. Keller, "Femtosecond high-power quantum dot vertical external cavity surface emitting laser," Opt. Express 19, 8108-8116 (2011).
21. R. Bek, G. Kersteen, H. Kahle, T. Schwarzbäck, M. Jetter, and P. Michler, "All quantum dot mode-locked semiconductor disk laser emitting at 655 nm," Appl. Phys. Lett. 105, 082107 (2014).

22. R. Aviles-Espinosa, G. Filippidis, C. Hamilton, G. Malcolm, K. J. Weingarten, T. Südmeyer, Y. Barbarin, U. Keller, S. I. C. O. Santos, D. Artigas, and P. Loza-Alvarez, "Compact ultrafast semiconductor disk laser: targeting GFP based nonlinear applications in living organisms," Biomed. Opt. Express 2, 739-747 (2011).

23. C. A. Zaugg, A. Klenner, M. Mangold, A. S. Mayer, S. M. Link, F. Emaury, M. Golling, E. Gini, C. J. Saraceno, B. W. Tilma, and U. Keller, "Gigahertz self-referenceable frequency comb from a semiconductor disk laser," Opt. Express 22, 16445-16455 (2014).

24. A. Klenner, S. Schilt, T. Südmeyer, and U. Keller, "Gigahertz frequency comb from a diode-pumped solid-state laser," Opt. Express 22, 31008-31019 (2014).

25. A. H. Quarterman, L. E. Hooper, P. J. Mosley, and K. G. Wilcox, "Gigahertz pulse source by compression of mode-locked VECSEL pulses coherently broadened in the normal dispersion regime," Opt. Express 22, 12096-12101 (2014).

26. H. R. Telle, G. Steinmeyer, A. E. Dunlop, J. Stenger, D. H. Sutter, and U. Keller, "Carrier-envelope offset phase control: a novel concept for absolute optical frequency measurement and ultrashort pulse generation," Appl. Phys. B 69, 327-332 (1999).

27. A. Klenner, A. S. Mayer, A. R. Johnson, K. Luke, M. R. E. Lamont, Y. Okawachi, M. Lipson, A. L. Gaeta, and U. Keller, "Gigahertz frequency comb offset stabilization based on supercontinuum generation in silicon nitride waveguides," Opt. Express 24, 11043-11053 (2016).

28. A. S. Mayer, A. Klenner, A. R. Johnson, K. Luke, M. R. E. Lamont, Y. Okawachi, M. Lipson, A. L. Gaeta, and U. Keller, "Frequency comb offset detection using supercontinuum generation in silicon nitride wave-guides," Opt. Express 23, 15440-15451 (2015).

29. C. Hönninger, R. Paschotta, F. Morier-Genoud, M. Moser, and U. Keller, "Q-switching stability limits of continuous-wave passive mode locking," J. Opt. Soc. Am. B 16,46-56 (1999).

30. A. Klenner and U. Keller, "All-optical Q-switching limiter for high-power gigahertz modelocked diode-pumped solid-state lasers," Opt. Express 23, 8532-8544 (2015).

31. D. Hillerkuss, R. Schmogrow, T. Schellinger, M. Jordan, M. Winter, G. Huber, T. Vallaitis, R. Bonk, P. Kleinow, F. Frey, M. Roeger, S. Koenig, A. Ludwig, A. Marculescu, J. Li, M. Hoh, M. Dreschmann, J. Meyer, S. Ben Ezra, N.

Narkiss, B. Nebendahl, F. Parmigiani, P. Petropoulos, B. Resan, A. Oehler, K. Weingarten, T. Ellermeyer, J. Lutz, M. Moeller, M. Huebner, J. Becker, C. Koos, W. Freude, and J. Leuthold, "26 Tbit s-1 line-rate super-channel transmission utilizing all-optical fast Fourier transform processing," Nat. Photonics 5, 364-371 (2011).

32. M. Mangold, C. A. Zaugg, S. M. Link, M. Golling, B. W. Tilma, and U. Keller, "Pulse repetition rate scaling from 5 to 100 GHz with a high-power semiconductor disk laser," Opt. Express 22, 6099-6107 (2014).
33. D. Waldburger, C. G. E. Alfieri, S. M. Link, E. Gini, M. Golling, M. Mangold, B. W. Tilma, and U. Keller, "Pulse shortening of an ultrafast VECSEL," Proc. SPIE 9734, 973409 (2016).
34. O. D. Sieber, M. Hoffmann, V. J. Wittwer, M. Mangold, M. Golling, B. W. Tilma, T. Südmeyer, and U. Keller, "Experimentally verified pulse formation model for high-power femtosecond VECSELs," Appl. Phys. B 113, 133-145 (2013).
35. C. R. Head, A. Hein, A. P. Turnbull, M. Polanik, E. A. Shaw, T. Chen Sverre, P. Unger, and A. C. Tropper, "High-order dispersion in sub- 200- fs pulsed VECSELs," Proc. SPIE 9734, 973408 (2016).
36. D. J. H. C. Maas, B. Rudin, A.-R. Bellancourt, D. Iwaniuk, S. V. Marchese, T. Südmeyer, and U. Keller, "High precision optical characterization of semiconductor saturable absorber mirrors," Opt. Express 16, 7571-7579 (2008).
37. M. Mangold, V. J. Wittwer, O. D. Sieber, M. Hoffmann, I. L. Krestnikov, D. A. Livshits, M. Golling, T. Südmeyer, and U. Keller, "VECSEL gain characterization," Opt. Express 20, 4136-4148 (2012).
38. G. J. Spühler, K. J. Weingarten, R. Grange, L. Krainer, M. Haiml, V. Liverini, M. Golling, S. Schon, and U. Keller, "Semiconductor saturable absorber mirror structures with low saturation fluence," Appl. Phys. B 81, 27-32 (2005).
39. S. Hoogland, S. Dhanjal, A. C. Tropper, S. J. Roberts, R. Häring, R. Paschotta, and U. Keller, "Passively mode-locked diode-pumped surface-emitting semiconductor laser," IEEE Photon. Technol. Lett. 12, 1135-1137 (2000).
40. A. Gosteva, M. Haiml, R. Paschotta, and U. Keller, "Noise-related resolution limit of dispersion measurements with white-light interferometers," J. Opt. Soc. Am. B 22, 1868-1874 (2005).
41. I. Kilen, S. W. Koch, J. Hader, and J. V. Moloney, "Fully microscopic modeling of mode locking in microcavity lasers," J. Opt. Soc. Am. B 33,75-80 (2016).

Chapter 3

Performance Scaling

To further scale the performance of SDLs, we investigated the current limitations in this chapter. First we study the multipulse instabilities arising at hight pump powers, which limit the average output power in fundamental modelocking. The modelocking analysis supplemented by simulations shows the influence of new effects such as kinetic-hole burning which becomes prominent at the short pulse durations. The details are presented in the following submitted journal publication (section 3.1):

Title: "Multipulse instabilities of a femtosecond SESAM-modelocked VECSEL", [38]
Journal: *Optics Express*
doi: 10.1364/OE.26.021872

Another approach to scale the average output power is evaluated by taking a closer look at a CPM SDL. We show that both the CEO and the pulse repetition frequencies of the two output beams are locked together. This allows the two output beams to be coherently combined for a resulting four-time increased power in comparison with a single beam, which we demonstrated in a first proof-of-principle experiment. The details are

presented in the following journal publication (section 3.2):

Title: "Coherent beam combining and noise analysis of a colliding pulse modelocked VECSEL", [39]
Journal: *Optics Express*
doi: 10.1364/OE.25.019281

In the next section, we present a record short pulse MIXSEL with pulse durations as short as 139 fs. It is this MIXSEL used in dual-comb operation which enable the dual-comb spectroscopy of acetylene, as presented in section 5.2. A fundamental aspect of this result is the good thermal conductivity of the MIXSEL chip which reduced the thermal cross talk between the two laser spots of the dual-comb MIXSEL. The details are presented in the following journal publication in preparation (section 3.3):

Title: "Sub-150-fs pulses from a broadband MIXSEL"
Journal: submitted to *Optics Letters*

For the the thermal characterization of the semiconductor structures, we use a thermal camera. The details of the characterization setup is described in section 3.4.

We also grew a VECSEL structure using our MBE machine. The increased thermal conductivity compared to the 100 fs VECSEL of chapter 2 allowed us to further scale the output power. In modelocked operation, this VECSEL produced 100-fs pulses with an increased average output power of 150 mW resulting in a pulse peak power of 1.16 kW (section 3.5).

The optical-to-optical efficiency of ultrafast SDL is reduced the shorter their pulse duration. A closer look reveals that spectral hole burning is the main cause of the reduced gain at shorter pulse durations, which in combination with the short lifetime of the excited carriers strongly reduces the optical pump efficiency. The details are presented in the following journal publication (section 3.6):

Title:	"Optical efficiency and gain dynamics of modelocked semiconductor disk lasers", [19]
Journal:	*Optics Express*
doi:	10.1364/OE.25.006402

In the remaining two sections, we investigate two types of QDs, one grown by the SK technique and one by the SML technique. Semiconductor gain media based on QDs promise a longer carrier life time compared to QWs which is expected to significantly increase the optical-to-optical efficiency of SDLs. It emerges that SK QDs enable more efficient sub-300-fs modelocked operation while SML QDs are better suited for cw operation. The details of the SK QDs are presented in the following journal publication (section 3.7):

Title:	"High-power Sub-300-Femtosecond Quantum Dot Semiconductor Disk Lasers", [40]
Journal:	*IEEE Photonics Technology Letters*
doi:	10.1109/LPT.2018.2801024

and the details of the SML QDs are presented in the following journal publication (section 3.8):

Title: "Mode-locking Instabilities for High-Gain Semiconductor Disk Lasers Based on Active Submonolayer Quantum Dots"
Journal: *Physical Review Applied*
doi: 10.1103/PhysRevApplied.10.044015

3.1 Multipulse instabilities of a femtosecond SESAM-modelocked VECSEL

Dominik Waldburger[1], *Cesare G. E. Alfieri*[1], *Sandro M. Link*[1], *Stefan Meinecke*[2], *Lina C. Jaurigue*[2], *Kathy Lüdge*[2], *Matthias Golling*[1] *and Ursula Keller*[1]

[1]Department of Physics, Institute for Quantum Electronics, ETH Zürich, Zürich, Switzerland

[2]Institut für Theoretische Physik, TU Berlin, Berlin, Germany

Optically pumped passively modelocked vertical external-cavity surface-emitting lasers (VECSELs) can generate pulses as short as 100 fs with an intracavity semiconductor saturable absorber mirror (SESAM). Very stable soliton modelocking can be obtained, however, the high-Q-cavity, the short gain lifetime, and the kinetic-hole burning can also support rather complex multipulse instabilities which we analyze in more details here. This onset of multipulse operation limits the maximum average output power with fundamental modelocking and occurs at the roll-over of the cavity round trip reflectivity. Unfortunately, such multipulse operation sometimes can mimic stable modelocking when only limited diagnostics are available.

3.1.1 Introduction

Optically pumped semiconductor disk lasers (SDLs) are high-power laser sources which convert low-coherence light from pump diode arrays into high brightness beams with excellent quality. Semiconductor bandgap engineering can set the center wavelength of this source from the visible to the mid-infrared [1]. In particular, optically pumped vertical external-cavity surface-emitting lasers (VECSELs, [2]) have demonstrated continous wave (cw) operation with an average output power as high as 20 W in fundamental transverse mode and 106 W in multimode [3, 4]. The first ultrafast VECSEL was modelocked with a semiconductor saturable absorber mirror (SESAM, [5]) in 2000 [6]. Since then, the performance of ultrafast SDL has been improved, as summarized in recent reviews

[1, 7-9]. In SESAM-modelocked operation, pulse repetition rates range from 85 MHz up to 100 GHz [10, 11] and emission wavelengths from 489 nm up to 1960 nm have been demonstrated [12, 13]. The best performance in terms of power and pulse duration has been achieved in the 1-µm wavelength range (Fig. 3.1), with pulse durations as short as 100 s combined with pulse peak powers in the kW-range at gigahertz repetition rates. The performance of modelocked SDL has become comparable with fiber, Ti:sapphire, and diode-pumped solid state lasers. Many applications have been demonstrated such as multi-photon imaging [14, 15] and frequency comb metrology [16-19].

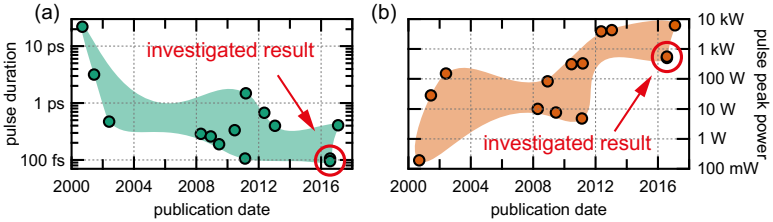

Figure 3.1: Timeline of record performance results from SESAM-modelocked optically pumped VECSELs at a center wavelength of around 1 µm in terms of (a) pulse duration and (b) pulse peak power (Refs. in [1, 7-9]). (Red circle) High-power 100-fs modelocking result as described in more details in Ref. [20].

Here, we investigate the complex multipulse instabilities of a high-power 100-fs SESAM-modelocked VECSEL (red circles in Fig. 3.1) [20]. We carefully analyze different modelocking states and their hysteresis depending on the pump power. We find that the maximum power in fundamental modelocking operation is not limited by thermal effects, but by the onset of multipulse instabilities, where more than one pulse oscillates in the laser cavity. While some applications may tolerate multipulse operation or some minor intensity fluctuations, other applications such as frequency metrology become only possible with low intensity noise, low timing jitter, or even a stabilized carrier envelope offset frequency [21]. Stable modelocking with excellent low noise operation has been demonstrated for such lasers [22, 23]. The onset of multipulse operation currently limits the output power and a better understanding is required to further scale the

power in fundamental modelocking. Additionally, the multipulse analysis provides new insights in the physics of highly inverted semiconductor structures at the timescale of 100 fs, where interesting effects start to play a role, such as kinetic hole burning, theoretically predicted by fully microscopic many-body models [24, 25]. Comprehensive modelocking characterization allows us to compare the different modelocking states. The similarity of single measurement parameters for different modelocking states shows the importance of a clean and complete characterization to proof fundamental modelocking [26, 27]. Finally, with an extensive characterization of the nonlinear reflectivity of the VECSEL and SESAM, we can show that the onset of multipulse operation occurs at the roll-over of the total cavity round trip reflectivity.

3.1.2 Characterization

The VECSEL used for the more detailed investigation of multipulse dynamics can generate stable 100-fs pulses in fundamental modelocking and has been described in [20]. We operate the laser in the same configuration that allowed the shortest pulses reported in [20] (i.e. same SESAM and VECSEL chips, same cavity design and heat-sink temperatures), however, we then continued to increase the pump power.

We observe that, once the laser has reached a certain maximum average output power in fundamental modelocking operation, more pump power does not simply increase of average output power with the same slope efficiency. Before thermal roll-over starts to occur, we observe several steps in increased output power with different modelocking states for which multiple pulses simultaneously oscillate in the cavity. We also observe a hysteresis effect for which these modelocking states depend on the pump history with continuously increased or decreased pump power (Fig. 3.2). To carefully analyze every modelocking state, we therefore characterized the laser performance at different pump powers. Clear discontinuities in average output power appear when ramping up the pump power (Fig. 3.2a), which also indicate a new modelocking regime (Fig. 3.2b).

Increasing the pump intensity starting from a low level, we observe a first threshold at a pump power of 20 W, where lasing action in fundamental modelocking begins. Then at 22.6 W, we observe an abrupt increase of

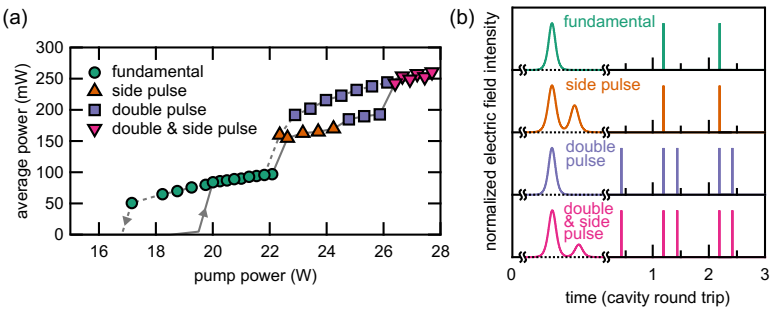

Figure 3.2: (a) Average output power from a SESAM-modelocked VECSEL measured for increasing (solid line) and decreasing (dashed line) pump power. (Markers) measurement points color coded according to their modelocking state: (green circle) *fundamental*, (orange triangle) *side pulse*, (violet square) *double pulse*, and (pink triangle) *double & side pulse* operation. (b) Representative electric field intensity for the corresponding modelocking states with a zoom into the first pulse: (green) *fundamental*, (orange) *side pulse*, (violet) *double pulse*, and (pink) *double & side pulse*. The side pulse visible in the zoom is below the resolution on the cavity round trip scale.

the average output power by a factor of 1.6 and, similarly, new discontinuities are observed at 24.8 W and 27 W. A clear hysteresis effect is observed when starting from a high pump level and continuously decreasing the pump power during which we do not reproduce the same average output power and also not in all cases the same multipulse state. Compared to the "increasing pump path", the laser delivers a higher average output power when the pump is between 27.7 and 22.9 W. Fundamental modelocking operation, with only one pulse per cavity round trip, extends to a lower pump power of 17.2 W. Hysteresis behaviors for SDLs in modelocking operation were already reported for picosecond pulses [28]. However, the femtosecond modelocking states we want to analyzed here (Fig. 3.2b) differ from what was previously characterized and are referred to as:

- *Fundamental modelocking*: One single pulse oscillates in the laser cavity.
- *Side pulse*: An additional side pulse close to the main pulse with a temporal spacing much shorter than the cavity round trip time.
- *Double pulse*: Two pulses oscillate in the laser cavity, spaced by approximately a quarter of the cavity round trip time.

- Double & side pulse: A combination of *side pulse* and *double pulse* operation, where a total of four pulses oscillate in the laser cavity. Each of the two pulses of the *double pulse* operation are accompanied by a side pulse, respectively.

A Pulse duration

The pulse duration is measured with a non-collinear second harmonic generation (SHG) autocorrelation (FR-103MN from *Femtochrome Research, Inc*). The autocorrelation traces of the *fundamental* and the *double pulse* states (Fig. 3.2a) are fitted with the autocorrelation of a sech^2-pulse with a pulse duration τ_{pulse}. They feature one single pulse, whereas the autocorrelation of the *side pulse* and *double & side pulse*states indicates the presence of two pulses next to each other (Fig. 3.2a). These traces can be fitted with two subsequent sech^2-pulses separated by τ_{sep} with an asymmetric intensity ratio of the two pulses (Fig. 3.2b).

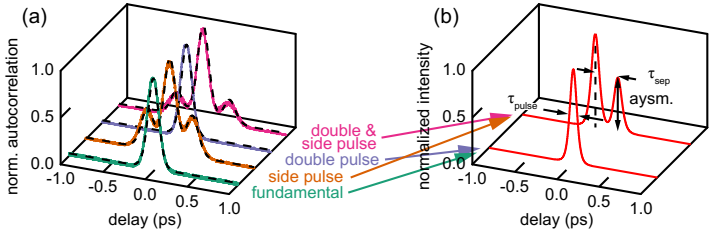

Figure 3.3: (a) Normalized autocorrelation measurement for each of the four modelocking states (colored solid line) with the corresponding fit (black dashed line). (b) Pulse fit function in the time domain featuring one sech^2-pulse or two consecutive sech^2-pulses with a pulse separation τ_{sep} and an asymmetric intensity ratio.

The pulse duration of the *fundamental* state reaches the minimum value just before the transition to *side pulse* operation (Fig. 3.4a), as the laser cavity is optimized for the shortest pulse duration in fundamental modelocking at the highest possible average power. The pulse durations of the *side pulse* and *double & side pulse*states are slightly longer with a *side pulse* asymmetry of roughly 61% and 27%, respectively. We also remark that the separation of the side pulse increases with increasing pump power

from 270 to 340 fs. For the *double pulse* state, the pulse duration is shorter again, similar to the values observed for the *fundamental* state (Fig. 3.4a). Interestingly, sweeping the hysteresis path going down from high pump intensity, we obtain even shorter pulse durations (94 fs instead of 96 fs) for the *fundamental* state when we reach it from a multipulse state (Fig. 3.4a).

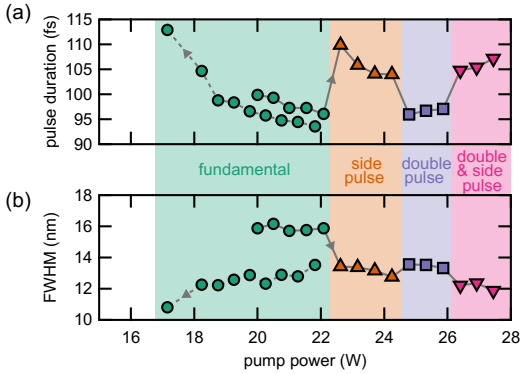

Figure 3.4: (a) Pulse duration measured for increasing (solid line) and decreasing (dashed line) pump powers. (b) Corresponding full width at half maximum (FWHM) of the optical spectrum for (solid line) increasing and (dashed line) decreasing pump powers.

B Optical spectrum

The optical spectrum is measured with a fiber coupled optical spectrum analyzer HP 70952B with a resolution of 0.1 nm (Fig. 3.5a). All optical spectra show no indication of any instability or continuous wave breakthroughs. While the optical spectra are almost sech^2-shaped for the *fundamental* and *double pulse* states, the optical spectra of the *side pulse* and *double & side pulse*states feature shoulders on both the short and long wavelength side. The center wavelength shifts almost linearly (0.65 nm/W) to higher wavelengths with increasing pump power. The *fundamental* state features the broadest spectral full width at half maximum (FWHM), while the multipulse states at higher pump powers have a narrower spectrum (Fig. 3.4b). Interestingly, the optical bandwidths of the *fundamental* states are reduced

(from 15.9 nm to 13.5nm) after the back transition from multipulse states. Combined with the shorter pulse duration, this corresponds to a decrease of the time-bandwidth product from 0.43 to 0.34 at the center wavelength of 1035 nm. Which means that the chirp of the pulse substantially changed while the average output power of 96 mW stayed the same.

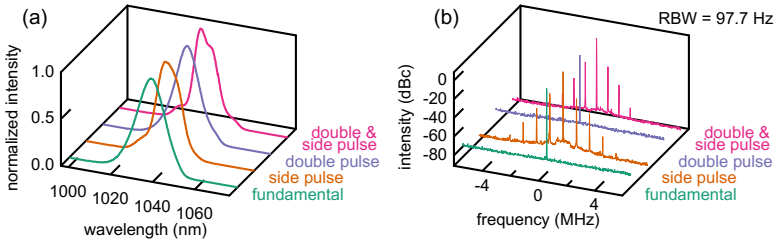

Figure 3.5: (a) Optical spectra of the different modelocking states measured with a 0.1 nm resolution. (b) Microwave spectrum of the laser intensity showing first harmonic of the repetition rate for the different modelocking states measured with a resolution bandwidth (RBW) of 97.7 Hz.

C Noise characterization

The first harmonic of the pulse repetition rate is analyzed with the signal source analyzer E5052B from Agilent with a resolution bandwidth of 97.7 Hz resulting in a high signal-to-noise ratio of approximately 80 dB. For this, the laser intensity is measured with a highly linear photodiode (HLPD from *Discovery Semiconductor*). The microwave spectra are centered around the pulse repetition rate of 1.641 GHz with a span of 10 MHz (Fig. 3.5b). For the *fundamental* and the *double pulse* states, the microwave spectra feature a delta like peak, without any visible broadening or pedestal, as it is theoretically expected for stable fundamental modelocking. The *side pulse* and *double & side pulse*states can be clearly identified by the 3 pairs of side peaks below -25 dBc next to the main peak of the pulse repetition rate. The side peak separation is 0.95 and 0.81 MHz for the *double pulse* and *double & side pulse*state, respectively. This indicates a modulation of the pulse trains, which is further revealed by the additional noise peaks in the amplitude and phase noise at the given frequencies

(Fig. 3.6). The amplitude and phase noise of the first harmonic of the repetition rate is measured using the same signal source analyzer.

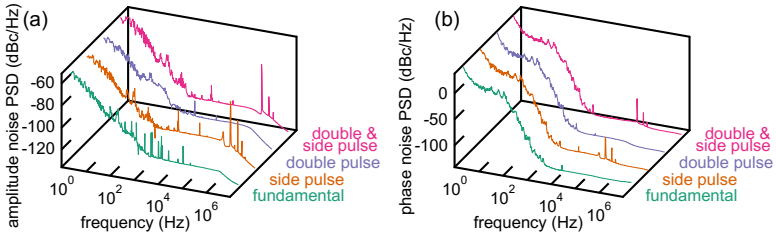

Figure 3.6: (a) Amplitude noise and (b) phase noise power spectral density (PSD) of the first harmonic of the repetition rate for the different modelocking states.

C Temporal dynamics

So far, the presented measurements do not differentiate between the *fundamental* and the *double pulse* state or between the *side pulse* and the *double & side pulse*state. But, a difference becomes evident when looking at the laser intensity over several cavity round trip times (Fig. 3.7a). The time traces are measured with a sequential equivalent-time sampling scope (CSA 803 from *Tektronix* with a 50-GHz sampling unit SD-32) and a high-speed photodetector (Model 1454 from *Newport* with an 18.5-ps rise time) amplified by an 18-GHz bandwidth preamplifier (87405C from *Agilent*).

While for *fundamental* and the *side pulse* state one pulse per round trip is measured, an additional pulse is observed for the *double pulse* and the *double & side pulse*state. In contrast to second harmonic modelocking where the separation of the additional pulse is given by one half of the round trip time [28], the additional pulse is separated by one quarter of the round trip time. For the *side pulse* and *double & side pulse*states, the pulse separation τ_{sep} is too small and cannot be resolved with the sampling scope. Only when we characterize the modelocking with both the autocorrelation and the sampling scope we can directly observe the full number of pulses simultaneously oscillating in the cavity (i.e. one pulse for the *fundamental*, two for the *side pulse*, two for the *double pulse*, and four for the *double &*

*side pulse*state).

The dynamics of the VECSEL is further characterized by a microwave spectrum analyzer (8565EC from *Agilent*) using the same high-speed photodetector and preamplifier. A stable fundamentally modelocked laser creates equally powerful harmonic peaks positioned at the repetition rate and at multiples of the repetition rate as measured for the *fundamental* and *side pulse* states (Fig. 3.7b), only limited by the bandwidth of the preamplifier for frequencies >18 GHz. Again, the two pulses separated by τ_{sep} of the *side pulse* and *double & side pulse*state are below the resolution of the photodetector and therefore are not resolved in the microwave spectrum measurement. For the *double pulse* and *double & side pulse*states, where the pulses are spaced by a quarter of the round trip time, the higher harmonics are periodically modulated (Fig. 3.7b). This stands in contrast to second harmonic modelocking, where only even harmonics would be visible and the fundamental frequency, corresponding to the inverse of the cavity round trip time, would not be visible at all.

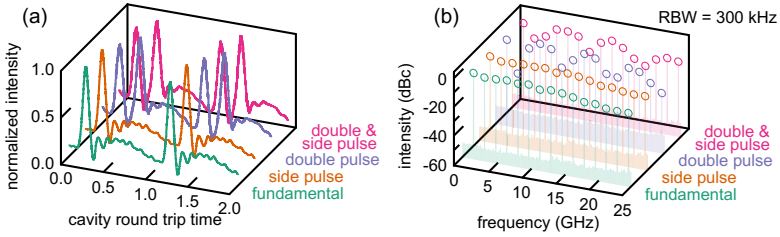

Figure 3.7: (a) Laser intensity time traces of the different modelocking states measured with a sampling scope. For the *double pulse* and the *double & side pulse*state an additional peak is visible, separated by roughly one quarter of the cavity round trip time. (b) Microwave spectrum of the laser intensity showing the high harmonics of the repetition rate for the different modelocking states measured with a resolution bandwidth (RBW) of 300 kHz. For better visibility, the peak maxima are highlighted with circles.

3.1.3 Discussion

A Hysteresis

The modelocking analysis reveals different hysteresis effects. Similar to what was reported for the antiresonant gain medium design in [28], we see a large hysteresis loop of the *fundamental* state, such that the stable fundamental modelocking continues far below the original threshold (Fig. 3.2a). Smaller hysteresis loops are observed for the other modelocking states. The *double pulse* state is special. It is more stable than the *side pulse* state and sometimes it switches directly back to fundamental modelocking, if the pump power is reduced. The *double pulse* states also have an increased average power with slightly longer pulses during the "decreasing pump path" when compared to the "increasing pump path".

Interesting is also the hysteresis of the *fundamental* states which have shorter pulse durations with narrower spectral bandwidths on the "decreasing pump path". This shows that different stable modelocking states can exist for one given pump power. These features are going beyond the theoretical predictions of a fully microscopic many-body simulation [25].

To gain insights into the dynamical formation and stability of different modelocked pulse trains, we are using a simulation based on coupled multi-delay differential equations. In contrast to the delay model widely used for a ring cavity modelocked laser [29-31], our modeling approach considers the geometry of the V-shape without the need to change to the numerically demanding traveling wave approach. Previous works on VECSEL simulations either do not consider the effects induced by the cavity geometry [32, 33] or do not allow for an efficient simulation of large external cavities [25, 34]. To obtain our numerically efficient description of the VECSEL dynamics, we integrate the traveling-wave equation for the electric field amplitude $E^{\pm}(z,t)$ and the excess charge-carrier density $N(z,t)$ [35]:

$$\left(\partial_t \pm \frac{1}{v_g}\right) E^{\pm}(z,t) = \left[-\frac{\alpha_{\text{int}}}{2} + \frac{1}{2}N(z,t)\right] \cdot E^{\pm}(z,t) \tag{3.1}$$

along its characteristic curve [36] for small sections Δz. We then consider the limit of infinitely thin gain and SESAM sections with integrated carrier densities $G(t)$ and $Q(t)$. The free space between the optical elements is treated as large passive sections. Expressing the electric fields in all

sections in terms of the electric field $A(t)$ at the out-coupling mirror (OC) leads to a system of three coupled multi-delay differential equations Eq. (3.2)-(3.4):

$$\frac{d}{dt}A(t) = \gamma \cdot \left(\sqrt{\kappa} \cdot A(t-T) \cdot e^{\frac{1}{2}(G(t-\tau_1)+G(t-\tau_1-2\tau_2))+Q(t-\tau_1-\tau_2)} - A(t)\right) \tag{3.2}$$

$$\begin{aligned}\frac{d}{dt}G(t) =& J_G - \gamma_G \cdot G(t) - \left(e^{G(t)} - 1\right) \cdot \\ & \left(|A(t-\tau_1)|^2 + |A(t-\tau_1-2\tau_2)|^2 \cdot e^{2Q(t-\tau_1)+G(t-\tau_2)}\right)\end{aligned} \tag{3.3}$$

$$\frac{d}{dt}Q(t) = J_Q - \gamma_Q \cdot Q(t) - r_s \cdot \left(e^{2\cdot Q(t)} - 1\right) \cdot e^{G(t-\tau_2)} \cdot |A(t-\tau_1-\tau_2)|^2 \tag{3.4}$$

Note that these equations, although similar to those presented in [29], contain both propagation directions and the spatial configuration of the VECSEL cavity, which is encoded in the time delays τ_1 and τ_2. Charge-carrier induced amplitude-phase coupling is omitted in this model, but could easily be included for future studies by introducing an alpha-factor in Eq. (3.1). The gain bandwidth is denoted by γ, the intensity losses per round trip by κ, the cold-cavity round trip time by T, the pump current by J_G, the unsaturated absorption by J_Q, the gain and absorber recovery times by γ_G and γ_Q, and the ratio between the gain and absorber differential by r_s. The delay times are determined by the resonator configuration $\tau_1 = L_{\mathrm{OC-VECSEL}}/v_g$ and $\tau_2 = L_{\mathrm{VECSEL-SESAM}}/v_g$, where $L_{\mathrm{OC-VECSEL}}$ is the distance between OC and VECSEL chip, $L_{\mathrm{VECSEL-SESAM}}$ is the distance between VECSEL chip and SESAM, and v_g is the group velocity. In this model, we use an "ideal" pump current directly setting the electron density for the VECSEL gain, which is simpler than using an optical pump power.

Table 3.1: Parameter values normalized to the round trip time $T = 625$ ps used to produce the following simulation results

parameter	γ	κ	γ_G	γ_Q	J_Q	r_s
norm. value	2000	0.99	0.625	122.5	-100	2

For the parameter values given in Table 3.1, the laser described with Eq (3.2)-(3.4) exhibits a range of pump currents J_G with stable modelocked

pulses whose width directly depend on the gain bandwidth γ and therefore on the number of longitudinal modes that participate in the modelocking process. We choose $\gamma = 2000$, which yields pulses that have a width of about 1 - 2 ps. This is longer than observed in the experiments, but in order to reach the experimental value much larger γ would be necessary leading to much longer computation times. We use the above value in the following numeric characterization to be able to effectively scan a wide parameter region. Investigations of the effects of larger γ are still ongoing.

This simulation reveals multistability and their hysteresis in a parameter scan of the pump current J_G (Fig. 3.8a). The dynamics for increasing and decreasing pump current are simulated. For illustration, the pulse peak intensities of a simulated pulse train are shown. We can clearly distinguish three regimes: *fundamental modelocking*, irregular pulse trains, and *double pulse* emission.

The region of irregular pulse trains is characterized by a periodic emission of irregular pulse "cluster" with varying pulse intensities (Fig. 3.8b). Interestingly, the autocorrelation function determined from these irregular pulsating time series shows similarities with the experimentally found *side pulse* state, because also in the simulations side pulses show up next to the main peak of the autocorrelation. Due to the chosen gain bandwidth γ, the pulse width is on the picosecond scale and thus also the distance between side and main peak is larger than experimentally observed. However, the similarities to both the experimentally observed parameter region and the measured autocorrelation suggest that these kind of dynamic instabilities can be one reason for the emergence of side pulses in the autocorrelation. An additional explanation of the dynamics behind the observed side pulse regime will be discussed in section 3.1.3.D.

After the region of irregular pulse trains, the laser switches to the double pulse state. Compared to the fundamental state, the intensity of the double pulse states are drastically decreased because for this regime two pulses need to be amplified per round trip. And additionally, the absorber can completely recover between two pulses thus cause increased absorption which leads to a reduced output power. Such that for a given pump current, two double pulses, bistable to a single pulse, carry less combined

power than the single pulse. For reducing pump current, the double pulse emission extends in the region of irregular pulse trains, similar to our experiments (Fig. 3.2a).

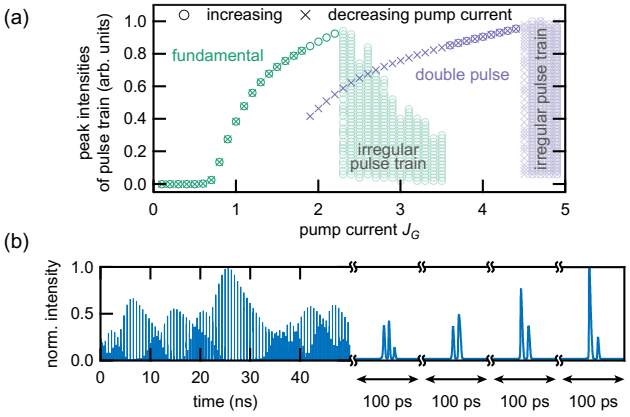

Figure 3.8: Simulation results based on the coupled multi-delay differential equations (Eq. 3.1-3.4 and Table 3.1): (a) Peak pulse intensity as a function of pump current. The dynamics for increasing (circle) and decreasing (cross) pump current clearly show *fundamental modelocking* (green), irregular pulse train (light green), and *double pulse* operation (violet). (b) Irregular pulse train as a function of time, on a time scale much larger (left) and much shorter (right) than one cavity round trip.

B Double pulse operation

The two pulses of the *double pulse* state are spaced by roughly one quarter of the cavity round trip time, which differs from second harmonic modelocking where the pulse separation would be half of the cavity round trip time. This *double pulse* operation is similar to the multipulse operation reported in [10]. In both cases a similar modulation of the higher harmonics of the repetition rate is measured with a microwave spectrum analyzer (Fig. 3.7b).

Simulations using the above mentioned coupled multi-delay differential equations indicate that the type of multipulse state strongly depend on the arrangement of the V-shaped laser cavity. Changing the delay times τ_1 and τ_2 corresponds to changing the resonator configuration, i.e. the two

arms $\tau_1 = L_{\mathrm{OC-VECSEL}}/v_g$ and $\tau_2 = L_{\mathrm{VECSEL-SESAM}}/v_g$ of the V-shaped geometry. By keeping the total cavity length L_{CAVITY} constant, we can scan the gain chip position within the cavity. Varying both the gain chip position and the pump current reveals different stability regions: no lasing, *fundamental* operation, *double pulse* state, second harmonic modelocking, irregular pulse trains, and higher order states. Parameter ranges clearly favoring second harmonic modelocking or the *double pulse* state are found (Fig. 3.9a). At sufficient pump currents, the laser is expected to operate in the *double pulse* state when the gain chip is placed in the center of the cavity. Whereas, second harmonic modelocking is favored when the gain chip is placed closer to the OC or closer to the SESAM.

This can be explained by looking at the time evolution of the electric field intensity and the evolution of the gain for two cavity geometries (Fig. 3.9b). The preferred pulse configuration is obtained for the case where the two pulses hit the gain chip are equally spaced in time. This allows for a balanced recovery of the gain between the pulses. Since the recovery of the SESAM absorption is much faster, it is not limiting here. When the gain chip is in the center of the cavity ($L_{\mathrm{OC-VECSEL}}/L_{\mathrm{CAVITY}} = 0.5$) the *double pulse* state is preferred and when the gain chip is closer to the OC or to the SESAM ($L_{\mathrm{OC-VECSEL}}/L_{\mathrm{CAVITY}} = 0.25$ or 0.75) second harmonic modelocking is preferred. For the distance ratio of 0.53 used in the experimental cavity, the favored configuration is the observed *double pulse* state.

Moreover, a central positioning of the gain chip also increases the region of stable fundamental modelocking towards higher pump currents and thereby allows for higher output powers. Similar to the multi-pulse operation, the central configuration ensures equal times between pulse incidents in the gain chip and thus ensures a balanced recovery.

C Cavity round trip reflectivity

To gain a deeper insight of the modelocking mechanisms and the multi-pulse operation, we investigated in more details the saturation characterization of the VECSEL cavity. With the measured nonlinear reflectivities of the pumped VECSEL gain chip and the SESAM, we can estimate the cavity round trip reflectivity [20, 37]. For this, we consider a full cavity round trip

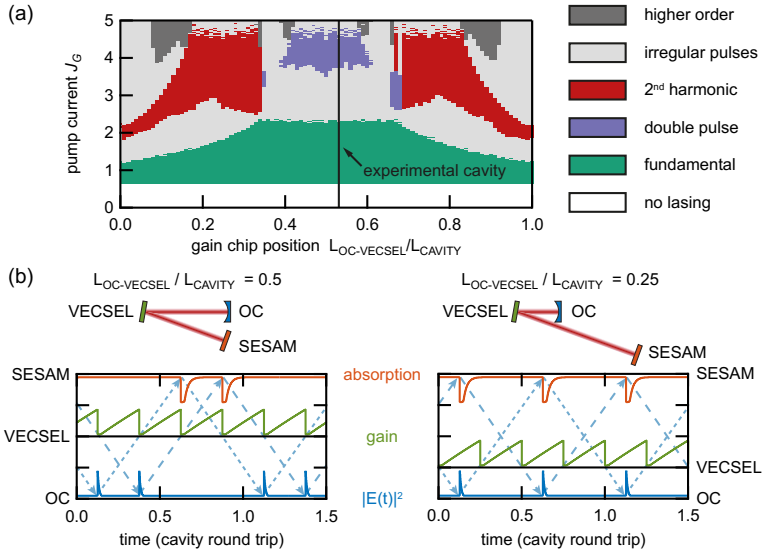

Figure 3.9: Simulation results based on the coupled multi-delay differential equations (Eq. 3.1-3.4 and Table 3.1): (a) Simulation for different pump currents and different positions of the gain chip (described by the distant $L_{\mathrm{OC-VECSEL}}$ between the output coupler (OC) and the VECSEL chip at constant total cavity length L_{CAVITY}). The different stability regions are color coded: no lasing (white), *fundamental* state (green), *double pulse* state (violet), second harmonic modelocking (magenta), irregular pulse trains (grey), higher order states (dark grey). The black line indicates the gain chip position in the investigated experimental cavity. (b) Time evolution of the electric field intensity at the OC position (blue), of the VECSEL gain (green), and of the SESAM absorption (orange) shown for the two cavity configurations $L_{\mathrm{OC-VECSEL}}/L_{\mathrm{CAVITY}} = 0.5$ and 0.25.

by multiplying the output coupler reflectivity with the SESAM reflectivity and with twice the VECSEL reflectivity. The VECSEL reflectivity is probed with 170-fs pulses at different probing fluences, for different probing wavelengths, for different pump powers, and for different heat sink temperatures, as described in [20]. Similarly, the fluence-dependent SESAM reflectivity is measured for different heat-sink temperatures where a temperature dependent wavelength shift of 0.32 nm/K for the spectral absorption of the SESAM is assumed. The measurements intrinsically include all optical losses and a reflectivity exceeding 100% corresponds to gain.

The round trip reflectivity is estimated for the *fundamental* state at 20.0 W pump power (Fig. 3.10a). The measured average output power of 84 mW lies slightly in the roll-over of the round trip reflectivity. This behavior is common for SESAM-modelocked lasers and has been reported for SDLs based on active QWs [37], QDs [38] and for thin disk lasers [39]. It appears, that the SESAM is not fully saturated and thus is not operated at the point of minimal loss. Hence, higher output power could be achieved with a fully saturated SESAM. Further investigations are ongoing which address the question: Does a fully saturated SESAM maintain the short pulse duration? However this is beyond the scope of this paper. The estimation of the cavity round trip reflectivity can nicely reproduce the measured output power for all the *fundamental* states (Fig. 3.2a).

To investigate the transition to the *side pulse* state, we calculate the round trip reflectivity at 22.6 W pump power as if the laser would remain in the *fundamental* state (Fig. 3.10a), even though in the experiment the laser would have switched to the *side pulse* state. Despite the increased pump power, the reflectivity, and therefore the gain, of the VECSEL gain chip seems nearly unchanged. The reason is that the additional gain due to higher pumping is balanced by a reduction of gain caused by a red-shift of the laser spectrum with consequently lower gain at longer wavelengths. The red-shift of the laser is also the cause for the reflectivity increase of the SESAM. With this, the theoretical operation point is even further in the roll-over. On the other hand, the reflectivity for low power pulses is increased to nearly 100%. Thus, they are not efficiently suppressed anymore. The rise of additional low energy pulses appears as a more favorable configuration for the laser, confirming the experimentally observed switch to

side pulse operation.

This model cannot be extended to the *side pulse* and *double pulse* states as the successive pulses would see a partially saturated VECSEL gain and SESAM absorption and therefore substantially changing the reflectivity.

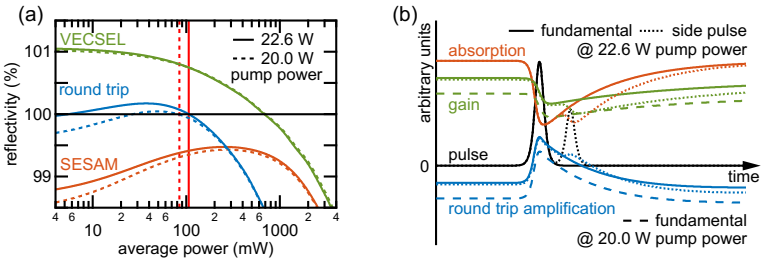

Figure 3.10: (a) Measured and interpolated reflectivity of the VECSEL chip (green), the SESAM (orange), and the cavity round trip (blue) depending on the average output power. The reflectivity curves are shown for the *fundamental* state at 20.0 W pump power (dashed lines) and for a theoretical *fundamental* state at 22.6 W (solid lines) together with the predicted average output power (red) which is in good agreement with our measurement in Fig. 3.2a. (b) Simulation (see section 3.1.3.D for more details) of the instantaneous gain of a double passage on the VECSEL chip (green), the instantaneous absorption of the SESAM (orange), and the instantaneous cavity round trip amplification (blue). The simulation shows the response to a 100-fs probe pulse at 20.0 W of pump power (dashed lines) and at 22.6 W pump power (solid lines). In analogy to the *side pulse* state, the response is shown for a 100-fs probe pulse with an additional side pulse separated by 300 fs at 22.6 W pump power (dotted lines).

D Side pulse operation

On the 100-fs timescale new effects of the semiconductor material start to play a role, such as kinetic hole burning, theoretically predicted by fully microscopic many-body models [24, 25]. The related kinetic hole filling can explain the two time scales in the recovery of the VECSEL reflectivity measured in-situ during modelocking operation [40]. This in-situ measurements revealed an initial fast gain recovery of up to 80% taking place in few hundreds of femtoseconds, followed by a slow recovery in the hundreds of picoseconds determined by the slow refilling of the quantum well by diffusion of the optically pumped carriers.

These 100-fs timescale effects are not included in the coupled multi-

delay differential equations introduced in section 3.1.3.D. Thus, we implemented another simpler rate equation model to study the fast quantum well dynamics, as described in [37]. This model cannot describe modelocking formation, but it describes the instantaneous response to an incoming pulse for both the gain of the VECSEL chip and the absorption of the SESAM. This allows for an estimation of the instantaneous round trip amplification, by considering two passes on the VECSEL chip, one pass on the SESAM, and taking into account all the cavity losses, such as the output coupler loss.

This simulation shows that for a 100-fs pulse at 20.0 W pump power the round trip amplification is limited to the temporal pulse width (Fig. 3.10b). But for 22.6 W pump power, the instantaneous round trip amplification stays positive for an interval after the trailing edge of the pulse. Thus, the combination of the initial fast recovery of the gain and the partially saturated SESAM from the first pulse supports a weaker side pulse to reach lasing threshold. The corresponding simulation for a 100-fs probe pulse with an additional delayed side pulse separated by 300 fs reveals the increased positive instantaneous amplification for the side pulse, which enables the experimentally observed *side pulse* operation.

Side pulse operations have also been reported for example in a colliding pulse cavity or with a graphene saturable absorber [41, 42]. The optical spectra of these previously reported results look like the combination of two spectra with different center wavelength. However in our case, the optical spectra of the *side pulse* states are still close to sech^2-shaped with only two small shoulders on the side (Fig. 3.5a).

3.1.4 Conclusion

In conclusion, we present an analysis of the pump power dependent modelocking performance of a SESAM-modelocked VECSEL. We identify four different modelocking states correlated with a step-like increase of the average output power. Besides an initial *fundamental modelocking* state, we find stable multipulse operations, such as *side pulse*, *double pulse*, and *double & side pulse*states. A single characterization technique is not sufficient to distinguish between all these different modelocking states. Therefore, we can confirm again that modelocking results obtained with SDLs must

be accompanied by a comprehensive characterization [26, 27].

The modelocking analysis reveals interesting hysteresis effects, such as a hysteresis loops of the different modelocking states and also a shortening of the pulse duration combined with a narrower optical spectrum of the *fundamental* state when operating in the "decreasing pump path" of the hysteresis curve (Fig. 3.2a).

At higher pump power beyond stable fundamental modelocking, simulations show that the type of multipulse state strongly depends on the cavity arrangement. Different multipulse operation can be obtained with different gain chip positions within the cavity round trip. Operation is optimized when the two pulses hit the gain chip equally spaced in time. The highest power in fundamental modelocking is therefore achieved when the VECSEL gain chip is centered in the cavity (Fig. 3.9).

To improve the average output power of fundamental modelocking, which in our case is not limited by thermal effects but by multipulse instabilities, we have investigated the onset of multipulse instabilities in great detail. We find that the transition to multipulse states takes place in the roll-over of the cavity round trip reflectivity resulting from the interplay between the saturation of the VECSEL gain and the saturation of the SESAM absorption. The combination of the rapid filling of the kinetic hole in the electron-hole distribution, burned by the short femtosecond pulses, and the partially saturated SESAM by the first pulse favors the onset of a weaker side pulse. To prevent these *side pulse* operations, one could use a SESAM with a faster recovery time. Another possibility could be to operate the laser in a chirped pulse configuration with a slow SESAM, which would reduce the effect of kinetic hole burning and simultaneously increase the efficiency of the laser. Further increase in power could also be achieved by increasing the round trip reflectivity which would sustain a higher output coupler transmission. The cavity round trip reflectivity is mainly limited by the saturation of the VECSEL gain.

Funding. Swiss Confederation Program Nano-Tera.ch,
German Research Foundation (DFG), Collaborative Research Centre 787.

Acknowledgement We thank the technology and cleanroom facility FIRST of ETH Zürich for advanced micro- and nanotechnology. This work was financed by the Swiss Confederation Program Nano-Tera.ch, which was scientifically evaluated by the Swiss National Science Foundation (SNSF) and by the German Research Foundation (DFG) within the framework of Collaborative Research Centre 787.

3.1.5 References

1. M. Guina, A. Rantamäki, and A. Härkönen, "Optically pumped VECSELs: review of technology and progress," J. Phys. D: Appl. Phys. 50, 383001 (2017).

2. M. Kuznetsov, F. Hakimi, R. Sprague, and A. Mooradian, "High-Power (>0.5-W CW) Diode-Pumped Vertical-External-Cavity Surface-Emitting Semiconductor Lasers with Circular TEM00 Beams," IEEE Photon. Technol. Lett. 9, 1063-1065 (1997).

3. B. Rudin, A. Rutz, M. Hoffmann, D. J. H. C. Maas, A.-R. Bellancourt, E.Gini, T. Südmeyer, and U. Keller, "Highly efficient optically pumped vertical emitting semiconductor laser with more than 20-W average output power in a fundamental transverse mode," Opt. Lett. 33, 2719-2721 (2008).

4. B. Heinen, T. L. Wang, M. Sparenberg, A. Weber, B. Kunert, J. Hader, S. W. Koch, J. V. Moloney, M. Koch, and W. Stolz, "106 W continuous-wave output power from vertical-external-cavity surface-emitting laser," Electron. Lett. 48, 516-U102 (2012).

5. U. Keller, K. J. Weingarten, F. X. Kärtner, D. Kopf, B. Braun, I. D. Jung, R. Fluck, C. Hönninger, N. Matuschek, and J. Aus der Au, "Semiconductor saturable absorber mirrors (SESAMs) for femtosecond to nanosecond pulse generation in solid-state lasers," IEEE J. Sel. Top. Quantum Electron. 2, 435-453 (1996).

6. S. Hoogland, S. Dhanjal, A. C. Tropper, S. J. Roberts, R. Häring, R. Paschotta, and U. Keller, "Passively modelocked diode-pumped surface-emitting semiconductor laser," IEEE Photon. Technol. Lett. 12, 1135-1138 (2000).

7. B. W. Tilma, M. Mangold, C. A. Zaugg, S. M. Link, D. Waldburger, A. Klenner, A. S. Mayer, E. Gini, M. Golling, and U. Keller, "Recent advances in ultrafast semiconductor disk lasers," Light Sci. Appl. 4, e310 (2015).
8. M. A. Gaafar, A. Rahimi-Iman, K. A. Fedorova, W. Stolz, E. U. Rafailov, and M. Koch, "Mode-locked semiconductor disk lasers," Adv. Opt. Photonics 8, 370-400 (2016).
9. A. Rahimi-Iman, "Recent advances in VECSELs," J. Opt. 18 (2016).
10. M. Butkus, E. A. Viktorov, T. Erneux, C. J. Hamilton, G. Maker, G. P. A. Malcolm, and E. U. Rafailov, "85.7 MHz repetition rate mode-locked semiconductor disk laser: fundamental and soliton bound states," Opt. Express 21, 25526-25531 (2013).
11. M. Mangold, C. A. Zaugg, S. M. Link, M. Golling, B. W. Tilma, and U. Keller, "Pulse repetition rate scaling from 5 to 100 GHz with a high-power semiconductor disk laser," Opt. Express 22, 6099-6107 (2014).
12. O. Casel, D. Woll, M. A. Tremont, H. Fuchs, R. Wallenstein, E. Gerster, P. Unger, M. Zorn, and M. Weyers, "Blue 489-nm picosecond pulses generated by intracavity frequency doubling in a passively mode-locked optically pumped semiconductor disk laser," Appl. Phys. B 81, 443-446 (2005).
13. A. Härkönen, C. Grebing, J. Paajaste, R. Koskinen, J. P. Alanko, S. Suomalainen, G. Steinmeyer, and M. Guina, "Modelocked GaSb disk laser producing 384 fs pulses at 2 μm wavelength," Electron. Lett. 47, 454-455 (2011).
14. R. Aviles-Espinosa, G. Filippidis, C. Hamilton, G. Malcolm, K. J. Weingarten, T. Südmeyer, Y. Barbarin, U. Keller, S. I. C. O. Santos, D. Artigas, and P. Loza-Alvarez, "Compact ultrafast semiconductor disk laser: targeting GFP based nonlinear applications in living organisms," Biomed. Opt. Express 2, 739-747 (2011).
15. F. F. Voigt, F. Emaury, P. Bethge, D. Waldburger, S. M. Link, S. Carta, A. van der Bourg, F. Helmchen, and U. Keller, "Multiphoton in vivo imaging with a femtosecond semiconductor disk laser," Biomed. Opt. Express 8, 3213-3231 (2017).
16. C. A. Zaugg, A. Klenner, M. Mangold, A. S. Mayer, S. M. Link, F. Emaury, M. Golling, E. Gini, C. J. Saraceno, B. W. Tilma, and U. Keller, "Gigahertz self-referenceable frequency comb from a semiconductor disk laser," Opt. Express 22, 16445-16455 (2014).
17. P. Brochard, N. Jornod, S. Schilt, V. J. Wittwer, S. Hakobyan, D. Waldburger, S. M. Link, C. G. E. Alfieri, M. Golling, L. Devenoges, J. Morel, U. Keller, and

T. Südmeyer, "First investigation of the noise and modulation properties of the carrier-envelope offset in a modelocked semiconductor laser," Opt. Lett. 41, 3165-3168 (2016).

18. S. M. Link, D. J. H. C. Maas, D. Waldburger, and U. Keller, "Dual-comb spectroscopy of water vapor with a free-running semiconductor disk laser," Science (2017).
19. N. Jornod, K. Gürel, V. J. Wittwer, P. Brochard, S. Hakobyan, S. Schilt, D. Waldburger, U. Keller, and T. Südmeyer, "Carrier-envelope offset frequency stabilization of a gigahertz semiconductor disk laser," Optica 4, 1482-1487 (2017).
20. D. Waldburger, S. M. Link, M. Mangold, C. G. E. Alfieri, E. Gini, M. Golling, B. W. Tilma, and U. Keller, "High-power 100 fs semiconductor disk lasers," Optica 3, 844-852 (2016).
21. H. R. Telle, G. Steinmeyer, A. E. Dunlop, J. Stenger, D. H. Sutter, and U. Keller, "Carrier-envelope offset phase control: A novel concept for absolute optical frequency measurement and ultrashort pulse generation," Appl. Phys. B 69, 327-332 (1999).
22. V. J. Wittwer, R. van der Linden, B. W. Tilma, B. Resan, K. J. Weingarten, T. Sudmeyer, and U. Keller, "Sub-60-fs Timing Jitter of a SESAM Modelocked VECSEL," IEEE Photon. J. 5 (2013).
23. M. Mangold, S. M. Link, A. Klenner, C. A. Zaugg, M. Golling, B. W. Tilma, and U. Keller, "Amplitude Noise and Timing Jitter Characterization of a High-Power Mode-Locked Integrated External-Cavity Surface Emitting Laser," IEEE Photon. J. 6 (2014).
24. J. Hader, M. Scheller, A. Laurain, I. Kilen, C. Baker, J. V. Moloney, and S. W. Koch, "Ultrafast non-equilibrium carrier dynamics in semiconductor laser mode-locking," Semicond. Sci. Technol. 32, 013002 (2016).
25. I. Kilen, S. W. Koch, J. Hader, and J. V. Moloney, "Non-equilibrium ultrashort pulse generation strategies in VECSELs," Optica 4, 412-417 (2017).
26. M. Mangold, M. Golling, E. Gini, B. W. Tilma, and U. Keller, "Sub-300-femtosecond operation from a MIXSEL," Opt. Express 23, 22043-22059 (2015).
27. K. G. Wilcox and A. C. Tropper, "Comment on SESAM-free mode-locked semiconductor disk laser," Laser Photon. Rev. 7, 422-423 (2013).
28. E. J. Saarinen, J. Lyytikainen, and O. G. Okhotnikov, "Hysteresis and multiple pulsing in a semiconductor disk laser with a saturable absorber," Phys Rev E 78, 016207 (2008).

29. A. G. Vladimirov and D. Turaev, "Model for passive mode locking in semiconductor lasers," Phys. Rev. A 72, 033808 (2005).

30. C. Otto, L. C. Jaurigue, E. Schöll, and K. Lüdge, "Optimization of Timing Jitter Reduction by Optical Feedback for a Passively Mode-Locked Laser," IEEE Photonics Journal 6, 1-14 (2014).

31. L. Jaurigue, B. Krauskopf, and K. Lüdge, "Multipulse dynamics of a passively mode-locked semiconductor laser with delayed optical feedback," Chaos 27, 114301 (2017).

32. M. Marconi, J. Javaloyes, S. Balle, and M. Giudici, "Passive Mode-Locking and Tilted Waves in Broad-Area Vertical-Cavity Surface-Emitting Lasers," IEEE J. Sel. Top. Quan. Electron. 21, 85-93 (2015).

33. S. V. Gurevich and J. Javaloyes, "Spatial instabilities of light bullets in passively-mode-locked lasers," Phys. Rev. A 96, 023821 (2017).

34. J. Mulet and S. Balle, "Mode-Locking Dynamics in Electrically Driven Vertical-External-Cavity Surface-Emitting Lasers," IEEE J. Quantum Electron. 41, 1148-1156 (2005).

35. B. Tromborg, H. E. Lassen, and H. Olesen, "Traveling wave analysis of semiconductor lasers: modulation responses, mode stability and quantum mechanical treatment of noise spectra," IEEE J. Q. E. 30, 939-956 (1994).

36. A. G. Vladimirov, A. S. Pimenov, and D. Rachinskii, "Numerical Study of Dynamical Regimes in a Monolithic Passively Mode-Locked Semiconductor Laser," IEEE Journal of Quantum Electronics 45, 462-468 (2009).

37. C. G. E. Alfieri, D. Waldburger, S. M. Link, E. Gini, M. Golling, G. Eisenstein, and U. Keller, "Optical efficiency and gain dynamics of modelocked semiconductor disk lasers," Opt. Express 25, 6402-6420 (2017).

38. C. G. E. Alfieri, D. Waldburger, M. Golling, and U. Keller, "High-power Sub-300-Femtosecond Quantum Dot Semiconductor Disk Lasers," IEEE Photon. Technol. Lett. 30, 525-528 (2018).

39. I. J. Graumann, A. Diebold, C. G. E. Alfieri, F. Emaury, B. Deppe, M. Golling, D. Bauer, D. Sutter, C. Kränkel, C. J. Saraceno, C. R. Phillips, and U. Keller, "Peak-power scaling of femtosecond Yb:Lu2O3 thin-disk lasers," Opt. Express 25, 22519-22536 (2017).

40. C. Baker, M. Scheller, S. W. Koch, A. R. Perez, W. Stolz, R. Jason Jones, and J. V. Moloney, "In situ probing of mode-locked vertical-external-cavity-surface-emitting lasers," Opt. Lett. 40, 5459-5462 (2015).

41. A. Laurain, R. Rockmore, H.-T. Chan, J. Hader, S. W. Koch, A. R. Perez, W. Stolz, and J. V. Moloney, "Pulse interactions in a colliding pulse mode-locked vertical external cavity surface emitting laser," J. Opt. Soc. Am. B 34, 329-337 (2017).

42. S. Husaini and R. G. Bedford, "Graphene saturable absorber for high power semiconductor disk laser modelocking," Appl. Phys. Lett. 104, 161107 (2014).

3.2 Coherent beam combining and noise analysis of a colliding pulse modelocked VECSEL

Sandro M. Link, Dominik Waldburger, Cesare G. E. Alfieri, Matthias Golling and Ursula Keller

Department of Physics, Institute for Quantum Electronics, ETH Zürich, 8093 Zürich, Switzerland

Optically-pumped SESAM-modelocked semiconductor disk lasers have become interesting ultrafast lasers with gigahertz pulse repetition rates, high average power and adjustable lasing wavelength. It is well established that colliding pulse modelocking (CPM) can generate both shorter pulses and improved stability. These improvements however typically come at the expense of a more complex ring cavity and two output beams. So far similar modelocking results have been obtained with CPM vertical external-cavity surface-emitting lasers (VECSELs) and with SESAM-modelocked VECSELs or modelocked integrated external-cavity surface-emitting lasers (MIXSELs) in a linear cavity. However coherent beam combining of the two output beams of a CPM VECSEL could result in a significantly higher peak power. This is interesting for example for applications in biomedical microscopy and frequency metrology. Here we demonstrate with a more detailed noise analysis that for both output beams of a CPM VECSEL the pulse repetition rates and the carrier envelope offset frequencies are locked to each other. In contrast to standard SESAM-modelocked VECSELs in a linear cavity, we only have been able to actively stabilize the pulse repetition rate of the CPM VECSEL by cavity length control and not by pump-power control. Furthermore, a first coherent beam combining experiment of the two output beams is demonstrated.

3.2.1 Introduction

Colliding pulse modelocking (CPM) was first introduced with passively modelocked dye lasers [1]. The modelocking is based on dynamic gain saturation for which a critical balance between loss and gain saturation opens

up a net gain window [2]. Better modelocking stability and shorter pulses were achieved with a ring laser when the distance between the absorber and the gain is about one quarter of the resonator roundtrip length. In this case, the two pulses propagating in opposite direction collide in the saturable absorber and saturate the absorber more strongly. In addition, the time between the pulses in the gain corresponds to half the roundtrip time which allows for the gain to recover to the same value for both pulses. The optimization of the CPM Rhodamine 6G laser resulted in world-record pulse durations of only 27 fs [3]. The CPM technique then has been also applied for semiconductor lasers with a monolithic edge-emitting quantum well laser in a linear cavity [4, 5]. However, the critical cavity stability requirements seem to have prevented a stronger impact of this approach so far. More recently the CPM technique has been used for an optically pumped vertical external-cavity surface-emitting laser (VECSEL) in a ring cavity [6] generating pulses as short as 128 fs with an average power of 90 mW per output beam at a pulse repetition rate of 3.27 GHz [7].

However, it is not clear that the additional complexity of a ring cavity is justified when we compare CPM VECSELs with standard SESAM-modelocked VECSELs [8, 9]. Stable modelocking with pulses as short as 96 fs with 100 mW of output power in a more simple linear cavity has been demonstrated [10]. In addition, CPM is not possible with the more compact approach of a modelocked integrated external-cavity surface-emitting laser (MIXSEL) [11] integrating the saturable absorber and the gain within the same semiconductor wafer. To date with optically pumped MIXSELs pulses as short as 184 fs with 115 mW average output power have been demonstrated [12]. The MIXSEL also provides a very stable optical frequency comb even without any further active stabilizations: for example a free-running single 2-GHz MIXSEL comb has a comb line spacing variation of only $\approx 2.5 \times 10^{-4}$ integrated over a measurement time of 10 ms [13]. Such excellent modelocking stability enabled dual comb spectroscopy in water vapor with only one laser cavity and without any further active stabilization [14].

A CPM VECSEL has two output beams and so far it has not been demonstrated that these two beams are fully coherent and potentially could be combined to obtain a higher peak power. This could be interest-

ing for applications in biomedical microscopy [15] and supercontinuum generation [16]. Coherent beam combining requires that both the pulse repetition frequencies and the carrier envelope-offset (CEO) frequencies [17] are identical for both beams, which has not been demonstrated for CPM VECSELs to date. Here, we analyze the noise behavior of a CPM VECSEL and confirm that indeed, both the pulse repetition frequencies and the CEO frequencies of both beams are intrinsically locked to each other. We coherently combine the two beams in a proof-of-principle second harmonic generation (SHG) experiment.

3.2.2 Laser setup

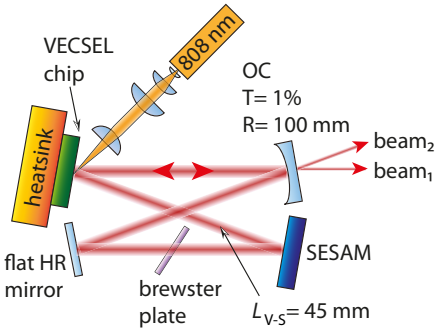

Figure 3.11: Colliding pulse modelocking (CPM) VECSEL. The VECSEL chip is optically pumped by a cw 808-nm diode laser array. The ring cavity enables two pulses propagating in opposite directions. Stable CPM is obtained when the cavity length between the VECSEL chip and the SESAM (LV-S) is a quarter of the total cavity roundtrip length. OC, output coupler; HR, high reflector.

The details of the VECSEL chip used to build the ring cavity can be found in [10]. The cavity comprises the VECSEL chip, the SESAM, a flat high reflectance mirror and an output coupler (OC) with 1% transmission and a radius of curvature of 100 mm [Fig. 3.11]. The total cavity length is 180 mm. Since there is no direction-selective element in the ring cavity, two pulses can propagate in opposite direction around the ring cavity. The CPM technique introduces a stronger saturation of the saturable absorber based on interference of the two counter-propagating beams. This intrin-

sically favors the same linear polarization for both output beams which was also observed in our experiment. However, depending on the pump power, we have observed that both beams can simultaneously switch from p- to s-polarization. This was also observed in the linear cavity configuration using the same VECSEL chip. Since part of the experiment is polarization sensitive such as the second harmonic crystal, we introduced an intracavity Brewster plate to fix the polarization. For the distance between the VECSEL chip and the SESAM (LV-S) a quarter of the total cavity length is chosen to enable an equal pumping duration and gain recovery time for both counter-propagating pulses [6].

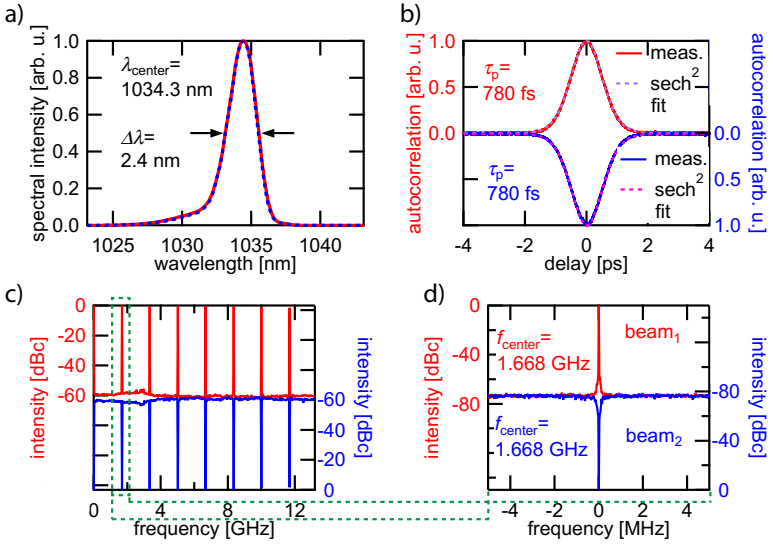

Figure 3.12: CPM VECSEL modelocking results for the two output beams: $beam_1$ (red) and $beam_2$ (blue). a) The optical spectrum is identical for both beams. b) Second harmonic autocorrelations show for each beam a pulse duration of 780 fs. c) Microwave spectrum measured over the full span of the microwave spectrum analyzer with a resolution bandwidth (RBW) of 30 kHz. d) Microwave spectrum zoomed in around the first harmonic with a span of 10 MHz and a RBW of 1 kHz confirms that both beams have the same pulse repetition frequency.

The VECSEL chip and the SESAM are operated at 20°C and 18°C, respectively. The cavity and pump spot on the gain chip have a beam ra-

dius of 177 μm and the beam radius on the SESAM is 100 μm. With a total pump power of 20 W, we achieved 170 mW average output power per beam. The diagnostics show that both beams have identical modelocking characteristics [Fig. 3.12]. The center wavelength of both beams is 1034.3 nm with a full width at half maximum (FWHM) of 2.4 nm [Fig. 3.12(a)]. The pulse duration, measured with a second-harmonic autocorrelation, is for both beams 780 fs [Fig. 3.12(b)] and the pulse repetition frequencies are identical with 1.668 GHz, shown for the full span of the microwave spectrum analyzer (MSA) of 13 GHz with a resolution bandwidth (RBW) of 30 kHz [Fig. 3.12(c)] and magnified around the first harmonic in a span of 10 MHz with a RBW of 1 kHz [Fig. 3.12(d)]. The goal of this experiment was not to obtain a new record performance of CPM VECSELs but to study the coherence of the two output beams and investigate if coherent beam combining is possible. Therefore, we did not optimize the CPM VECSEL for short pulse durations but used a very stable configuration at room temperature that delivered reproducible parameters over weeks of operation.

3.2.3 Pulse repetition frequency analysis

In CPM operation both pulses collide in the SESAM. Constructive interference of the two pulses increases the saturation of the SESAM which is energetically favorable. Therefore we expect that CPM locks the pulse repetition rates of the two counter-propagating beams. We recently observed similar intrinsic locking in case of a dual-comb modelocked SDL with sufficient spatial and temporal overlap on the absorber [18]. However, the microwave spectrum measurement of the pulse repetition frequency [Fig. 3.12(d)] is not sufficient as proof for perfectly synchronized pulses, since small asynchronous timing jittering would not be resolved with an MSA measurement.

We actively stabilize the pulse repetition frequency of one of the two beams (beam_1) by actively controlling the cavity roundtrip length. We then measure the phase noise of both beams with a signal source analyzer (SSA) [Fig. 3.13]. For this stabilization approach we detect the pulse repetition frequency of beam_1 with a photodetector and mix the signal with a low noise electronic reference set to the same frequency. The phase error

of the mixed signal is fed to a phase-locked loop (PLL). We exchanged the half-inch output coupler with a 2-mm thick output coupler that we mount on a piezo actuator. By sending the correction voltage of the PLL to the piezo, the cavity length is actively changed to compensate for the phase error. With a second photodetector, we measure the phase noise of $beam_1$ out-of-loop with the SSA. A strong reduction of the phase noise of over 100 dB is observed from free-running to stabilized operation [Fig. 3.13]. We keep the stabilization of $beam_1$ active and measure the phase noise of $beam_2$. Also for the pulse repetition frequency of $beam_2$ the phase noise is reduced by the same amount [Fig. 3.13], confirming that both pulse repetition rates are fully locked.

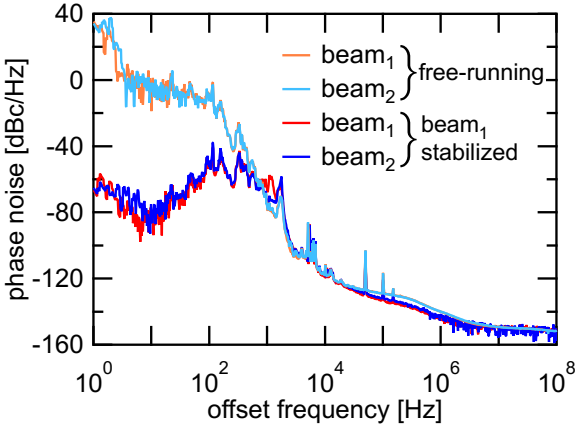

Figure 3.13: Phase noise measurements of the pulse repetition frequencies of the two output beams from the CPM VECSEL. If the pulse repetition frequency of $beam_1$ is actively stabilized by controlling the cavity roundtrip time, the noise is drastically reduced for both beams simultaneously, confirming that the two pulse repetition frequencies are locked with CPM. Note that it was not possible to obtain the same stabilization by controlling the pump power.

In CPM the intrinsic lock of the pulse repetition rate is based on the colliding pulses on the saturable absorber which is a pulse-energy dependent and interferometric mechanism. Thus, stabilization via the cavity length is an independent feedback mechanism. To investigate further, we also try to stabilize the pulse repetition frequency of $beam_1$ by modulating the

current of the pump diode instead of the cavity length. All other parts of the detection and the PLL remain unchanged. In this configuration, it is not possible to lock the phase noise. We did try to stabilize the CPM laser via pump-power modulation under different operation parameters such as cooling temperatures, pump power levels and cavity lengths, but still no locking was achieved.

Previously without CPM we stabilized the pulse repetition frequency of a standard SESAM-modelocked VECSEL via both cavity length and pump-power control and obtained the same stabilization performance. However, the pump power modulation changes the pulse energy and therefore starts to affect the CPM. The effect is so strong that no active stabilization of the pulse repetition rate is possible with pump-power control any more.

3.2.4 Carrier envelope offset (CEO) frequency analysis

For coherent beam combining we need a fully locked frequency comb with both a locked pulse repetition frequency and a carrier envelope-offset (CEO) frequency. For the following analysis of CEO frequencies, the pulse repetition frequency is not stabilized. Assuming the two CEO frequencies in each output beam are different but relatively stable with respect to each other, we should be able to detect the difference in CEO frequency as a beat signal on a photodetector. We obtain both a spatial and temporal overlap of the two output beams in the same polarization with a delay stage in the path of beam_2 before the spatial combination of the two beams with a 50:50 beams splitter (BS) [Fig. 3.14(a)]. The temporal overlap is confirmed by an autocorrelation measurement. However, no relative CEO beat frequency is visible in the microwave spectrum [Fig. 3.14(b)]. This means that either both CEO frequencies are identical or their relative noise is so high that the beat frequency stays below the noise floor of the MSA. To distinguish these two possibilities, we send beam_2 through an acousto-optic modulator (AOM) with a modulation frequency of 60 MHz [Fig. 3.14(c)]. We take the first diffraction order which introduces a frequency shift by 60 MHz for the full frequency comb of beam_2, resulting in an effective CEO frequency that is 60 MHz higher than before. If both CEO frequencies were the same, a relative beat signal should become visible at 60 MHz.

We combine the frequency-shifted beam_2 with beam_1 and measure the

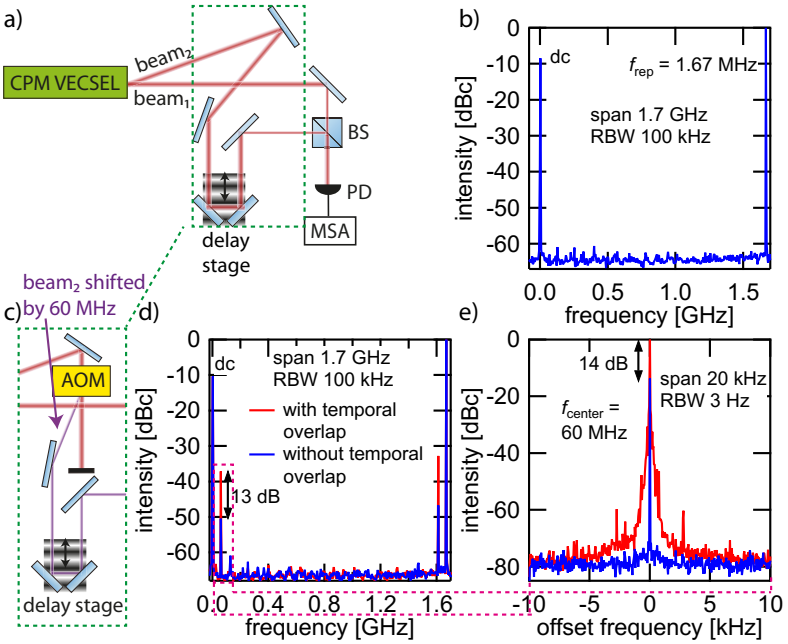

Figure 3.14: Locked carrier envelope-offset (CEO) frequencies of the two output beams from the CPM VECSEL: a) Setup to combine both beams with temporal overlap. BS, beams splitter; PD, photodetector; MSA, microwave spectrum analyzer. b) The microwave spectrum shows no relative CEO beat frequency, maybe indicating that both CEO frequencies are identical. c) This is confirmed by shifting the frequency of $beam_2$ with an acousto-optic modulator (AOM) by 60 MHz and again combining the two beams with temporal overlap. d) CEO beat frequency is detected in the microwave spectrum at 60 MHz (red line) which is stronger than the peak coming from the radio frequency driver of the AOM that is also present without temporal overlap (blue line). e) Magnification of the microwave spectrum around the CEO beat frequency.

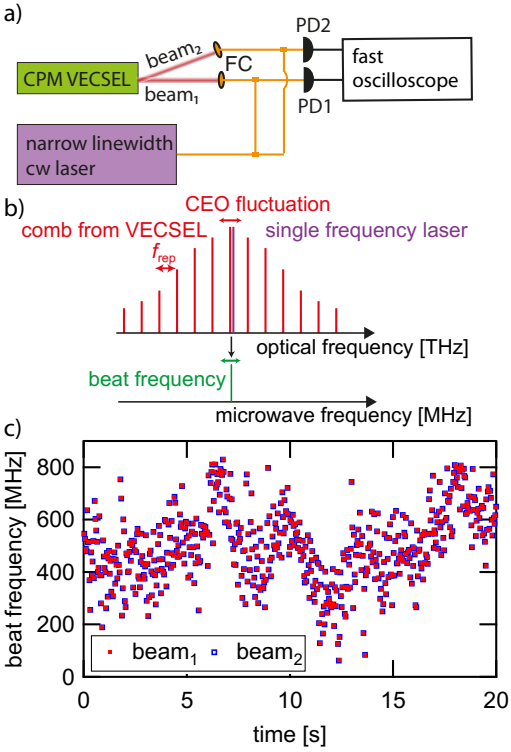

Figure 3.15: Long-term CEO frequency fluctuations of the two output beams of the CPM VECSEL: a) Setup to detect the CEO frequency fluctuations of both beams simultaneously, by beating each comb with a narrow linewidth laser. FC, fiber coupling; PD, photodetector. b) The interference between each comb of the VECSEL and the narrow linewidth laser generate a beat frequency, whose fluctuations are equal to the fluctuations of the CEO frequency of the VECSEL comb. Since we only want to observe, if both CEO frequencies fluctuate identically, we can ignore the fluctuations due to the pulse repetition frequency since we already confirmed that they are intrinsically locked with CPM. c) The perfectly synchronized fluctuations of the two beat frequencies are measured over 20 s with a gate time of 5 µs. Due to the calculation time of the Fourier transformation, the time between two measurements is 37 ms.

microwave spectrum. Without temporal overlap, there is already a signal detectable at 60 MHz. This signal comes from the strong radio frequency signal generated by the driver of the AOM and has a linewidth below the resolution of our MSA [blue line in Fig. 3.14(d), (e)]. When both beams are combined with temporal overlap, the beat signal at 60 MHz increases by 13 dB [red line in Fig. 3.14(d)]. The magnification of the CEO beat signal with a span of 20 kHz and a resolution bandwidth of 3 Hz shows a coherent peak of 23 dB on top of a noise pedestal of roughly 1 kHz width [Fig. 3.14(e)]. The residual noise in the 1 kHz range is not caused by a difference in CEO of the two beams but is a result of the phase noise accumulated on the different paths of the beams, especially due to the mechanically not perfectly stable delay stage. We confirm the origin of the noise by splitting beam_1 with a beam splitter, sending one part through the AOM and the delay stage and then recombine it with the other part. The measured CEO beating shows the same noise pedestal, even though we beat the CEO frequency of beam_1 with itself, shifted by 60 MHz.

The measurement confirms that both CEO frequencies are identical, at least on a shorter time scale. To finally prove that they are perfectly locked also on a long time scale, we measure the CEO frequency of each beam simultaneously. This is realized by beating both beams with a fiber-coupled single frequency laser (Toptica DLC CTL 1050). The wavelength of the single frequency laser is tuned to the center wavelength of the two beams and combined with each beam using fiber combiners [Fig. 3.15(a)]. Both beat signals are recorded simultaneously with a photodetector and a fast oscilloscope with 1 GHz bandwidth. The Fourier transformation of each time signal gives a frequency peak that fluctuates with the change of the CEO frequency of the corresponding beam [Fig. 3.15(b)]. Fluctuations of the pulse repetition frequency can be ignored since we have already confirmed in Section 3.2.3 that they are locked for both beams with CPM. We measure simultaneously the frequency fluctuations of the CEO frequency of each beam with a gate time of 5 µs [Fig. 3.15(c)]. The measurement shows clearly that both beat frequencies and therefore both CEO frequencies fluctuate in perfect synchronization. The large drifts of the CEO frequencies can be explained be the absence of any housing or shielding for the laser setup.

3.2.5 Coherent beam combining

Since we have established that both beams of the CPM VECSEL have the same pulse repetition frequency and the same CEO frequency, all criteria for successful coherent beam combing of the two output beams are fulfilled. We test the coherent combination of the two beams in a peak-power sensitive second harmonic generation (SHG) experiment. Both beams are combined with a BS and the temporal overlap is controlled with the delay stage in one of the beam paths [Fig. 3.16(a)]. The beams are then focused into a lithium triborate (LBO) crystal of 20 mm length that was temperature stabilized at 184°C for non-critical phase matching. A dichroic mirror is used to separate the near infrared light at 1034 nm and the generated green light at 517 nm. The green light is measured with a photodetector and a fast oscilloscope.

If one of the beams is blocked, only half of the power of the other beam will go through the 50:50 BS and generate green [case I and II in Fig. 3.16(b)]. If both beams reach the BS but without temporal overlap, no interference occurs and half of the power of each beam will reach the crystal (case III). The power of the SHG signal scales with the square of the infrared pulse peak power. Therefore, without coherent combination the green signal in case III will be just the sum of the signals of case I and case II.

The situation drastically changes for case IV in [Fig. 3.16]: If the pulses of both beams arrive at the same time on the beam splitter, they interfere constructively or destructively, depending on the phase difference of the beams accumulated in their respective beam paths. For ideal constructive interference, all of the power of each beam will go through the BS and arrive simultaneously on the SHG crystal and the peak power will add up. This leads to an eight-fold stronger green generation compared to case III. Since the interference is phase sensitive, it varies from constructive to destructive within half a wavelength (517 nm) of path-difference of the two beams. The experimental setup was on the open table without housing or special care for mechanically stable mounts. This explains why the SHG green power signal fluctuates strongly in case IV. However, it reaches a maximum of 7.7, normalized to case III, which is very close to the ideal maximum of 8. The small difference to the ideal case can be explained

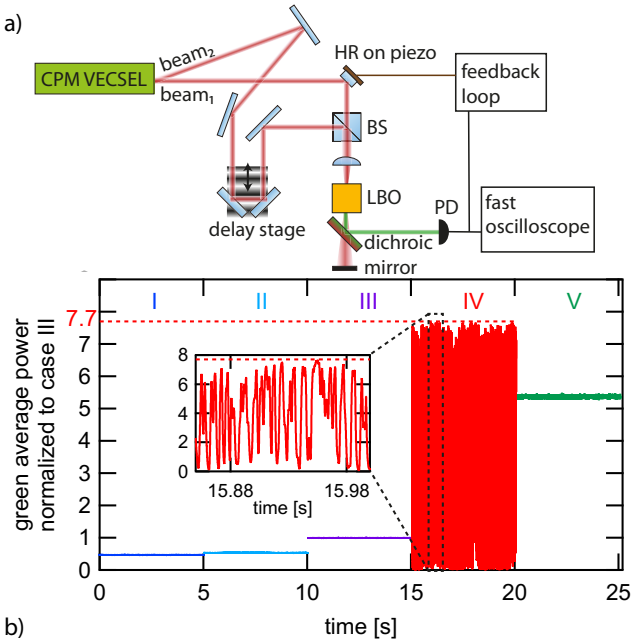

Figure 3.16: Proof-of-principle experiment for coherent beam combining of the two output beams from the CPM VECSEL. a) Both beams are coherently combined and focused into a 20-mm long lithium triborate (LBO) crystal to generate green light through second harmonic generation. PD, photodetector; BS, beams splitter. b) The generated green light is measured with a PD and a fast oscilloscope for 5 different cases: (I): $beam_2$ is blocked and only half of the power of $beam_1$ arrives at the LBO crystal. (II): $beam_1$ is blocked and only half of the power of $beam_2$ arrives at the crystal. (III): half of the power of both beams arrive at the crystal without temporal overlap which is simply a incoherent superposition of the two intensities. (IV): both beams are coherently combined and interfere constructive and destructive. (V): the coherently combined signal is stabilized by changing the path-length difference with a with a feedback loop and a piezo actuator.

by the fact that the power per beam reaching the BS was not identical and by the imperfection of the BS. The oscillation-periods of the green signal are mostly above 1 ms. This is confirmed by measuring the intensity noise of the SHG signal by taking the Fourier transformation of the signal in time [Fig. 3.17]. The noise drops to the noise floor in case IV above ≈1 kHz, which is a typical value for mechanical noise and air disturbances. This also corresponds to the noise pedestal for the relative CEO frequency measurement [Fig. 3.14(e)], since the origin of the noise is the same.

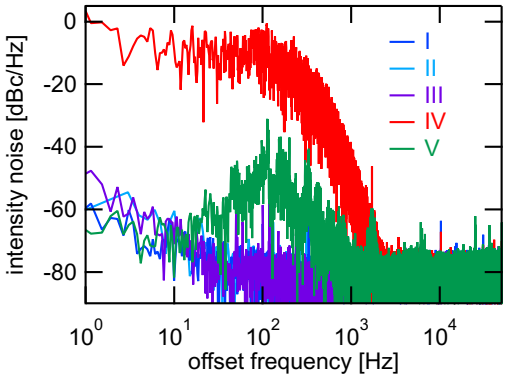

Figure 3.17: Intensity noise of the second harmonic generation (SHG), calculated via Fourier transformation from the time-dependent power signal measured in [Figure 3.16(b)] for the five different cases. The mechanical fluctuations changing the beam path difference in case IV show a bandwidth of ≈1 kHz before reaching the noise floor. They can be stabilized with a feedback loop and a piezo (case V).

The slow SHG power fluctuations with a bandwidth of 1 kHz can be compensated with a mirror mounted on a piezo actuator. The voltage signal of the green light in case IV is compared to a fixed voltage from a power supply. The error signal is fed to the same PLL used in section 3.2.3 and the correction voltage is send to a piezo actuator to control the path length of beam$_1$ [Fig. 3.16(a)]. With this method, we achieved a stabilized second harmonic signal at a level 5.3 times higher (case V) than in case III. With this simple stabilization method, it is not possible to stabilize the signal to the maximum level, since the error signal must be on the slope of the voltage signal. The intend is here to show that the coherently combined

signal can be stabilized with little effort even in a setup not optimized for low-noise operation. With a more advanced detection scheme such as a lock-in amplification method [19] or the Hänsch-Couillaud method using a polarizing beam splitter [20], it is also possible to stabilize the coherently combined signal to the maximum value.

3.2.6 Conclusion and outlook

We have realized colliding pulse modelocking (CPM) of a VECSEL-SESAM ring cavity. Our measurements show that both output beams have both identical pulse repetition frequencies and CEO frequencies. As expected from CPM we could only actively stabilize the pulse repetition rates of the two output beams with feedback over cavity length control and not with pump-power control. We can conclude that coherent beam combining of the two output beams is possible for further power scaling. We have demonstrated coherent beam combining in a proof-of-principle experiment with second harmonic generation.

For the current noise analysis experiments we did not optimize the VECSEL and the ring cavity for new world-record performance in terms of pulse duration and peak power. However, previously sub-200 fs pulses have been generated in such a CPM cavity configuration [7]. A coherent combination of the two beams has the potential to lead to a peak power of more than 1 kW, which should be sufficient to enable coherent supercontinuum generation in silicon nitride waveguides [16] and generate a self-referenced octave-spanning optical frequency comb from such a CPM VECSEL without any external pulse amplification. Other applications may also benefit from two output beams with identical frequency comb properties.

Funding. Swiss Confederation Program Nano-Tera.ch, which was scientifically evaluated by the Swiss National Science Foundation (SNSF).

Acknowledgement The authors acknowledge support of the technology and cleanroom facility FIRST of ETH Zurich for advanced micro-and nanotechnology.

3.2.7 References

1. R. L. Fork, B. I. Greene, and C. V. Shank, "Generation of optical pulses shorter than 0.1 ps by colliding pulse modelocking," Appl. Phys. Lett. 38, 617-619 (1981).
2. G. H. C. New, "Modelocking of quasi-continuous lasers," Opt. Commun. 6, 188-192 (1972).
3. J. A. Valdmanis and R. L. Fork, "Design Considerations for a Femtosecond Pulse Laser Balancing Self Phase Modulation, Group Velocity Dispersion, Saturable Absorption, and Saturable Gain," IEEE J. Quantum Electron. 22, 112-118 (1986).
4. Y. K. Chen, M. C. Wu, T. Tanbun-Ek, R. A. Logan, and M. A. Chin, "Sub-picosecond monolithic colliding-pulse modelocked multiple quantum well lasers," Appl. Phys. Lett. 58, 1253-1255 (1991).
5. Y.-K. Chen and M. C. Wu, "Monolithic Colliding Pulse Modelocked Quantum Well Lasers," IEEE J. Quantum Electron. 28, 2176-2185 (1992).
6. A. Laurain, D. Marah, R. Rockmore, J. McInerney, J. Hader, A. R. Perez, W. Stolz, and J. V. Moloney, "Colliding pulse mode locking of vertical-externalcavity surface-emitting laser," Optica 3, 781-784 (2016).
7. A. Laurain, R. Rockmore, H. T. Chan, J. Hader, S. W. Koch, A. R. Perez, W. Stolz, and J. V. Moloney, "Pulse interactions in a colliding pulse mode-locked vertical external cavity surface emitting laser," J. Opt. Soc. Am. B, 34, 329-337 (2017).
8. R. L. Fork, B. I. Greene, and C. V. Shank, "Generation of optical pulses shorter than 0.1 ps by colliding pulse modelocking," Appl. Phys. Lett. 38, 617-619 (1981).
9. G. H. C. New, "Modelocking of quasi-continuous lasers," Opt. Commun. 6, 188-192 (1972).
10. J. A. Valdmanis and R. L. Fork, "Design Considerations for a Femtosecond Pulse Laser Balancing Self Phase Modulation, Group Velocity Dispersion, Saturable Absorption, and Saturable Gain," IEEE J. Quantum Electron. 22, 112-118 (1986).
11. Y. K. Chen, M. C. Wu, T. Tanbun-Ek, R. A. Logan, and M. A. Chin, "Sub-picosecond monolithic colliding-pulse modelocked multiple quantum well lasers," Appl. Phys. Lett. 58, 1253-1255 (1991).
12. Y.-K. Chen and M. C. Wu, "Monolithic Colliding Pulse Modelocked Quantum Well Lasers," IEEE J. Quantum Electron. 28, 2176-2185 (1992).

13. A. Laurain, D. Marah, R. Rockmore, J. McInerney, J. Hader, A. R. Perez, W. Stolz, and J. V. Moloney, "Colliding pulse mode locking of vertical-externalcavity surface-emitting laser," Optica 3, 781-784 (2016).
14. A. Laurain, R. Rockmore, H. T. Chan, J. Hader, S. W. Koch, A. R. Perez, W. Stolz, and J. V. Moloney, "Pulse interactions in a colliding pulse mode-locked vertical external cavity surface emitting laser," J. Opt. Soc. Am. B, 34, 329-337 (2017).
15. B. W. Tilma, M. Mangold, C. A. Zaugg, S. M. Link, D. Waldburger, A. Klenner, A. S. Mayer, E. Gini, M. Golling, and U. Keller, "Recent advances in ultrafast semiconductor disk lasers," Light Sci Appl 4, e310– (2015).
16. M. A. Gaafar, A. Rahimi-Iman, K. A. Fedorova, W. Stolz, E. U. Rafailov, and M. Koch, "Mode-locked semiconductor disk lasers," Adv. Opt. Photonics 8, 370-400 (2016).
17. D. Waldburger, S. M. Link, M. Mangold, C. G. E. Alfieri, E. Gini, M. Golling, B. W. Tilma, and U. Keller, "High-power 100 fs semiconductor disk lasers," Optica 3, 844-852 (2016).
18. D. J. H. C. Maas, A.-R. Bellancourt, B. Rudin, M. Golling, H. J. Unold, T. Südmeyer, and U. Keller, "Vertical integration of ultrafast semiconductor lasers," Appl. Phys. B 88, 493-497 (2007).
19. C. G. E. Alfieri, D. Waldburger, S. M. Link, E. Gini, M. Golling, G. Eisenstein, and U. Keller, "Optical efficiency and gain dynamics of modelocked semiconductor disk lasers," Opt. Express 25, 6402-6420 (2017).
20. M. Mangold, S. M. Link, A. Klenner, C. A. Zaugg, M. Golling, B. W. Tilma, and U. Keller, "Amplitude noise and timing jitter characterization of a high-power mode-locked integrated external-cavity surface emitting laser," IEEE Photon. J. 6, 1-9 (2014).
21. S. M. Link, D. J. H. C. Maas, D. Waldburger, and U. Keller, "Dual-comb spectroscopy of water vapor with a free-running semiconductor disk laser," Science 356, 1164-1168 (2017).
22. F. F. Voigt, F. Emaury, P. Bethge, D. Waldburger, S. M. Link, S. Carta, A. v. d. Bourg, F. Helmchen, and U. Keller, "Multiphoton in vivo imaging with a femtosecond semiconductor disk laser," Biomed. Opt. Express 8, 3213-3231 (2017).
23. A. Klenner, A. S. Mayer, A. R. Johnson, K. Luke, M. R. E. Lamont, Y. Okawachi, M. Lipson, A. L. Gaeta, and U. Keller, "Gigahertz frequency comb offset stabilization based on supercontinuum generation in silicon nitride waveguides," Opt. Express 24, 11043-11053 (2016).

24. H. R. Telle, G. Steinmeyer, A. E. Dunlop, J. Stenger, D. H. Sutter, and U. Keller, "Carrier-envelope offset phase control: A novel concept for absolute optical frequency measurement and ultrashort pulse generation," Appl. Phys. B 69, 327-332 (1999).

25. S. M. Link, A. Klenner, and U. Keller, "Dual-comb modelocked lasers: semiconductor saturable absorber mirror decouples noise stabilization," Opt. Express 24, 1889-1902 (2016).

26. T. M. Shay, V. Benham, J. T. Baker, A. D. Sanchez, D. Pilkington, and C. A. Lu, "Self-synchronous and self-referenced coherent beam combination for large optical arrays," IEEE J. Sel. Top. Quantum Electron. 13, 480 (2007).

27. T. W. Hänsch and B. Couillaud, "Laser frequency stabilization by polarization spectroscopy of a reflecting reference cavity," Opt. Commun. 35, 441-444 (1980).

3.3 Sub-150-fs pulses from a broadband MIXSEL

Cesare G. E. Alfieri,[1,2] *Dominik Waldburger,*[1,2] *Jacob Nürnberg,*[1] *Matthias Golling*[1] *and Ursula Keller*[1]

[1] Department of Physics, Institute for Quantum Electronics, ETH Zürich, 8093 Zürich, Switzerland

[2] These authors contributed equally.

Pulse durations as short as 139 fs are achieved with a modelocked integrated external-cavity surface-emitting lasers (MIXSELs). The MIXSEL operates at a center wavelength of 1033 nm with 13 nm of full width at half maximum (FWHM) optical bandwidth. At 2.73 GHz of pulse repetition rate, the laser delivers 30 mW of average output power. Structural novelties such as multi-pair dielectric top-coating, large bandgap $AlAs_xP_{1-x}$ materials for strain compensation and improved thermal properties are implemented to allow optimized broadband dual comb operation for gas spectroscopy applications.

After a decade of constant and rapid development [1, 2], ultrafast semiconductor disk laser (SDL) arise now as a mature class of laser sources for diverse application platforms. Dual comb spectroscopy [3], multiphoton microscopy [4] and frequency metrology [5, 6] profit nowadays from the compactness and cost-efficient wavelength flexibility of gigahertz SDLs. Vertical external-cavity surface-emitting lasers (VECSELs) passively modelocked with semiconductor saturable absorber mirrors (SESAMs) [7] achieve the best ultrafast performances of SDLs, providing sub-100 fs pulse durations [8] and several kilowatts of pulse peak power [9]. The modelocked integrated external-cavity surface-emitting laser (MIXSEL) [10] on the other hand, represents the ultimate solution for compactness and simplicity. Thanks to the integration of the saturable absorber inside the epitaxial gain structure, the MIXSEL with its straight, linear cavity stays as one of the simplest femtosecond modelocked oscillators. Until now, MIXSELs demonstrated average output power up to 6.4 W [11], pulse repetition rates up to 100 GHz [12] and sub-200-fs pulses [13]. As an additional advantage, the semiconductor gain medium provides equal ampli-

fication for s- and p-polarized beams. In combination with the symmetry of the cavity geometry, the MIXSEL oscillator does not fix any preferred lasing polarization. A birefringent crystal inside the optical cavity can therefore separate the initially unpolarized beam in two cross-polarized pulse trains with slightly different pulse repetition rates sharing the same cavity [14], making the MIXSEL an ideal dual comb source.

After the first successful proof-of-principle demonstration of dual comb spectroscopy of water vapor performed with a free running picosecond MIXSEL emitting at 968 nm [3], a new generation of MIXSEL chips with larger optical bandwidth and different emission wavelengths is highly required for further spectroscopy applications of industrially relevant gases.

Differently from previous sub-300-fs MIXSELs grown using both metalorganic vapour phase epitaxy (MOVPE) and molecular beam epitaxy (MBE) in a regrowth scheme [15], the new chip is grown on a single MBE machine to avoid the defects and the additional optical losses introduced by regrowth. In dual comb operation, two distinct but overlapping spots on the MIXSEL surface need to be simultaneously pumped [14]. For this reason, we spend here particular attention for achieving the highest chip uniformity and minimize thermal cross-talks. To select the best epitaxial technique for this purpose, we compare the thermal behavior of two 100-fs class VECSEL chips. The chips consist of the same nominal epitaxial layer stack but are grown with MOVPE [8] and MBE [5] respectively. After substrate removal and flip-chip bonding on 5×5-mm, 1-mm thick diamond substrates, we mount the samples on a copper heatsink. Through a Peltier element, we set the heatsink temperature to 10°C and optically pump the center of the chips with an 808-nm multimode laser diode. We shape the pump spot size to 400 μm diameter, set the absorbed pump power to ≈30 W and observe the surface temperature profile with a thermal camera with a resolution of 25 μm, as depicted in Fig. 3.18a and 1b. The pumped spots reach temperatures of ≈75°C for both samples. The MBE VECSEL shows a more efficient 1D heat flow resulting in a significantly decreased surface temperature at moderate distances from the pumped area.

Compared to the MOVPE chip, the surface temperature of the MBE VECSEL is ≈10°C lower at a 300-μm distance from the pump spot (Fig. 3.18c) which corresponds to the typical separation of the cross-

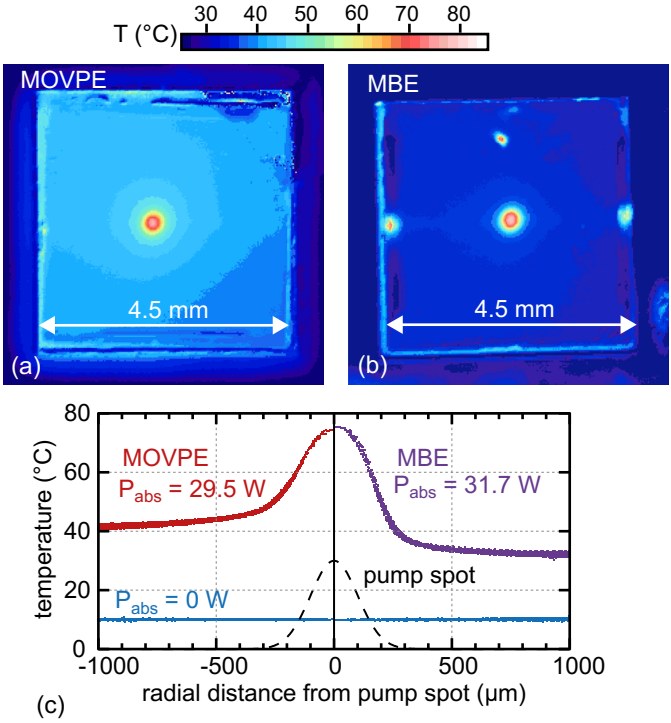

Figure 3.18: Thermal picture of optically pumped VECSEL chips grown with MOVPE (a) and MBE (b), respectively. The MOVPE chip shows a pronounced lateral heat flow and a uniform heating of the entire surface. For the MBE chip the heated region is more restricted to the pumped area (hot points on the boarder are etch residuals). (c) Surface temperature as a function of the radial distance from the pumped spot. The MBE chip features an efficient 1D heat flow. At a distance of 300 µm from the center of the pump spot, its surface temperature is ≈10°C lower compared to the MOVPE chip.

polarized beams in dual comb operation [14]. Therefore, MBE structures seem to offer reduced undesired effects of overheated surfaces and thermal cross-talks in dual comb operation. Considering this, the new MIXSEL is grown with an MBE machine. The epitaxial layer stack of the MIXSEL chip is depicted in Fig. 3.19a. From bottom to top, the design features a 24-pair GaAs/$Al1_{0.98}Ga_{0.02}As_{0.98}P_{0.02}$ distributed Bragg reflector (DBR) forming a high-reflectivity mirror with a stop band centered at the desired center lasing wavelength of 1033 nm. The small P-content provides a strain-free DBR, while 2% of Ga decreases oxidation in the thick Al layers for a longer chip lifetime. The absorber section is formed by a single 9-nm thick $In_{0.23}Ga_{0.77}As$ quantum well (QW) embedded in AlAs and locally strain-compensated with 2 $AlAs_{0.86}P_{0.14}$ layers. A second 9.5-pair $Al_{0.15}Ga_{0.85}As$/AlAs pump DBR avoids absorber bleaching from residual pump light at 808 nm. The following active region consists of 11 $In_{0.2}Ga_{0.8}As$ QWs embedded in GaAs. Most of strain-compensated SDLs operating at 1 μm usually use pump-absorbing tensile $GaAs_xP_{1-x}$ layers to balance the compressive strain introduced by the QWs [8, 13, 16]. In contrast, we use here $AlAs_{0.86}P_{0.14}$ strain compensation (SC) layers. The large bandgap AlAsP-based materials are pump transparent and create a strong confinement for the carriers optically generated in the pump-absorbing GaAs barriers. This limits their diffusion and provides individual reservoirs of rapidly available carriers for each QW. In addition, large bandgap materials heavily reduce two photon absorption (TPA) effects in the active region, reducing the losses for short pulses [17]. The QWs are alternatively placed in slightly asymmetric pairs or singularly around the antinodes of the laser standing wave. The thickness and mutual position of QWs, SC and pump absorbing GaAs layers are optimized to simultaneously achieve perfect strain compensation, broadband operation and sufficient absorption of the standing electric pump wave for every QW reservoir (>3%, Fig. 3.19b). Additionally, the non-periodic gain structure prevents sub-resonator effects that could be raised by the high refractive index contrast between GaAs and SC layers. The total pump absorption in the active region is maximized to ≈93% and its reflection minimized to ≈3% by a numerically optimized anti-reflection (AR) final section consisting of 3 Ta_2O_5/SiO_2 pairs. The AR section is deposited

with ion beam sputtering (IBS), which provides better thickness uniformity over the chip surface and higher film packing density [18, 19] for more humidity-resistant layers compared to our plasma-enhanced chemical vapor deposition (PECVD). The entirely dielectric AR section further reduces additional TPA losses in the intense-field regions close to the chip surface and provides the desired flat ($<\pm 200$ fs^2) group delay dispersion (GDD) profile in a ± 15 nm bandwidth around the designed central lasing wavelength. The DBR, the GaAs barriers and the SC layers in the active region are grown at 580°C and the gain QWs at 510°C. The absorber QW is grown at 280°C to introduce defect recombination centers and assure the fast recovery dynamics indispensable for short pulse generation.

The structure is grown upside-down. After substrate removal through wet etching, the MIXSEL is flip-chip bonded on 1-mm thick, 5x5 mm diamond heat sink and finally mounted on a Peltier-controlled, water-cooled copper substrate. The MIXSEL chip represents one end mirror of the straight laser cavity and a curved output coupler (OC) with a 100-mm radius of curvature and a 0.3% transmission the other (Fig. 3.20a). We insert an intracavity AR coated 1-mm thick calcite ($CaCO_3$) birefringent crystal and align the cavity for the ordinary beam to select the lasing polarization. At 1033 nm, calcite introduces 42 fs^2/mm of group velocity dispersion (GVD) in the s-polarized ordinary beam (Fig. 3.20b). This allows to fine tune the cavity roundtrip GDD to ideally small positive values ($<$50 fs^2) for ultrashort pulse generation [20] in the desired 1025-1035 nm lasing range (Fig. 3.20b). As an additional advantage, using the birefringent calcite crystal at this early stage will allow in a second step to easily switch to dual comb operation by pumping a second spot on the MIXSEL chip for the extraordinary beam.

For lasing operation, the chip temperature is stabilized to 4.5°C. Stable self-starting modelocking is reached at an incident pump power of 7.9 W and at a pulse repetition rate of 2.73 GHz. The relatively low average output power of 30 mW (compared to [15]) is a consequence of the broadband chip design; however, these power values are sufficient for high SNR spectroscopy applications [21, 22]. The optical-to-optical pump efficiency of $<$0.5% lies in the typical value range of sub-200-fs SDLs [2, 13].

A thorough pulse characterization was carried out using second har-

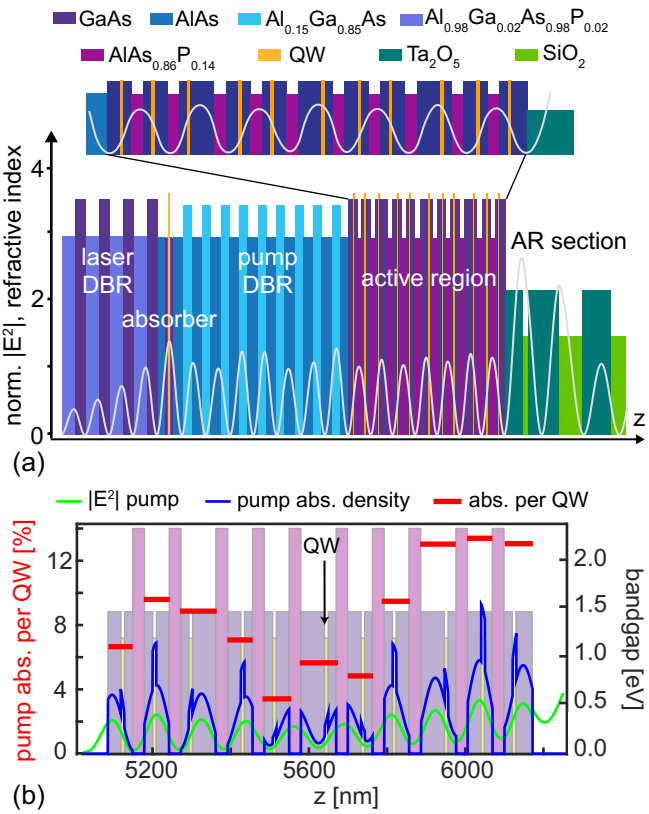

Figure 3.19: (a) Layer stack of the semiconductor MIXSEL chip with zoom of the active region. The standing electric intensity wave is normalized to 4 outside of the fully reflective structure. The field intensity is enhanced at the absorber position to reduce its saturation fluence. (b) Pump absorption in the active region. The large-bandgap $AlAs_{0.86}P_{0.14}$ strain compensation layers do not absorb the pump light (abs. density = 0) and confine the optically generated carriers. The absorption of the standing pump wave for every QW reservoir (red bars) goes from a minimum of 3.3% corresponding to a pump node to a maximum of 13%.

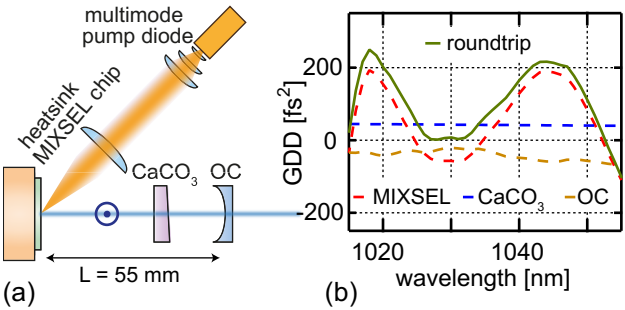

Figure 3.20: (a) Straight linear MIXSEL cavity. The semiconductor MIXSEL chip forms one cavity end mirror and the output coupler (OC) the other. The intracavity calcite crystal fixes the laser polarization. The MIXSEL chip is pumped at 808 nm with a multimode diode laser array under a 45° angle. The total cavity length is set to 55 mm. (b) Dispersion profile of the cavity elements. The calcite crystal compensates the negative GDD of chip and OC at the designed lasing wavelength. The total cavity GDD is small and positive in the designed lasing spectral region.

monic generation frequency resolved optical gating (SHG FROG). The experimental and retrieved spectrograms depicted in Fig. 3.21a-b show good agreement, with a FROG error < 0.2% (matrix size: 512x512). The retrieved temporal intensity reveals pulse duration of 144 fs (Fig. 3.21c). The small discrepancy with the 139-fs pulse duration indicated by the sech^2-fit of the SHG autocorrelation trace (Fig. 3.21d) is due to a not-perfect sech^2 shape of the modelocked pulses. The difference between these values is within the experimental error margins of the two measurement devices ($\pm$5%). This result represents the shortest pulses yet achieved with the MIXSEL technology. The resulting pulse peak power is 70 W. The microwave spectrum confirms fundamental modelocking with a narrow peak at the pulse repetition frequency and more than 60 dB of signal to noise ratio (Fig. 3.21e). All the higher harmonics of the fundamental pulse repetition rate appear with equal power in the long-span measurement of the microwave spectrum (Fig. 3.21e, inset). SHG FROG and optical spectrum analyzer show with excellent overlap that the optical spectrum is centered at 1033 nm and features 13 nm of FWHM bandwidth (Fig. 3.21f). Such bandwidth could support sub-100-fs transform-limited pulses, but the not perfectly flat retrieved spectral phase indicates a chirp of the high-wavelength tail of the spectrum, where the roundtrip GDD sig-

nificantly deviates from the optimum small positive value. To highlight the enhanced spectroscopic potential of this structure, we underline that the large spectral width achieved here is >70% wider compared to the previous record MIXSEL described in [13] and 40 times wider that in the first proof-of-principle dual-comb experiment [3].

To conclude, we presented a significant step towards fully integrated 100-fs class SDLs. With the aim for a new MIXSEL generation optimized for dual comb applications, we compared the thermal behavior of structures grown with our different epitaxial machines. In contrast to MOVPE, we showed that MBE provides better 1D heat flow, which is essential for pumping two close spots on the MIXSEL surface. We implemented high-bandgap SC layers to reduce TPA losses at short pulse durations and obtain higher carrier confinement in the gain regions. Finally, we deposited a fully dielectric AR section with IBS, which offers better material homogeneity than PECVD. With this chip, the MIXSEL technology demonstrated for the first time sub-150-fs pulses and 13 nm of FWHM optical bandwidth. This was possible thanks to the broadband gain of the semiconductor structure and to the accurate optimization of the GDD profile for each cavity element.

We are confident that the technological improvements and design guidelines described here will soon allow even shorter sub-100-fs pulses from MIXSELs. In addition, we believe that this particular chip will allow performing simple and reliable dual comb spectroscopy experiments for gases featuring absorption lines in the 1 μm range.

Funding. Swiss Confederation Program Nano-Tera.ch, which was scientifically evaluated by the Swiss National Science Foundation (SNSF).

Acknowledgement The authors acknowledge support of the technology and cleanroom facility FIRST of ETH Zürich for advanced micro- and nanotechnology. The authors thank Dr. Valentin Wittwer from the University of Neuchâtel for technical help and IBS depositions.

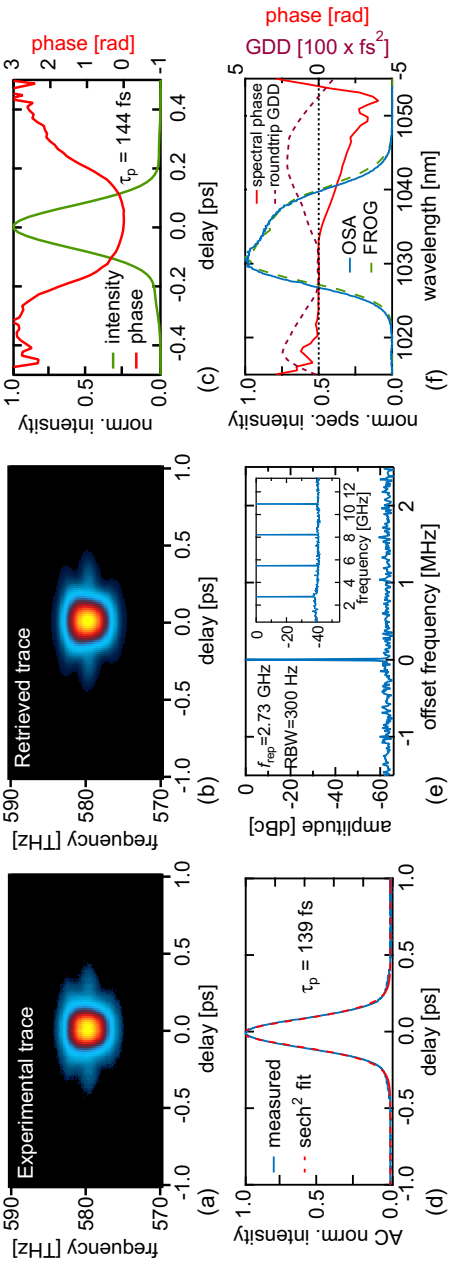

Figure 3.21: Modelocking diagnostics. Measured (a) and retrieved (b) FROG spectrograms, respectively. (c) Retrieved FROG temporal intensity, revealing a pulse duration of 144 fs and a flat temporal phase at the pulse center. (d) Autocorrelation trace; the sech^2-fit indicates a pulse duration of 139 fs. (e) Microwave spectrum with high signal to noise ratio (SNR) >60 dB for the peak corresponding to the pulse repetition rate of 2.73 GHz. Inset: large span of the microwave spectrum: all the higher harmonics of the pulse repetition rate are present with equal spectral power. (f) Optical spectrum; the retrieved FROG trace and the one taken with the optical spectrum analyzer (OSA) overlap. The spectral phase is relatively flat but indicates a chirp in the tail of the spectrum, spectrally corresponding to where the roundtrip GDD significantly deviates from zero.

3.3.1 References

1. M. Guina, A. Rantamäki, and A. Härkönen, J. Phys. D: Appl. Phys. 50, 383001 (2017).
2. B. W. Tilma, M. Mangold, C. A. Zaugg, S. M. Link, D. Waldburger, A. Klenner, A. S. Mayer, E. Gini, M. Golling, and U. Keller, Light Sci Appl 4 (2015).
3. S. M. Link, D. J. H. C. Maas, D. Waldburger, and U. Keller, Science 356, 1164-1168 (2017).
4. F. F. Voigt, F. Emaury, P. Bethge, D. Waldburger, S. M. Link, S. Carta, A. v. d. Bourg, F. Helmchen, and U. Keller, Biomed. Opt. Express 8, 3213-3231 (2017).
5. D. Waldburger, A. S. Mayer, C. G. E. Alfieri, A. R. Johnson, X. Ji, A. Klenner, Y. Okawachi, M. Lipson, A. L. Gaeta, and U. Keller, Laser Congress 2017 (ASSL, LAC) (Optical Society of America, Nagoya, Aichi, 2017), p. ATu6A.3.
6. N. Jornod, K. Gürel, V. J. Wittwer, P. Brochard, S. Hakobyan, S. Schilt, D. Waldburger, U. Keller, and T. Südmeyer, Optica 4, 1482-1487 (2017).
7. U. Keller, K. J. Weingarten, F. X. Kärtner, D. Kopf, B. Braun, I. D. Jung, R. Fluck, C. Hönninger, N. Matuschek, and J. Aus der Au, IEEE J. Sel. Top. Quantum Electron. 2, 435-453 (1996).
8. D. Waldburger, S. M. Link, M. Mangold, C. G. E. Alfieri, E. Gini, M. Golling, B. W. Tilma, and U. Keller, Optica 3, 844-852 (2016).
9. C. W. Baker, M. Scheller, A. Laurain, A. Ruiz-Perez, W. Stolz, S. Addamane, G. Balakrishnan, S. W. Koch, R. J. Jones, and J. V. Moloney, IEEE Photon. Technol. Lett. 29, 326-329 (2017).
10. D. J. H. C. Maas, A.-R. Bellancourt, B. Rudin, M. Golling, H. J. Unold, T. Südmeyer, and U. Keller, Appl. Phys. B 88, 493-497 (2007).
11. B. Rudin, V. J. Wittwer, D. J. H. C. Maas, M. Hoffmann, O. D. Sieber, Y. Barbarin, M. Golling, T. Südmeyer, and U. Keller, Opt. Express 18, 27582-27588 (2010).
12. M. Mangold, C. A. Zaugg, S. M. Link, M. Golling, B. W. Tilma, and U. Keller, Opt. Express 22, 6099-6107 (2014).
13. C. G. E. Alfieri, D. Waldburger, S. M. Link, E. Gini, M. Golling, G. Eisenstein, and U. Keller, Opt. Express 25, 6402-6420 (2017).
14. S. M. Link, A. Klenner, M. Mangold, C. A. Zaugg, M. Golling, B. W. Tilma, and U. Keller, Opt. Express 23, 5521-5531 (2015).
15. M. Mangold, M. Golling, E. Gini, B. W. Tilma, and U. Keller, Opt. Express 23 (2015).

16. A. Laurain, R. Rockmore, H.-T. Chan, J. Hader, S. W. Koch, A. R. Perez, W. Stolz, and J. V. Moloney, J. Opt. Soc. Am. B 34, 329-337 (2017).
17. C. G. E. Alfieri, A. Diebold, F. Emaury, E. Gini, C. J. Saraceno, and U. Keller, Opt. Express. 24, 27587-27599 (2016).
18. J. E. Klemberg-Sapieha, J. Oberste-Berghaus, L. Martinu, R. Blacker, I. Stevenson, G. Sadkhin, D. Morton, S. McEldowney, R. Klinger, P. J. Martin, N. Court, S. Dligatch, M. Gross, and R. P. Netterfield, App. Opt. 43, 2670-2679 (2004).
19. E. Çetinörgü, B. Baloukas, O. Zabeida, J. E. Klemberg-Sapieha, and L. Martinu, Appl. Opt. 48, 4536-4544 (2009).
20. O. D. Sieber, M. Hoffmann, V. J. Wittwer, M. Mangold, M. Golling, B. W. Tilma, T. Südmeyer, and U. Keller, Appl. Phys. B 113, 133-145 (2013).
21. T. Ideguchi, A. Poisson, G. Guelachvili, N. Picque, and T. W. Hänsch, Nat. Commun. 5, 3375 (2014).
22. X. Zhao, G. Hu, B. Zhao, C. Li, Y. Pan, Y. Liu, T. Yasui, and Z. Zheng, Opt. Express. 24, 21833-21845 (2016).

3.4 Thermal Surface Images

During laser operations of a VECSEL, the heatsink on the backside of the VECSEL is cooled, sometimes below 0°C, while the laser spot on the frontside of the chip is optically pumped. This results in a temperature gradient from ≈100°C (at the laser spot) to below 0°C (on the back side of the chip). We observed that for the VECSELs grown by MBE the chip surface away from the pump spot was covered with ice for very strong cooling. For the VECSELs grown by MOVPE on the other hand, the hole surface of the chip remained ice free. Encouraged by this observation, we investigated the thermal properties of the two VECSEL chips more carefully.

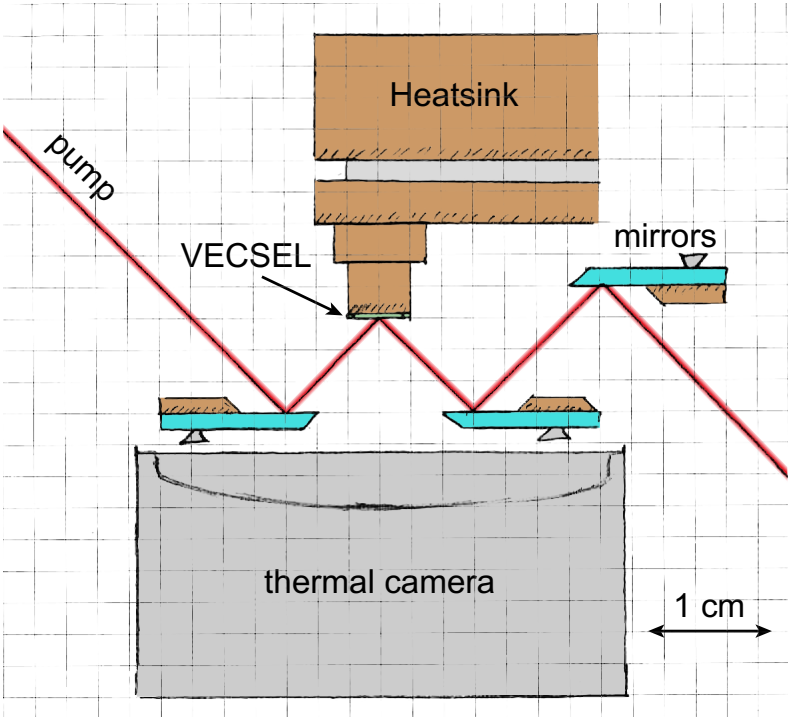

Figure 3.22: Schematic of the thermal surface image setup. The short working distant of the macro objective requires a sophisticated routing of the pump beam.

We used a thermal camera (640 x 480 microbolometer pixels, SC640, *FLIR*) with a fix-focus macro objective to achieve a spacial resolution of 25 µm. The light of the measured thermal radiation has a wavelength around 10 µm with is absorbed in the dielectric top-coating of the VECSEL chips. Thus, the temperature measured is mainly the one of the chip surface. The camera is position in front of the VECSEL chip and focused on the chip surface. The short working distance of the marco objective of 18 mm requires a sophisticated mirror setup to focus the pump beam on the chip (Fig. 3.22). The pump light reflected by the VECSEL chip is routed away and measured with a power meter. For calibration of the temperature, thermal images are recorded for different heatsink temperatures (without pump light) and a per-pixel calibration is calculated. This calibration is then used to measure the surface temperature of the VECSEL chips for various pump powers.

As described in section 3.3 and illustrated in figure 3.18, the VECSEL chip grown by our MBE machine features a better thermal conductivity as the chip grown by our MOVPE machine. We assume that the cause lays in different layer interfaces resulting from growth differences of the two epitaxial machines. This findings are specificly valid for the growth facilities at FIRST (ETH Zürich) and does not nessescarly relate to the MBE or MOVPE growth technique. Consequently, the surface of the MBE VECSEL chip is colder, which can explain the observed ice on the chip surface for strong cooling.

3.5 Ultrafast VECSEL with kilowatt peak power

After the high-power 100 fs result presented in chapter 2 with a VECSEL grown by MOVPE, we regrow the same VECSEL structure on our MBE machine. We observe a better thermal conductivity and slightly more gain with the structures grown by our MBE machine. The resulting SESAM-modelocking VECSEL performed even better than the result presented in chapter 2.

We observe that we can achieve more or less the same maximal average power for different cavity lengths. Thus for scaling pulse peak power, we used a rather long cavity resulting in a lower pulse repetition rate of 1.12 GHz (Fig. 3.23). The cavity is V-shaped with the VECSEL chip as folding mirror and the SESAM and the OC as end mirrors. The cavity opening angle is ≈20°. The distance between the OC and the VECSEL is 6.9 cm and the distance between the VECSEL and the SESAM is 6.5 cm. The OC has a radius of curvature of 150 mm and a transmission of 1%. We observed that for this laser the pulses are shorter if no intracavity Brewster plate is used. The laser still operates in a single polarization, which we controlled with a polarizing beam splitter. The VECSEL is optically pumped under an angle of 45° with a commercial multimode pump diode at 808 nm.

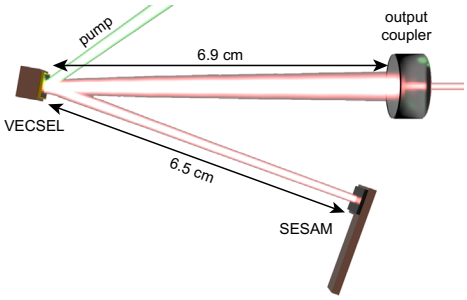

Figure 3.23: V-shaped VECSEL cavity with the output coupler and the SESAM as end-mirrors and the VECSEL chip as folding mirror. The cavity is rather long to achieve a high pulse peak power.

The pulses are characterized with an SHG autocorrelator and a SHG FROG. The resulting pulse durations of 101 fs (autocorrelator) and 100 fs (FROG) are in good agreement (Fig. 3.24a-c). The optical spectrum is centered at 1029 nm and has a FWHM of 14.1 nm (Fig. 3.24d). The optical spectrum measured with an optical spectrum analyzer and the reconstructed spectrum of the FROG measurement overlap nicely. The VECSEL chip is cooled to -10°C and the SESAM temperature is 22°C. With 19.7 W of pump power, an average output power of 150 mW is achieved. This corresponds to a pulse peak power of 1.16 kW.

It is this VECSEL chip which will be used in chapter 4 to fully stabilized the OFC of a SDL without external pulse amplification or compression.

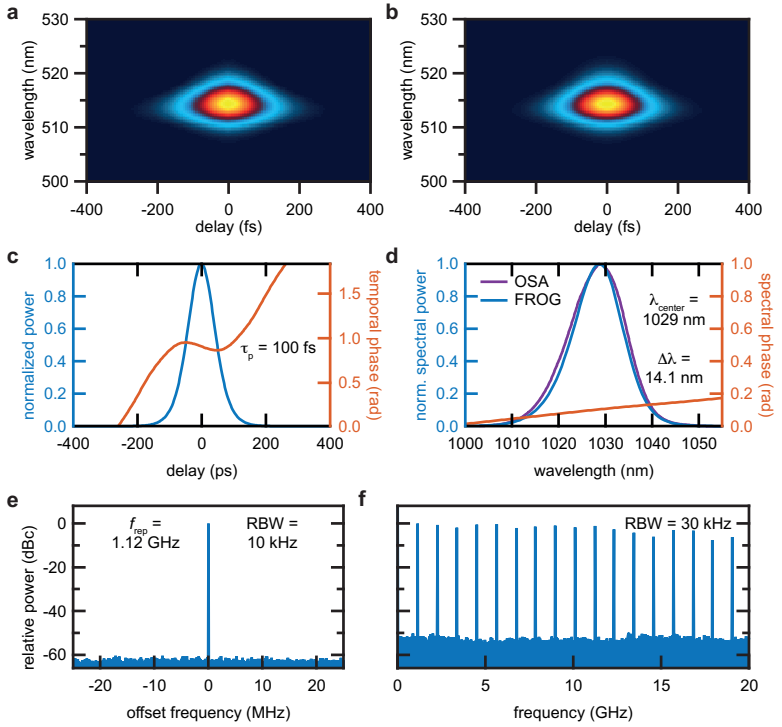

Figure 3.24: VECSEL modelocking performance. **a**, Measured SHG FROG spectrogram. **b**, Retrieved FROG spectrogram. **c**, Retrieved temporal intensity profile and temporal phase with a pulse duration of 100 fs. **d**, Retrieved spectrum and spectral phase overlaid with the measured optical spectrum with a FWHM bandwidth of 14.1 nm. **e**, Microwave spectrum of the pulse repetition rate at 1.12 GHz with a span of 50 MHz measured with a RBW of 10 kHz. **f**, Long-span microwave spectrum with a RBW of 30 kHz showing the equal powerful harmonics of the pulse repetition rate.

3.6 Optical efficiency and gain dynamics of modelocked semiconductor disk lasers

Cesare G. E. Alfieri,[1] *Dominik Waldburger,*[1] *Sandro M. Link,*[1]
Emilio Gini,[2] *Matthias Golling*[1] *Gadi Eisenstein,*[3] *and Ursula Keller*[1]

[1] Department of Physics, Institute for Quantum Electronics, ETH Zürich, 8093 Zürich, Switzerland

[2] FIRST Center for Micro- and Nanoscience, ETH Zürich, 8093 Zürich, Switzerland

[3] Electrical Engineering Department and Russell Berrie Nanotechnology Institute, Technion Haifa, Israel

Compact optically pumped passively modelocked semiconductor disk lasers (SDLs) based on active quantum wells (QWs) such as vertical external-cavity surface-emitting lasers (VECSELs) or modelocked integrated external-cavity surface-emitting lasers (MIXSELs) are wavelength-versatile sources that offer a unique combination of gigahertz pulse repetition rates and short pulse durations. In this paper, we present record-short pulses of 184 fs from a gigahertz MIXSEL emitting at a center wavelength of 1048 nm. This result comes at the expense of low optical-to-optical pump efficiency (<1%) and average output power limited to 115 mW. We experimentally observe that shorter pulses significantly reduce the macroscopic gain saturation fluence and develop a QW model based on rate equations to reproduce the gain saturation behavior and quantitatively explain the VECSEL and MIXSEL modelocking performances. We identify spectral hole burning as the main cause of the reduced gain at shorter pulse durations, which in combination with the short lifetime of the excited carriers strongly reduces the optical pump efficiency. Our better understanding will help to address these limitations in future ultrafast SDL designs.

3.6.1 Introduction

We have obtained systematic improvements of ultrafast optically pumped semiconductor disk lasers (SDLs) [1] during the last decade [2, 3] since

the first demonstration in 2000 [4]. Semiconductor bandgap engineering of optically pumped vertical external-cavity surface-emitting laser (VECSEL) [5] provides selected lasing wavelengths optimized for specific applications. To date, modelocked operation has been demonstrated from the UV up to 2 μm and in continous wave (cw) operation even up to the mid-IR (i.e. up to 5 μm) [5–8]. The highest output power is achieved with InGaAs quantum well gain materials emitting at a center wavelength of around 1 μm. In cw operation, InGaAs based VECSELs demonstrated up to 20 W of output power in a fundamental Gaussian mode [9] and 106 W in multimode [10]. For modelocked SDLs, optically pumped VECSELs passively modelocked with semiconductor saturable absorber mirrors (SESAMs) [11] provide the shortest pulses of 96 fs with 100 mW of average output power in fundamental modelocking (i.e. one single pulse per roundtrip) [12]. A more compact ultrafast SDL is obtained with the modelocked integrated external-cavity surface-emitting laser (MIXSEL) [13], where the SESAM's saturable absorber is vertically integrated in the VECSEL gain structure. This results in a simple linear cavity with just 2 end mirrors represented by the semiconductor MIXSEL chip and the curved output coupler [Fig. 3.25(c)]. MIXSELs have demonstrated the highest output power of any modelocked SDLs, with 6.4 W in 28 ps pulses [14] and have reached pulse durations as short as 253 fs so far [15]. Furthermore the simple linear cavity enabled record-high pulse repetition rates up to 100 GHz [16] and dual-comb modelocking with excellent stability [17, 18]. Following the design guidelines explained in [19], we present here further performance improvement with a MIXSEL generating pulses as short as 184 fs at a pulse repetition rate of 4.33 GHz. The average output power was limited to 115 mW, corresponding to a peak power of 127 W, and the optical-to-optical pump efficiency was 0.65%.

For cw InGaAs QW-VECSELs, optical-to-optical pump efficiencies as high as 45% in multimode output [10] and 43.2% in fundamental Gaussian mode output [9] are reported. For femtosecond pulse durations, however, the efficiency is typically reduced to below 1% [12, 15]. Furthermore, for shorter pulse durations we typically observe a decreased pulse energy and therefore a limited average output power. This trade-off in both the pump efficiency and average output power with shorter pulse dura-

tions sets serious restrictions for applications that require a combination of short femtosecond pulses and high peak power to drive nonlinear optical processes such as frequency doubling for material processing [20], multiphoton microscopy [21] and supercontinuum generation for metrology and frequency comb applications [22, 23]. For this reason we recently focused our efforts to relax the hard peak power requirements of sub-100-femtosecond pulses necessary to detect and stabilize the carrier envelope-offset (CEO) frequency in a self-referenced f-to-2f interferometry scheme [24] for frequency comb stabilization thanks to promising results with Si_3N_4 waveguides for supercontinuum generation [25, 26].

In this paper, we want to develop a simple model that explains the observed trade-off between short pulse duration and pump efficiency. Recently, simulations relying on the development of fully microscopic many-body QW models based on Maxwell semiconductor Bloch equations [27–29] revealed that amplification of short pulses significantly decreases the carrier population in the inverted distribution creating kinetic holes. Under strong pumping conditions we have a reservoir of unused carriers outside of the spectral pulse domain that can seed additional pulses which destabilize fundamental modelocking. Such abinitio models offer a deep understanding for modelocked QW-VECSELs, but rely on a considerable computational effort and were up to now calculated only for resonant periodic gain structures [30]. Furthermore, several important quantities that cannot be theoretically predicted like inevitable growth inaccuracies, inhomogeneity of the layer thicknesses and influence of defect-recombination on the carrier lifetime limit the quantitative prediction capability of fully microscopic models for real structures, forcing a final adjustment of the theoretical results to macroscopic experimental data to obtain a proper quantitative description of the modelocking process.

Following the more phenomenological approach we introduced in [19] to simulate pulse formation processes in ultrafast SDLs, we expand here our efforts with a simplified QW gain model based on single carrier type rate equations (REs) [31, 32]. Our model provides a better understanding on various limitations of current SDLs and can reproduce the experimental values of output power and pump efficiency for different MIXSELs and VECSELs [12, 15]. As a key advantage of the introduced simplifications,

most physical input parameters necessary for simulation can be directly measured.

We distinguish three time scales involved in SDL carrier dynamics [29]: a nanosecond time scale for the diffusion process of the optically pumped electrons and holes into the QW gain region, a 100-ps time scale for interband spontaneous recombination and finally a time scale in the hundreds of femtoseconds for intraband scattering phenomena. Through pump-probe and gain/absorption saturation measurements of our VECSELs, MIXSELs and SESAMs, we directly obtain or fit the model input parameters and arrive at a quantitative explanation for the limited pulse fluence that is experimentally observed during modelocking.

Consistently with [33], we confirm in this paper that spectral hole burning is responsible for a lower gain saturation fluence with shorter pulse durations and is currently preventing power scaling in the sub-200-fs regime. In addition we can demonstrate that two-photon absorption (TPA) does not yet set a significant limitation for the output power even though TPA becomes stronger with shorter pulses [34, 35]. In contrast, we confirm that a short carrier lifetime in the conduction band in the order of 100 ps strongly reduces the optical-to-optical pump efficiency.

The paper is structured as follows. In section 3.6.2 we describe the recent modelocking improvements for our MIXSEL generating 184-fs pulses; section 3.6.3 focuses on the description of the RE QW model, while sections 3.6.4 and 3.6.5 show that the measured pulse-energy-dependent gain dynamics and gain saturation can be reproduced by this model. In section 3.6.6 and 3.6.7 we use this model to simulate and explain the modelocking performances and pump efficiencies of the SESAM modelocked VECSEL generating 100-fs pulses, as described in more details in [12], and of the 184-fs MIXSEL result.

3.6.2 Experimental MIXSEL modelocking results

A MIXSEL design and fabrication

In Fig. 3.25(a) we show the semiconductor epitaxial layer stack of the MIXSEL chip which is the same as described in [15]. The structure is designed for an operation wavelength around 1040-1050 nm. Going from

the bottom to the top, the MIXSEL chip consists of a bottom 24-pair AlAs/GaAs distributed Bragg reflector (DBR) which forms a high reflective mirror for the lasing wavelength, followed by an absorber section with a single 11-nm thick $In_{0.2}Ga_{0.8}As$ W and a 9.5 pair $Al_{0.15}Ga_{0.85}As$/AlAs DBR designed to reflect the pump wavelength and prevent bleaching of the absorber due to the residual pump light. This is followed by an active region with 10 $In_{0.19}Ga_{0.81}As$ QWs of 9 nm thickness embedded in GaAs barriers. The compressive strain of the gain QWs is balanced by tensile strained layers of $GaAs_{0.94}P_{0.06}$.

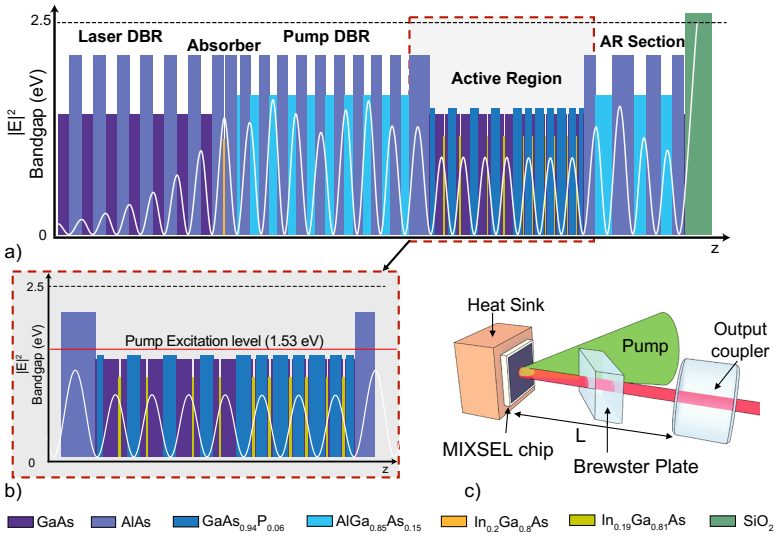

Figure 3.25: Modelocked integrated external-cavity surface-emitting laser (MIXSEL))which generates pulses as short as 184 fs: (a) Layer stack of the semiconductor MIXSEL chip. The standing electric intensity wave pattern is normalized to 4 outside of the structure. (b) Zoom into the active region of the layer stack: AlAs barriers with a higher bandgap energy define the active region and confine the carriers generated through optical pump absorption in the GaAs and $GaAs_{0.94}P_{0.06}$ layers. (c) Simple linear MIXSEL cavity. The semiconductor MIXSEL chip forms one cavity end mirror and the output coupler (OC) the other. The OC has a 350-mm radius of curvature (ROC) and a transmission T_{OC} of 0.44%. An intracavity Brewster plate is used for polarization selection. The MIXSEL chip is pumped with a high-power diode laser array under a 45° angle. For a pulse repetition rate of ≈4.3 GHz in fundamental modelocking, we use a cavity length L of ≈3.5 cm.

Passive modelocking is achieved following the design guidelines in [19]. The average electric field intensity enhancement factor at the QW positions was reduced to 0.65 (normalized to 4 out of a 100% reflective mirror) to increase the gain saturation fluence and flattened with variations below 10% over a range of $\pm$20 nm around the center wavelength to support broadband operation. A numerically optimized antireflection (AR) section with seven alternating layers of $Al_{0.15}Ga_{0.85}As$ and AlAs followed by a single fused silica (FS) layer finalizes the structure. This last AR section minimizes the pump reflection and provides a close to constant group delay dispersion (GDD) in a range of $\pm$200 fs^2 over a 40-nm bandwidth around the lasing wavelength.

As described in [15], the semiconductor layer structure was grown in the FIRST lab at ETH Zurich. The growth was in reverse order for subsequent flip-chip bonding on a diamond heat spreader. The etch-stop layer, the AR section and the active region were grown in a metalorganic vapor phase epitaxy (MOVPE) machine to benefit from the P-based strain compensation layers. The two DBRs and the saturable absorber were grown using a molecular beam epitaxy (MBE) system to take advantage of the currently lower saturation fluence achieved with saturable absorbers grown by MBE. The single fused silica layer was deposited by plasma enhanced chemical vapor deposition (PECVD).

Compared to the structure used in [15], we improved the precision of the PECVD deposition process and adapted the fused silica thickness to partially compensate small deviations from design observed in the epitaxial structure due to growth errors. This provided a better dispersion management and enabled generation of shorter pulses.

B Modelocking performance

The MIXSEL chip was mounted on a copper heatsink and temperature stabilized at 9°C. A linear laser cavity is obtained with the MIXSEL chip as one end mirror and a curved output coupler (OC) as the other [Fig. 3.25(c)]. The OC has a 350-mm radius of curvature (ROC) and a transmission T_{OC} of 0.44%. The cavity length was set to 34.6 mm, corresponding to a pulse repetition rate of 4.33 GHz in fundamental modelocking operation. The MIXSEL chip was pumped under an angle of 45° with a commercial mul-

timode 808 nm fiber coupled diode array. To ensure single transverse mode operation, the laser spot size on the MIXSEL was set to a 184-µm radius, slightly larger than the circular pump spot size of a 180-µm radius on the MIXSEL chip. A 1-mm thick wedged fused silica plate was inserted into the cavity at Brewster angle to obtain a single linear polarization output. With the incident pump power to 17.6 W, self-starting stable modelocking operation was achieved at an average output power of 115 mW, corresponding to a pulse peak power of 127 W. A detailed pulse characterization carried out with second harmonic generation frequency resolved optical gating (SHG FROG) revealed a duration of 184 fs, which represents the shortest pulse duration ever achieved with the MIXSEL technology. Good agreement between the measured and the retrieved trace is visible in Figs. 3.26(a) and 3.26(b), with a reconstruction error of 0.0011 [36]. The pulse spectrum, measured with both FROG and optical spectrum analyzer, shows a center wavelength of 1048 nm and a full width at half maximum (FWHM) bandwidth of 7.4 nm, corresponding to 1.15 times the time-bandwidth product for an ideal transform-limited sech^2–shaped pulse.

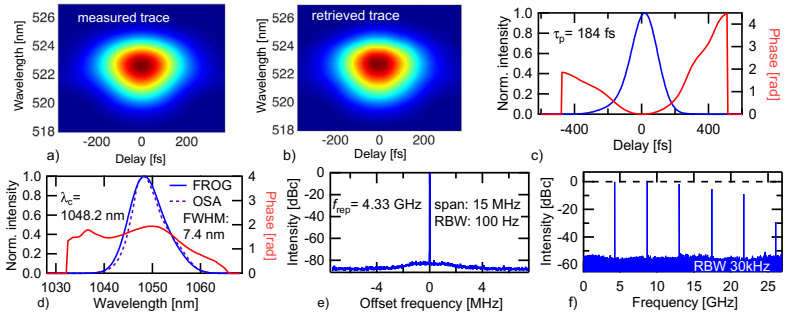

Figure 3.26: Modelocking results of the 184-fs MIXSEL: (a) Measured SHG-FROG spectrogram. (b) Retrieved FROG spectrogram (error 0.0011). (c) Retrieved temporal profile and spectral phase. (d) Retrieved spectral intensity and spectral phase overlapped with the measured optical spectrum centered at 1048 nm with a FWHM of 7.4 nm. (e) Microwave spectrum centered at the fundamental repetition rate of 4.33 GHz with a span of 15 MHz and 100 Hz RBW. (f) Microwave spectrum over a larger frequency span with a RBW of 30 kHz. The power decrease for the higher harmonics is a consequence of the limited bandwidth of the photodetector.

The detected microwave spectrum was measured with a 22-GHz photodetector without additional amplification. The fundamental pulse repetition rate of 4.33 GHz measured in a 15-MHz span with a narrow resolution bandwidth (RBW) of 100 Hz shows a high signal-to-noise ratio of more than 80 dB indicating fundamental modelocking operation [Fig. 3.26(e)]. In addition, we show several harmonics of the fundamental pulse repetition rate in a large-span measurement taken with a RBW of 30 kHz [Fig. 3.26(f)]. The reduced power in the higher harmonics results from the limited detection bandwidth.

C Current limitations

With this new modelocking result we demonstrate for the first time pulse durations below 250 s with a MIXSEL. This improvement validates our design guidelines as presented in [19]. However, it unfortunately confirms again the significant trade-off in output power and pump efficiency with shorter pulse durations. In particular, for our 184-fs result the optical-to-optical pump efficiency does not exceed the low value of 0.65%. Moreover, the intracavity pulse fluence on the MIXSEL device during modelocked operation was limited to 5.8 $\mu J/cm^2$ and the OC transmission to 0.44%.

To better understand the physical origin for this trade-off, we develop a QW rate equation model that can benefit from our measured input parameters.

3.6.3 QW rate equation model

We have employed a rate equation model for the strain compensated $In_{0.19}Ga_{0.81}As$ gain QWs embedded in GaAs barriers used in both a MIXSEL (Fig. 3.25) and a SESAM modelocked VECSEL presented in [12]. Our goal is to obtain a precise quantitative description of the laser performance and a better understanding of their limitations. It is therefore important to minimize the number of input parameters for our model which cannot be measured directly. This leads to the introduction of several assumptions and simplifications that are explained as follows.

- Flat-band approximation. No external electric field is applied and no net current is flowing in the undoped laser structure. Carriers dif-

fuse in the optically pumped GaAs barriers and are captured in the QW. An internal electric field is always formed due to a Coulomb interaction between electrons and holes that diffuse with different diffusion coefficients. The electric field causes a nonuniform carrier distribution with a larger carrier density close to the P side of the junction [32]. However, in the present structure the effect is minor and the carrier transport can be modeled as an ambipolar process [37].

- Band structure of the QW. The band-offset between GaAs barriers and strain compensated $In_{0.19}Ga_{0.81}As$ QW is 255 meV at 300 K. Since the temperature dependence of the energy bandgap is similar for the two materials, we consider the band-offset constant and keep the same value for the laser operation temperature in the active region, which is assumed to be 370-400 K. We define the zero energy in correspondence of the bottom of the bulk $In_{0.19}Ga_{0.81}As$ conduction band and estimate a band-offset ratio of 0.67 [38], meaning that the GaAs barriers are 170 meV high. The confinement effects shift the first energy sub-band at $\approx$30 meV and the second at $\approx$110 meV respectively (Fig. 3.27).

- Capture and escape rates. The different QWs in the laser structure are separated by several tens of nanometers, making electron coupling (by tunneling) between them negligible. We define a constant net carrier capture rate into the QW ($1/\tau_c$) which is determined by carrier diffusion through the pumped barriers and the relaxation rate into the QW itself. This net rate considers also the escape rate, which is related, at equilibrium to the capture rate by the principle of detailed balance. The ratio of escape-to-capture rate is assumed to remain constant under steady-state modelocking conditions. This is verified by the fact that under normal operation, the QW is not completely filled and $2-3\ k_BT$ separate the last occupied QW state and the barriers which ensures that the escape probability is unperturbed.

- Two-level approximation. We divide the continuum of the energy states in the QW into two spectral regions. We define an interaction

region which corresponds to the lowest 18-20 meV of the conduction band (sufficient to support the full spectral content of a ≈100 fs pulse at 1 μm), and call N_1 the corresponding carrier density (Fig. 3.27). We make the assumption that spontaneous and stimulated emission events take place in this region independently of the spectral bandwidth of the incoming pulse, which is reasonable for pulses longer than the typical Rabi oscillation time scale (≈50 fs [39–41]). The population at higher energies, referred to as N_2 acts as a carrier reservoir.

- Carrier dynamics. We assume that carriers diffuse from the barriers into N_2 with a capture time constant τ_c in the nanosecond regime [42]. The relaxation to N_1 (i.e. the bottom of the band) takes place with a relative slow intraband time constant τ_{intra} in the hundreds of femtoseconds [43]. Carriers in N_1 decay through spontaneous recombination with a time constant τ_{life} in the hundreds of picoseconds. The local internal carrier re-distributions inside the single regions N_1 and N_2 are dominated by highly efficient intraband scattering processes involving small energy transfers with characteristic times in the tens of femtosecond range [40, 44], significantly shorter than the considered pulse durations. They are therefore assumed to be instantaneous.

- Fermi-Dirac distribution. The maximum occupancy in N_1 at equilibrium is governed by a Fermi-Dirac probability distribution and is therefore related to the total carrier density of the QW. While lasers are naturally not in real equilibrium, this approximation is commonly used in ambipolar models and works well.

These assumptions and approximations lead us to the following rate equations:

$$\frac{\partial N_1}{\partial t} = -\frac{N_1(t) - N'_{10}(t)}{\tau_{intra}} \frac{N_2(t)}{N_{20}} - \frac{N_1(t)}{\tau_{life}} - \Gamma_{gain} \cdot Pulse(t, F_p, \tau_p, \tau_0) \quad (3.5)$$

$$\frac{\partial N_2}{\partial t} = -\frac{N_2(t) - N_{20}(t)}{\tau_c} + \frac{N_1(t) - N'_{10}(t)}{\tau_{intra}} \frac{N_2(t)}{N_{20}} \quad (3.6)$$

where gain Γ_{gain} is the stimulated emission coefficient that couples the carriers in N_1 with the modelocked sech^2-pulse interacting with the gain

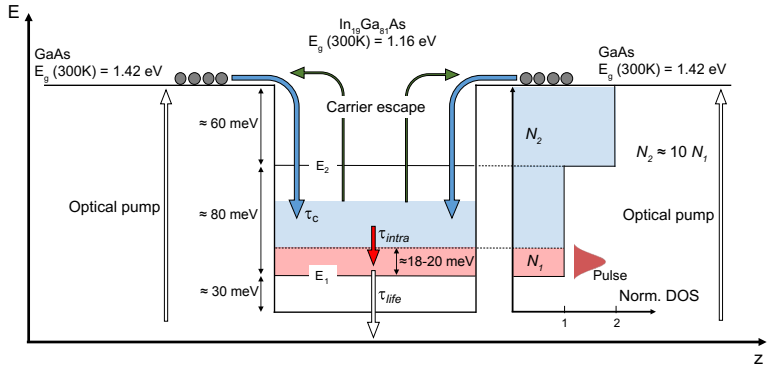

Figure 3.27: Ambipolar quantum well (QW) model. Carriers diffuse from the optically pumped GaAs barriers into the QW with a time constant τ_c, then relax to the bottom of the band with an intraband time constant τ_{intra}. Finally, they spontaneously recombine with a time constant τ_{life}. The normalized density of states (DOS) is depicted on the right side of the QW. N_1 corresponds to the region interested by stimulated emission and spontaneous recombination; N_2 acts as a carrier reservoir.

chip at τ_0 with a fluence F_p and a pulse duration τ_p. $N'_{10}(t)$ is given by:

$$N'_{10}(t) = \frac{N_{10}}{1 + \exp\left(\frac{E_0 - E_F(t)}{k_B T}\right)} \tag{3.7}$$

where N_{10} is the total amount of states in the N_1 region and E_0 is the average carrier energy (i.e. ≈9-10 meV); $E_F(t)$ is the Fermi energy which depends on the total carrier density of the QW. Normalization of the density of states (DOS) (Fig. 3.27), leads to $E_F(t) = N_1(t) + N_2(t)$ until the second sub-band is reached. Defining ΔE as the energy difference between the two confined sub-bands, we obtain after the second sub-band: $E_F(t) = 0.5\,(N_1(t) + N_2(t) + \Delta E)$.

In order to reproduce all the elements of a SDL cavity, we need to introduce an additional rate equation for the saturable absorber. We describe the population dynamics in the SESAM QW as follows:

$$\frac{\partial N_{abs}}{\partial t} = -\frac{N_{abs}(t)}{\tau_{abs}} + \Gamma_{abs} \cdot [1 - N_{abs}(t)] \cdot Pulse(t, F_p, \tau_p, \tau_0) \tag{3.8}$$

where τ_{abs} is the SESAM recovery time defined by the recovery time of the reflectivity to the $1/e$ – value of its maximum saturation. Γ_{abs} represents

the absorption rate related to the saturation fluence and K is the ratio between the fluence on the SESAM and the fluence on the gain chip ($K = 1$ in a MIXSEL with the same intensity enhancement in absorber and gain, assuming obviously the same laser spot size and the equal number of passages per roundtrip on gain and absorber).

Assuming the gain proportional to N_1, we define the reflectivity experienced by a modelocked pulse after a full roundtrip time T in a straight MIXSEL cavity:

$$R_{\mathrm{MIXSEL}}(F_\mathrm{p}, \tau_\mathrm{p}) = \frac{\int_0^T Pulse(t, F_\mathrm{p}, \tau_\mathrm{p}, \tau_0) \cdot \{1 + \sigma \cdot N_1(t) - \Delta R \cdot [1 - N_{\mathrm{abs}}(t)] - \Delta R_{\mathrm{ns}}\}\, dt}{\int_0^T Pulse(t, F_\mathrm{p}, \tau_\mathrm{p}, \tau_0) dt} \cdot e^{-\frac{F_\mathrm{p}}{F_2(\tau_\mathrm{p})}} \tag{3.9}$$

where ΔR is the absorber modulation depth, ΔR_{ns} represents the nonsaturable losses of the structure, $F_2(\tau_\mathrm{p})$ is the TPA coefficient defined as in [34] and σ is:

$$\sigma = \frac{g_{\mathrm{ss}}}{N_1(\infty)} \tag{3.10}$$

With g_{ss} being the measurable small signal gain and $N_1(\infty)$ the asymptotic value of N_1 obtained through (3.5) and (3.6) with no incoming pulse. If we take into account the double pass in the gain chip and the different laser spot sizes on VECSEL and SESAM, the roundtrip reflectivity is calculated for a VECSEL V-shaped cavity:

$$R_{\mathrm{VECSEL}}(F_\mathrm{p}, \tau_\mathrm{p}) = \frac{\int_0^T Pulse(t) \cdot \{1 + 2\sigma \cdot N_1(t) - \Delta R \cdot [1 - N_{\mathrm{abs}}(t)] - 2\Delta R_{\mathrm{ns},VECSEL} - 2\Delta R_{\mathrm{ns},SESAM}\}\, dt}{\int_0^T Pulse) dt} \cdot e^{-\frac{2F_\mathrm{p}}{F_{2VECSEL}(\tau_\mathrm{p})} - \frac{KF_\mathrm{p}}{F_{2SESAM}(\tau_\mathrm{p})}} \tag{3.11}$$

We expect small pulse variations during a single roundtrip during steady-state modelocking and therefore the same pulse reaches the VECSEL twice and the SESAM once per cavity roundtrip.

3.6.4 Measurement and fit for the model input parameters

We fitted the RE model to experimental data in order to quantitatively reconstruct the gain dynamics and obtain values for the three time con-

stants τ_c, τ_{intra}, τ_{life} as well as for the stimulated emission coefficient Γ_{gain}. To directly obtain a value range for τ_{intra} and τ_{life}, we performed pump-probe measurements on a structure consisting of a DBR on top of which we placed a single $In_{0.19}Ga_{0.81}As$ QW, grown by MOVPE with the same growth parameters used for the active QWs of [12, 15] and for the 184-fs MIXSEL.

We used a standard degenerate pump-probe setup with a tunable Ti:sapphire laser generating 100-fs pulses (stretched to 130 fs at the sample position) at 80 MHz with an average power of 900 mW. The center wavelength was adjusted to the photoluminescence peak of the QW at room temperature (1020 nm). During the pump-probe measurement the structure was not cw pumped with 808-nm diode. The measurement revealed a saturation recovery with a fast temporal component of ≈300-400 fs followed by a slow component of 130-140 ps [Fig. 3.28(a)]. These correspond to the value ranges used in the following for τ_{intra} and τ_{life} respectively.

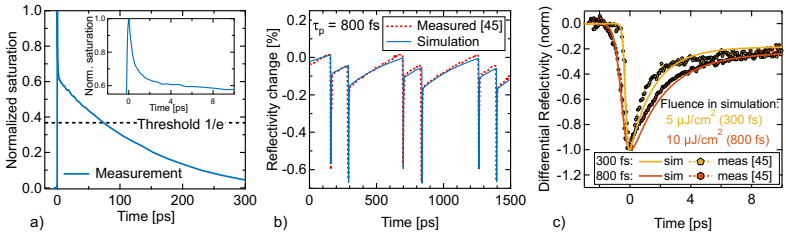

Figure 3.28: (a) Saturation recovery measurement for a single $In_{0.19}Ga_{0.81}As$ QW. Inset: zoom into the initial fast recovery. (b) Gain dynamics of a modelocked VECSEL on a multi-roundtrip time scale. The gain chip folds a V-shaped cavity with unbalanced arm lengths. The strong drops in reflectivity correspond to the pulse arrival times on the gain chip. Our simulation is compared to measurements performed in [45]. (c) VECSEL fast gain recovery for two different pulse durations. The simulation is in good agreement with the measurements of [45].

Recently, *in situ* measurements of gain dynamics during modelocking operation have been shown in [45] for two VECSELs generating 300 fs and 800 fs pulses (these samples will be called hereon 300-fs VECSEL and 800-fs VECSEL). The fit of these experimental curves allowed us to extract values for τ_c and for Γ_{gain} (listed in Table 3.2). With all the parameters implemented in the RE model, the curves presented in [45] are well repro-

duced for both the 300-fs VECSEL and 800-fs VECSEL result [Figs. 3.28(b) and 3.28(c)].

3.6.5 Gain saturation

To verify the effect of pulse duration on gain saturation, we measured the pulse-fluence-dependent reflectivity of a diode pumped VECSEL probing the sample with different pulse durations but keeping the probe spectrum unchanged. To achieve a better signal-to-noise ratio in gain measurements, we designed for this experiment a high-gain, 10-QW, strain compensated VECSEL with relatively high average field intensity enhancement factor of 0.7 at the QW positions (at 1020 nm). This VECSEL chip (that we will call the 672-fs VECSEL) up to 10 W of output power in cw operation and 700 mW of modelocked average output power with 672-fs pulses at 1022 nm.

We probed 672-fs VECSEL chip with the same Ti:sapphire laser previously described for the pump-probe measurements; the center wavelength was adjusted to 1020 nm and with a measured FWHM bandwidth of 12.3 nm [Fig. 3.29(a)].

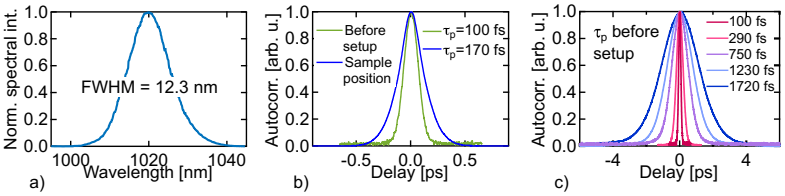

Figure 3.29: Modelocking characterization of the Ti:sapphire laser used to probe the gain saturation of SDLs. (a) Measured optical spectrum centered at 1020 nm with FWHM bandwidth of 12.3 nm. (b) Autocorrelation trace directly at the laser output and at the sample position: the setup adds ≈5000 fs^2 of positive GDD. (c) Autocorrelation trace (measured before setup) of the stretched pulses used to probe the gain.

To accurately measure the VECSEL reflectivity, we used a setup similar to [46]. The setup adds about 5000 fs^2 of group delay dispersion (GDD), therefore stretching the initial 100-fs pulse to 170 fs [Fig. 3.29(b)]. We test different pulse durations by stretching the pulses with 1, 3, 5, and 7 passages through a 9-cm block of SF-10 glass, adding roughly 9000 fs^2 of GDD per passage. As shown in Fig. 3.29(c), we obtained a maximum pulse duration of 1.72 ps before the setup, corresponding to 1.89 ps on the sample. The VECSEL was mounted on a temperature stabilized heat sink and pumped with a cw multimode 808-nm diode laser array. During the measurement, we set the heat sink temperature to 5°C and the pump intensity to 57 kW/cm^2.

The measured reflectivity curves are shown in Fig. 3.30(a). We observe that the small signal gain is not significantly affected by the pulse duration. However, longer pulse durations decrease the induced TPA losses [Fig. 3.30(a)] and also increase the gain saturation fluence [Fig. 3.30(b)]. When we use the input parameters summarized in Table3.2 for the 672-fs VECSEL into the RE model, we obtain simulated reflectivity curves which are in good agreement with the measured data points [Fig. 3.30(a)]. The extracted numerical values for the gain saturation fluence (defined as in [46]) could also be reproduced by the simulation [Fig. 3.30(b)].

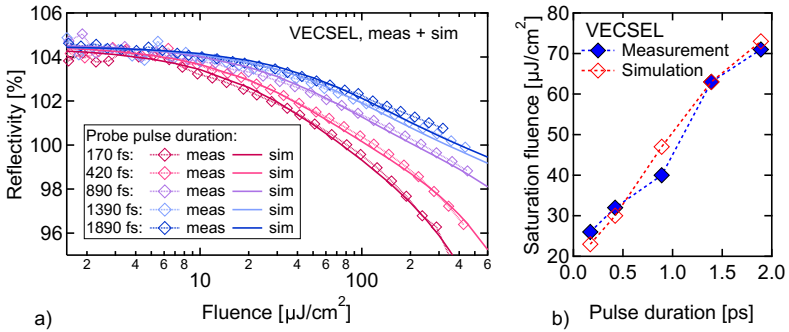

Figure 3.30: (a) VECSEL gain saturation measurements. The VECSEL shows an earlier saturation when probed with shorter pulses. (b) Values of measured and simulated gain saturation fluences. The experimental values are obtained through least-square fit of the measured data point to the model described in [46].

The measured behavior is explained as a consequence of spectral hole burning as follows. The incoming pulse stimulates recombination in the QW energetic region covered by the pulse spectrum (N_1 in our model) and burns a spectral hole in the QW population. For low pulse fluence, the spectral hole is shallow and no effect of pulse duration on the small signal gain is observed. On the other hand, as the pulse fluence increases, the spectral hole deepens and is consequently filled via the decay of carriers from the reservoir (N_2). However, if the pulse duration is shorter or comparable to the typical intraband carrier relaxation time τ_{intra}, the hole is not completely refilled during the time the pulse is interacting with the QW. This decreases the carrier density available for the pulse amplification and results in a gain saturation which limits the laser average output power and pulse energy in ultrafast operation.

3.6.6 Analysis of the 100-fs VECSEL

In this section, we apply the RE model to fully describe the cavity elements used in the 100-fs VECSEL result reported in [12]. In particular, we obtain quantitative information on the maximum pulse fluence reachable in modelocked operation and on the maximum achievable output coupling (OC) rates. Moreover, we explore the possible advantages of chirped ps-pulses (with subsequent external pulse compression) in terms of output power and efficiency.

Finally, since two different mechanisms (i.e. TPA and gain saturation) are decreasing the effective gain for short pulses, we want to better understand their significance in limiting high-power and efficient ultrafast operation.

A Simulation of the 100-fs VECSEL result

We measured gain saturation for the 100-fs VECSEL under the same experimental conditions that allowed short pulse generation, as reported in [12]. We matched the probing center wavelength to the lasing center wavelength (1034 nm) and applied the same heat-sink temperature (1°C) and pump intensity (21 kW/cm^2). We then fitted the measurement to obtain the correct parameters for the RE model [Fig. 3.31(a)]. The same was

done to reproduce the saturation characteristic of the SESAM used in [12] [Fig. 3.31(b)]. The SESAM recovery time of 1.5 ps was directly measured in the pump-probe setup. The parameters used in simulations for the 100-fs VECSEL are summarized in Table 3.2. It is important to emphasize that the model parameters summarized in Table 3.2 are in the same range for the different SDLs, which is not surprising since all the SDL materials are very similar.

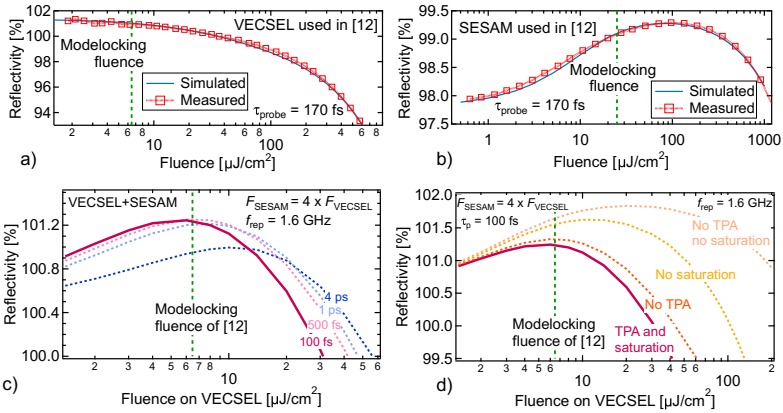

Figure 3.31: (a) Fluence-dependent reflectivity for the 100-fs VECSEL chip probed with 170-fs pulses under the same operation conditions described in [12]. The probe pulse is centered at the VECSEL emission wavelength of 1034 nm and has a comparable FWHM spectral bandwidth. The measured saturation behavior is compared to the simulated one. (b) Absorption saturation curve of the SESAM used in [12] and correspondent simulation. (c) Simulation of combined VECSEL and SESAM effects for 100-fs pulses in a V-shaped cavity as described in [12] (solid line). The dashed lines simulate the effects of longer pulses for the same lasing conditions. (d) Simulation of the actual lasing conditions of [12] including gain saturation and TPA (solid line); without TPA in the gain chip (orange dashed line); without gain saturation (yellow dashed line); without TPA and saturation effects in the VECSEL (apricot dashed line).

Using Eq. (3.11), we reproduced the reflectivity of the 100-fs VECSEL cavity (obtained as the sum of the VECSEL's and SESAM's saturation curves) with a pulse repetition rate of 1.6 GHz and a 100-fs pulse duration as described in [12]. In Fig. 3.31(c) we observe a cavity reflectivity maximum at a fluence of $F_0 = 6\ \mu J/cm^2$, which is in good agreement with the

Table 3.2: Model input parameters for the analyzed SDLs. In black, fitted parameters. In red, fixed parameters during fitting procedure. In red bold italic, fixed parameters directly obtained from measurement. For τ_{life} we fixed the value extracted from pump-probe measurement. The gain QWs used in the 672-fs VECSEL, 100-fs VECSEL and the 184-fs MIXSEL were grown under the same conditions in the same MOVPE machine, therefore we fitted τ_{intra} only for the 672-fs VECSEL, keeping the value fixed for successive structures. The embedded QW absorber in the 184-fs MIXSEL is similar to the one in the SESAM used to modelock the 100-fs VECSEL, but we assume that long time annealing during growth slightly increased τ_{abs}. The F_2 values are measured with a probe pulse duration of 170 fs.

LASER	**300-fs VECSEL [45]**	**800-fs VECSEL [45]**	**672-fs VECSEL**	**100-fs VECSEL]12]**	**184-fs MIXSEL**
τ_c **[ns]**	1.4	1.4	0.9	1.1	1.1
τ_{intra} **[ps]**	0.03	0.35	0.37	0.37	0.37
τ_{life} **[ps]**	140	140	140	140	140
τ_{abs} **[ps]**	-	-	-	**1.5**	2.5
Γ_{gain} **[ps^{-1}]**	0.07	0.07	0.05	0.03	0.05
Γ_{abs} **[ps^{-1}]**	-	-	-	0.2	0.4
g_{ss} **[%]**	-	-	**5.2**	**2.2**	3.0
$\Delta R_{ns,gain}$ **[%]**	-	-	**0.8**	**0.85**	**1.30**
ΔR_{abs} **[%]**	-	-	-	**1.7**	1.35
$\Delta R_{ns,abs}$ **[%]**	-	-	-	**0.5**	-
$F_{2,gain}$ **[mJ/cm^2]**	-	-	**9.2**	**9.2**	**6.8**
$F_{2,SESAM}$ **[mJ/cm^2]**	-	-	-	**75**	-

actual modelocking fluence of 6.5 $\mu J/cm^2$. As expected from the model, the laser operates close to the maximum of cavity amplification, where an optimal balance between the effects of unsaturated SESAM, saturated gain and TPA losses occurs.

The quantity F_0 indicates the intracavity pulse fluence that the laser reaches in modelocked operation while the OC rate (defined as $R(F_0)$ - 100% - cavity losses) sets the power fraction that can be extracted at every roundtrip. Therefore, the combination of the two quantities represents a figure of merit for output power and efficiency of SDLs.

From Fig. 3.31(c), we extracted $R(F_0)$ = 101.2% for for the 100-fs VECSEL generating 100-fs pulses at 1.6 GHz. In addition, we need to consider $\approx$0.3% of additional fluence-independent cavity losses mainly introduced by the intracavity Brewster plate, which leads to a total OC rate of 0.9%, in agreement with our previous results [12].

B Simulation of long pulse operation

We simulated the same cavity for 100-fs VECSEL with different pulse durations. We clearly observe that longer pulses shift F_0 to higher fluences [Fig. 3.31(c)]: for a 4-ps pulse, F_0 = 12 $\mu J/cm^2$ which is two times the intracavity pulse energy compared to a 100-fs pulse under the same conditions. This comes at the expense of a reduced OC rate for two reasons:

1. The fast SESAM recovery introduces significant losses for long pulses, increasing the effective absorber saturation fluence. This can be avoided by using a slower saturable absorber.

2. A long pulse extracts carriers more efficiently from the gain QWs. Due to the high repetition rate of the pulse interacting with the gain on the VECSEL (for a V-shaped cavity $\approx 2\ f_{rep}$), the QW cannot be completely refilled in the short interval between two pulses. The stationary population level reached by the QWs after several roundtrips is then reduced together with the gain.

In conclusion, the advantages of a chirped pulse formation in SDL cavities, which would in principle allow for a higher F_0 are strongly reduced when a fast saturable absorber is used. In addition, repetition rates below the GHz range cannot be reached without encountering multi pulse instabilities due to the short carrier lifetime in the QW conduction band and

also intracavity multi-pass geometries [47, 48] do not reduce the effective repetition rate experienced by the gain chip.

C Effects of gain saturation and TPA

Without modifying the SESAM parameters, we simulated the 100-fs VECSEL cavity for 100-fs pulses removing separately the effects of gain saturation and TPA in the VECSEL chip. As seen in Fig. 3.31(d), TPA is not playing a dominant role at the low F_0 values we are considering. In contrast, gain saturation is seriously limiting the VECSEL performance: an unsaturable VECSEL could reach an F_0 value twice as high with roughly 1.5 times the OC rate compared to the actual results, meaning 3 times the average output power and pulse energy. The best performances would be clearly achieved in case of absent saturation and TPA, approaching the behavior of solid state lasers, which don't suffer from these limitations [49].

3.6.7 Analysis of the 184-fs MIXSEL and optical-to-optical efficiency

A MIXSEL saturation

We measured the fluence-dependent reflectivity for the 184-fs MIXSEL and for the 253-fs MIXSEL described in [15]. Thanks to its monolithic structure including both gain and absorber in the same chip, the MIXSEL offers a direct access to F_0. We probed the MIXSEL reflectivity at the same lasing conditions (same center wavelength, pump intensity, heat-sink temperature and comparable pulse durations).

As shown in Fig. 3.32(a) the measured F_0 values are in good agreement with the experimental modelocking fluences observed for the two lasers, confirming the correlation between F_0 and laser's operation point. We fitted the reflectivity measurements of 184-fs MIXSEL chip [Fig. 3.32(b)] according to Eq. (3.10) and extracted the parameters reported in Table 1, which we then use in the following for optical-to-optical efficiency calculations. The maximum OC rate for 184-fs MIXSEL is measured to be 0.68% and F_0 around 7 $\mu J/cm^2$, both slightly higher compared to the experimental modelocking values. The low probing repetition rate of 80 MHz allows

for maximum refilling of the QWs and therefore a higher F_0 compared to the 4.33-GHz pulse repetition rate, while the cavity losses, principally introduced by the intracavity Brewster plate, reduced TOC to 0.44%. When these effects are taken into account, the model reproduces correctly the actual performance.

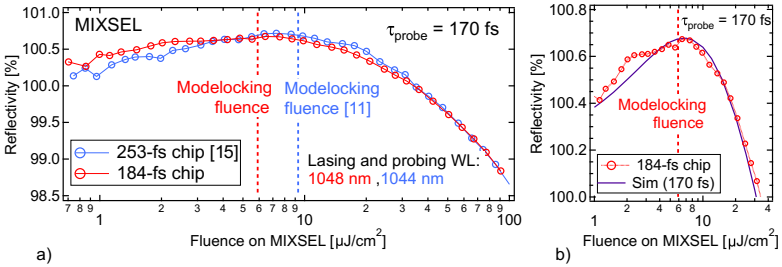

Figure 3.32: (a) Measured saturation curve of the 253-fs MIXSEL [15] and of the 184-fs MIXSEL. For both chips, the modelocking fluence almost corresponds to the point of maximum reflectivity. (b) Zoom of the saturation curve of the 184-fs MIXSEL chip and comparison with simulation.

B Calculation of optical-to-optical efficiency

We define the optical-to-optical pump efficiency η of the MIXSEL as the ratio between the emitted modelocked power and the incident optical pump power. We used the RE model to numerically reproduce the experimental efficiency value observed for the 184-fs MIXSEL result. Efficiency is a fluence-dependent quantity and hereinafter we will calculate its value at the laser working fluence F_0, which in turn varies with the pulse duration and the pulse repetition rate. We determine η_{calc} from:

$$\eta_{\text{calc}} = Q_{\text{def}} \cdot A_{\text{pump}} \cdot \frac{N_{\text{stim}}}{N_{\text{stim}} + N_{\text{spont}}} \cdot \frac{OC(F_0)}{OC(F_0 + \Delta R_{\text{ns,cavity}} + \Delta R_{\text{ns}} + \Delta R \cdot (1 - N_{\text{abs}}))} \cdot e^{-\frac{F_0}{F_2}} \tag{3.12}$$

Q_{def} is the ratio between pump and laser wavelengths (quantum defect); A_{pump} is the fraction of the pump power absorbed in the active region (calculated from the design of the semiconductor layer stack with typical values between 0.6 and 0.8); $\Delta R_{\text{ns,cavity}}$ represents the intracavity losses,

estimated here to be 0.2%; N_{stim} are the carriers recombined via laser stimulation over one roundtrip time T and used for pulse amplification; finally, N_{spont} represents the carriers that spontaneously recombine over T calculated as:

$$N_{\text{spont}} = -\int_0^T \frac{N_1(t)}{\tau_{\text{life}}} dt \tag{3.13}$$

We obtain calc η = 0.97% for the 184-fs MIXSEL at a pulse repetition rate of 4.33 GHz, in good agreement with the experimental value η_{meas} = 0.65%. Since we do not take into account any recombination process during carrier diffusion in the pumped GaAs and $GaAs_{0.94}P_{0.06}$ barriers, we expected the calculated efficiency to be slightly higher than the real efficiency.

C Possible solutions to reach higher pump efficiency

Higher pump efficiencies of several percent are reported in [14, 50] for ultrafast SDLs generating picosecond pulses. However, we would like to emphasize that η_{calc} stays below 1.3% for the 184-fs MIXSEL chip when modelocking is simulated for pulse durations up to 10 ps. As discussed for the 100-fs VECSEL, in ps-operation the incomplete QW refilling and the increased absorber losses prevent significant increases in F_0 and OC. This cancels the beneficial effects on the efficiency of the higher gain saturation experimented by long ps-pulses (Fig. 3.33).

A different behavior is observed when the recovery time of the embedded absorber is increased by a factor of 10, from 2.5 ps to 25 ps. According to [19], sub-300-fs operation cannot be obtained with such a slow saturable absorber but from Fig. 3.33 we can conclude that η_{calc} would actually be increased to about 3% for 10-ps pulses, which is in agreement with the previously demonstrated better pump efficiency for picosecond MIXSELs.

According to Eq. (3.13), a short carrier lifetime in the conduction band of the QW gain is the most detrimental parameter for the optical-to-optical pump efficiency. The pulse can interact with the gain medium only for a small fraction of a roundtrip time, while for the remaining time carriers diffuse through the barriers into the QWs and spontaneously recombine before contributing to pulse amplification. We simulated the 184-fs MIXSEL with a τ_{life} five times higher compared to the experimental value,

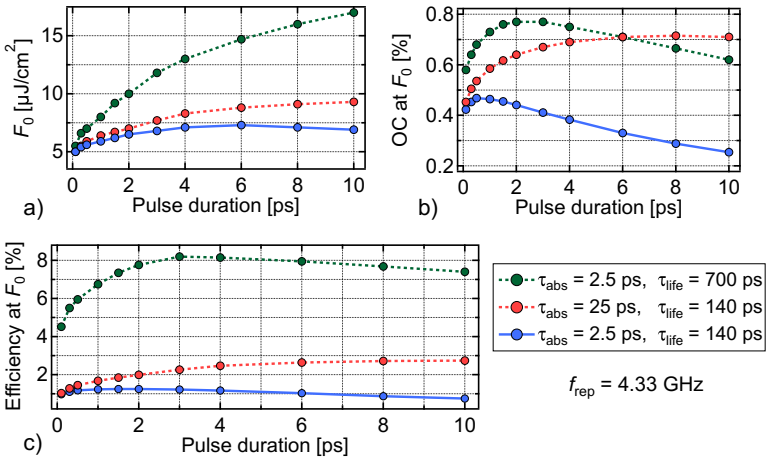

Figure 3.33: Ultrafast SDL performance with different absorber recovery time and QW gain lifetimes: (a) Calculated F_0 for different pulse durations and MIXSEL parameters. (b) Calculate OC rate at F_0. (c) Calculated efficiency at F_0. Solid lines are obtained with the model parameters for the 184-fs MIXSEL (Table 3.2); dashed lines represent simulation with an increased absorber recovery time or an increased gain QW lifetime.

obtaining a significant efficiency increase for all pulse durations, with η_{calc} exceeding 8% for a 3-ps pulse duration.

As indicated in Eq. (3.13), a shorter roundtrip time reduces the relative efficiency drop caused by spontaneous emission. We simulated modelocked operation for the 184-fs MIXSEL at higher pulse repetition rates of 10 and 30 GHz keeping the pulse duration fixed at 184 fs. In Fig. 3.34(a) we cannot observe an improvement of F_0 and available OC rate with higher pulse repetition rates. This is consistent with what was measured in [16]: higher repetition rates come at the expense of reduced intracavity pulse fluence and OC rate.

Compared to the 4.33-GHz result we observe a higher efficiency at 10 GHz (η_{calc} = 1.66%), but then a lower efficiency for 30 GHz (η_{calc} = 0.85%). This means that reduced gain for higher pulse repetition rates cancels the potential benefit of the reduced losses of the excited carriers with shorter cavity roundtrip times. One can compare the QW population dynamics in Figs. 3.34(b)-3.34(d), simulated at different repetition rates at the respective F_0. The overall carrier population, and therefore the gain is

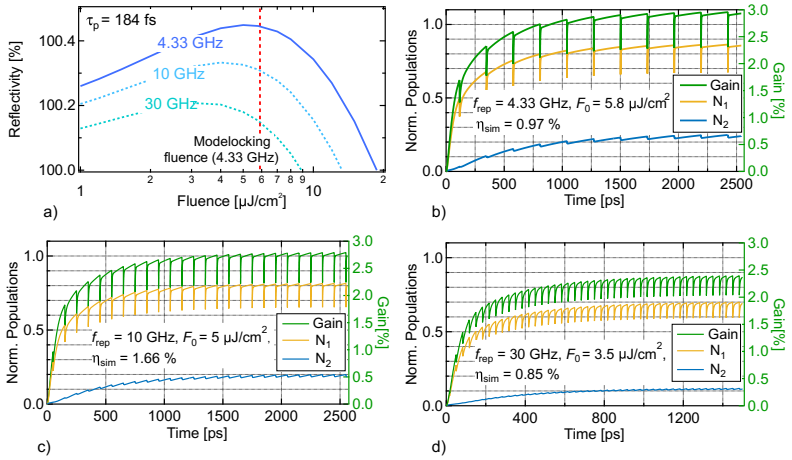

Figure 3.34: Ultrafast SDL performance with different pulse repetition rates: (a) MIXSEL saturation curve calculated at different repetition rates. The solid line represents the simulation obtained with the 184-fs MIXSEL parameters at 4.33 GHz: the model reproduces correctly the actual performance; the dashed lines simulate the results for different repetition rates of 10 and 30 GHz; cavity losses are included. (b), (c) and (d): gain and carrier dynamics in the QW gain simulated for different pulse repetition rates. Starting from an initially empty QW, the overall QW population and gain reached at steady-state decrease for reduced roundtrip time. Populations are normalized to the respective maximum values N_{10} and N_{20}.

decreased by the more frequent incoming pulses on the MIXSEL chip.

In conclusion, a longer carrier lifetime in the conduction band is the most promising solution to increase the optical-to-optical pump efficiency for femtosecond SDLs.

3.6.8 Conclusion and outlook

In this paper, we have demonstrated a new world-record MIXSEL performance with pulses as short as 184 fs, with an average output power of 115 mW, a pulse repetition rate of 4.33 GHz and a center wavelength of 1048 nm. This corresponds to a peak power of 127 W. The MIXSEL chip has 10 InGaAs QWs for the gain and one single InGaAs QW for the saturable absorber. We used a simple linear cavity with an output coupler transmission of 0.44% and an intracavity Brewster plate to obtain linear polarization. This new result was obtained with a pump efficiency of

only 0.65% and unfortunately confirms the trade-off in output power and optical-to-optical pump efficiency with shorter pulses.

To explain in more details the physical reasons for this trade-off, we employed and justified a rate equation (RE) model describing the InGaAs QWs normally used as active medium. By making careful approximations it was possible to make the model parameters accessible through direct measurements or fits of available experimental data. Despite its simplicity compared to other QW laser dynamical models, our model succeeds to accurately reproduce the experimental gain saturation curves obtained by probing the reflectivity of a pumped VECSEL at different pulse durations and correctly describes the output power and the pump efficiency for several different ultrafast SDL results based on SESAM modelocked VECSELs and MIXSELs. For shorter pulses, spectral hole burning decreases the carrier density available for the pulse amplification and therefore increases gain saturation effects and lowers the output power.

With the intent of analyzing the behavior of a full SDL cavity, we measured and fitted the VECSEL and the SESAM used for the 100-fs pulse generation presented in [12]. We concluded that the operation point of a modelocked SDL is set by the macroscopic fluence parameter F_0, where the cavity round-trip pulse amplification is maximized. We can conclude that gain saturation in general and not TPA in the VECSEL chip is the dominant process that limits F_0, the output coupling rate and therefore the output power.

The saturation characteristic was also measured and fitted for the 184-fs MIXSEL and confirmed our understanding from the ultrafast VECSEL analysis. Furthermore, a more detailed study on optical-to-optical pump efficiency was carried out searching for possible improvements. Long picosecond pulses are less affected by spectral hole burning but can achieve higher efficiencies only if the absorber recovery is kept slow (in the tens of picosecond). Higher repetition rates can in principle benefit from higher frequent and efficient amplification in the gain chip, but they do not offer improved efficiency performances because of the incomplete carrier refilling of the QWs between two consecutive pulses. We found that the main efficiency limitation is given by the short carrier lifetime in the conduction band of our QWs (measured to be approximately 140 ps). This low car-

rier lifetime is typical for high-power ultrafast SDLs with a typical output coupler of less than 1%.

From this analysis we can conclude that the main parameter that needs to be optimized for more efficient femtosecond SDLs is the carrier lifetime. We believe that significant improvements can be achieved with quantum dot (QD) instead of QW gain materials.

Funding. Swiss Confederation Program Nano-Tera.ch, which was scientifically evaluated by the Swiss National Science Foundation (SNSF).

Acknowledgement The authors acknowledge support of the technology and cleanroom facility FIRST for advanced micro-and nanotechnology.

3.6.9 References

1. U. Keller and A. C. Tropper, "Passively modelocked surface-emitting semiconductor lasers," Phys. Rep. 429(2), 67–120 (2006).
2. B. W. Tilma, M. Mangold, C. A. Zaugg, S. M. Link, D. Waldburger, A. Klenner, A. S. Mayer, E. Gini, M. Golling, and U. Keller, "Recent advances in ultrafast semiconductor disk lasers," Light Sci. Appl. 4(7), e310 (2015).
3. M. Gaafar, A. Rahimi-Iman, K. A. Fedorova, W. Stolz, E. U. Rafailov, and M. Koch, "Mode-locked semiconductor disk lasers," Adv. Opt. Photonics 8(3), 370–400 (2016).
4. S. Hoogland, S. Dhanjal, A. C. Tropper, J. S. Roberts, R. Haring, R. Paschotta, F. Morier-Genoud, and U. Keller, "Passively mode-locked diode-pumped surface-emitting semiconductor laser," IEEE Photonics Technol. Lett. 12(9), 1135–1137 (2000).
5. M. Kuznetsov, F. Hakimi, R. Sprague, and A. Mooradian, "High-power (>0.5-W CW) diode-pumped vertical-external-cavity surface-emitting semiconductor lasers with circular TEM00 beams," IEEE Photonics Technol. Lett. 9(8), 1063–1065 (1997).
6. S. H. Park, J. Kim, H. Jeon, T. Sakong, S. N. Lee, S. Chae, Y. Park, C. H. Jeong, G. Y. Yeom, and Y. H. Cho, "Room-temperature GaN vertical-cavity surface-emitting laser operation in an extended cavity scheme," Appl. Phys. Lett. 83(11), 2121–2123 (2003).

7. M. Guina, A. Härkönen, V.-M. Korpijärvi, T. Leinonen, and S. Suomalainen, "Semiconductor Disk Lasers: Recent Advances in Generation of Yellow-Orange and Mid-IR Radiation," Adv. Opt. Technol. 2012(19), 265010 (2012).
8. R.-I. Arash, "Recent advances in VECSELs," J. Optics-UK 18(9), 093003 (2016).
9. B. Rudin, A. Rutz, M. Hoffmann, D. J. H. C. Maas, A.-R. Bellancourt, E. Gini, T. Südmeyer, and U. Keller, "Highly efficient optically pumped vertical-emitting semiconductor laser with more than 20 W average output power in a fundamental transverse mode," Opt. Lett. 33(22), 2719–2721 (2008).
10. B. Heinen, T. L. Wang, M. Sparenberg, A. Weber, B. Kunert, J. Hader, S. W. Koch, J. V. Moloney, M. Koch, and W. Stolz, "106 W continuous-wave output power from vertical-external-cavity surface-emitting laser," Electron. Lett. 48(9), 516–517 (2012).
11. U. Keller, K. J. Weingarten, F. X. Kärtner, D. Kopf, B. Braun, I. D. Jung, R. Fluck, C. Hönninger, N. Matuschek, and J. Aus der Au, "Semiconductor saturable absorber mirrors (SESAMs) for femtosecond to nanosecond pulse generation in solid-state lasers," IEEE J. Sel. Top. Quantum Electron. 2(3), 435–453 (1996).
12. D. Waldburger, S. M. Link, M. Mangold, C. G. E. Alfieri, E. Gini, M. Golling, B. W. Tilma, and U. Keller, "High-power 100 fs semiconductor disk lasers," Optica 3(8), 844–852 (2016).
13. D. J. H. C. Maas, A.-R. Bellancourt, B. Rudin, M. Golling, H. J. Unold, T. Südmeyer, and U. Keller, "Vertical integration of ultrafast semiconductor lasers," Appl. Phys. B 88(4), 493–497 (2007).
14. B. Rudin, V. J. Wittwer, D. J. H. C. Maas, M. Hoffmann, O. D. Sieber, Y. Barbarin, M. Golling, T. Südmeyer, and U. Keller, "High-power MIXSEL: an integrated ultrafast semiconductor laser with 6.4 W average power," Opt. Express 18(26), 27582–27588 (2010).
15. M. Mangold, M. Golling, E. Gini, B. W. Tilma, and U. Keller, "Sub-300-femtosecond operation from a MIXSEL," Opt. Express 23(17), 22043–22059 (2015).
16. M. Mangold, C. A. Zaugg, S. M. Link, M. Golling, B. W. Tilma, and U. Keller, "Pulse repetition rate scaling from 5 to 100 GHz with a high-power semiconductor disk laser," Opt. Express 22(5), 6099–6107 (2014).
17. S. M. Link, A. Klenner, M. Mangold, C. A. Zaugg, M. Golling, B. W. Tilma, and U. Keller, "Dual-comb modelocked laser," Opt. Express 23(5), 5521–5531 (2015).

18. S. M. Link, D. J. H. C. Maas, D. Waldburger, and U. Keller, Submitted to Science (January 2017).

19. O. D. Sieber, M. Hoffmann, V. J. Wittwer, M. Mangold, M. Golling, B. W. Tilma, T. Südmeyer, and U. Keller, "Experimentally verified pulse formation model for high-power femtosecond VECSELs," Appl. Phys. B 113(1), 133–145 (2013).

20. K. Sugioka and Y. Cheng, "Ultrafast lasers—reliable tools for advanced materials processing," Light Sci. Appl. 3(4), e149 (2014).

21. R. Aviles-Espinosa, G. Filippidis, C. Hamilton, G. Malcolm, K. J. Weingarten, T. Südmeyer, Y. Barbarin, U. Keller, S. I. C. O. Santos, D. Artigas, and P. Loza-Alvarez, "Compact ultrafast semiconductor disk laser: targeting GFP based nonlinear applications in living organisms," Biomed. Opt. Express 2(4), 739–747 (2011).

22. C. A. Zaugg, A. Klenner, M. Mangold, A. S. Mayer, S. M. Link, F. Emaury, M. Golling, E. Gini, C. J. Saraceno, B. W. Tilma, and U. Keller, "Gigahertz self-referenceable frequency comb from a semiconductor disk laser," Opt. Express 22(13), 16445–16455 (2014).

23. A. H. Quarterman, L. E. Hooper, P. J. Mosley, and K. G. Wilcox, "Gigahertz pulse source by compression of mode-locked VECSEL pulses coherently broadened in the normal dispersion regime," Opt. Express 22(10), 12096–12101 (2014).

24. H. R. Telle, G. Steinmeyer, A. E. Dunlop, J. Stenger, D. H. Sutter, and U. Keller, "Carrier-envelope offset phase control: A novel concept for absolute optical frequency measurement and ultrashort pulse generation," Appl. Phys. B 69(4), 327–332 (1999).

25. A. Klenner, A. S. Mayer, A. R. Johnson, K. Luke, M. R. E. Lamont, Y. Okawachi, M. Lipson, A. L. Gaeta, and U. Keller, "Gigahertz frequency comb offset stabilization based on supercontinuum generation in silicon nitride waveguides," Opt. Express 24(10), 11043–11053 (2016).

26. A. S. Mayer, A. Klenner, A. R. Johnson, K. Luke, M. R. E. Lamont, Y. Okawachi, M. Lipson, A. L. Gaeta, and U. Keller, "Frequency comb offset detection using supercontinuum generation in silicon nitride waveguides," Opt. Express 23(12), 15440–15451 (2015).

27. J. V. Moloney, I. Kilen, A. Bäumner, M. Scheller, and S. W. Koch, "Nonequilibrium and thermal effects in mode-locked VECSELs," Opt. Express 22(6), 6422–6427 (2014).

28. I. Kilen, J. Hader, J. V. Moloney, and S. W. Koch, "Ultrafast nonequilibrium carrier dynamics in semiconductor laser mode locking," Optica 1(4), 192–197 (2014).
29. J. Hader, M. Scheller, A. Laurain, I. Kilen, C. Baker, J. V. Moloney, and S. W. Koch, "Ultrafast non-equilibrium carrier dynamics in semiconductor laser mode-locking," Semicond. Sci. Technol. 32(1), 013002 (2017).
30. I. Kilen, S. W. Koch, J. Hader, and J. V. Moloney, "Fully microscopic modeling of mode locking in microcavity lasers," J. Opt. Soc. Am. B 33(1), 75–80 (2016).
31. N. Tessler and G. Eisenstein, "Modelling carrier dynamics and small-signal modulation response in quantum-well lasers," Opt. Quantum Electron. 26(7), S767–S787 (1994).
32. N. Tessler and G. Eistenstein, "On carrier injection and gain dynamics in quantum well lasers," IEEE J. Quantum Electron. 29(6), 1586–1595 (1993).
33. H. Dery, B. Tromborg, and G. Eisenstein, "Carrier-carrier relaxation kinetics in quantum well semiconductor structures with nonparabolic energy bands," Phys. Rev. B 68(16), 165323 (2003).
34. C. G. E. Alfieri, A. Diebold, F. Emaury, E. Gini, C. J. Saraceno, and U. Keller, "Improved SESAMs for femtosecond pulse generation approaching the kW average power regime," Opt. Express 24(24), 27587–27599 (2016).
35. T. R. Schibli, E. R. Thoen, F. X. Kärtner, and E. P. Ippen, "Suppression of Q-switched mode locking and breakup into multiple pulses by inverse saturable absorption," Appl. Phys. B 70(S1 Suppl.), S41–S49 (2000).
36. R. Trebino, K. W. DeLong, D. N. Fittinghoff, J. N. Sweetser, M. A. Krumbügel, B. Richman, and D. J. Kane, "Measuring ultrashort laser pulses in the time-frequency domain using frequency-resolved optical gating," Rev. Sci. Instrum. 68(9), 3277–3295 (1997).
37. N. Tessler, R. Nagar, and G. Eisenstein, "Structure dependent modulation responses in quantum-well lasers," IEEE J. Quantum Electron. 28(10), 2242–2250 (1992).
38. H. Toktamis, B. Gönül, and M. Oduncuoglu, "Comparative study of the band-offset ratio of conventionally strained and strain-compensated InGaAs/GaAs QW lasers," Physica E 24(3–4), 183–186 (2004).
39. S. T. Cundiff, A. Knorr, J. Feldmann, S. W. Koch, E. O. Göbel, and H. Nickel, "Rabi flopping in semiconductors," Phys. Rev. Lett. 73(8), 1178–1181 (1994).
40. J. Hader, J. V. Moloney, and S. W. Koch, "Microscopic analysis of non-equilibrium dynamics in the semiconductor-laser gain medium," Appl. Phys. Lett. 104(15), 151111 (2014).

41. O. Karni, A. K. Mishra, G. Eisenstein, V. Ivanov, and J. P. Reithmaier, "Coherent control in room-temperature quantum dot semiconductor optical amplifiers using shaped pulses," Optica 3(6), 570–576 (2016).

42. A. P. Ongstad, D. J. Gallant, and G. C. Dente, "Carrier lifetime saturation in InGaAs single quantum wells," Appl. Phys. Lett. 66(20), 2730–2732 (1995).

43. C. K. Sun, B. Golubovic, H. K. Choi, C. A. Wang, and J. G. Fujimoto, "Femtosecond investigations of spectral hole burning in semiconductor lasers," Appl. Phys. Lett. 66(13), 1650–1652 (1995).

44. M. Asada, "Intraband relaxation time in quantum-well lasers," IEEE J. Quantum Electron. 25(9), 2019–2026 (1989).

45. C. Baker, M. Scheller, S. W. Koch, A. R. Perez, W. Stolz, R. Jason Jones, and J. V. Moloney, "In situ probing of mode-locked vertical-external-cavity-surface-emitting lasers," Opt. Lett. 40(23), 5459–5462 (2015).

46. M. Mangold, V. J. Wittwer, O. D. Sieber, M. Hoffmann, I. L. Krestnikov, D. A. Livshits, M. Golling, T. Südmeyer, and U. Keller, "VECSEL gain characterization," Opt. Express 20(4), 4136–4148 (2012).

47. M. Butkus, E. A. Viktorov, T. Erneux, C. J. Hamilton, G. Maker, G. P. A. Malcolm, and E. U. Rafailov, "85.7 MHz repetition rate mode-locked semiconductor disk laser: fundamental and soliton bound states," Opt. Express 21(21), 25526–25531 (2013).

48. C. A. Zaugg, A. Klenner, O. D. Sieber, M. Golling, B. W. Tilma, and U. Keller, "Sub-100 MHz Passively Modelocked VECSEL," in CLEO: 2013, OSA Technical Digest (online) (Optical Society of America, 2013), CW1G.6.

49. A. Klenner, M. Golling, and U. Keller, "High peak power gigahertz Yb:CALGO laser," Opt. Express 22(10), 11884–11891 (2014).

50. C. G. E. Alfieri, D. Waldburger, S. M. Link, E. Gini, M. Golling, B. W. Tilma, M. Mangold, and U. Keller, "Recent progress in high power ultrafast MIXSELs," in Proc. SPIE (2016), p. 973407.

3.7 High-Power Sub-300-Femtosecond Quantum Dot Semiconductor Disk Lasers

Cesare G. E. Alfieri, Dominik Waldburger, Matthias Golling and Ursula Keller

Department of Physics, Institute for Quantum Electronics, ETH Zürich, 8093 Zürich, Switzerland

Self-assembled quantum dots (QDs) as active media for ultrafast semiconductor disk laser offer large gain bandwidths, fast gain dynamics, and high temperature stability. We report on the shortest pulses and the highest pulse peak power from an optically pumped vertical external-cavity surface-emitting laser (VECSEL) based on QDs and optimized for passive modelocking at 1035 nm using a semiconductor saturable absorber mirror. We demonstrate 216-fs pulses with an average output power of 269 mW at a pulse repetition rate of 2.77 GHz and 396 W peak power. At a lower pulse repetition rate of 1.67 GHz, we achieve 193-fs pulses with 112 mW of average output power. We remark a higher optical-to-optical pump efficiency compared to our previous QW VECSELs in the sub-300-fs regime. This is further confirmed by a comparative analysis of the saturation recovery which reveals longer carrier lifetimes for the QD compared to QW VECSELs.

3.7.1 Introduction

Ultrafast optically pumped semiconductor disk lasers (SDLs) [1], [2] are interesting for many applications such as dual comb spectroscopy [3] and multiphoton microscopy [4]. SDLs can operate within a large spectral range with high-power emission and diffraction-limited output beams. In particular, vertical external-cavity surface-emitting lasers (VECSELs) [5] passively modelocked with semiconductor saturable absorber mirrors (SESAMs) [6], [7] and the more compact modelocked integrated external-cavity surface-emitting laser (MIXSEL) [8] have shown considerable improvements during the last years in terms of output power and pulse

duration [9], [10]. To date, the best ultrafast SDLs in terms of average output power and pulse duration use InGaAs quantum wells (QWs) for both gain and absorber structures and operate close to a center wavelength of 1 μm. Although QWs offer high density of states (DOS) for high modal gain and moderately large emission bandwidth, we recently have demonstrated with our results that a significantly reduced gain saturation fluence due to spectral hole burning limits the maximum pulse energy in the femtosecond pulse duration regime [10]. Furthermore, the short carrier lifetime in highly inverted QWs reduces the optical-to-optical pump efficiency to typically ≈0.5% in the sub-300-fs pulse duration regime [1], [2]. In fact, the electron-hole pairs (created by the continuous pumping) spontaneously recombine in the QW before they can be used for pulse amplification. Additionally, the strong temperature dependence of emission and absorption spectra represents a serious technological challenge for fully QW-based MIXSELs, where two different QW designs need to be carefully calibrated to compensate the temperature gradient between gain and absorber regions inside the epitaxial structure [11].

In contrast, self-assembled quantum dots (QDs) offer a number of fundamental benefits for ultrafast SDLs such as broad and flat gain bandwidth, low lasing threshold, very fast gain dynamics owing to the stronger spatial confinement and extended wavelength range with no need of strain compensation layers even though they have a reduced DOS [12]–[15]. Furthermore, the high degree of freedom in the growth process can lead to engineered QDs with greatly reduced temperature sensitivity [16], [17] and longer carrier lifetimes [18]. To date, QD-based SDLs in continous wave (cw) operation achieved wavelength tuning up to 69 nm [19] and output powers up to 8.4 W [20]. With SESAM modelocking, the shortest pulse duration of 416 fs was achieved with 143 mW of average output power using a QD SESAM [21]. Here we report a significant further improvement of SESAM-modelocked QD VECSELs pushing the pulse duration into the sub-300-femtosecond regime while still maintaining an average output power of more than 250 mW.

3.7.2 Growth and Characterization

The QDs used in this work are based on Stranski–Krastanov (SK) growth formation technique. Each QD layer consists of a sevenfold deposition at 480°C of 0.1 nm InAs and 0.1 nm $In_{0.2}Ga_{0.8}As$, for a total nominal thickness of 1.4 nm and an average 60% indium. The room-temperature photoluminescence (PL) spectrum of the self-assembled QDs is centered at 1025 nm. The large QD-size variation results in a broad 135-nm full width at half maximum (FWHM) bandwidth, which is almost 100 nm broader compared to the PL emission of the QWs used for our recent 100-fs VECSELs (Fig. 3.35a) [9]. The comparison between the absorptions of a QW-based and a QD-based SESAM performed at 30°C and 70°C confirms the expected lower temperature sensitivity of the self-assembled QDs. We measure an absorption temperature shift of ≈0.17 nm/K for the QDs, in comparison ≈0.32 nm/K for the QWs. We use a degenerate pump-probe setup with a center pump-probe wavelength of 1010 nm and 130-fs pulses at the sample position to measure the saturation recovery of the SK QDs. With this technique, we measure a signal proportional to the instantaneous carrier population in the active layers, therefore taking into account radiative and non-radiative recombination. For this reason, we obtain lifetimes significantly shorter than the nanosecond timescale usually measured for only radiative lifetimes [18]. In particular, we obtain for the QDs a slow component of the recovery time of 406 ps which is significantly longer than the 132-ps measured in [10] for QWs (Fig. 3.35b). This longer saturation recovery time is obtained with reduced non-radiative losses and results in a higher optical-to-optical pump efficiency [10], [22].

The VECSEL structure is designed for operation around 1035 nm. The laser light is reflected by a 23.5-pair AlAs-GaAs distributed Bragg reflector (DBR). The active region consists of 16 QD layers embedded in pump-absorbing GaAs barriers and positioned in pairs with 50-nm separation on adjacent sides of the antinodes of the standing wave pattern (Fig. 3.36a). Atomic force microscope (AFM) measurements of uncapped QD islands reveal that the lattice constant mismatch of the InGaAs layer with the underlying GaAs causes the formation of pyramidal SK QDs with 2-4 nm height and 20 to 40 nm width (Fig. 3.36b). The average enhancement of the standing electric field intensity pattern in the QD active layers is kept

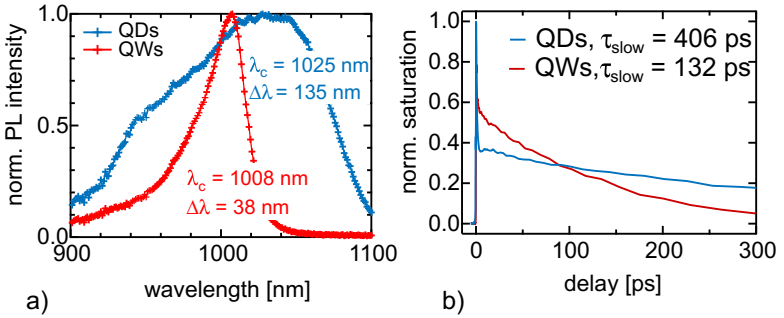

Figure 3.35: a) Photoluminescence (PL) at room temperature of InGaAs QWs and SK QDs. b) Transient of the saturation of SK QDs and InGaAs QWs. The QDs clearly exhibit a slower recovery time which improves the optical-to-optical pump efficiency.

at the rather high value of 0.71 (normalized to 4 outside the fully reflective structure) to increase the small signal gain and partially compensate the lower gain cross section of SK QDs compared to QWs. The increased gain, however, reduces the gain bandwidth and decreases the gain saturation fluence [23] (Fig. 3.36d) introducing a trade-off that needs to be optimized for different operation parameters. A final anti-reflection (AR) section combines five alternating layers of AlAs and $Al_{0.15}Ga_{0.85}As$ and a single layer of silicon oxide (SiO_x). The AR section is optimized to reduce the pump reflection at 808 nm and ensure a flat and low structural group delay dispersion (GDD) ± 100 fs^2 over a bandwidth of ± 20 nm around the lasing center wavelength (Fig. 3.36c).

The VECSEL chip is grown in reverse order on an undoped GaAs (100) substrate with a molecular beam epitaxy (MBE) for subsequent flip-chip bonding.

The etch-stop layer, the anti-reflection section and the DBR are grown at 620°C while the GaAs barriers in the active region are grown at 580°C. After growth, the chip is Indium soldered onto a 5 x 5mm, 1 mm thick chemical vapour deposition (CVD) diamond heat spreader and the GaAs substrate is removed through wet etching. The final layer is deposited with plasma-enhanced chemical vapor deposition (PECVD). The difference between the measured and designed GDD profile (Fig. 3.36c) can be explained by the epitaxial growth errors and deviations from the nominal

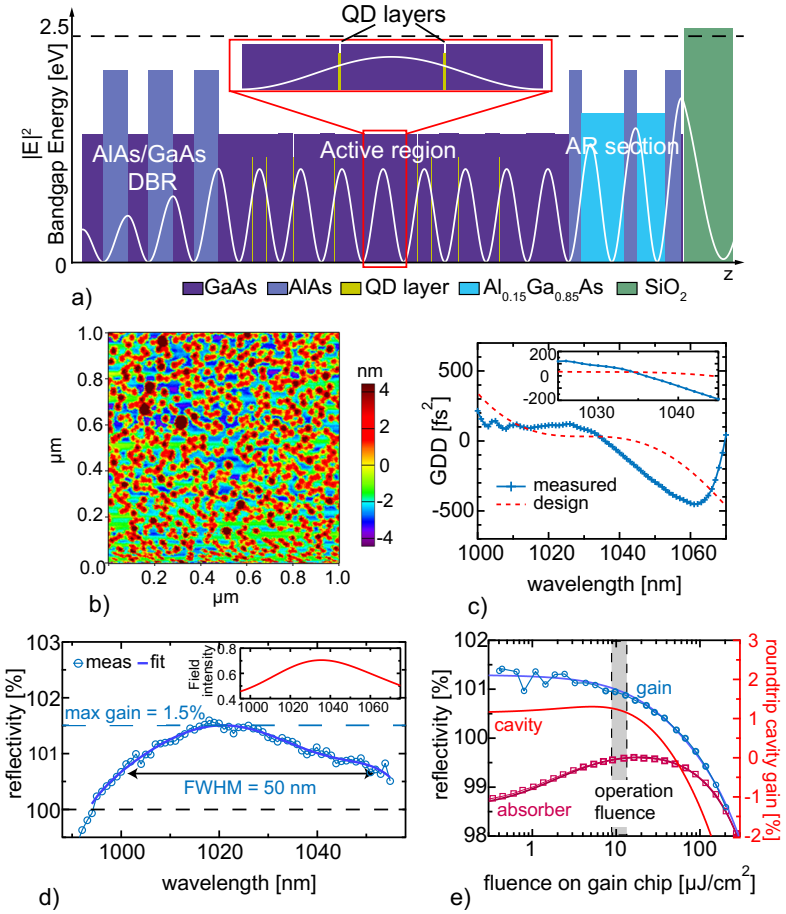

Figure 3.36: a) Epitaxial structure of the QD VECSEL with the standing wave intensity profile at the center wavelength of 1035 nm (white curve). b) Atomic force microscope (AFM) picture of the surface of a SK QD layer. c) Measured and designed dispersion of the VECSEL chip. The measurement is performed at room temperature and normal incidence. Inset: zoom around the lasing center wavelength. d) Spectral gain of the QD VECSEL, measured at ≈10°C at a pump intensity of 25 kW/cm^2. Inset: designed average field intensity in the QD layers, peaked at 1035 nm. e) Nonlinear reflectivity measurements (markers) and fits (solid line) of the gain and absorber elements in the VECSEL cavity. The red solid line represents the roundtrip cavity gain, taking into account that a V-shaped cavity produces a double pass on the gain chip and a single pass on the absorber per roundtrip. The laser operation point is slightly shifted into the rollover of the roundtrip cavity gain.

optical thickness (±1%). Nevertheless, we reach a flatness of ±200 fs^2 over a bandwidth of ±10 nm around the designed lasing center wavelength.

The optical gain of the VECSEL chip is characterized with the setups described in [24] and probed with small sub-20 μm spot sizes. Under an optical pump intensity of 25 kW/cm^2 (total pump power ≈2 W) and a heatsink temperature T_{HS} = ≈10°C, the spectrally resolved reflectivity shows a maximum small signal gain of 1.5% at 1020 nm and a broad gain bandwidth of more than 50 nm (Fig. 3.36d).

Under the same conditions, the fluence-dependent gain saturation is probed at 1035 nm with 170-fs pulses. We measure a small signal gain of 1.3% and a saturation fluence of 37.6 $\mu J/cm^2$ (Fig. 3.36e). We observe that despite the higher average field intensity in the QDs, the saturation behavior is comparable to state-of-the-art ultrafast QW VECSELs, but the small signal gain is roughly twice as low [9].

3.7.3 Modelocking Result

The SESAM used for modelocked operation consists of a standard MBE-grown single InGaAs QW absorber embedded in AlAs barriers on top of a 30-pair GaAs/AlAs DBR and top-coated with a $\lambda/4$ Si_3N_4 layer [25] Low-temperature MBE growth at 280°C was chosen to provide both a sufficiently fast saturable absorber as required for femtosecond pulse generation and still preserving a low nonsaturable loss of 0.1%. At 1035 nm and 22°C heatsink temperature the measured saturation fluence is 4.6 $\mu J/cm^2$ and the modulation depth is 1.4% (Fig. 3.36e).

The laser resonator is based on a standard V-shaped cavity with 20° angle between the two cavity legs. A curved output coupler (OC) and the SESAM are used as end mirrors and the gain structure forms the folding mirror (Fig. 3.37a). The OC has a radius of curvature (ROC) of 60 mm and a transmission of 1.2% at 1035 nm. The distance between VECSEL and OC is set to 28 mm while the second cavity leg is 26 mm. For a stronger absorber saturation, the resonator mode on the gain chip is designed to be roughly twice as large as on the SESAM (i.e. a 139 μm and 73 μm radius, respectively). The VECSEL chip is pumped at 45° with an 808-nm low-brightness diode laser and the pump spot is shaped to be circular with 130 μm radius on the gain chip's surface. During operation,

the VECSEL chip and the SESAM are temperature stabilized to ≈19°C and 24.5°C respectively. At a pump power of 13 W, we obtain a Gaussian output beam with M square value (M^2) < 1.1 and stable fundamental modelocking operation confirmed by a detailed pulse characterization (Fig. 3.37a). The measured optical spectrum is centered at 1035 nm, with a FWHM bandwidth of 5.7 nm and the autocorrelation trace, fitted to a $sech^2$ pulse shape, reveals a pulse duration of 216 fs. With an average output power of 269 mW at a repetition rate of 2.77 GHz, the VECSEL generates a record-high pulse peak power of 396 W for a QD SDL. Finally, an optical-to-optical efficiency of 2.1% makes this QD VECSEL the most efficient compared to any other sub-300-fs SDL. As observed before with QW SDLs [26], [27] and other SESAM-modelocked lasers such as high-power Yb-doped thin disk lasers [28], the QD VECSEL operates just in the rollover of the roundtrip cavity gain (Fig. 3.36e). Further increase of the pump power pushes the laser from clean fundamental modelocking to multiple pulses per cavity roundtrip.

The same VECSEL chip and SESAM, again temperature stabilized to ≈19°C and 24.5°C respectively, are tested in a longer cavity with a different OC (i.e. 100-mm ROC and 0.7% output coupling at 1035 nm) (Fig. 3.37b). In this case, the pump spot radius is increased to 177 μm and we obtain larger laser mode radii on the gain and on the absorber of 184 μm and 92 μm respectively. An additional 1 mm thick fused silica wedged Brewster plate is inserted into the cavity to add a small amount of positive cavity GDD (≈64 fs^2) to obtain shorter pulses [23] (Fig. 3.37e). With this cavity configuration, we pushed the pulse duration into the sub-200-fs regime. At a pulse repetition rate of 1.67 GHz, we obtain 193-fs pulses that represent the shortest pulses from a QD VECSEL to date. The optical spectrum is centered at 1038 nm with 6.6 nm FWHM bandwidth (Fig. 3.37b). However, the non-perfect surface smoothness on the chip introduces a decreased average gain for larger cavity modes. Furthermore, the extra losses introduced by the intracavity Brewster plate and the more considerable thermal load on the structure compared to the previous experiment reduce the average output power to 112 mW at 23.7 W of optical pump power. With a 306-W peak power, however, the performance is still comparable to previous QW VECSELs [9], [29]. The lower gain provided

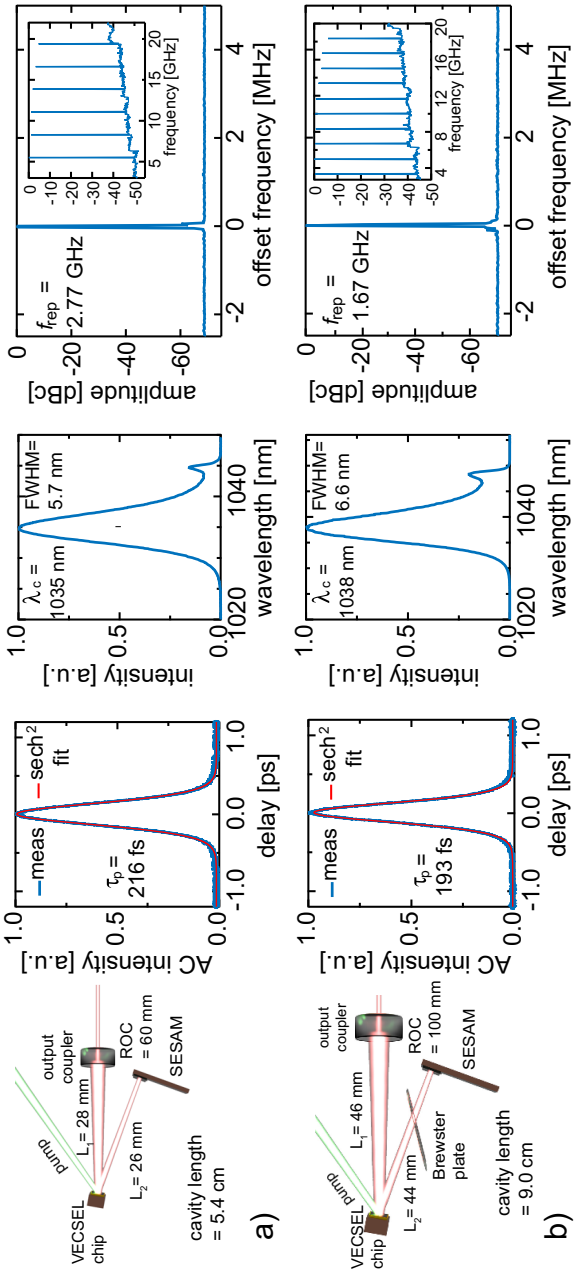

Figure 3.37: SESAM modelocked VECSEL generating pulses as short as (a) 216 fs and (b) 193 fs. For both results we show the cavity design, the non-collinear SHG autocorrelation trace, the optical spectrum and the microwave spectrum with a high signal-to-noise ratio of 70 dB (resolution bandwidth of 1 kHz). Inset: long span of the microwave spectrum (resolution bandwidth of 300 kHz) showing that all the harmonics of the pulse repetition rate are present with equal power. A side peak appears on the right side of the optical spectrum, probably due to a non-flat OC rate combined with a smaller SESAM modulation at higher wavelengths.

by QDs and the not perfectly optimized GDD profile are preventing the current QD VECSEL to reach the record short-pulse performance demonstrated for QWs in [9].

3.7.4 Conclusion

To summarize, we have pushed SESAM-modelocked QD VECSELs to a new level of performance reporting sub-200-fs operation and the highest pulse peak power from a QD VECSEL together with the highest optical-to-optical efficiency for any sub-300-fs SDL.We confirm that QD gain media offers an attractive alternative to QWs for ultrafast SDLs, with some clear advantages for future applications and devices.We expect that especially the MIXSEL technology platform could greatly benefit from the QD temperature stability. We show that a longer carrier lifetime in the QD gain directly translates into a higher optical-to-optical pump efficiency. Currently further power scaling is limited by the larger mode size requirement in modelocked SDLs due to surface defects and heat dissipation. Further improvements towards kW peak power performance can be expected to be obtained with better optimized GDD and field intensity profiles, increased number of QD layers for increased gain and better surface quality.

Acknowledgement The authors acknowledge support of the technology and cleanroom facility FIRST of ETH Zurich for advanced micro- and nanotechnology. The authors acknowledge funding within the D-A-CH program with the QD-MIXSEL project, which was scientifically evaluated by the Swiss National Science Foundation (SNSF) and the Deutsche Physikalische Gesellschaft (DPG).

3.7.5 References

[1] B. W. Tilma et al., "Recent advances in ultrafast semiconductor disk lasers," Light Sci. Appl., vol. 4, p. e310, Jul. 2015.

[2] M. Guina, A. Rantamäki, and A. Härkönen, "Optically pumped VECSELs: Review of technology and progress," J. Phys. D, Appl. Phys., vol. 50, no. 38, p. 383001, 2017.

[3] S. M. Link, D. J. H. C. Maas, D. Waldburger, and U. Keller, "Dualcomb spectroscopy of water vapor with a free-running semiconductor disk laser," Science, vol. 356, no. 6343, pp. 1164–1168, 2017.

[4] F. F. Voigt et al., "Multiphoton in vivo imaging with a femtosecond semiconductor disk laser," Biomed. Opt. Express, vol. 8, no. 7, pp. 3213–3231, 2017.

[5] M. Kuznetsov, F. Hakimi, R. Sprague, and A. Mooradian, "High-power (>0.5-W CW) diode-pumped vertical-external-cavity surface-emitting semiconductor lasers with circular TEM00 beams," IEEE Photon. Technol. Lett., vol. 9, no. 8, pp. 1063–1065, Aug. 1997.

[6] U. Keller et al., "Semiconductor saturable absorber mirrors (SESAM's) for femtosecond to nanosecond pulse generation in solid-state lasers," IEEE J. Sel. Top. Quantum Electron., vol. 2, no. 3, pp. 435–453, Sep. 1996.

[7] U. Keller and A. C. Tropper, "Passively modelocked surface-emitting semiconductor lasers," Phys. Rep., vol. 429, no. 2, pp. 67–120, Jun. 2006.

[8] D. J. H. C. Maas et al., "Vertical integration of ultrafast semiconductor lasers," Appl. Phys. B, Lasers Opt., vol. 88, no. 4, pp. 493–497, 2007.

[9] D. Waldburger et al., "High-power 100 fs semiconductor disk lasers," Optica, vol. 3, no. 8, pp. 844–852, 2016.

[10] C. G. E. Alfieri et al., "Optical efficiency and gain dynamics of modelocked semiconductor disk lasers," Opt. Express, vol. 25, no. 6, pp. 6402–6420, 2017.

[11] M. Mangold, M. Golling, E. Gini, B. W. Tilma, and U. Keller, "Sub-300-femtosecond operation from a MIXSEL," Opt. Express, vol. 23, no. 17, pp. 22043–22059, 2015.

[12] T. D. Germann et al., "Quantum-dot semiconductor disk lasers," J. Cryst. Growth, vol. 310, no. 23, pp. 5182–5186, Nov. 2008.

[13] D. Bimberg, N. Kirstaedter, N. N. Ledentsov, Z. I. Alferov, P. S. Kop'ev, and V. M. Ustinov, "InGaAs-GaAs quantum-dot lasers," IEEE J. Sel. Topics Quantum Electron., vol. 3, no. 2, pp. 196–205, Apr. 1997.

[14] J. Gomis-Bresco et al., "Impact of coulomb scattering on the ultrafast gain recovery in InGaAs quantum dots," Phys. Rev. Lett., vol. 101, no. 25, p. 256803, Dec. 2008.

[15] M. S. Skolnick and D. J. Mowbray, "Self-assembled semiconductor quantum dots: Fundamental physics and device applications," Annu. Rev. Mater. Res., vol. 34, no. 1, pp. 181–218, 2004.

[16] F. Klopf, S. Deubert, J. P. Reithmaier, and A. Forchel, "Correlation between the gain profile and the temperature-induced shift in wavelength of quantum-dot lasers," Appl. Phys. Lett., vol. 81, no. 2, pp. 217–219, 2002.

[17] T. D. Germann et al., "Temperature-stable operation of a quantum dot semiconductor disk laser," Appl. Phys. Lett., vol. 93, no. 5, p. 051104, 2008.

[18] O. Nasr et al., "Carrier dynamics of strain-engineered InAs quantum dots with (In) GaAs surrounding material," J. Opt., vol. 19, no. 2, p. 025401, 2017.

[19] M. Butkus et al., "Quantum dot based semiconductor disk lasers for 1–1.3 μm," IEEE J. Sel. Topics Quantum Electron., vol. 17, no. 6, pp. 1763–1771, Nov./Dec. 2011.

[20] D. A. Nakdali et al., "High-power quantum-dot vertical-external-cavity surface-emitting laser exceeding 8 W," IEEE Photon. Technol. Lett., vol. 26, no. 15, pp. 1561–1564, Aug. 5, 2014.

[21] M. Hoffmann et al., "Femtosecond high-power quantum dot vertical external cavity surface emitting laser," Opt. Express, vol. 19, no. 9, pp. 8108–8116, 2011.

[22] A. Laurain et al., "Influence of non-radiative carrier losses on pulsed and continuous VECSEL performance," Proc. SPIE, vol. 8242, p. 82420S, Feb. 2012.

[23] O. Sieber et al., "Experimentally verified pulse formation model for high-power femtosecond VECSELs," (in English), Appl. Phys. B, Lasers Opt., vol. 113, no. 1, pp. 133–145, 2013.

[24] M. Mangold et al., "VECSEL gain characterization," Opt. Express, vol. 20, no. 4, pp. 4136–4148, 2012.

[25] G. J. Spühler et al., "Semiconductor saturable absorber mirror structures with low saturation fluence," Appl. Phys. B, Lasers Opt., vol. 81, no. 1, pp. 27–32, 2005.

[26] D. Waldburger, S. M. Link, C. G. Alfieri, M. Golling, and U. Keller, "High-power 100-fs SESAM-modelocked VECSEL," in Proc. Lasers Congr. (ASSL, LSC, LAC), Boston, MA, USA, 2016, paper ATu1A.

[27] I. Kilen, S. W. Koch, J. Hader, and J. V. Moloney, "Non-equilibrium ultrashort pulse generation strategies in VECSELs," Optica, vol. 4, no. 4, pp. 412–417, Apr. 2017.

[28] I. J. Graumann et al., "Peak-power scaling of femtosecond Yb:Lu2O3 thin-disk lasers," Opt. Express, vol. 25, no. 19, pp. 22519–22536, Sep. 2017.

[29] A. Laurain et al., "Pulse interactions in a colliding pulse mode-locked vertical external cavity surface emitting laser," J. Opt. Soc. Amer. B, Opt. Phys., vol. 34, no. 2, pp. 329–337, Feb. 2017.

3.8 Mode-locking Instabilities for High-Gain Semiconductor Disk Lasers Based on Active Submonolayer Quantum Dots

Cesare G. E. Alfieri,[1] *Dominik Waldburger,*[1] *Jacob Nürnberg,*[1]
Matthias Golling,[1] *Lina Jaurigue,*[2] *Kathy Lüdge*[2] *and Ursula Keller*[1]

[1]Department of Physics, Institute for Quantum Electronics, ETH Zürich, Zürich, Switzerland

[2]Institut für Theoretische Physik, TU Berlin, Berlin, Germany

Sub-monolayer quantum dots (SML QDs) combine the large gain cross section of quantum wells (QWs) with the potential benefits of a stronger confinement. We demonstrate here an optically pumped vertical external-cavity surface-emitting laser (VECSEL) based on active SML QDs. The ultrafast SML QD VECSEL is optimized for passive modelocking with an intracavity semiconductor saturable absorber mirror (SESAM) around 1030 nm. Nevertheless, we have achieved the highest continous wave (cw) output power of 11.2 W from a QD-based VECSEL to date. With a birefringent filter inside the VECSEL cavity we obtained a tuning range of 47 nm centered at 1028 nm. Any attempt to passively modelock the VECSEL with a QW SESAM revealed fundamental limitations. The intrinsically higher linewidth enhancement factor of SML QDs compared to QWs or self-assembled Stranski-Krastanov QDs is further increased at higher pump powers. Our experiments confirm prior theoretical predictions that a strong amplitude-phase coupling can destabilize cw modelocking and introduce chaotic multiple pulse fluctuations.

3.8.1 Introduction

Optically pumped passively modelocked vertical external-cavity surface-emitting lasers (VECSELs) [1-3] and modelocked integrated external-cavity surface-emitting lasers (MIXSELs) [4] are also referred to as ultrafast semiconductor disk lasers (SDLs). SDLs represent a compact and

wavelength-flexible solution for diverse application fields such as dual comb spectroscopy [5] and multiphoton imaging [6]. The best SDLs in terms of output power perform in the 1-μm spectral region, where they can benefit from the high-index contrast, lattice-matched GaAs/AlAs material systems. Thanks to the high modal gain provided by active InGaAs quantum wells (QWs), output powers up to 106 W could be demonstrated in continous wave (cw) operation [7]. Passive modelocking is achieved with semiconductor saturable absorber mirrors (SESAMs) [8] with the first demonstration in 2000 [9]. Since then, record-ultrafast results have been demonstrated with an optically pumped MIXSEL generating picosecond pulses and more than 6 W of average power [10], with a quantum dot (QD) VECSEL generating femtosecond pulses with more than 1 W average power [11], with a MIXSEL with scalable pulserepetition rates between 5 and 100 GHz [12] and with record-low noise performance very similar to diode-pumped solid-state lasers [13]. The simple straight cavity of a MIXSEL inspired the invention of dual-comb modelocking [14] and the successful proof-of-principle demonstration of dual-comb molecular spectroscopy using only one unstabilized semiconductor laser (i.e. dual-comb MIXSEL) [5] which can be considered a paradigm shift in frequency metrology applications.

One of our research effort is focused on the optimization of ultrafast SDLs towards femtosecond high-power operation with sufficient pulse peak power to generate a coherent supercontinuum without the external pulse amplification demonstrated before [15, 16]. With SESAM-modelocked QW VECSELs we obtained pulses as short as 100-fs [17] and with QW MIXSELs as short as 184 fs [18] with an average output power around 100 mW. However ultrafast QW SDLs suffer from spectral hole burning effects [18, 19], which currently seem to limit further pulse shortening with high pulse energy. Furthermore, the high non-radiative losses reduce the carrier lifetime in the active QWs, drastically decreasing the optical-to-optical efficiency of sub-300-fs SDLs to below 1% [18]. Ultrafast SDLs based on self-assembled QDs grown by the Stranski–Krastanov (SK) method can benefit from some key advantages over QWs due to their broadband emission, temperature insensitivity and fast gain recovery [20-22]. To date SK QD VECSELs have demonstrated broadband tunability

up to 69 nm in cw operation [23] and recently achieved pulses as short as 193 fs with relatively high optical-to-optical efficiency [24]. The trade-off is that the QD areal density achievable with SK epitaxial technique is typically limited to 10^{10}-10^{11} cm^{-2} [25, 26], which results in a reduced density of states (DOS) and therefore lower available optical gain. For this reason, the highest output power reported for a QD VECSEL is limited to 8.4 W in cw operation [27].

In this paper, we want to explore the potential of sub-monolayer (SML) QDs [28] as active media for high-peak-power ultrafast SDLs. The growth of SML superlattices involves a cycled deposition of InAs submonolayers capped with few monolayers of GaAs, creating vertically correlated InAs agglomeration with typically high areal densities in the order of 1012 cm^{-2} [29]. The heterodimensional morphology of SML QDs combines the beneficial signatures of a zero-dimensional (0D) confinement such as high excitonic gain and very fast gain dynamics with the large DOS and high modal gain usually featured by 2D-confined structures [30]. In addition, the absence of a wetting layer prevents detrimental carrier trapping in states not contributing to lasing and makes SML QDs particularly suited for high-speed optoelectronic devices [31, 32]. To date, SML VECSELs were tested only in continous wave (cw) operation, where the maximum reported output power of 1.4 W was obtained at 1034 nm [33]. To our knowledge, no modelocking was ever tried with such devices.

Here, we report on a high-power SML QD VECSEL. Even if the semiconductor epitaxial layer stack is designed and optimized for ultrafast operation and not for high-power cw operation, we could demonstrate up to 11.2 W cw output power at 1028 nm - the highest output power from any QD VECSEL to date. We characterize the wavelength tunability of the device and obtain lasing operation from 1003 nm to 1050 nm, with high output powers above 1 W from 1008 nm to 1044 nm, confirming the large gain bandwidth of the structure and the high modal gain delivered by SML QDs.

However, despite the promising cw lasing performance we show here that any attempts to SESAM-modelock the SML QD VECSEL do not produce the expected better ultrafast performance. A limited-stability modelocking result is obtained only for short periods (< 5 minutes) just above

the lasing threshold, with pulses not shorter than 1.18 ps at a repetition rate of 1.65 GHz and an average output power of 84 mW. At higher pump levels the laser becomes unstable with intermittent transitions from cw modelocking to irregular spikings and multi-pulse fluctuations. This noisy behavior can be explained by the strong amplitude-phase coupling in SML QDs typically characterized by the linewidth enhancement factor (α-factor) [34, 35]. With this result we present experimental verification of theoretical predictions by models of passive modelocking in semiconductor lasers from more than 10 years ago [36]. We can justify these theoretical predictions also with our pulse formation model [37] which confirms a sudden breakup of stable cw modelocking to a chaotic behavior with increasing gain linewidth enhancement factors. This leads us to the conclusion that SML QDs are not suited for ultrafast SDLs.

3.8.2 VECSEL design, growth and characterization

The SML QD VECSEL described in this work is grown using molecular beam epitaxy (MBE) on undoped 100-oriented GaAs substrates. The VECSEL gain is optimized for lasing operation at 1030 nm. The VECSEL chip epitaxial stack (Fig. 3.38a) shows starting from the bottom the last few layers of a 23.5-pair AlAs-GaAs distributed Bragg reflector (DBR), followed by an active region featuring 10 SML QD layers embedded in pump-absorbing GaAs barriers and then finally an anti-reflection (AR) coating section. Each SML QD layer is formed by a tenfold alternate deposition of pure binary InAs and GaAs. The short superlattice period consists of nominally 0.4 monolayer (ML) InAs and 2.1 ML GaAs. A single InAs deposition stays below the critical thickness required by SK QD formation and creates islands, which are immediately buried by the GaAs spacer. The larger lattice constant of InAs compared to GaAs produces local tensile strain in the GaAs coverage where it occurs to cap an InAs island. The locally increased lattice constant facilitates the successive nucleation of the following InAs island on the same site and finally, indium segregation creates favorable conditions for a vertically correlated InGaAs non-SK QD system [38] (Fig. 3.38b). The tuning of the center emission wavelength is performed simply by adjusting the InAs deposition time, yielding to wavelength control and a robust reproducibility.

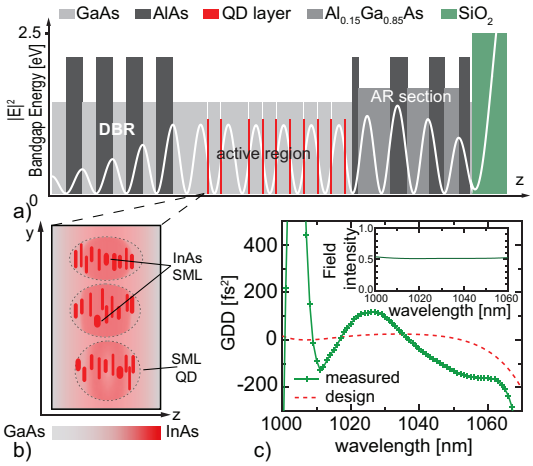

Figure 3.38: (a) SML QD VECSEL: a) Schematic of the SML VECSEL's epitaxial structure: bandgap profile and calculated electric field intensity (white). Note that only the last few layers are shown of the bottom 23.5-pair AlAs-GaAs glsDBR. b) A schematic view of a single SML-QD layer with a ten-fold InAs SML deposition (red dashes). Indium diffusion creates a vertical correlation between the SML islands and forms the SML QD (dashed ovals). c) Measured and designed dispersion of the VECSEL gain mirror. The measurement is performed at normal incidence and room temperature. Inset: designed average field intensity in the QD layers, optimized to be flat over a broad wavelength bandwidth around the lasing center wavelength to avoid structural spectral filtering.

The active SML QD layers are positioned in the middle between a node and an antinode of the standing electric field intensity wave pattern (Fig. 3.38a). The QDs are equally spaced with a $\lambda/4$ separation corresponding to 65.5 nm, with the exception of the two most distant active layers from the surface, which present on one side a $\lambda/2$ spacing layer to collect more optically generated carriers and compensate for the exponential decrease of the pump intensity. The average enhancement of the electric field intensity in the SML QDs is set to a low value of 0.5 (normalized to 4 outside the structure) and its spectral profile is designed to be flat over a ± 30 nm bandwidth around the designed center lasing wavelength (Fig. 3.38c, inset). This is not an optimized design for cw performance, where the QD layers would be placed at the antinodes of the standing wave. The epitaxial layer stack is terminated by a 3.5-pair AlAs-$Al_{0.15}Ga_{0.85}As$ AR section. This VECSEL design is particularly suited for

ultrafast operation since it prevents structural spectral filtering of the gain bandwidth and increases the gain saturation fluence with the low field intensity inside the structure.

In contrast to SK QDs but similarly to QWs, SML QDs show a non-negligible temperature dependence of the emission and absorption wavelengths [39]. Reflectivity measurements performed on the unpumped SML VECSEL at different temperatures show a thermal red-shift of ≈0.4 nm/K (Fig. 3.39a). Taking this into account, we set the peak wavelength of the room temperature photoluminescence (PL) around 1003 nm to obtain a shifted emission at ≈1030 nm for an estimated operation temperature of 90°C. A comparable analysis of the PL intensities emitted under identical experimental conditions by SML QD, QW and SK QD active test structures with similar inter-layer spacing confirms the high modal gain of SML QDs, which deliver the highest intensity (Fig. 3.39b).

The VECSEL is grown in reverse order for standard flip-chip bonding. The DBR, the AR section and an $Al_{0.85}Ga_{0.15}As$ etch stop layer are grown at 620°C, while the GaAs spacers in the active region are grown at 580°C and the SML QDs at 500°C. After growth, the chip is indium soldered onto a 5x5 mm, 1-mm thick diamond heat spreader and the GaAs substrate is removed through chemical wet etching. A single fused silica (FS) layer is then deposited with plasma enhanced chemical vapor deposition (PECVD) to finalize the AR section and obtain a minimized pump reflection at 808 nm together with a flat and low structural group delay dispersion (GDD) for short pulse generation. The difference between designed and measured GDD is explained by growth deviations from the nominal epitaxial layer thickness and deposition errors for the FS layer, estimated in ±1%. Nonetheless, we obtain a GDD profile lying in a ±150 fs^2 range for a 40-nm bandwidth centered at 1030 nm (Fig 3.38c).

The carrier lifetime in SDLs gives an important indication of the non-radiative losses and represents a crucial parameter for achieving high optical-to-optical pump efficiency in modelocked operation [40, 41]. To measure and compare the carrier lifetimes of SML QDs, SK QDs and QWs, we use a degenerate pump-probe setup with 130-fs pulses and a tunable center pump-probe wavelength, set to the respective PL-maximizing wavelengths of the analyzed gain media. Fitting the saturation recoveries with

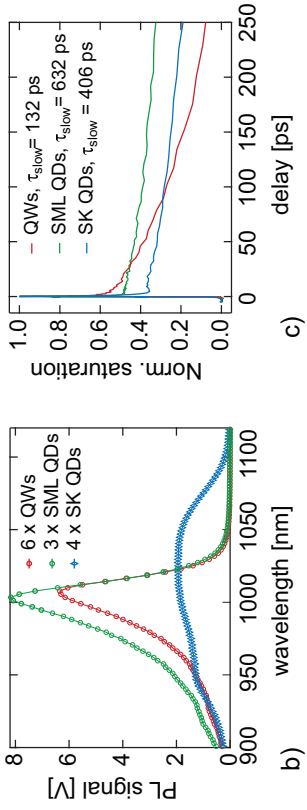

Figure 3.39: SML QD VECSEL characterization: a) Reflectivity measurements of the unpumped SML QD VECSEL at different temperatures. The absorption of the SML QDs presents a temperature dependent red-shift of 0.4 nm/K, similar to what was observed for QWs. b) Photoluminescence (PL) measurements of different active test structures based on SML QDs, QWs and SK QDs. 3 SML QD layers without strain compensation show a higher PL intensity than 6 QW layers with strain compensation and comparable full width at half maximum (FWHM) emission bandwidth (40 nm and 37 nm, respectively). SK QDs feature the lowest intensity but also the broadest bandwidth of 134 nm. c) Degenerate pump-probe measurement of a SML, QW and SK VECSEL's saturation. The pump fluence is set to 30 µJ/cm^2. QDs show a long carrier lifetime compared to QWs.

a double exponential decay, we measure a comparable fast component below 1 ps for the three different structures, whereas we remark sensible differences in the slow components of the recovery time. The QW samples exhibit a slow component of 132 ps [18], significantly shorter than the 406 ps and the 632 ps featured by the SK and SML QDs respectively. SML QDs seem then to offer decreased non-radiative losses and can potentially generate more efficient energetic short pulses.

3.8.3 Continuous wave (cw) operation

The SML QD VECSEL chip is tested in a cw straight linear cavity with just the gain mirror and a concave output coupler (OC) used as end mirrors. The chip is mounted on a water-cooled copper heatsink (HS) and pumped with a low-brightness 808-nm diode under a 45° angle. The HS temperature (T_{HS}) is Peltier-controlled and set to -10°C. No additional intracavity heat spreader is used. The OC features a radius of curvature (ROC) of 200 mm and a transmission of 1%, which delivers the best performance. The total cavity length is set to 75 mm. The focused pump spot is circular on the VECSEL surface with a 177-μm radius; the cavity mode spot size on the chip is calculated to have exactly the same radius. The laser operates in a transverse multimodal regime and the maximum output power of 11.2 W is achieved at an optical pump power on the sample of 37 W. The optical-to-optical efficiency reaches 30% at the maximum power before a thermal roll-over occurs. The slope efficiency is 39% (Fig. 3.40a). We characterize the emission wavelength tunability of the SML QD VECSEL by inserting a 1-mm thick quartz birefringent filter (BRF) at Brewster's angle inside the optical cavity (Fig. 3.40b). For this experiment, we obtain the broadest tuning range with a reduced ROC of the output coupler of 100 mm and a smaller laser spot size of 125 μm on the VECSEL. Consequently, also the pump spot size is decreased to 135 μm. To compensate for the additional loss introduced by the intracavity filter, we reduce the output coupler to 0.5%. We measure the wavelength tuning characteristics at a fix pump power of 18.2 W and a T_{HS} of 0°C. By rotation of the BRF in its surface plane, we tune the wavelength from 1003 nm to 1050 nm. The highest output power of 2.43 W is obtained at 1018 nm (Fig. 3.40b). For a 36-nm span (from 1008 nm to 1044 nm) the output power exceeds

1 W. The small signal reflectivity of the SML VECSEL is measured on small spot sizes (<20 μm) at a pump intensity of 35 kW/cm^2 and a T_{HS} of 0°C. The higher total pump power in the tuning experiment increases the temperature of the active region of ≈60°C compared to the small signal reflectivity measurements. Considering a thermal wavelength shift of 24 nm, the spectral gain overlaps with the tuning curve in Fig. 3.40b.

3.8.4 Noisy modelocking operation

The cavity configuration is changed to a standard V-shape for the pulsed experiments. The VECSEL chip is used as the folding mirror, while a SESAM and the curved OC serve as folding mirrors. The MBE-grown SESAM consists of a single InGaAs QW absorber embedded in AlAs barriers on top of a 30-pair GaAs/AlAs DBR. A final $\lambda/4$ silicon nitride (Si_3N_4) layer is deposited to increase the field intensity inside the semiconductor. At 1034 nm and 30°C of heat sink temperature, the measured SESAM saturation fluence is 5.2 μJ/cm^2 and the modulation depth is 1.7%. For the OC we choose a transmission of 0.5% and a ROC of 100 mm. The pump spot on the chip's surface is set to 177 μm and the laser mode radius is kept slightly larger (182 μm) to assure single mode operation. For a stronger absorber saturation, the laser spot on the SESAM is focused to a radius of 93 μm. The angle between the two cavity legs is set to 20°; the distances OC-VECSEL and VECSEL-SESAM are almost balanced and set to 47 mm and 44 mm respectively. A 1-mm thick wedged intracavity Brewster plate is inserted to obtain a single polarization output.

For a T_{HS} of 0°C and a SESAM temperature stabilized to 28°C, we obtain laser light from the VECSEL at 15.3 W of optical pump power. The laser starts in pulsed operation and just above threshold, for 15.8 W of pump power and 84 mW of average output power, we obtain unstable modelocking (unstable ML) which still reveals a rather clean autocorrelation. However, a more careful characterization with a microwave spectrum analyzer clearly reveals the unstable pulsed behavior. The non-collinear second harmonic generation (SHG) autocorrelation (AC) trace is pedestal-free and can be fitted by a sech^2 shape with a pulse duration of 1.18 ps (Fig. 3.41a). The optical spectrum is centered at 1035 nm and, even if not sech^2-shaped, presents a regular and smooth profile, except for some

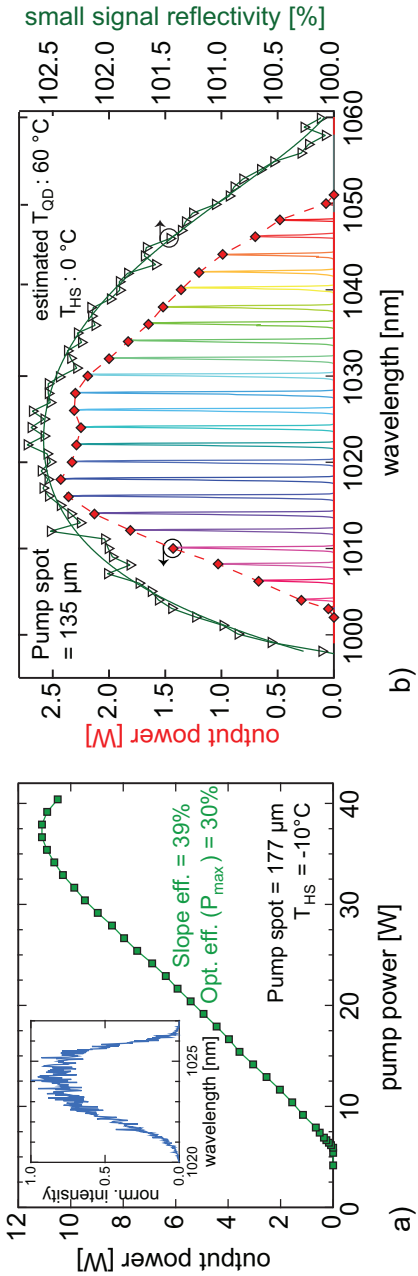

Figure 3.40: Continous wave (cw) performance of the SML QD VECSEL: a) average output power versus optical pump power characteristic of the SML QD VECSEL at a heatsink temperature of -10°C. Inset: optical spectrum at 8.5 W of output power. b) Wavelength tuning characteristic obtained at a constant pump power of 18.2 W, with a wavelength tuning range of 47 nm and 2.43 W of maximum output power at 1018 nm. The measured spectral gain follows the experimental output power profile if a 24-nm red-shift is taken into account ($\Delta T \approx 60$°C). The measured spectra are shown in rainbow colors, scaled to the respective average output power.

noisy fringes close to the peak intensity (Fig. 3.41b). The microwave spectrum features a strong peak corresponding to the fundamental pulse repetition rate of 1.65 GHz, with a high signal-to-noise ratio (SNR) close to 70 dB (Fig. 3.41c).

Nevertheless, small side peaks appear as an indication of a not clean modelocking. The high harmonics of the fundamental pulse repetition rate are all present with almost equal power (Fig. 3.41c, inset).

In contrast to what has been reported for ultrafast QW SDLs, where increasing the pump power allowed for the transition from strong pulsations to clean modelocking [42], we observe here that at higher pump levels we obtain chaotic operation without ever reaching a stable modelocking situation.

In Fig. 3.42, we present the diagnostics of the SML QD VECSEL recorded for 4 different pump powers of 17.2 W, 18.2 W, 20.6 W and 27.6 W. As the pump power increases, the non-collinear SHG ACs cannot be fitted anymore to a sech^2 shape. The traces assume a triangular profile with enlarging temporal width and an increasing number of noise spikes. This indicates multiple pulsations rising temporally close to each other. The optical spectra move toward longer wavelengths as a consequence of the increased thermal load. In addition, the spectral profiles become uneven, with irregular peaks. Finally, also the peaks on the sides of the fundamental repetition rate in the microwave spectrum grow in intensity; already at 17.2 W of pump power, they appear as non-resolved noise sidebands, suggesting the generation of many pulsations with unstable repetition rates. At 27.6 W of pump power, the intense noise sidebands span over 1 MHz. In the four configurations presented, the average output power rises up to a maximum of 275 mW for a pump power of 27.6 W and an optical-to-optical efficiency of 1%. At higher pump levels, the output power decreases and the laser operation stops without having reached stable modelocking.

3.8.5 Simulation

Semiconductor gain media show significant refractive index changes after an optical perturbation, usually referred to as amplitude-phase coupling. This effect is commonly quantified through the linewidth enhancement

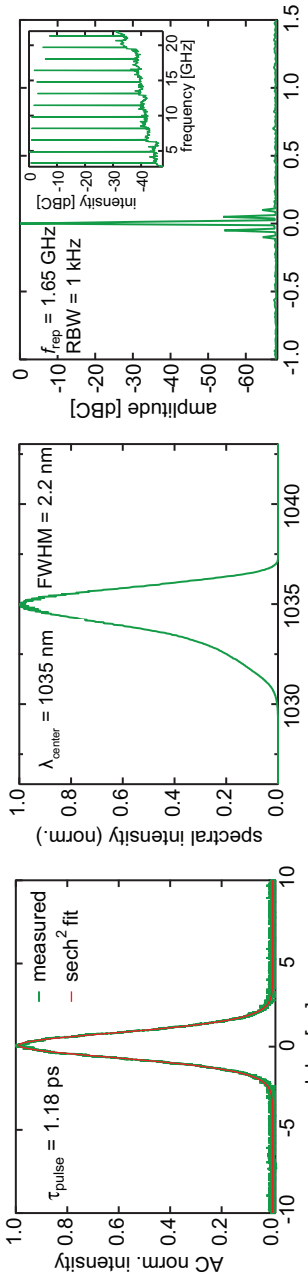

Figure 3.41: Ultrafast SML QD VECSEL at low power with unstable modelocking: pulse diagnostics of the SML QD VECSEL pumped with 15.8 W of optical power, just above the lasing threshold of around ≈15.3 W. We define this mode of operation as unstable modelocking. a) The non-collinear SHG autocorrelation (AC) trace can be fitted to a sech^2 pulse shape with a pulse duration of 1.18 ps. b) The optical spectrum is relatively smooth, except for weak noise fringes close to the intensity maximum. c) The microwave spectrum, recorded with a resolution bandwidth (RBW) of 1 kHz, features a high signal-to-noise ratio close to 70 dB in correspondence of the fundamental pulse repetition rate of 1.65 GHz but we clearly can observe the presence of side peaks. Inset: long span of the microwave spectrum (resolution bandwidth of 300 kHz) showing that all the harmonics of the pulse repetition rate are present with almost equal power.

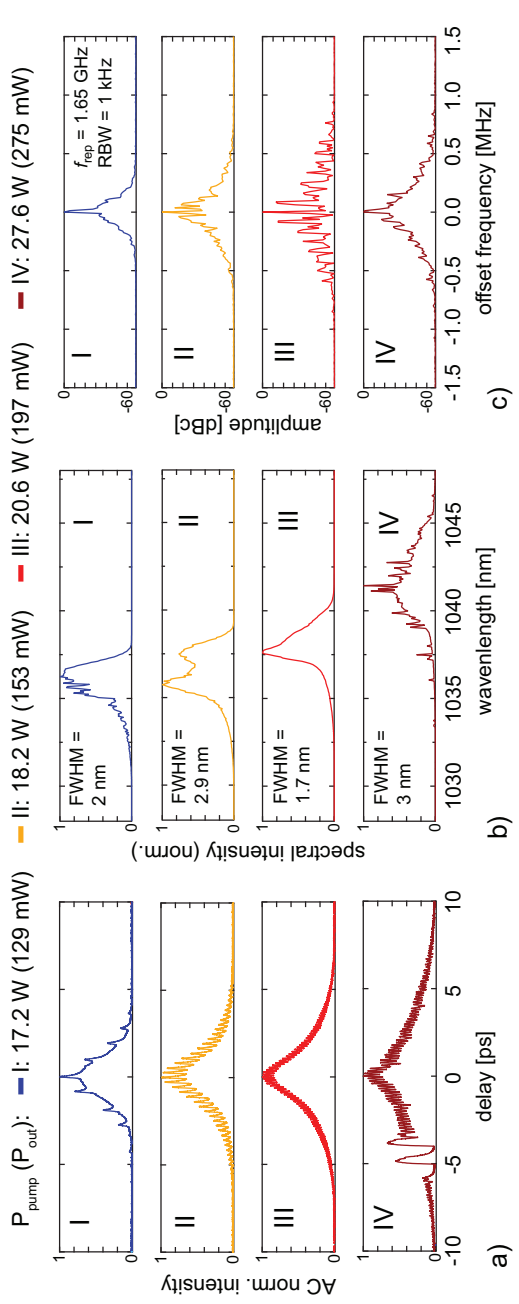

Figure 3.42: Ultrafast SML QD VECSEL with increasing pump power: recorded pulse diagnostics for optical pump powers of I→17.2 W; II→18.2 W; III→20.6 W; IV→27.6 W. a) Non-collinear SHG AC traces. As the pump power increases, the traces lose the sech^2 shape and indicate increasing multiple pulsations. b) For an increasing pump level the optical spectra shift towards longer wavelengths and assume irregular spiky shapes. c) Microwave spectra. At higher pump powers, the side peaks next to the fundamental pulse repetition rate increase their amplitude and cannot be singularly resolved anymore, finally giving raise to strong and broad noise sidebands.

factor α, defined as:

$$\alpha = -\frac{4\pi}{\lambda}\frac{dn/dN}{dg/dN} \tag{3.14}$$

where n is the refractive index, g is the gain per unit length, λ is the wavelength and N is the carrier density. Confined structures normally show lower α values due to a clear energetic separation between the active states and their carrier reservoir.

In SML QDs, the coexistence of 0D and 2D confinement has recently been shown [30]. The heavier holes are better confined in the In-rich islands, while the electron wavefunction sees only the lateral InGaAs QW barriers and is delocalized over several InAs agglomerations. This limited confinement in combination with the high areal densities of localization centers enhances a strong interdot coupling in contrast to SK QDs [43]. Furthermore the efficient lateral coupling with an optically inactive but fast accessible carrier reservoir can provide a very fast gain recovery but can also induce significant refractive index changes after an optical excitation [44]. Recent measurements revealed linewidth enhancement factors for SML QDs up to one order of magnitude higher compared to SK QDs and QWs [34].The numerical model for passive modelocking in SDLs developed by Vladimirov *et al.* [36] states that if the linewidth enhancement factor of the gain α_g exceeds the one of the absorber α_a, the modelocking becomes unstable and chaotic. The parameter space explored in Ref. [36] tells that the most stable operation with the highest pulse peak powers and shortest pulse durations can be achieved in the case of $\alpha_g = \alpha_a$. However, also in this optimal configuration with a large amplitude-phase coupling the modelocking breaks up again into a chaotic behavior.

We use our pulse formation model where the pulse is represented by an electric field using the slowly varying envelope approximation (SVEA). We typically start from a 10 nW noise floor and stop when we obtain a numerically stable pulse propagating through the cavity or we recognize an instability. The different intracavity elements are described by numerical operators either in the time or in the frequency domain also using measurable macroscopic input parameters such as small signal gain, gain bandwidth, GDD profile and saturation fluences as described in [37,45].

Previous theoretical investigations by Lingnau *et al.* reported on the failure of the α factor describing dynamical instabilities in SK QD lasers

[46]. Later publications by Lingnau *et al.* concluded, however, that for fast carrier scattering the QD laser behavior can be reasonably well characterized by an α factor [47]. Furthermore, again Herzog, Lingnau *et al.* used the α factor concept to describe the amplitude-phase coupling in SML QDs [34]. For these reasons, we also use the α factor for our description of the carrier induced refractive index changes.

We consider that the amplitude-phase coupling strongly depends on the amount of optically injected carriers [48, 49]. Therefore, we set α as a free parameter and increase the strength of the amplitude-phase coupling for higher pump powers. The other simulation parameters for the cavity, VECSEL and SESAM are listed in Table 3.3; the simulation results are depicted in Fig. 3.43. We indeed can confirm with our simulation the stability break-up of the ML state by increasing the linewidth enhancement factor in the gain (Fig. 3.43a).

The α-values are fitted to obtain a good match of the simulation outputs with the experimental data. For an initial α-factor of 9, we still obtain a stable solution with a pulse duration that overlaps with the AC measured for the unstable-ML state (Fig. 3.43b and Fig. 3.41). At α_g = 13, we observe a transition to a regime of quasi-periodic intensity fluctuations. The averaged AC computed from the simulation matches with the state II experimentally measured in the SML VECSEL cavity (Fig. 3.42).

A more pronounced effect is produced with α_g = 15: a chaotic pattern of intensity oscillations occurs, with intermittent buildup and breakup phases of the main pulse. This regime gives an output, which is comparable in terms of AC observed in the SML VECSEL for 20.6 W of pump power (state III in Fig. 3.42).

Finally, we set α_g = 16 which results in a fully chaotic regime with unstable spikings. The simulated averaged AC output is similar to what was observed for 27.6 W of pump power in state IV in Fig. 3.42.

The estimated α-values between 9 and 16 are significantly higher compared to the α-range assumed for SK QDs and QWs (normally between 2 and 10 [50-52]). They are consistent with the directly measured values reported in [34] for optical semiconductor amplifiers based on SML QDs.

Table 3.3: List of input parameters used for the pulse formation simulation. The input parameters in italic are not directly measured. The SML QD VECSEL saturation fluence is assumed to be comparable to similar QW-based structures [17]. The positive GDD is obtained from the intracavity Brewster's plate. The gain FWHM used in the simulation is deduced from the output spectra measured in pulsed operation. The SESAM recovery time is defined as the time necessary to reach $1/e$ of the normalized saturation.

Cavity		**VECSEL**		**SESAM**	
Other losses	0.8%	Recovery time	3 ns	Recovery time	1.5-2 ps
Repetition rate	1.65 GHz	α_g	9-17	α_a	2
λ_{center}	1035 nm	Small signal gain	2.9%	Modulation depth	1.8%
GDD	50 fs^2	Gain FWHM	5 nm		
TOD	-2000 fs^2	Beam radius	170-180 μm	Beam radius	80-100 μm

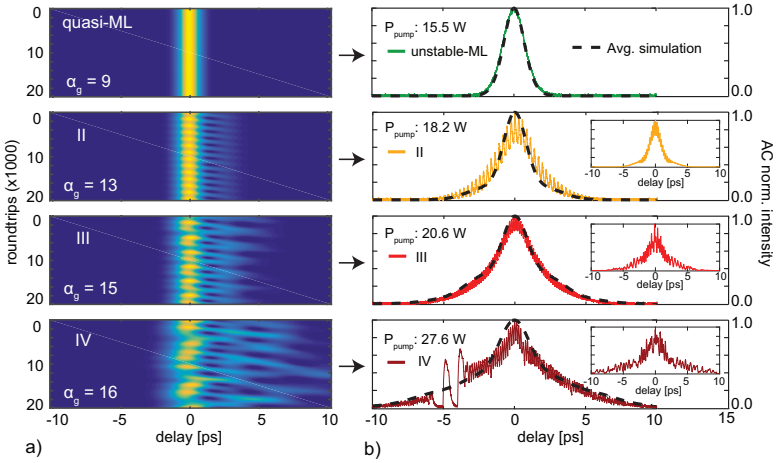

Figure 3.43: Simulation of the modelocking instabilities with an increasing amplitude-phase coupling in the gain chip. a) Simulation of the electric field intensity over 20'000 roundtrips with increasing α_g (color code: yellow→max intensity, blue→zero intensity). b) Comparison between the measured and the simulated autocorrelation (AC) traces. The simulated ACs are centered to delay = 0. Dashed black line: simulated AC averaged over 20'000 roundtrips. Insets: simulated ACs calculated to reproduce the experimental results shown in Fig. 3.41 and 3.42. The variable delay line leads to a binning of the time delay axis and to oscillating fringes in the experimental traces in case of strong intensity fluctuations. The experimental oscillations are qualitatively reproduced by the simulation.

3.8.6 Conclusions

In this work, we tested the potential of SML QDs as active gain media for ultrafast SDLs. In particular, we wanted to take advantage from the high modal gain of SML QDs for efficient generation of energetic ultrashort pulses. Therefore, we grew a VECSEL chip with 10 SML QD gain layers. This VECSEL structure was designed and optimized to produce fs-pulses at 1030 nm. Tests performed in cw confirmed the excellent gain properties of QD grown following the SML technique compared to other epitaxial methods for QD formation. We obtained the highest average output power of 11.2 W ever generated from a QD-based SDLs. To confirm the large gain bandwidth necessary for short pulse duration, we used the VECSEL as a high-power tunable cw source obtaining lasing operation over 47 nm.

In a second experiment, we inserted a SESAM in the optical cavity to

passively modelock the SML QD VECSEL. In this configuration we did not obtain a regime of stable fundamental modelocking. We observed strong instabilities that prevented the formation of short femtosecond pulses and showed clear symptoms of chaotic multiple pulsations appearing already at pump levels slightly above the lasing threshold. We took into account the recent research on the strong amplitude-phase coupling shown by SML QDs and simulated the output of the unstable ultrafast SML QD VECSEL with a pulse formation model based on measurable macroscopic input parameters such as small signal gain, gain bandwidth, GDD profile and saturation fluences. We observed that the intrinsically large α-value for SML QDs can prevent the formation of a stable modelocked solutions in the laser cavity, as predicted by other theories [36]. In addition, by fitting the simulated results with the experimental traces, we could confirm that the modelocking instabilities can be related to an increase of the linewidth enhancement factor at higher injections of optically generated carriers. With our results we confirm the great benefits of optically pumped SML QD VECSELs for high power cw outputs and large wavelength tuning. On the other side, we recognize that due to intrinsic physical properties connected to the growth method, SML QDs are not suited for stable modelocking.

Acknowledgement The authors acknowledge support of the technology and cleanroom facility FIRST of ETH Zurich for advanced micro- and nanotechnology. They also thank Dr. Benjamin Lingnau from the *Institut für Theoretische Physik, TU Berlin*, for the fruitful discussions. The authors acknowledge funding within the D-A-CH program with the QD-MIXSEL project, which was scientifically evaluated by the Swiss National Science Foundation (SNSF) and the Deutsche Physikalische Gesellschaft (DPG).

3.8.7 References

[1] M. Guina, A. Rantamäki, and A. Härkönen, "Optically pumped VECSELs: review of technology and progress," J. Phys. D: Appl. Phys. 50, 383001 (2017).

[2] B. W. Tilma, M. Mangold, C. A. Zaugg, S. M. Link, D. Waldburger, A. Klenner, A. S. Mayer, E. Gini, M. Golling, and U. Keller, "Recent advances in ultrafast semiconductor disk lasers," Light Sci. Appl. 4 (2015).

[3] U. Keller and A. C. Tropper, "Passively modelocked surface-emitting semiconductor lasers," Phys. Rep. 429, 67-120 (2006).

[4] D. J. H. C. Maas, A.-R. Bellancourt, B. Rudin, M. Golling, H. J. Unold, T. Südmeyer, and U. Keller, "Vertical integration of ultrafast semiconductor lasers," Appl. Phys. B 88, 493-497 (2007).

[5] S. M. Link, D. J. H. C. Maas, D. Waldburger, and U. Keller, "Dual-comb spectroscopy of water vapor with a free-running semiconductor disk laser," Science 356, 1164-1168 (2017).

[6] F. F. Voigt, F. Emaury, P. Bethge, D. Waldburger, S. M. Link, S. Carta, A. v. d. Bourg, F. Helmchen, and U. Keller, "Multiphoton in vivo imaging with a femtosecond semiconductor disk laser," Biomed. Opt. Express 8, 3213-3231 (2017).

[7] B. Heinen, T. L. Wang, M. Sparenberg, A. Weber, B. Kunert, J. Hader, S. W. Koch, J. V. Moloney, M. Koch, and W. Stolz, "106 W continuous-wave output power from vertical-external-cavity surface-emitting laser," Electron. Lett. 48, 516-517 (2012).

[8] U. Keller, K. J. Weingarten, F. X. Kärtner, D. Kopf, B. Braun, I. D. Jung, R. Fluck, C. Hönninger, N. Matuschek, and J. Aus der Au, "Semiconductor saturable absorber mirrors (SESAMs) for femtosecond to nanosecond pulse generation in solid-state lasers," IEEE J. Sel. Top. Quantum Electron. 2, 435-453 (1996).

[9] S. Hoogland, S. Dhanjal, A. C. Tropper, S. J. Roberts, R. Häring, R. Paschotta, and U. Keller, "Passively modelocked diode-pumped surface-emitting semiconductor laser," IEEE Photon. Technol. Lett. 12, 1135-1138 (2000).

[10] B. Rudin, V. J. Wittwer, D. J. H. C. Maas, M. Hoffmann, O. D. Sieber, Y. Barbarin, M. Golling, T. Südmeyer, and U. Keller, "High-power MIXSEL: an integrated ultrafast semiconductor laser with 6.4 W average power," Opt. Express 18, 27582-27588 (2010).

[11] M. Hoffmann, O. D. Sieber, V. J. Wittwer, I. L. Krestnikov, D. A. Livshits, Y. Barbarin, T. Südmeyer, and U. Keller, "Femtosecond high-power quantum dot vertical external cavity surface emitting laser," Opt. Express 19, 8108-8116 (2011).

[12] M. Mangold, C. A. Zaugg, S. M. Link, M. Golling, B. W. Tilma, and U. Keller, "Pulse repetition rate scaling from 5 GHz to 100 GHz with a high-power semiconductor disk laser," Opt. Express 22, 6099-6107 (2014).

[13] M. Mangold, S. M. Link, A. Klenner, C. A. Zaugg, M. Golling, B. W. Tilma, and U. Keller, "Amplitude noise and timing jitter characterization of a high-power modelocked integrated external-cavity surface emitting laser," IEEE Photon. J. 6, 1-9 (2014).

[14] S. M. Link, A. Klenner, M. Mangold, C. A. Zaugg, M. Golling, B. W. Tilma, and U. Keller, "Dual-comb modelocked laser," Opt. Express 23, 5521-5531 (2015).

[15] N. Jornod, K. Gürel, V. J. Wittwer, P. Brochard, S. Hakobyan, S. Schilt, D. Waldburger, U. Keller, and T. Südmeyer, "Carrier-envelope offset frequency stabilization of a gigahertz semiconductor disk laser," Optica 4, 1482-1487 (2017).

[16] C. A. Zaugg, A. Klenner, M. Mangold, A. S. Mayer, S. M. Link, F. Emaury, M. Golling, E. Gini, C. J. Saraceno, B. W. Tilma, and U. Keller, "Gigahertz self-referencable frequency comb from a semiconductor disk laser," Opt. Express 22, 16445-16455 (2014).

[17] D. Waldburger, S. M. Link, M. Mangold, C. G. E. Alfieri, E. Gini, M. Golling, B. W. Tilma, and U. Keller, "Highpower 100 fs semiconductor disk lasers," Optica 3, 844-852 (2016).

[18] C. G. E. Alfieri, D. Waldburger, S. M. Link, E. Gini, M. Golling, G. Eisenstein, and U. Keller, "Optical efficiency and gain dynamics of modelocked semiconductor disk lasers," Opt. Express 25, 6402-6420 (2017).

[19] I. Kilen, J. Hader, J. V. Moloney, and S. W. Koch, "Ultrafast nonequilibrium carrier dynamics in semiconductor laser mode locking," Optica 1, 192-197 (2014).

[20] D. Bimberg, N. Kirstaedter, and N. N. Ledentsov, "InGaAs-GaAs quantum-dot lasers," IIEEE J. Sel. Top. Quantum Electron. 3, 196-205 (1997).

[21] T. W. Berg and J. Mork, "Saturation and noise properties of quantum-dot optical amplifiers," IEEE J. Quantum Electron. 40, 1527-1539 (2004).

[22] J. Gomis-Bresco, S. Dommers, V. V. Temnov, U. Woggon, M. Laemmlin, D. Bimberg, E. Malic, M. Richter, E. Schöll, and A. Knorr, "Impact of Coulomb Scattering on the Ultrafast Gain Recovery in InGaAs Quantum Dots," Phys. Rev. Lett. 101, 256803 (2008).

[23] M. Butkus, J. Rautiainen, O. G. Okhotnikov, C. J. Hamilton, G. P. A. Malcolm, S. S. Mikhrin, I. L. Krestnikov, D. A. Livshits, and E. U. Rafailov, "Quantum Dot Based Semiconductor Disk Lasers for 1–1.3 μm," IEEE J. Sel. Top. Quantum Electron. 17, 176-1771 (2011).

[24] C. G. E. Alfieri, D. Waldburger, M. Golling, and U. Keller, "High-Power Sub-300-Femtosecond Quantum Dot Semiconductor Disk Lasers," IEEE Photon. Technol. Lett. 30, 525-528 (2018).

[25] N. A. Cherkashin, M. V. Maksimov, A. G. Makarov, V. A. Shchukin, V. M. Ustinov, N. V. Lukovskaya, Y. G. Musikhin, G. E. Cirlin, N. A. Bert, Z. I. Alferov, N. N. Ledentsov, and D. Bimberg, "Control over the parameters of InAs-GaAs quantum dot arrays in the Stranski-Krastanow growth mode," Semiconductors 37, 861-865 (2003).

[26] S. Gaan, G. He, R. M. Feenstra, J. Walker, and E. Towe, "Size, shape, composition, and electronic properties of InAs/GaAs quantum dots by scanning tunneling microscopy and spectroscopy," J. Appl. Phys. 108, 114315 (2010).

[27] D. A. Nakdali, M. K. Shakfa, M. Gaafar, M. Butkus, K. A. Fedorova, M. Zulonas, M. Wichmann, F. Zhang, B. Heinen, A. Rahimi-Iman, W. Stolz, E. U. Rafailov, and M. Koch, "High-Power Quantum-Dot Vertical-External-Cavity Surface-Emitting Laser Exceeding 8 W," IEEE Photon. Technol. Lett. 26, 1561-1564 (2014).

[28] S. Krishna, D. Zhu, J. Xu, K. K. Linder, O. Qasaimeh, P. Bhattacharya, and D. L. Huffaker, "Structural and luminescence characteristics of cycled submonolayerInAs/GaAs quantum dots with room-temperature emission at 1.3 μm," J. Appl. Phys. 86, 6135-6138 (1999).

[29] A. Lenz, H. Eisele, J. Becker, J.-H. Schulze, T. D. Germann, F. Luckert, K. Pötschke, E. Lenz, L. Ivanova, A. Strittmatter, D. Bimberg, U. W. Pohl, and M. Dähne, "Atomic structure and optical properties of InAs submonolayer depositions in GaAs," Journal of Vacuum Science & Technology B, Nanotechnology and Microelectronics: Materials, Processing, Measurement, and Phenomena 29, 04D104 (2011).

[30] S. Harrison, M. P. Young, P. D. Hodgson, R. J. Young, M. Hayne, L. Danos, A. Schliwa, A. Strittmatter, A. Lenz, H. Eisele, U. W. Pohl, and D. Bimberg, "Heterodimensional charge-carrier confinement in stacked submonolayer InAs in GaAs," Phys. Rev. B 93, 085302 (2016). [31

[31] F. Hopfer, A. Mutig, G. Fiol, M. Kuntz, V. A. Shchukin, V. A. Haisler, T. Warming, E. Stock, S. S. Mikhrin, I. L. Krestnikov, D. A. Livshits, A. R. Kovsh, C. Bornholdt, A. Lenz, H. Eisele, M. Dahne, N. N. Ledentsov, and D. Bimberg, "20 Gb/s 85°C Error-Free Operation of VCSELs Based on Submonolayer Deposition of Quantum Dots," IEEE J. Sel. Top. Quantum Electron. 13, 1302-1308 (2007).

[32] N. N. Ledentsov, D. Bimberg, F. Hopfer, A. Mutig, V. A. Shchukin, A. V. Savel'ev, G. Fiol, E. Stock, H. Eisele, M. Dähne, D. Gerthsen, U. Fischer, D. Litvinov, A. Rosenauer, S. S. Mikhrin, A. R. Kovsh, N. D. Zakharov, and P. Werner, "Submonolayer Quantum Dots for High Speed Surface Emitting Lasers," Nanoscale Res. Lett. 2, 417-429 (2007).

[33] T. D. Germann, A. Strittmatter, J. Pohl, U. W. Pohl, D. Bimberg, J. Rautiainen, M. Guina, and O. G. Okhotnikov, "High-power semiconductor disk laser based on InAs/GaAs submonolayer quantum dots," Appl. Phys. Lett. 92, 101123 (2008).

[34] B. Herzog, B. Lingnau, M. Kolarczik, Y. Kaptan, D. Bimberg, A. Maaßdorf, U. W. Pohl, R. Rosales, J.-H. Schulze, A. Strittmatter, M. Weyers, U. Woggon, K.

Lüdge, and N. Owschimikow, "Strong amplitude-phase coupling in submonolayer quantum dots," Appl. Phys. Lett. 109, 201102 (2016).

[35] B. Lingnau, K. Lüdge, B. Herzog, M. Kolarczik, Y. Kaptan, U. Woggon, and N. Owschimikow, "Ultrafast gain recovery and large nonlinear optical response in submonolayer quantum dots," Phys. Rev. B 94, 014305 (2016).

[36] A. G. Vladimirov and D. Turaev, "Model for passive mode locking in semiconductor lasers," Phys. Rev. A 72, 033808 (2005).

[37] O. D. Sieber, M. Hoffmann, V. J. Wittwer, M. Mangold, M. Golling, B. W. Tilma, T. Südmeyer, and U. Keller, "Experimentally verified pulse formation model for high-power femtosecond VECSELs," Appl. Phys. B 113, 133-145 (2013).

[38] V. A. Shchukin, D. Bimberg, V. G. Malyshkin, and N. N. Ledentsov, "Vertical correlations and anticorrelations in multisheet arrays of two-dimensional islands," Phys. Rev. B 57, 12262-12274 (1998).

[39] D. Arsenijevic, C. Liu, A. Payusov, M. Stubenrauch, and D. Bimberg, "Temperature-Dependent Characteristics of Single-Mode InAs Submonolayer Quantum-Dot Lasers," IEEE Photon. Technol. Lett. 24, 906-908 (2012).

[40] A. Laurain, J. Hader, Y.-Y. Lai, T.-L. Wang, M. Yarborough, G. Balakrishnan, T. J. Rotter, P. Ahirwar, and J. V. Moloney, "Influence of non-radiative carrier losses on pulsed and continuous VECSEL performance," in SPIE LASE, (SPIE, 2012), 8242.

[41] M. M. Karow, N. N. Faleev, A. Maros, and C. B. Honsberg, "Defect Creation in InGaAs/GaAs Multiple Quantum Wells – II. Optical Properties," J. Cryst. Growth 425, 49-53 (2015).

[42] M. Mangold, M. Golling, E. Gini, B. W. Tilma, and U. Keller, "Sub-300-femtosecond operation from a MIXSEL," Opt. Express 23(2015).

[43] B. Lingnau, B. Herzog, M. Kolarczik, U. Woggon, K. Lüdge, and N. Owschimikow, "Dynamic phase response and amplitude-phase coupling of self-assembled semiconductor quantum dots," Appl. Phys. Lett. 110, 241102 (2017).

[44] B. Herzog, N. Owschimikow, J.-H. Schulze, R. Rosales, Y. Kaptan, M. Kolarczik, T. Switaiski, A. Strittmatter, D. Bimberg, U. W. Pohl, and U. Woggon, "Fast gain and phase recovery of semiconductor optical amplifiers based on submonolayer quantum dots," Appl. Phys. Lett. 107, 201102 (2015).

[45] R. Paschotta, R. Häring, U. Keller, A. Garnache, S. Hoogland, and A. C. Tropper, "Soliton-like pulse-shaping mechanism in passively mode-locked surface-emitting semiconductor lasers," Appl. Phys. B 75, 445-451 (2002).

[46] B. Lingnau, K. Lüdge, W. W. Chow, and E. Schöll, "Failure of the α factor in describing dynamical instabilities and chaos in quantum-dot lasers," Phys. Rev. E 86, 065201 (2012).

[47] B. Lingnau, W. W. Chow, and K. Lüdge, "Amplitude-phase coupling and chirp in quantum-dot lasers: influence of charge carrier scattering dynamics," Opt. Express 22, 4867-4879 (2014).

[48] F. Grillot, B. Dagens, J. G. Provost, H. Su, and L. F. Lester, "Gain Compression and Above-Threshold Linewidth Enhancement Factor in 1.3 μm InAs-GaAs Quantum-Dot Lasers," IEEE J. Quantum Electron. 44, 946-951 (2008).

[49] S. Melnik, G. Huyet, and A. V. Uskov, "The linewidth enhancement factor α of quantum dot semiconductor lasers," Opt. Express 14, 2950-2955 (2006).

[50] T. C. Newell, D. J. Bossert, A. Stintz, B. Fuchs, K. J. Malloy, and L. F. Lester, "Gain and linewidth enhancement factor in InAs quantum-dot laser diodes," IEEE Photo. Technol. Lett. 11, 1527-1529 (1999).

[51] T. Ohtoshi and N. Chinone, "Linewidth enhancement factor in strained quantum well lasers," IEEE Photon. Technol. Lett. 1, 117-119 (1989).

[52] A. A. Ukhanov, A. Stintz, P. G. Eliseev, and K. J. Malloy, "Comparison of the carrier induced refractive index, gain, and linewidth enhancement factor in quantum dot and quantum well lasers," Appl. Phys. Lett. 84, 1058-1060 (2004).

Chapter 4

Optical frequency comb stabilization

In this chapter, we describe how we were able to fully stabilize the OFC of an ultrafast SDL in a self-referenced way without external pulse amplification or compression. For this achievement, we combined major advances in two fields: the development of the ultrafast 100 fs SESAM-modelocked VECSEL with 1-kilowatt pulse peak power (section 3.5) and a customized Si_3N_4 waveguide for efficient SCG, provided by the group of Prof. Alexander L. Gaeta and Prof. Michal Lipson from Columbia University. The details are presented in the following journal publication in preparation:

Title: "Tightly locked optical frequency comb from a semiconductor disk laser"

Journal: submitted to *Optica*

4.1 Tightly locked optical frequency comb from a semiconductor disk laser

Dominik Waldburger[1], *Aline S. Mayer*[1], *Cesare G. E. Alfieri*[1], *Jacob Nürnberg,*[1], *Adrea R. Johnson*[2,3], *Xingchen Ji*[4,5], *Alexander Klenner*[2], *Yoshitomo Okawachi*[2], *Michal Lipson*[4], *Alexander L. Gaeta*[2], *and Ursula Keller*[1]

[1]Department of Physics, Institute for Quantum Electronics, ETH Zürich, Auguste-Piccard-Hof 1, 8093 Zürich, Switzerland

[2]Department of Applied Physics and Applied Mathematics, Columbia University, New York, New York 10027, United States

[3]School of Applied and Engineering Physics, Cornell University, Ithaca, New York 14853, United States

[4]Department of Electrical Engineering, Columbia University, New York, New York 10027, United States

[5]School of Electrical and Computer Engineering, Cornell University, Ithaca, New York 1485, United States

Optically pumped semiconductor disk lasers (SDLs) provide excellent beam quality and large flexibility to cover wavelengths from the UV to the mid-IR. Ultrafast SDLs which are passively modelocked using semiconductor saturable absorber mirrors (SESAMs) can generate optical frequency combs (OFCs) with gigahertz line spacings - a regime where solid-state and fiber lasers struggle with geometrical and Q-switching limitations. To date the low peak power of ultrafast SDLs did not allow for full comb stabilization without external amplification. Here we solved this challenge with a new generation of silicon nitride (Si_3N_4) waveguides for highly-efficient supercontinuum generation. Only 17 pJ of pulse energy coupled into the waveguide was required using 122-fs-pulses from a SESAM-modelocked vertical external-cavity surface-emitting laser (VECSEL). We fully stabilized both the frequency comb spacing and the offset with the self-referencing f-to-$2f$ technique without any optical amplification and with an overall noise performance that is competitive with other gigahertz OFC sources.

Optically pumped SDLs have demonstrated significant progress during the past decade[1], both for continuous wave[2] and modelocked[3,4] operation. Compared to solid-state lasers with upper-state lifetimes of up to milliseconds, the carrier lifetime of SDLs only amounts to a few hundreds of picoseconds[5]. Modelocked SDLs are thus naturally suited to operate at (multi)-gigahertz pulse repetition rates, since the short lifetime combined with a large gain cross section prevents the build-up of Q-switching instabilities[6]. High repetition rate SESAM-modelocked solid-state lasers on the other hand require supplementary measures to prevent Q-switching such as for example advanced cavity designs[7] or additional intracavity nonlinear components[8]. Pulse repetition rates in the gigahertz regime are particularly interesting for applications such as ultrastable microwave generation[9] and photonic computing[10]. The resulting large comb line spacing allows for easier access to individual lines and results in more power per comb line for the same average power. These features are particularly useful for instance to calibrate astronomical spectrographs[11], generate arbitrary waveforms[12] or to perform comb line resolved spectroscopy[13–15].

In order to obtain a fully stable OFC, both the line spacing (given by the pulse repetition rate f_{rep}) and the carrier envelope-offset (CEO) frequency f_{CEO} have to be detected and actively controlled[16–18]. Extremely low noise of f_{rep} has been demonstrated with ultrafast SDLs[19], but their f_{CEO} has remained an inaccessible parameter for a long time. The combination of high repetition rates, moderate average output powers in the 100 mW-range, and pulse durations of several hundred femtoseconds prevented octave-spanning supercontinuum generation (SCG) in commercial photonic crystal fibers[20] and therefore self-referenced f_{CEO} detection using f-to-2f interferometry[16]. Thus, more complex setups including external pulse amplification and compression were necessary to reach the required pulse parameter regime with sub-100-fs duration and multi-kilowatt peak power, leading to the first self-referenced f_{CEO} detection[21] and f_{CEO} stabilization[22] of an ultrafast SDL.

Here, we present for the first time a fully stabilized, self-referenced SDL comb with excellent noise properties which does not require additional pulse amplification or pulse compression. This result became possible

with two major advances: the development of an ultrafast SDL approaching the kilowatt peak power regime with near 100-fs pulse durations[3] and a Si_3N_4 waveguide[23–25] with a novel design that supports coherent octave-spanning SCG with much lower pulse energy and comparatively long pulse durations.

The VECSEL used in this experiment operates with 122-fs-pulses at a pulse repetition rate of 1.6 GHz. Up to 160 mW of average output power have been achieved at a center wavelength of 1025 nm (see Methods). The Si_3N_4 waveguide has been optimized to handle the comparatively low peak power and long pulses of the SDL. It features two zero-dispersion crossings on either side of the anomalous group-velocity dispersion region that is centered around the pump wavelength (Fig. 4.1b). The new type of waveguide design enables the generation of two dispersive waves one octave apart. Instead of aiming for a spectrally flat supercontinuum (SC), the novel design focusses on transferring more spectral power into these dispersive waves. Hence, only $\approx$ 17 pJ of coupled pulse energy is needed to generate a coherent octave-spanning SC suitable for f-to-2f interferometry. This is a factor of two less than in previous Si_3N_4-waveguide results where a flatter SC was generated[23].

The compact stabilization setup is depicted in Fig. 4.1a (see Methods for more details). We use a reflection of the laser output beam from a glass wedge to measure f_{rep} with a fast photodiode. The remaining output power is coupled into the Si_3N_4 waveguide with a coupling efficiency of 28%. The generated SC features two coherent dispersive waves centered around 700 nm and 1440 nm (Fig. 4.1c), which are used to detect f_{CEO} in an f-to-2f interferometer (see Methods). The microwave spectrum of the f-to-2f photodiode signal shows the two CEO beat frequencies between DC and f_{rep} (Fig. 4.2a). The CEO beat signal is centered around 780 MHz and exhibits a signal-to-noise ratio (SNR) of 25 dB measured with a resolution bandwidth (RBW) of 10 kHz. The f_{CEO} can be shifted over 100 MHz by modulating the pump power (Fig. 4.2c). Note that the SNR of the CEO signal cannot simply be increased by increasing the pulse energy coupled into the waveguide. For coupled pulse energies exceeding 17 pJ, the CEO signal power decreases again while the noise floor rises at the same time, which indicates the onset of incoherence in the SCG (Fig. 4.2d).

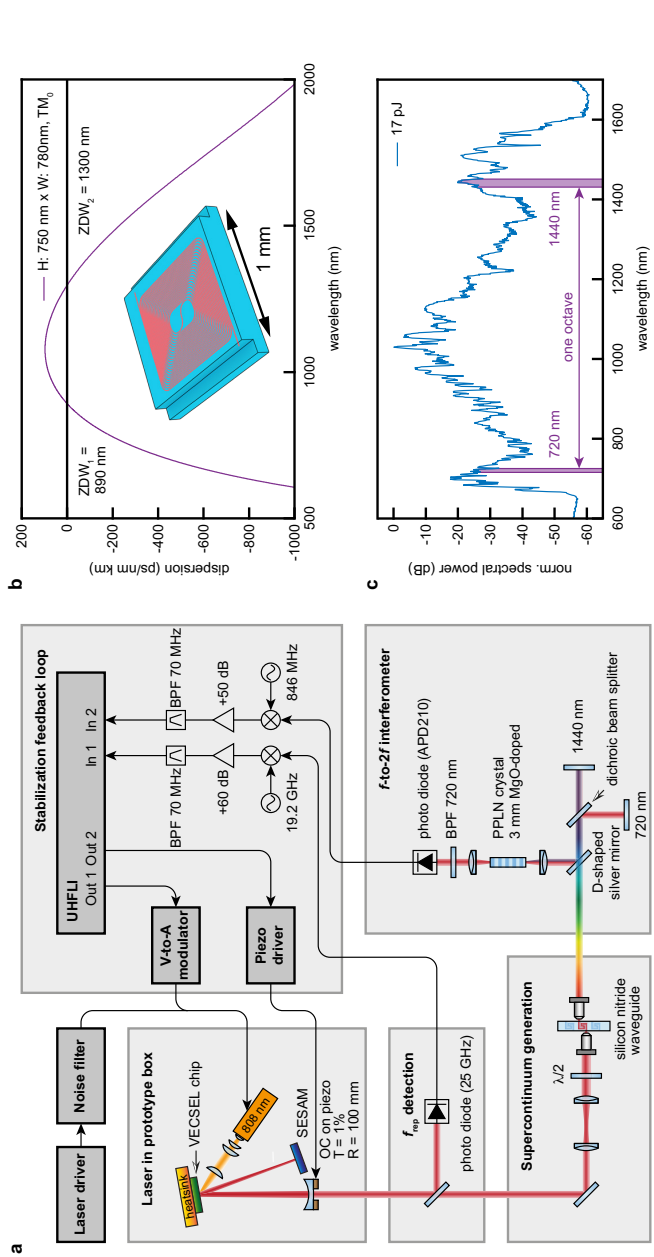

Figure 4.1: Laser and stabilization setup. a, Schematic of the laser and stabilization setup including the laser cavity, pulse repetition rate (f_{rep}) detection, supercontinuum generation, *f*-to-2*f* interferometry, signal pre-processing, and stabilization feedback loop. OC, output coupler; T, transmission; R, radius of curvature; PPLN, periodically poled lithium niobate; BPF, optical band-pass filter; UHFLI, digital ultra-high lock-in amplifier (*Zurich Instruments*); V-to-A, voltage to current; **b**, Silicon nitride waveguide dispersion for a cross-section of 750 x 780 nm simulated for the TM_0 mode featuring two zero-dispersion wavelengths (ZDWs). Inset: illustration of the 5-cm-long spiraled waveguide. **c**, Generated octave-spanning supercontinuum for a coupled pulse energy of 17 pJ. The highlighted wavelength regions are used for *f*-to-2*f* interferometry.

Simulations of the SCG in the waveguide confirm the loss of coherence for high pulse energies (Supplementary Fig. 4.6). In order to maintain highest coherence, the length of the waveguide must be chosen to match the desired pulse energy; it needs to be sufficiently long to allow for the generation of the two dispersive waves but should not significantly exceed the soliton fission length.

The free-running carrier envelope-offset (CEO) beat has a FWHM linewidth of only $\approx$ 20 kHz (Fig. 4.2b). The narrow linewidth represents a substantial improvement compared to the megahertz CEO linewidths[21,22] detected via external pulse amplification and compression, indicating that additional amplifier noise and amplitude-to-phase noise conversion in more complex lasers-amplifier systems can have a detrimental impact on the noise performance. Furthermore, it is also interesting to compare with the CEO frequency of a 1-GHz diode pumped solid-state laser (DPSSL) based on Yb:CALGO[26], which was detected using a previous generation of Si_3N_4 waveguides and showed a linewidth of 170 kHz. The Yb:CALGO laser material exhibits a comparatively long carrier lifetime of 420 µs[27], which acts like a low-pass filter for pump power fluctuations. However, its narrow absorption spectrum[27] increases the sensitivity to pump frequency fluctuations. The SDL on the other hand has a very broad absorption spectrum which is insensitive to pump frequency fluctuations but has a much shorter carrier lifetime (on the order of 100-200 ps)[5], which is below the cavity roundtrip time. The ability to directly measure the CEO frequency fluctuations opens up interesting possibilities to study the complex carrier-photon coupling dynamics within an SDL gain medium, which is the topic of ongoing work.

The f_{rep} and f_{CEO} are stabilized using an ultra-high frequency digital lock-in amplifier (UHFLI) (see Methods). To stabilize f_{rep}, the cavity length is modulated with a piezo-mounted output coupler and f_{CEO} is stabilized by pump current modulation. The f_{CEO} stabilization results in a coherent peak with a linewidth of 1 Hz limited by the measurement RBW (Fig. 4.2e) with clearly visible 50 Hz peaks from the European power grid. For the noise characterization of f_{rep} and f_{CEO}, we use a signal source analyzer connected in-loop. With active stabilization, the noise of both frequencies can be reduced below the β-separation line[28] (Fig. 4.3a,b).

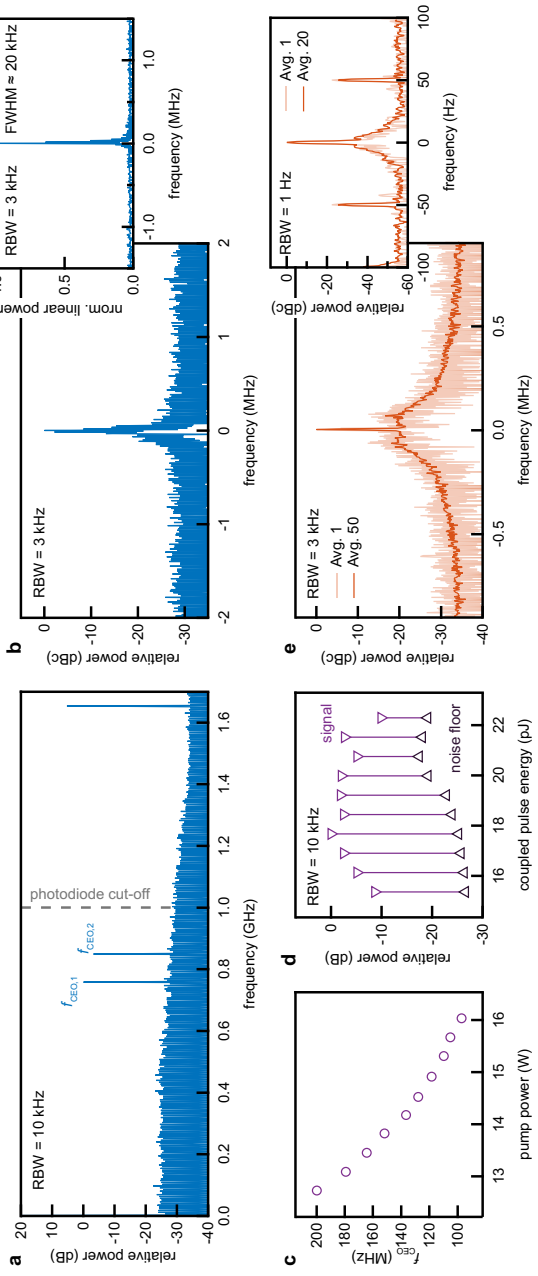

Figure 4.2: Carrier envelope-offset (CEO) frequency detection, control, and stabilization. **a**, Microwave spectrum of the f-to-$2f$ photodiode signal showing the two CEO beat frequencies f_{CEO} between DC and the pulse repetition rate f_{rep}. The signal-to-noise ratio of f_{CEO} measured with a resolution bandwidth (RBW) of 10 kHz is 25 dB. **b**, Free-running CEO beat in logarithmic and linear scale with a narrow full width at half maximum (FWHM) of $\approx$ 20 kHz. **c**, Tuning of the f_{CEO} as a function of pump power. **d**, Tuning of the f_{CEO} signal strength (violet) and the photodiode noise floor (dark violet) for different coupled pulse energies inside the silicon nitride waveguide. **e**, Stabilized CEO frequency featuring a resolution-limited coherent peak with averaging (dark orange) and without (light orange). A span of 2 MHz and 200 Hz is shown measured with a RBW of 3 kHz and 1 Hz, respectively.

Noise below the β-separation line only contributes to the wings, but not to the linewidth of the signal, indicating a tight lock characterized by the presence of a coherent peak. There is negligible influence of the f_{rep} stabilization loop on the f_{CEO} stabilization. The residual phase noise integrated from 1 Hz to 1 MHz is 448 mrad when the f_{rep} stabilization is off and 456 mrad when it is on. Taking into account the linear scaling with f_{rep}, these residual noise values are comparable to the best results obtained by stabilized gigahertz solid-state lasers[26] which are not monolithic[29], including commercial Ti:sapphire combs[30]. The noise measurement of f_{rep} above 1 kHz is limited by the detector shot noise (Fig. 4.3b). The timing jitter of the individually stabilized f_{rep} amounts to 52 fs, which is close to the best values for SDLs[19]. With a simultaneously stabilized f_{CEO}, the timing jitter increases to 257 fs. The additionally introduced noise lies above 1 kHz, which is higher than the modulation bandwidth of the piezo actuator used to stabilize f_{rep}.

Both f_{rep} and f_{CEO} were recorded over 15 min in the tight lock condition (Fig. 4.4c,d) (limited by data storage capacity, see Methods). The standard deviation with a 1-s averaging time is 2 mHz and 2 μHz for f_{CEO} and f_{rep}, respectively. The corresponding Allan deviations are linearly decreasing (Fig. 4.4e,f), showing that the frequency deviation can be reduced with longer average times without running out of the stabilization loop. Even though f_{rep} is more stable, the frequency stability of the optical frequencies $\nu_{opt} = f_{CEO} + n \cdot f_{rep}$ is limited by f_{rep} noise, which is multiplied by a factor $n \approx 182'300$ (corresponding to 1025 nm), and not by the stabilization of f_{CEO}.

In conclusion, we have presented the first fully stabilized OFC from an ultrafast SDL without external pulse amplification. A novel Si_3N_4 waveguide design allowed for energy-efficient self-referenced detection of f_{CEO}. Using an all-digital stabilization setup, a noise performance comparable to the best results achieved with other non-monolithic gigahertz laser sources was achieved already in this proof-of-principle experiment. This result opens up a new observable to study the underlying semiconductor laser physics and provides a new compact OFC source based on semiconductor lasers with a great flexibility in operation wavelength ranging from UV to mid-IR potentially enabling many future applications.

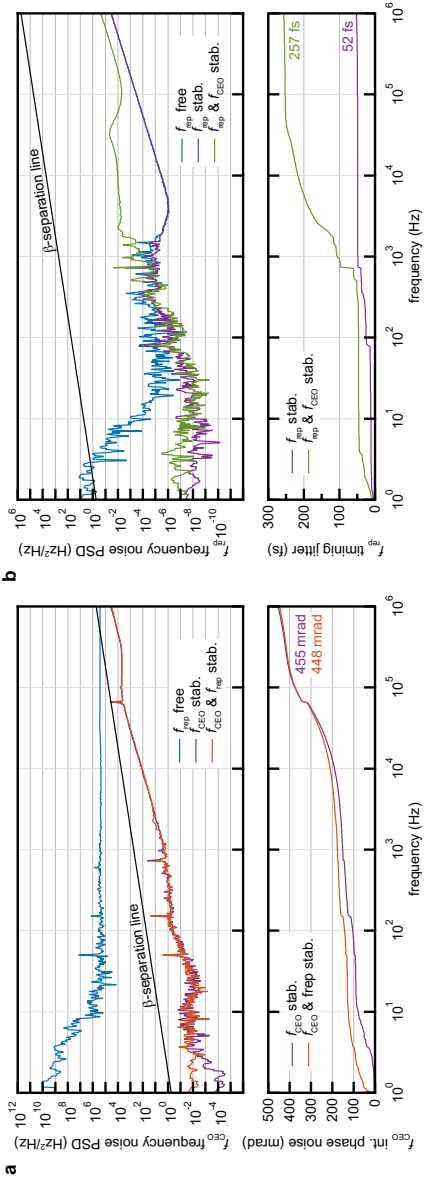

Figure 4.3: Noise characterization of the CEO frequency stabilization and the pulse repetition rate stabilization. a, Frequency noise power spectral density (PSD) of the CEO frequency f_{CEO}: free-running, f_{CEO} stabilized, and both f_{CEO} and pulse repetition rate f_{rep} stabilized. The noise of the stabilized f_{CEO} lies below the β-separation line indicating a tight lock. The corresponding integrated phase noise values are shown below. **b**, Frequency noise PSD of f_{rep}: free-running, f_{rep} stabilized, and both f_{rep} and f_{CEO} stabilized. The frequency noise PSD was measured at the 12$^{\mathrm{th}}$ harmonic of f_{rep} and subsequently divided by factor of 12^2 to account for the quadratic scaling of the noise with the harmonic number. The corresponding timing jitters are shown below.

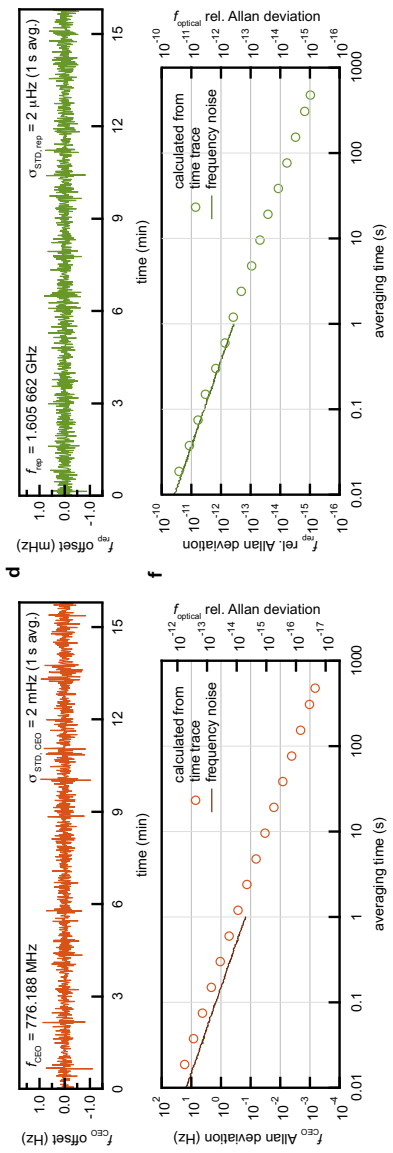

Figure 4.4: Noise characterization of the CEO frequency stabilization and the pulse repetition rate stabilization. c-d, Frequency stability of f_{CEO} (**c**) and f_{rep} (**d**) recorded over 15 min with an averaging time of 1 s. **e-f**, Allan deviation of the CEO frequency (**e**) and of the pulse repetition rate (**f**) with the corresponding relative Allan deviation with respect to the optical frequencies on the right axis. The Allan deviations are calculated from the recorded time traces and from the frequency noise PSDs.

Acknowledgement The authors want to thank Dr. S. Schilt from University of Neuchâtel for valuable discussions and Dr. M. Golling together with the cleanroom facility FIRST of ETH Zürich for the epitaxial growth of the SDL. The ETH Zurich authors acknowledge funding from the Swiss Confederation Program Nano-Tera.ch, which was scientifically evaluated by the Swiss National Science Foundation (SNSF).

4.1.1 References

1 Guina, M., Rantamäki, A. & Härkönen, A. Optically pumped VECSELs: review of technology and progress. J. Phys. D: Appl. Phys. 50, 383001 (2017).

2 Heinen, B. et al. 106 W continuous-wave output power from vertical-external-cavity surface-emitting laser. Electron. Lett. 48, 516-U102, doi:10.1049/el.2012.0531 (2012).

3 Waldburger, D. et al. High-power 100 fs semiconductor disk lasers. Optica 3, 844-852, doi:10.1364/Optica.3.000844 (2016).

4 Baker, C. W. et al. Multi-Angle VECSEL Cavities for Dispersion Control and Peak-Power Scaling. IEEE Photonics Technology Letters 29, 326-329, doi:10.1109/LPT.2017.2647956 (2017).

5 Alfieri, C. G. E. et al. Optical efficiency and gain dynamics of modelocked semiconductor disk lasers. Opt. Express 25, 6402-6420, doi:10.1364/OE.25.006402 (2017).

6 Hönninger, C., Paschotta, R., Morier-Genoud, F., Moser, M. & Keller, U. Q-switching stability limits of continuous-wave passive mode locking. J. Opt. Soc. Am. B 16, 46-56 (1999).

7 Klenner, A. & Keller, U. All-optical Q-switching limiter for high-power gigahertz modelocked diode-pumped solid-state lasers. Opt. Express 23, 8532-8544, doi:10.1364/Oe.23.008532 (2015).

8 Mayer, A. S., Phillips, C. R. & Keller, U. Watt-level 10-gigahertz solid-state laser enabled by self-defocusing nonlinearities in an aperiodically poled crystal. Nature Communications 8, 1673, doi:10.1038/s41467-017-01999-y (2017).

9 Fortier, T. M. et al. Generation of ultrastable microwaves via optical frequency division. Nature Photonics 5, 425, doi:10.1038/nphoton.2011.121 (2011).

10 Marandi, A., Wang, Z., Takata, K., Byer, R. L. & Yamamoto, Y. Network of time-multiplexed optical parametric oscillators as a coherent Ising machine. Nature Photonics 8, 937, doi:10.1038/nphoton.2014.249 (2014).

11 Steinmetz, T. et al. Laser frequency combs for astronomical observations. Science 321, 1335-1337, doi:10.1126/science.1161030 (2008).

12 Cundiff, S. T. & Weiner, A. M. Optical arbitrary waveform generation. Nature Photonics 4, 760, doi:10.1038/nphoton.2010.196 (2010).

13 Diddams, S. A., Hollberg, L. & Mbele, V. Molecular fingerprinting with the resolved modes of a femtosecond laser frequency comb. Nature 445, 627-630 (2007).

14 Schiller, S. Spectrometry with frequency combs. Optics Letters 27, 766-768, doi:10.1364/OL.27.000766 (2002).

15 Link, S. M., Maas, D. J. H. C., Waldburger, D. & Keller, U. Dual-comb spectroscopy of water vapor with a free-running semiconductor disk laser. Science 356, 1164-1168, doi:10.1126/science.aam7424 (2017).

16 Telle, H. R. et al. Carrier-envelope offset phase control: A novel concept for absolute optical frequency measurement and ultrashort pulse generation. Appl. Phys. B 69, 327-332, doi:10.1007/s003400050 (1999).

17 Apolonski, A. et al. Controlling the Phase Evolution of Few-Cycle Light Pulses. Phys. Rev. Lett. 85, 740-743, doi:10.1103/PhysRevLett.85.740 (2000).

18 Jones, D. J. et al. Carrier-envelope phase control of femtosecond mode-locked lasers and direct optical frequency synthesis. Science 288, 635-639, doi:10.1126/science.288.5466.635 (2000).

19 Mangold, M. et al. Amplitude Noise and Timing Jitter Characterization of a High-Power Mode-Locked Integrated External-Cavity Surface Emitting Laser. IEEE Photon. J. 6 doi:10.1109/Jphot.2013.2295464 (2014).

20 Dudley, J. M., Genty, G. & Coen, S. Supercontinuum generation in photonic crystal fiber. Reviews of Modern Physics 78, 1135-1184, doi:10.1103/RevModPhys.78.1135 (2006).

21 Zaugg, C. A. et al. Gigahertz self-referenceable frequency comb from a semiconductor disk laser. Opt. Express 22, 16445-16455, doi:10.1364/Oe.22.016445 (2014).

22 Jornod, N. et al. Carrier-envelope offset frequency stabilization of a gigahertz semiconductor disk laser. Optica 4, 1482-1487, doi:10.1364/OPTICA.4.001482 (2017).

23 Johnson, A. R. et al. Octave-spanning coherent supercontinuum generation in a silicon nitride waveguide. Optics Letters 40, 5117-5120, doi:10.1364/OL.40.005117 (2015).

24 Carlson, D. R. et al. Self-referenced frequency combs using high-efficiency silicon-nitride waveguides. Optics Letters 42, 2314-2317, doi:10.1364/OL.42.002314 (2017).

25 Guo, H. et al. Mid-infrared frequency comb via coherent dispersive wave generation in silicon nitride nanophotonic waveguides. Nature Photonics 12, 330-335, doi:10.1038/s41566-018-0144-1 (2018).

26 Klenner, A. et al. Gigahertz frequency comb offset stabilization based on supercontinuum generation in silicon nitride waveguides. Opt. Express 24, 11043-11053, doi:10.1364/OE.24.011043 (2016).

27 Petit, J., Goldner, P. & Viana, B. Laser emission with low quantum defect in Yb:CaGdAlO4. Opt. Lett. 30, 1345-1347 (2005).

28 Di Domenico, G., Schilt, S. & Thomann, P. Simple approach to the relation between laser frequency noise and laser line shape. Appl. Opt. 49, 4801-4807, doi:10.1364/AO.49.004801 (2010).

29 Shoji, T. D. et al. Ultra-low-noise monolithic mode-locked solid-state laser. Optica 3, 995-998, doi:10.1364/OPTICA.3.000995 (2016).

30 Heinecke, D. C., Bartels, A. & Diddams, S. A. Offset frequency dynamics and phase noise properties of a self-referenced 10 GHz Ti:sapphire frequency comb. Optics Express 19, 18440-18451 (2011)

4.1.2 Methods

In this methods section, we describe the semiconductor disk laser, the silicon nitride waveguide, the stabilization setup, and the noise analysis in more detail.

Laser setup & performance

In our experiment, we use a diode-pumped vertical external-cavity surface-emitting laser (VECSEL) modelocked with a semiconductor saturable absorber mirror (SESAM). The laser cavity is V-shaped with the SESAM and the output coupler (OC, 100 mm radius of curvature, 1% transmission) as end-mirrors and the VECSEL chip as folding mirror (Fig. 4.1a). The VECSEL gain chip is optically pumped by a commercial multimode pump diode at 808 nm at an angle of 45°. The pump diode is wavelength-stabilized with a volume holographic grating (VHG) and we use a custom-made low-pass filter for the electrical power supply of the diode. The VECSEL and SESAM structures are analogous to those presented by Waldburger et al.[3], with the difference being that the vertical external-cavity

surface-emitting laser (VECSEL) chip was grown by molecular beam epitaxy (MBE) instead of metalorganic vapour phase epitaxy (MOVPE). The VECSEL and the SESAM are temperature controlled with a water-cooled Peltier element. The laser is boxed in order to reduce the influence of mechanical vibration and air turbulences. The modelocking characterization are depicted in the Supplementary Figure 4.5. The VECSEL produces pulses with a pulse duration of 122 fs. The optical spectrum is centered at 1025.3 nm with a full width at half maximum (FWHM) of 11.8 nm and the pulse repetition rate is 1.599 GHz. The side-peak free microwave spectrum of the pulse repetition rate and the equally powerful higher harmonics indicate clean fundamental modelocking. To obtain the highest signal-to-noise ratio (SNR) of the detected carrier envelope-offset (CEO) beat, the laser was not operated at the maximum average output power of 160 mW, but at a reduced power of 120 mW with a pump power of 14.2 W (see discussion in main text).

Silicon nitride waveguide

The silicon nitride waveguide is compatible with complementary metal-oxide-semiconductor (CMOS) fabrication techniques. It has a sub-wavelength cross-section (height: 750 nm, width: 780 nm) and features a silicon oxide cladding. The waveguide dispersion is simulated using a finite element software and exhibits two zero-dispersion wavelengths (Fig. 4.1b). The 5-cm-long waveguide is spiraled to fit on the 1 x 1 mm writing area of the electron-beam lithography tool (Fig. 4.1b). For the free-space coupling into the waveguide, we use a telescope to enlarge the optical beam and an aspheric lens to focus onto the waveguide facet (Fig. 4.1a). The observed loss of coherence in the generated SC for increased pulse energies (Fig. 4.2d) is confirmed in our simulations (Supplementary Fig. S2). The propagation of the spectrum inside the waveguide is described by the generalized nonlinear Schrödinger equations including shot noise and spontaneous Raman scattering. The coupled pulse energies used in the simulation are smaller than the experimental values, since in the experiment, a fraction of the power is not coupled into the desired TM_0. The incoherence observed for increased pulse energies results from amplified noise inside the waveguide and can be avoided by using a shorter wave-

guide.

Pulse repetition rate stabilization

The pulse repetition rate f_{rep} is detected with a beam reflection from a glass wedge and measured with a fast fiber-coupled photodiode (Model 1434, *Newport*). For the stabilization of f_{rep}, the 12^{th} harmonic at 19.2 GHz is used which increases the sensitivity of the stabilization. To pre-process the signal, the 12^{th} harmonic is mixed down to 70 MHz (MM93PG-40, *Remec Inc.*) with an ultra-stable microwave source (83650A, *Hewlett-Packard*), amplified by a low noise amplifier (DUPVA-1-70, *Femto*), and bandpass filtered (BBP-70+, *Mini-Circuits*) (Fig. 4.1a). The pre-processed signal is then used as input to the ultra-high frequency digital lock-in amplifier (UHFLI, *Zurich Instruments*), where the input signal is demodulated with the internal ultra-stable oven-controlled oscillator. The resulting error signal is then sent through the UHFLI's proportional–integral (PI) loop filter to generate the correction signal. The correction signal modulates a piezo driver (SQV 1/150, *Piezomechanik GmbH*) which controls a piezo-mounted output coupler, similar to the one used by Mangold et al.[19] The -3 dB operation bandwidth of the actuator used for the pulse repetition rate is around 1 kHz.

CEO frequency stabilization

The CEO frequency f_{CEO} is measured by f-to-$2f$ interferometry (Fig. 4.1a). The octave-spanning SC is split into a short and a long wavelength part by a dichroic beam splitter for temporal overlap tuning. After recombination, the long wavelength part is frequency-doubled in a 3-mm long, magnesium-doped periodically poled lithium niobate (PPLN) crystal. Finally, an optical bandpass filter centered around 720 nm selects the desired spectral components before they interfere on a high-speed avalanche photodetector (APD 210, *Menlo Systems*). The photodetector has a bandwidth of 1 GHz visible in the drop of signal strength in the microwave spectrum (Fig. 4.2a). For pre-processing, the photodiode signal is mixed down to 70 MHz (ZX05-30W-S+, *Mini Circuits*) with an ultra-stable microwave source (83650B, *Agilent*), amplified by a low noise amplifier (DHPVA-100, *Femto*), and bandpass filtered (BBP-70+, *Mini Circuits*). The corresponding

correction signal is generated with the UHFLI in the same way as for f_{rep}. The correction signal drives a custom-made voltage-to-current converter which is connected in parallel to the noise-filtered electronic power supply of the pump diode to modulated the pump current. The modulation bandwidth is estimated to be around 100 kHz.

Noise characterization

The noise of f_{rep} and f_{CEO} is analyzed with a signal source analyzer (SSA; E5052B, *Agilent*). The noise is measured inside the feedback loop using the pre-processed signals before the input of the UHFLI. For the characterization of f_{rep}, the reference source/phase-locked loop (PLL) method is applied. This method uses a PLL to lock the internal reference source of the SSA to the carrier frequency of the device under test (DUT) in phase quadrature. The signal of the DUT and the internal reference source are compared in a double-balanced mixer and analyzed with baseband spectrum analyzer. The reference source/PLL method has a very good sensitivity and is insensitive to amplitude noise. The frequency noise PSD was measured at the 12^{th} harmonic of f_{rep} and then subsequently divided by factor of 12^2 to account for the quadratic scaling of the frequency noise with the harmonic number.

The stabilized f_{CEO} is also characterized with the reference source/PLL method. However, the higher drift rate of free-running f_{CEO} together with the limited SNR do not allow to measure the phase noise with the reference source/PLL method. Thus, we use the heterodyne (digital) discriminator method of the SSA which is modified digital version of the analog delay-line discriminator method. Whereby instead of the internal reference source, the signal of the DUT is compared to a delayed copy of itself. The discriminator method is able to track the free-running f_{CEO} but it degrades the measurement sensitivity, especially with our limited SNR. Consequently, the measured phase noise of the free-running f_{CEO} is only an upper estimate. This explains, why free-running phase noise is not compatible with the measured CEO linewidth of $\approx$ 20 kHz and why the noise spectrum of the stabilized f_{CEO} does not reach the level of the free-running case above the modulation feedback bandwidth >1 MHz. For the discriminator measurement, the f-to-$2f$ photodiode signal is mixed to 300

MHz and bandpass filtered (3TF-250/500-5S, *Lorch*).

Frequency stability

The frequency time series is calculated from the measured phase deviation. The phase deviation is recorded by the UHFLI while simultaneously calculating the PI-loop correction signal. The input signal is demodulated with the internal reference oscillator at a fixed frequency, to which the signal is stabilized. We then record the phase of the demodulated signal, which allows us to calculate the corresponding frequency offset. From this, we calculated the overlapping relative Allan deviation estimator (ADEV)[31,32]:

$$\sigma_y(\tau = m\tau) = \sqrt{\frac{1}{2m^2\tau_0^2 \cdot (N-2m)} \sum_{i=1}^{N-2m} (x_{i+2m} - 2x_{i+m} + x_i)^2}, \quad (4.1)$$

where τ is a multiple of the measurement interval τ_0, N is the number of measurements, and x_i is the i$^{\text{th}}$ measurement of the time-error function $x(t) = \Phi(t)/(2\pi\nu_0)$. The instantaneous frequency $\nu(t) = \nu_0 + \partial_t\Phi(t)/(2\pi)$ is then given by the nominal frequency ν_0 the measured phase deviation $\Phi(t)$. For the characterization of f_{CEO}, the nominal frequency is given by $\nu_0 = f_{\text{CEO}} = 776$ MHz. Since the Allan deviation is not expected to scale with the CEO frequency, the absolute Allan deviation given by $\sigma_y(t) \cdot f_{\text{CEO}}$ is shown in Fig. 4.3a. For the characterization of f_{rep}, the nominal frequency is given by the 12$^{\text{th}}$ harmonic: $\nu_0 = 12 f_{\text{rep}} =$ 19.2 GHz. The measurement interval ν_0 = 1.14 µs leads to confidence intervals below visibility in Fig. 4.4e, f, which thus are omitted.

To distinguish between white phase noise and flicker phase noise, we calculated the modified Allan deviation. The $\tau^{-3/2}$-slope of the modified Allan deviance (MDEV, not shown)[32] implies that white phase noise is dominant for f_{CEO} and f_{rep}. The recording time of 15 min was not limited by the laser stabilization, but by the available storage space. The Allan deviation is calculated from the in-loop phase deviation, thus drifts of the electronic reference oscillators do not contribute.

For validation of the measurement, the Allan deviation is also calculated from the measured one-sided frequency noise PSD $S_y(f)$[33]:

$$\sigma_y(\tau) = \sqrt{\int_0^\infty S_y(f) \frac{2\sin^4(\pi\tau f)}{(\pi\tau f)^2} df}, \quad (4.2)$$

which is in good agreement with the overlapping Allan deviation calculated from the timeseries with a discrepancy factor of 2.0 and 1.2 for f_{CEO} and f_{rep}, respectively.

4.1.3 References Methods

31 Howe, D. A., Allan, D. U. & Barnes, J. A. in Thirty Fifth Annual Frequency Control Symposium. 669-716.

32 Riley, W. & Howe, D. A. Handbook of Frequency Stability Analysis Special Pulbications (NIST SP) 1065 (2008).

33 Riehle, F. in Frequency Standards: Basics and Applications Ch. 3. Characterization of Amplitude and Frequency Noise, (Wiley-VCH, 2006).

4.1.4 Supplementary Figures

The figure 4.5 and 4.6 follow on the next two pages.

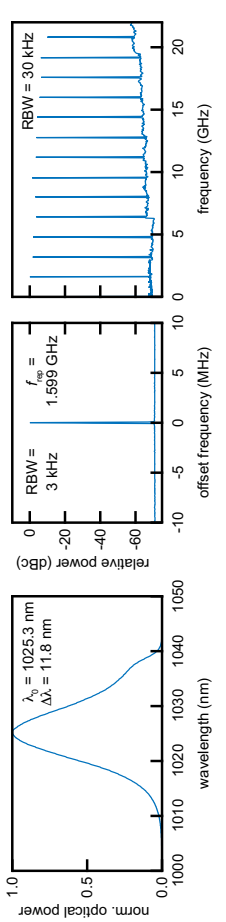

Figure 4.5: Modelocking characterization of the semiconductor disk laser (SDL). a, Autocorrelation of the modelocked pulses fitted with a 122 fs sech^2-shaped pulse. **b**, Optical spectrum centered around 1025.3 nm with a full width at half maximum (FWHM) of 11.8 nm. **c**, Microwave spectra of the 1.599 GHz pulse repetition rates showing a 20 MHz span measured with a resolution bandwidth (RBW) of 3 kHz. d, Microwave spectra of the equally powerful higher harmonics of the repetition rates measured with a RBW of 30 kHz.

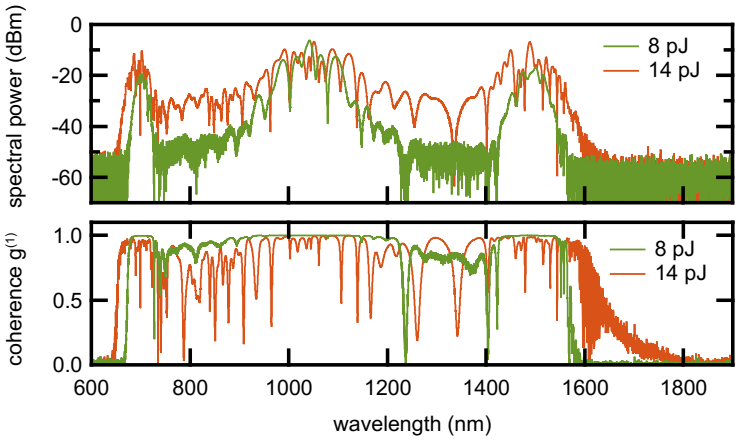

Figure 4.6: Simulation of the generated supercontinuum. The simulation of the generated supercontinuum by the silicon nitride waveguide for 8 pJ (green) and 14 pJ (orange) of coupled pulse energy, respectively. For the pulse energy of 14 pJ, the coherence of the spectral parts used for f-to-$2f$ interferometry is drastically reduced. The coupled pulse energies in the simulation are smaller than the pulse energies in the experiment, since in the experiment, not all the power is coupled into the desired TM_0 mode.

Chapter 5

Dual-comb MIXSEL

In this chapter, we introduce the concept of the dual-comb MIXSEL. The dual-comb modelocked laser generates two orthogonally polarized OFCs from the same laser cavity with different pulse repetition rates. This fulfills the requirements for dual-comb spectroscopy, which was demonstrated in a proof-of-principle free-running dual-comb spectroscopy measurement of water vapor. The details are presented in the following journal publication (section 5.1):

Title:	"Dual-comb spectroscopy of water vapor with a free-running semiconductor disk laser", [35]
Journal:	*Science*
doi:	10.1126/science.aam7424

With the new short pulse MIXSEL presented in section 3.3, the dual-comb MIXSEL was pushed from tens of picoseconds to femtosecond operation with a more than ten-fold increase of the optical bandwidth. A fundamental aspect of this result is the good thermal conductivity of the new MIXSEL chip which reduced the thermal cross talk between the two laser spots of the dual-comb MIXSEL. The upgraded version of the dual-comb MIXSEL is then used to measure the transmittance spectrum in the near-IR of an acetylene-filled gas cell in free-running operation (section 5.2).

5.1 Dual-comb spectroscopy of water vapor with a free-running semiconductor disk laser

S. M. Link,[1] *D. J. H. C. Maas,*[2] *D. Waldburger,*[1] *U. Keller*[1]

[1]Department of Physics, Institute for Quantum Electronics, ETH Zürich, 8093 Zürich, Switzerland.
[2]ABB Switzerland Ltd., Corporate Research, Segelhofstrasse 1K, 5405 Baden-Daettwil, Switzerland.

Dual-comb spectroscopy offers the potential for high accuracy combined with fast data acquisition. Applications are often limited, however, by the complexity of optical comb systems. Here we present dual-comb spectroscopy of water vapor using a substantially simplified single-laser system. Very good spectroscopy measurements with fast sampling rates are achieved with a free-running dual-comb mode-locked semiconductor disk laser. The absolute stability of the optical comb modes is characterized both for free-running operation and with simple microwave stabilization. This approach drastically reduces the complexity for dual-comb spectroscopy. Band-gap engineering to tune the center wavelength from the ultraviolet to the mid-infrared could optimize frequency combs for specific gas targets, further enabling dual-comb spectroscopy for a wider range of industrial applications.

A fully stabilized optical frequency comb (OFC) consists of equally spaced frequencies with a relative uncertainty as low as 10^{-19} (1) and can serve as a very precise ruler for optical frequency measurements. The combs can be generated by mode-locked lasers with sufficient peak power in femtosecond pulses for supercontinuum generation in a single pass through a fiber or waveguide (2-4); generation with continuous-wave lasers (5) requires sufficient average power in a narrow-frequency linewidth to couple into a high-Q microresonator for highly nonlinear parametric interactions. Many applications require frequency combs in the 100-MHz to 10-GHz regime, where equally spaced microresonator combs become more challenging (6). Although mode-locked laser technology has enabled frequency-spacing stabilization since the 1980s (7, 8),

stabilizing the frequency comb offset requires substantial spectral broadening (2). To date, stabilized GHz OFCs have had to rely on rather bulky and complex ultrafast diode-pumped solid-state (9), fiber (10), or titanium-sapphire (Ti:sapphire) lasers (11). In comparison, optically pumped semiconductor disk lasers such as the modelocked integrated external-cavity surface-emitting lasers (MIXSELs) (12) are often better suited for mass production and widespread applications, as they are based on a wafer-scale technology with reduced packaging requirements and potentially a higher level of integration.

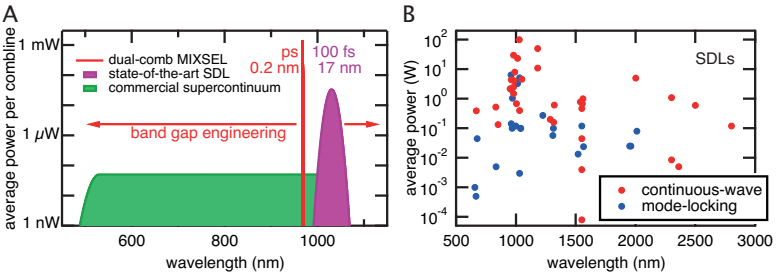

Figure 5.1: Current state-of-the-art performance in frequency comb characteristics. (A) A commercial OFC (e.g., Menlo FC1500-250-WG MVIS) can cover an octave of optical spectrum. The large bandwidth, however, strongly reduces the average power per comb line to about 50 nW. Optically pumped semiconductor disk lasers (SDLs) can provide more than 1 mW of average power per comb line. With pulse durations as short as 100 fs, their optical spectrum spans up to 17 nm at a center wavelength around 1 mm (41). The center wavelength of ultrafast SDLs can be shifted with semiconductor band-gap engineering. (B) Large spectral coverage of optically pumped SDLs. Overview of continuous-wave and passively mode-locked SDL results in terms of center operation wavelength and average output power on a logarithmic scale. The plotted results are summarized in recent review papers (14-19).

Here we demonstrate dual-comb spectroscopy of water vapor with a single mode-locked laser cavity. The dual-comb mode-locked laser (13) generates two collinear, perpendicularly polarized OFCs with an adjustable frequency difference in comb spacing. A fast scan rate and the single-laser cavity approach support spectroscopic measurements even when using the free-running laser without any additional external spectral broadening or stabilization. This is a potential paradigm shift in frequency

metrology: to use a narrowband OFC, which is then tuned to the desired spectral range on the basis of the specific target to be tested. This approach provides more power per comb line and a resulting higher signal-to-noise ratio (Fig. 5.1A). A dual-comb MIXSEL generates two OFCs from the same laser cavity and provides a potentially very attractive source for this approach. Tuning the OFC center wavelength from ultraviolet (UV) to mid-infrared (mid-IR) for different gas targets can be achieved with semiconductor band-gap engineering (14-19) (Fig. 5.1B). For the demonstration on water vapor, the dual-comb MIXSEL (Fig. 5.2A) was operated around a center wavelength of 968 nm with a pulse repetition rate of $\approx$1.7 GHz and a frequency offset of 4 MHz with an average power of $>$60 mW and a pulse duration of about 18 ps (Fig. 5.5).

Dual-comb spectroscopy is generally very attractive for molecular spectroscopy (20, 21), as well as asynchronous optical sampling (22), distance measurements (23), and fiber Bragg grating sensing (24). The technique often offers marked improvements in spectral resolution, sensitivity, and data-acquisition speed compared to traditional optical spectrometer techniques. With the dual-comb principle, a direct link between the optical frequencies and the microwave regime is established (Fig. 5.2B). This dual-comb approach is very attractive for applications such as spectroscopy. A key drawback of dual-comb spectroscopy is the requirement for two fully stabilized OFCs with slightly different comb spacing (Fig. 5.2B). For mode-locked lasers, this requires stabilization of both the pulse repetition frequency (i.e., the frequency comb spacing) and the carrier envelope-offset (CEO) frequency (i.e., the frequency comb zero offset) for two separate OFCs. Therefore, four separate stabilization loops and two highly nonlinear processes for supercontinuum generation are required.

There is a concerted ongoing effort in the research community to find ways to simplify these systems (25-28). The detection of the CEO frequency with optical f-to-2f interferometry (2) requires a coherent octave-spanning supercontinuum, which is very demanding on the laser performance and substantially reduces the power per mode. Unfortunately, most of the time the broad spectrum cannot be fully used for spectroscopy directly but needs to be filtered to avoid aliasing effects as described by the Nyquist-Shannon sampling condition (29). Therefore, very often it is

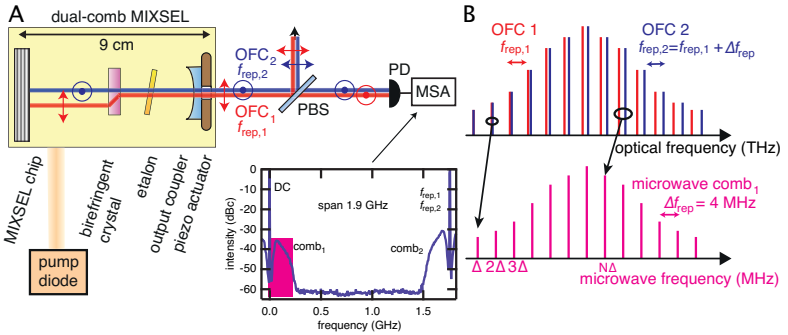

Figure 5.2: Dual-comb source and operating principle. (A) Dual-comb MIXSEL. The diode-pumped dual-comb MIXSEL is a specialized SDL for which both the gain and the saturable absorber are integrated into the same semiconductor wafer. The semiconductor MIXSEL chip forms one cavity-end mirror, and the output coupler forms the other. In addition, two intracavity elements are used: first, an etalon to adjust the center wavelength, and second, a birefringent crystal for polarization splitting and dual-comb generation. The output coupler can be mounted on a piezo actuator to adjust the cavity length (and then the repetition rate). The dual-comb MIXSEL generates two collinear perpendicularly polarized (polarization indicated by circles and arrows) mode-locked pulse trains with a small difference in the pulse repetition frequency due to the difference in optical path length in the birefringent crystal. Thus, we obtain two collinear OFCs). A polarizing beam splitter (PBS), with an optical axis at an angle of 45° to the polarization axes of the OFCs, combines both OFCs into the same polarization, which then optically interfere on a photodetector (PD). A microwave spectrum analyzer (MSA) directly measures the microwave frequency comb, which manifests as a comb structure (comb_1) between dc and the pulse repetition rates $f_{\text{rep},1}$and $f_{\text{rep},2}$. The pink rectangle indicates the microwave comb. dBc, decibels relative to the carrier. (B) The microwave frequency comb results from the optical interference on the PD between all the optical frequencies of the two collinear and combined OFCs with their offset in pulse repetition rate Δf_{rep}, which can be adjusted with the optical path length in the birefringent crystal. With this dual-comb principle, we obtain a direct link between the optical and the microwave frequencies.

sufficient to use a dual-comb source with a narrower optical spectrum centered at a wavelength that can be tailored to the region of interest (e.g., matching absorption lines of gases of interest).

We consider the dual-comb MIXSEL an ideal source for dual-comb spectroscopy. Generally, given an optical source at the required wavelength, key requirements for molecular spectroscopy include (i) as much power per line as possible, resulting in better signal-to-noise ratio and faster measurement time; (ii) sufficiently narrow line spacing to resolve the spectroscopic feature (e.g., the mode-locked repetition rate equals the optical line spacing); and (iii) sufficiently narrow optical linewidth, of the individual comb lines, to resolve the spectroscopic features. For example, the water linewidth near 960 nm is ≈10 GHz; obtaining five sampling points per line requires a comb spacing of 1 to 2 GHz. Typical comb linewidth should be less than 10 to 100 MHz. MIXSEL combs have been successfully demonstrated in the 1- to 100-GHz regime (30), and in contrast to microcombs (27, 31) or quantum cascade laser combs (32, 33), the MIXSEL combs have shown even better performance in the 1- to 10-GHz regime so far. For example, without any further active stabilization, a single 2-GHz MIXSEL comb has a comb line-spacing variation of only $\approx 2.5 \times 10^{-4}$ integrated over a measurement time of 10 ms (34), which is a longer measurement time than required for most dual-comb spectroscopy applications (typically >1 ms to ideally ≈1 ms). The simplicity of the dual-comb MIXSEL (Fig. 5.2A) allows for fundamental mode-locking in a simple straight linear cavity, and the operation wavelength can be adjusted with an intracavity etalon to a center wavelength of 968.3 nm (10,327 cm^{-1}) to match an absorption line of water vapor. The pulse repetition rate can be set by the laser-cavity length, which corresponds to about 9 cm in air for the 1.7-GHz comb spacing used in this work. For dual-comb mode-locked operation (13), we insert a birefringent crystal inside this linear cavity, which splits the cavity beam on the side toward the MIXSEL chip into two spatially separated and cross-polarized beams with slightly different optical-cavity round-trip path lengths, defining a small difference in the comb frequency spacing Δf_{rep} of 4 MHz. This frequency difference can be adjusted by the thickness of the intracavity birefringent crystal (Fig. 5.2A). At the other side of the birefringent crystal, the two beams propagate

collinearly but with perpendicular polarization, making them easy to separate, e.g., with a polarizing beam splitter (PBS). Therefore, both OFCs share the same optical components, pump laser, and electronics, leading to intrinsically strong mutual coherence.

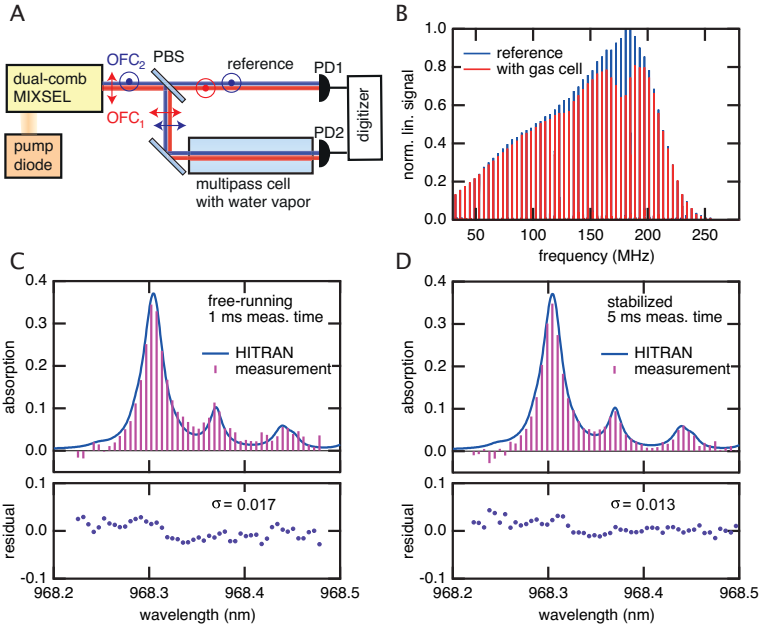

Figure 5.3: Dual-comb spectroscopy results. (A) Schematic of the experimental setup with two combined dual-comb OFCs. A reference microwave spectrum is measured with PD1, and the microwave spectrum after the multipass gas cell is simultaneously measured with PD2, making the setup insensitive to phase errors. (B) Microwave frequency combs for the reference measurement (blue) and the measurement with the gas cell (red), which is modulated because of the absorption of the water vapor. (C) Absorption measurement with the free-running system on water vapor and comparison with the HITRAN database, with the residual error shown below in purple. (D) Same measurements as in (C) with the stabilized microwave comb.

When we first explored dual-comb modelocking (13), we encountered a very unexpected result. Cavity-length adjustments to stabilize one comb's spacing did not appreciably affect the other comb's spacing. We were con-

cerned that the incoherent pump laser might be responsible, which would have been a more serious problem for dual-comb spectroscopy. We therefore had to first resolve this mysterious behavior. We gained insight into the underlying physics by comparing semiconductor and neodymium-doped:yttrium-aluminum-garnet (Nd:YAG) laser-gain materials, leading to the conclusion that the time delay introduced by the fully saturated saturable absorber is responsible for decoupling the two combs in an uncorrelated but deterministic way that can be fully stabilized (35). We therefore could then proceed to application of dual-comb spectroscopy. Dual-comb spectroscopy of water vapor (Fig. 5.3) was first explored with the laser operating in free-running mode without any further active stabilization. A 40-m-long multipass cell was used to enhance the absorption, as the absorption cross section of water vapor at 968.3 nm is four orders.of magnitude smaller than in the mid-IR. The.two perpendicularly polarized collinear OFCs at the output of the dual-comb laser were combined into the same polarization with a PBS (Fig. 5.3A). One such combined dual-comb was directly detected with a photodetector (PD1) and a digitizer to serve as a reference (Fig. 5.3B, blue microwave spectrum). Analogous to Fourier spectrometers, the second frequency comb replaces the scanning mirror, which typically limits the scan rate to a few hertz in Michelson-type systems. With a frequency offset of 4 MHz between the two combs, we have a minimum acquisition time of only 0.25 μs (Fig. 5.6) for the time-dependent interferograms detected by PD1. A simple Fourier transformation of the interferogram generates the spectrum shown in Fig. 5.3B. The other combined dual-comb after the PBS in Fig. 5.3A was sent through the air-filled multipass gas cell with a relative humidity of 60% at 36°C under ambient pressure and detected with PD2 (Fig. 5.3B, red microwave spectrum). The change introduced by the water-vapor absorption was clearly visible; the absorption was calculated by taking the difference between the two microwave spectra and normalizing the difference with the reference comb (Fig. 5.3B, blue microwave spectrum) (Fig. 5.3C) (36). Here we directly use the absorption line of water to calibrate the absolute wavelength (36), which is a commonly used method for dual-comb spectroscopy. A comparison with the high-resolution transmission molecular absorption (HITRAN) database (37) simulation using the laboratory pa-

rameters shows excellent agreement even though no active stabilization of the dual-comb laser was used. The residual error, with a standard deviation of 0.017, is shown below these data (Fig. 5.3C). We could further improve the signal-to-noise ratio and prevent long-term drifts with a simple stabilization scheme. For example, a longer measurement duration of 5 ms with this active stabilization switched on shows even better agreement with the HITRAN data (Fig. 5.3D). For the stabilization scheme shown in Fig. 5.4A, both OFCs are superimposed in the same polarization on the photodetector (PD3) and analyzed with a microwave spectrum analyzer (MSA). The generated microwave frequency comb (Fig. 5.4B) results from the interference of the optical modes of the two beams, representing a direct link between the optical frequencies and the electronically accessible microwave regime (Fig. 5.2B). All lines of the microwave comb can be clearly resolved without any stabilization. With a measurement time of 10 s, the comb lines fluctuate by only ≈200 kHz, shown here for a single comb line by holding the maximum of the trace for 10 s (blue line in Fig. 5.4C). This could be further improved with active stabilization. A single line (red line in Fig. 5.4B) of the comb was digitally filtered and locked to a stable electronic reference with an ultra-high frequency lock-in amplifier (UHFLI, Zurich Instruments). The error signal was corrected by current modulation to the multimode pump diode laser in the dual-comb MIXSEL. The stability of the comb line was substantially improved and the linewidth decreased to below 300 Hz (red line in Fig. 5.4C). In addition to one comb line, Δf_{rep}, was stabilized by using a second input port of the UHFLI. The corresponding error signal was corrected by modulation of the cavity length by means of a piezo actuator-controlled output coupler.With both a stabilized comb line and a stabilized Δf_{rep}, all microwave comb lines were stabilized simultaneously, shown here for an arbitrarily chosen second comb line (green line in Fig. 5.4C) (36). Therefore, by applying only two feedback loops to signals that are measured directly with photodetectors without the need for any optical f-to-$2f$-interferometry (2), the full microwave frequency comb could be stabilized.

After characterizing the microwave frequency comb, we measured the absolute stability of the modes of the optical frequency combs. A single frequency laser was used to generate a beat signal with one of the modes

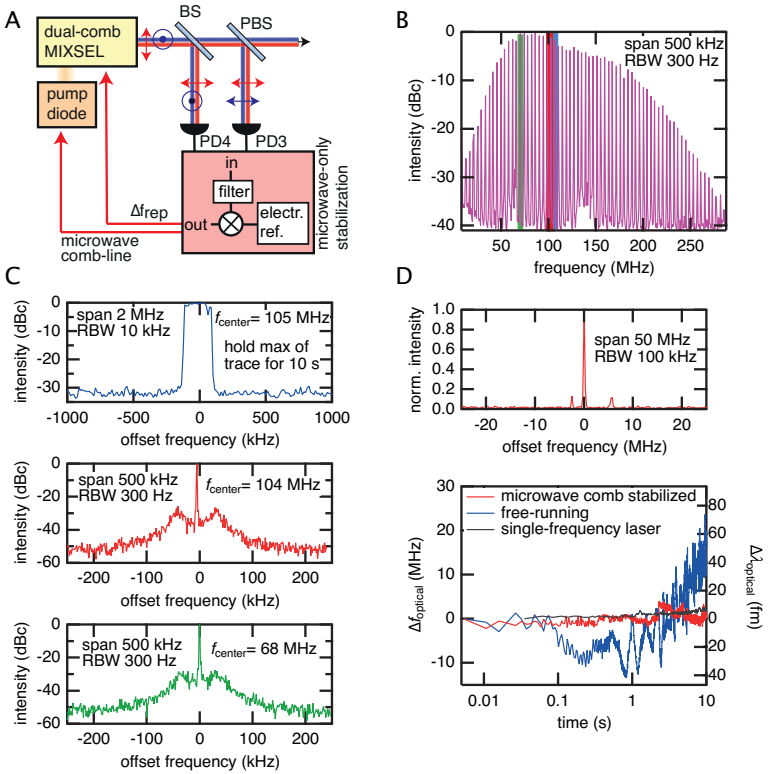

Figure 5.4: Stabilization of the microwave comb and optical mode stability. (A) Schematic of the stabilization setup. By using a beams splitter (BS), both OFCs (red and blue lines) are superimposed in cross-polarization on PD4 to prevent optical interference and to simply measure and stabilize the difference in pulse repetition rate Δf_{rep}. With a PBS, both combined OFCs are superimposed in the same polarization on PD3, where the microwave comb is measured and one of the comb lines is stabilized. Electr. ref., electronic reference. (B) Microwave spectrum of the free-running microwave comb$_1$ (Fig. 5.2A) with a resolution bandwidth (RBW) of 10 kHz. (C) Magnification of a single microwave comb line. The blue line shows the fluctuations of a free-running comb line. The maximum of the trace is recorded for 10 s with a RBW of 10 kHz. The red line shows a stabilized comb line with a RBW of 300 Hz. The green line demonstrates that all comb lines are simultaneously stabilized if the red line, and additionally Δf_{rep}, are stabilized (RBW 300 Hz) (36). (D) Measurement of the absolute stability of the optical modes. The microwave spectrum shows the beat signal between the single-frequency laser and one optical comb line with a RBW of 100 kHz. The fluctuations of the beat frequency and the consequent fluctuations of the optical comb line are measured with a frequency counter over time in case of the free-running system (blue line) and with the microwave comb stabilization active (red line). The fluctuations of the single-frequency laser are measured with a wavelength meter (gray line). Stabilizing the microwave comb drastically improves the long-term stability of the optical comb lines.

of the two optical OFCs (Fig. 5.7). The strong beat frequency was measured at 100-kHz resolution bandwidth (RBW) with the MSA (Fig. 5.4D). The small side peaks originate from the beat between the single-frequency laser and a mode of the other optical spectrum, because the suppression is limited by the suppression ratio of the PBS. We then measured the beat frequency during 10 s every 5 ms with a gate time duration of 1 ms with a frequency counter to characterize the fluctuations of the optical mode (Fig. 5.4D). The measurement confirmed that the short-term (few milliseconds) stability of the optical modes is sufficient even for the free-running system. The long-term (few seconds) stability of the optical modes drastically improved by turning on the stabilization of the microwave comb. The measurement was not limited by the stability of the single-frequency laser, which was characterized with a wavelength meter (gray line in Fig. 5.4D). For a measurement time of 1 s, we could average more than 10^6 interferograms, and the standard deviation of the beat frequency in the case of the stabilized microwave comb was below 800 kHz (2.5 fm), which is more than three orders of magnitude smaller than the comb spacing of 1.76 GHz (5.5 pm). Because the line width of typical atmospheric absorption features is on the order of several gigahertz, an optical stability of 800 kHz is more than sufficient for most applications (38), and no further additional stabilization of the optical spectrum is required.

The main trade-off with the free-running dual-comb MIXSEL approach compared to current systems is the reduced frequency comb bandwidth, requiring different lasers for applications with substantially different center wavelengths. However, semiconductor technology allows the OFC center wavelength to be tailored to the region of interest through band-gap engineering from the UV to the mid-IR and can be very cost effective because of its wafer scalability. We have observed a similar trend in biomedical imaging where the expensive, broadly tunable Ti:sapphire lasers are being replaced by much simpler optically pumped semiconductor disk lasers (SDLs) with a specific selection of operation wavelengths (39). In addition, we have shown that electrically pumped ultrafast SDLs are also possible with an average output power up to 50 mW to potentially further reduce complexity (40). We believe that the dual-comb MIXSEL approach has the potential to bring dual-comb spectroscopy from a labo-

ratory environment to the field for a wide range of industrial applications.

Acknowledgements We thank M. Kroner and A. Imamoglu for lending us the single-frequency laser (Toptica DL pro); J. Deiglmayr and F. Merkt for the wavelength meter (High-Finesse WS-7); and G. Villares, M. Rösch, and J. Faist for the frequency counter (Agilent 53220A). The authors acknowledge the support of the technology and cleanroom facility at Frontiers in Research: Space and Time (FIRST) of ETH Zurich for advanced micro- and nanotechnology. This work was financed by the Swiss Confederation program Nano-Tera.ch, which was scientifically evaluated by the Swiss National Science Foundation (SNSF). S.M.L., B. W. Tilma, M. Mangold, C. A. Zaugg, A. Klenner, and U.K. are inventors on a patent application (WO 2016/049787 A1) held and submitted by ETH Zurich that covers dual-comb mode-locking. Data can be obtained by contacting U.K. at keller@phys.ethz.ch.

5.1.1 References and notes

1. L.-S. Ma et al., Science 303, 1843-1845 (2004).
2. H. R. Telle et al., Appl. Phys. B 69, 327-332 (1999).
3. D. J. Jones et al., Science 288, 635-640 (2000).
4. A. Apolonski et al., Phys. Rev. Lett. 85, 740-743 (2000).
5. P. Del'Haye et al., Nature 450, 1214-1217 (2007).
6. J. Li, H. Lee, T. Chen, K. J. Vahala, Phys. Rev. Lett. 109, 233901 (2012).
7. D. Cotter, in Ultrafast Phenomena IV, D. H. Auston, K. B. Eisenthal, Eds. (Springer Series in Chemical Physics, Springer, 1984), vol. 38, pp. 78-80.
8. M. J. W. Rodwell, D. M. Bloom, K. J. Weingarten, IEEE J. Quantum Electron. 25, 817-827 (1989).
9. A. Klenner, S. Schilt, T. Südmeyer, U. Keller, Opt. Express 22, 31008-31019 (2014).
10. I. Hartl, H. A. McKay, R. Thapa, B. K. Thomas, J. Dong, M. E. Ferman, "GHz Yb-femtosecond-fiber laser frequency comb," paper presented at the Conference on Lasers and Electro-Optics (CLEO), CMN1, San Jose, CA, 2009.
11. A. Bartels, D. Heinecke, S. A. Diddams, Science 326, 681 (2009).
12. D. J. H. C. Maas et al., Appl. Phys. B 88, 493-497 (2007).

13. S. M. Link et al., Opt. Express 23, 5521-5531 (2015).
14. U. Keller, A. C. Tropper, Phys. Rep. 429, 67-120 (2006).
15. N. Schulz, J. M. Hopkins, M. Rattunde, D. Burns, J. Wagner, Laser Photonics Rev. 2, 160-181 (2008).
16. M. Guina, A. Härkönen, V.-M. Korpijärvi, T. Leinonen, S. Suomalainen, Adv. Opt. Technol. 2012, 265010 (2012).
17. B. W. Tilma et al., Light Sci. Appl. 4, e310 (2015).
18. A. Rahimi-Iman, J. Opt. 18, 093003 (2016).
19. M. A. Gaafar et al., Adv. Opt. Photonics 8, 370-400 (2016).
20. S. Schiller, Opt. Lett. 27, 766-768 (2002).
21. I. Coddington, N. Newbury, W. Swann, Optica 3, 414-426 (2016).
22. A. Bartels et al., Rev. Sci. Instrum. 78, 035107 (2007).
23. I. Coddington, W. C. Swann, L. Nenadovic, N. R. Newbury, Nat. Photonics 3, 351-356 (2009).
24. K. O. Hill, Y. Fujii, D. C. Johnson, B. S. Kawasaki, Appl. Phys. Lett. 32, 647-649 (1978).
25. T. Ideguchi, A. Poisson, G. Guelachvili, N. PicquÈ, T. W. Hänsch, Nat. Commun. 5, 3375 (2014).
26. Y. Liu et al., Opt. Express 24, 21392-21398 (2016).
27. M.-G. Suh, Q.-F. Yang, K. Y. Yang, X. Yi, K. J. Vahala, Science 354, 600-603 (2016).
28. T. Yasui et al., Sci. Rep. 5, 10786 (2015).
29. C. E. Shannon, Proc. IEEE 86, 447-457 (1998) [reprinted from Proc. IRE 37, 10-21 (1949)].
30. M. Mangold et al., Opt. Express 22, 6099-6107 (2014).
31. T. J. Kippenberg, R. Holzwarth, S. A. Diddams, Science 332, 555-559 (2011).
32. G. Villares, A. Hugi, S. Blaser, J. Faist, Nat. Commun. 5, 5192 (2014).
33. G. Villares et al., Appl. Phys. Lett. 107, 251104 (2015).
34. M. Mangold et al., IEEE Photonics J. 6, 1-9 (2014).
35. S. M. Link, A. Klenner, U. Keller, Opt. Express 24, 1889-1902 (2016).
36. Materials and methods are available as supplementary materials.
37. L. S. Rothman et al., J. Quant. Spectrosc. Radiat. Transf. 130, 4-50 (2013).
38. P. J. Schroeder et al., Proc. Combust. Inst. 36, 4565-4573 (2017).
39. G. Vicidomini et al., Nat. Methods 8, 571-573 (2011).
40. C. A. Zaugg et al., Appl. Phys. Lett. 104, 121115 (2014).
41. D. Waldburger et al., Optica 3, 844-852 (2016).

5.1.2 Supplementary materials

A Experimental setup

The dual-comb MIXSEL benefits from the simple straight linear cavity. The linear cavity is defined by the MIXSEL chip and an output coupler (radius of curvature 100 mm, transmission 0.5%) as the two end mirrors (Fig. 5.2A). It is straightforward with this cavity design to apply the concept of polarization duplexing by inserting a 2-mm thick, wedged birefringent $CaCO_3$ crystal into the cavity to split the one cavity beam into two cross-polarized and spatially separated beams (13). Both cavity spots on the MIXSEL chip are pumped under an angle of 45° with a commercial multimode pump diode at 808 nm, which is split with a 50:50 beams splitter (BS). Both optical spectra are tuned with an intracavity etalon to a center wavelength of 968.3 nm to match an absorption line of water vapor. The pulse duration is 17.6 ps and 18.6 ps and the average output power is 60 mW and 78 mW for the p- and s-polarized beam, respectively (Fig. 5.5). The temperature of the MIXSEL chip is kept constant with a Peltier element at 14°C.

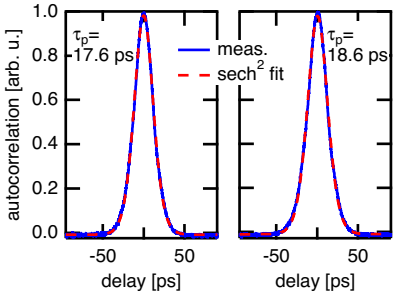

Figure 5.5: Second-harmonic autocorrelation of the two cross-polarized laser beams.

B Absorption calculation

The time-dependent interferograms (Fig. 5.6) of the reference arm and the multi-pass cell arm are recorded simultaneously with two photodetectors (PD1 and PD2) with a 5-GHz bandwidth and a high-speed oscilloscope with a 1-GHz bandwidth (Fig. 5.3A). The Fourier transformations of the two time-dependent interferograms result in the two microwave combs (Fig. 5.3B) from which the area below each peak is calculated with numeric integration. The absorption at each peak position A_i is then calculated by subtracting the area of the ith peak of the reference spectrum $a_\mathrm{i,ref}$ from the area of the corresponding peak in the spectrum measured with the multi-pass gas cell $a_\mathrm{i,MPC}$. Dividing this value by $a_\mathrm{i,ref}$ gives the absorption:

$$a_\mathrm{i} = \frac{a_\mathrm{i,ref} - a_\mathrm{i,MPC}}{a_\mathrm{i,ref}} \tag{5.1}$$

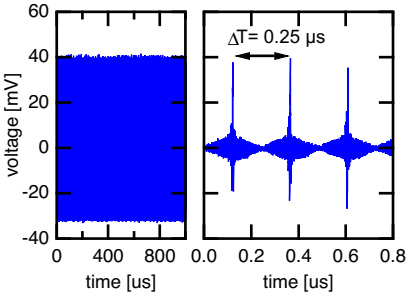

Figure 5.6: Signal from optical interference of the two combined OFCs recorded with the PD in the time domain showing time-dependent interferograms over a time span of 1 ms and 0.8 μs. Whenever one pulse of each OFC hits the detector at the same time a strong burst peak is recorded. The bursts are repeated every 0.25 μs, corresponding to the inverse of the difference in pulse repetition rate Δf_rep of 4 MHz.

The wavelength axis can be calibrated using the optical mode spacing and Δf_rep. For the absolute wavelength position one could take a single frequency laser with known frequency or an atomic transition. Here we directly use the absorption line of water to calibrate the absolute wave-

length, which is a commonly used method for dual-comb spectroscopy. The microwave axis (Fig. 5.3B) has to be inverted compared to the wavelength axis (Fig. 5.3C and D) in this case. This depends on which of the two combs between DC and the pulse repetition rates ($comb_1$ or $comb_2$ in Fig. 5.2A) have been used for the measurement because they mirror each other. Measuring the comb at lower microwave frequencies is preferred, since less bandwidth is required for the PDs and the oscilloscope. The HITRAN simulation is calculate with the HITRAN database taking the temperature, pressure, relative humidity and path length as input parameters (Fig. 5.3C and D).

C Full stabilization of the microwave comb

Stabilizing only a single line of the microwave comb is not sufficient to stabilize the full comb since it depends on two parameters: the difference in repetition rate Δf_{rep} and the difference in carrier envelope-offset (CEO) frequency Δf_{CEO}. Therefore two feedback loops are required. The comb lines are a result of the beating of the optical modes of the two combined collinear OFCs. The red line (Fig. 5.4B) f_{red} is given by

$$f_{\mathrm{red}} = (N_2 \cdot f_{\mathrm{rep},2} + f_{\mathrm{CEO},2}) - (N_1 \cdot f_{\mathrm{rep},1} + f_{\mathrm{CEO},1}) \approx const, \tag{5.2}$$

where N_1 and N_2 are integers. This beat frequency is kept constant within the limits of the feedback loop. The expression can be re-written as

$$f_{\mathrm{red}} = \Delta f_{\mathrm{CEO}} + (N_2 - N_1) \cdot f_{\mathrm{rep},1} + N_2 \cdot \Delta f_{\mathrm{rep}} \approx const. \tag{5.3}$$

with Δf_{rep} given by

$$\Delta f_{\mathrm{rep}} = f_{\mathrm{rep},2} - f_{\mathrm{rep},1} \tag{5.4}$$

and Δf_{CEO} described by

$$\Delta f_{\mathrm{CEO}} = f_{\mathrm{CEO},2} - f_{\mathrm{CEO},1} \tag{5.5}$$

The green line (Fig. 5.4B) f_{green} of the comb is given by

$$f_{\text{green}} = \left((N_2 + m) \cdot f_{\text{rep},2} + f_{\text{CEO},2}\right) - \left((N_1 + m) \cdot f_{\text{rep},1} + f_{\text{CEO},1}\right) \approx const, \tag{5.6}$$

where m is an integer counting the number of lines between the red and the green line. We can re-write f_{green} and express it as a function of f_{red},

$$\begin{aligned} f_{\text{green}} &= \Delta f_{\text{CEO}} + (N_2 - N_1) \cdot f_{\text{rep},1} + N_2 \cdot \Delta f_{\text{rep}} + m \cdot \Delta f_{\text{rep}} \\ &\approx const + m \cdot \Delta f_{\text{rep}} \end{aligned} \tag{5.7}$$

from which we can conclude that in order to stabilize the green line, we need to stabilize both Δf_{rep} and one comb line, which are directly detected with PD3 and PD4 (Fig. 5.4A). We use PD3 and PD4 to obtain a better signal-to-noise ratio, but in principle it would also be sufficient to take the signal from PD1 for the stabilization and therefore only use two detectors in total. Since Eq. 5.7 is true for any integer m, it is true for all microwave comb lines and therefore the full comb is stabilized simultaneously when both feedback loops are applied.

Even though the microwave comb is fully stabilized, both optical spectra could fluctuate the same amount in the same direction, e.g. if the two CEO frequencies are changing by the exact same amount, which would not be visible in the microwave spectrum and accordingly could not be prevented by the two feedback loops. Therefore, we characterize the absolute stability of the modes of the optical frequency combs as well (Fig. 5.7) (Fig 5.4D).

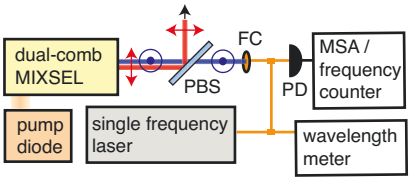

Figure 5.7: Measurement setup for the absolute stability of the optical modes of one of the two optical frequency combs (OFCs). A commercial highly stable single frequency laser (Toptica DL pro) is used to generate a beat frequency with one of the modes of one OFC on the photo detector (PD). This beat frequency is measured with a microwave spectrum analyzer (MSA) and a frequency counter. To make sure that the measurement is not limited by the fluctuations of the single frequency laser, its frequency is characterized with a wavelength meter. PBS polarizing beam splitter (polarizer axis turned such that the OFCs are spatially separated), FC fiber coupling.

5.2 Dual-comb spectroscopy of acetylene with a free-running semiconductor disk laser

The new short pulse MIXSEL (section 3.3) can also be operated in dual-comb mode. The introduced MIXSEL is not the first sub-300-fs MIXSEL [41]. But the first sub-300-fs MIXSEL did not allow for dual-comb operation. Not only was it grown on our MOVPE machine, which results in a reduced thermal conductivity (see section 3.3 and 3.4), but it is was grown in a MOVPE-MBE-regrowth scheme introducing further thermal resistance. With the first sub-300-fs MIXSEL, it was not possible to operate two laser spots close together due to thermal cross-talk. Thus, the first femtosecond dual-comb MIXSEL was only possible with the short pulse MIXSEL fully grown by MBE.

Compared to the first picosecond dual-comb MIXSEL, the center wavelength was shifted to 1030 nm with a ten-fold increased optical bandwidth of ≈3 nm. The pulse durations in dual-comb operation are ≈390 fs, slightly longer than in single beam operation. For dual-comb operation, we are not only using one birefringent crystal but two. This allows us to reduce the difference in pulse repetition rates of the two lasers to 51 kHz whereby the pulse repetition rate is 2.736 GHz. The reduced difference in pulse repetition rates is required to avoid aliasing issues due to the larger optical bandwidth.

With this new dual-comb MIXSEL, we measured the absorption of an 80 cm long multipass gas cell filed with acetylene at a pressure of 986.6 hPa. Only 100 ms of average time is sufficient for the free-running dual-comb spectroscopy measurement which is in good agreement a simulation based on the HITRAN database (Fig. 5.8). For further information on the experiment, I refer to the upcoming publication.

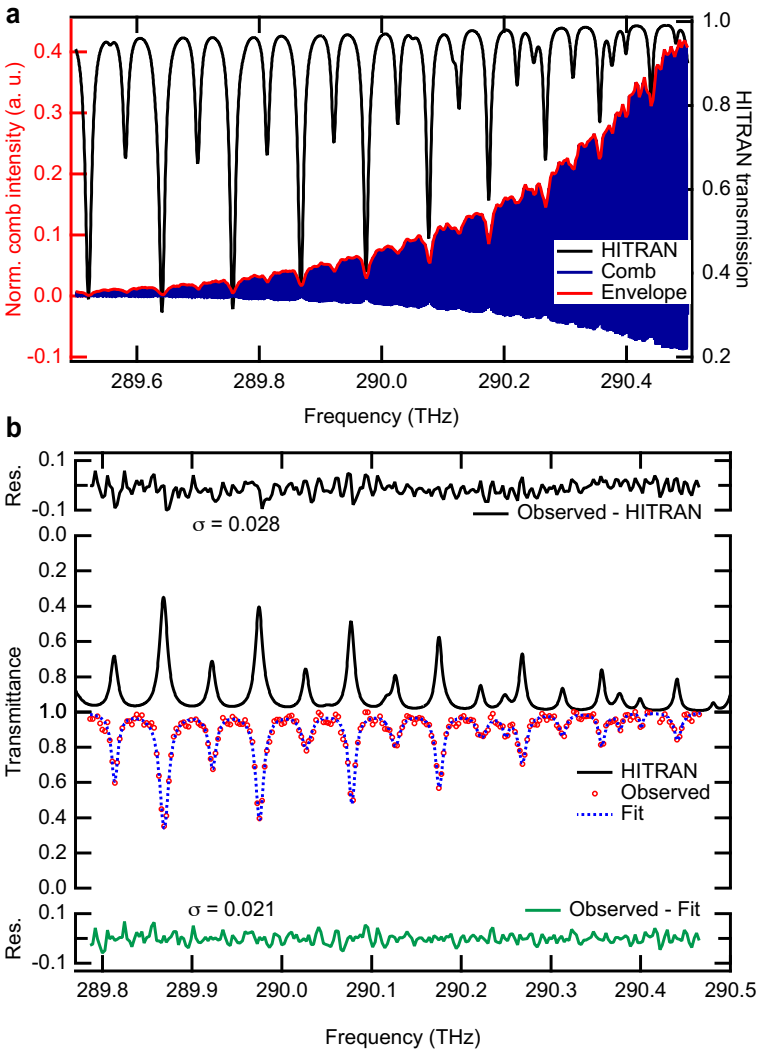

Figure 5.8: Free-running spectroscopy of Acetylene. **a**, Dual-comb spectrum shifted to the optical domain. The absorption lines visible in the comb envelope are matched with the HITRAN database which provides the absolute frequency calibration. **b**, Transmission spectrum of the acetylene filled multipass gas cell acquired with the unstabilized dual-comb MIXSEL spectrometer. The residual errors between the observed points and the HITRAN database are plotted in black. The residual error between the observed points and the fit are shown in green.

Chapter 6

Conclusion and Outlook

Within this thesis, an ultrafast SDL has been developed which allowed for self-referenced CEO frequency detection and stabilization without additional external pulse amplification or compression. Even further, the full OFC was stabilized for more than 15 min, during this time both the CEO frequency and the pulse repetition rate were tightly locked for which their frequencies are reduced to a coherent peak. This achievement became possible by combining major advances in two fields: the here developed ultrafast SDL and a novel customized Si_3N_4 waveguide design.

The presented results demonstrate the potential of these compact and high power ultrafast lasers at gigahertz repetition rates for frequency applications. In this thesis several milestone results are reported:

- The first octave-spanning supercontinuum generation with a SDL without external amplification or compression.
- The first CEO frequency detection of a SDL without external amplification or compression.
- The first CEO frequency stabilization of a SDL without external amplification or compression.
- The first tight CEO frequency stabilization of a SDL where the frequency noise power spectral density lies below the β-separation line.
- The first full stabilization of the OFC of a SDL where both the CEO frequency and the pulse repetition rate are stabilized.

- A CEO frequency stabilization with a noise performance comparable with the best performance of solid-state lasers (which are not monolithic).

The new SDL performance figures can not only be used for the OFC stabilization, but they also open up the door for new applications. For example, we demonstrated in-vivo multiphoton spectroscopy, high-power waveguide amplification, the calibration of high-precision spectrometers, and free-running dual-comb spectroscopy with a dual-comb MIXSEL. However, I am sure there are many more applications, of which I can not even think of.

By now, the principle of the dual-comb MIXSEL, which benefits from the mutual coherence between two lasers sharing the same cavity, is used by many other laser technologies [42, 43, 44, 45, 46, 47]. These numerous free-running dual-comb spectroscopy demonstrations underline the brilliancy of this principle.

Despite these remarkable achievements, there is still room for improving the performance of SDL. One optimization point is the bottom mirror. The ideal mirror should feature with the following properties:

- A broadband reflectivity to support short pulses.
- A structure which also reflects the pump wavelength to increase the pump absorption which leads to higher efficiency.
- A better thermal conductivity to scale the output power without thermal rollover.

There are different technologies, with different benefits and drawbacks:

- *Semiconductor DBR.* The standard choice is the semiconductor DBR. For the emission wavelength of 1 μm, one can use the well-engineered lattice-matched GaAs/AlAs DBRs with a decent reflection band and thermal conductivity. A double DBR reflecting both the laser and the pump light can be designed with the trade-off of a thicker DBR and thus, a lower thermal conductivity. At other wavelengths, lattice-matched DBRs with a good refractive index contrast

are rare and the thermal conductivity of the semiconductor materials usually degrade.

- *Dielectric DBR.* We tested the possibility of using a dielectric DBR directly deposited on the semiconductor structure. The high refractive index contrast available results in a broad reflection band and a high reflectivity can be achieved with only a few layer pairs. But the higher thermal resistivity is until now preventing the VECSEL from lasing.

- *Hybrid metal semiconductor mirror.* An alternative is proposed with the hybrid metal semiconductor mirror [48]. The combination of a semiconductor DBR and a gold mirror allows for a thinner mirror which also partially reflects the pump light. This technology is very promising but it needs additional engineering efforts to achieve a good adhesion of the gold layer on the semiconductor structure.

- *MECSEL.* Especially for wavelengths regions where no good semiconductor DBR is availavle, the concept of a DBR-free VECSEL named membrane external-cavity surface-emitting laser (MECSEL) [49] becomes attractive. A semiconductor membrane which is only few μm thick is contacted on both sides to optical quality transparent silicon carbide (SiC) heat spreaders. The excellent thermal conductivity of SiC allows for extremely efficient heat removal.

The next optimization point is the group delay dispersion management:

- *Short active region.* As confirmed by the simulations of the group of Prof. Molony [50, 51], a short active region is helping to control the dispersion of the structure which allows for shorter pulse durations.

- *Dielectric anti-reflection coating.* The full anti-reflection coating of the MIXSEL in section 3.3 is dielectric and deposited by IBS. A high refractive index contrast is possible and the resulting layers can be grown with a good accuracy and have a high quality. Since the coating is applied after the epitaxial growth, different coatings can be tested and possible deviations in the semiconductor growth from the ideal design can be taken into account and corrected.

Finally there are two novel lasers cavities, which could potentially bring benefits and which I personally suggest to investigate:

- *Chirp pulse operation* could be very attractive for SDLs. It could lead to shorter pulse durations and increase the optical efficiency.
- *Monolithic cavity.* With the development of transparent SiC, it becomes feasible to build a monolithic SDL with unmatched stability.

For spectroscopy application, it is of great interest to cover a broad wavelength range. Many vibrational absorption lines of molecules lie in the infrared. Thus, it is our endeavor to bring the emission of SDLs to new wavelength region. This can be achieved by clever engineering of the band gap energy, but the lack of good semiconductor DBRs in the mid-infrared makes the task challenging. An other approach is to use nonlinear frequency conversion such as SCG, SHG, or difference frequency generation (DFG).

Author Contributions

In the following, the contributions of Dominik Waldburger to the different journal publications are listed:

Tightly locked optical frequency comb from a semiconductor disk laser

D. Waldburger, A. S. Mayer, C. G. E. Alfieri, J. Nürnberg, A. R. Johnson, X. Ji, A. Klenner, Y. Okawachi, M. Lipson, A. L. Gaeta, U. Keller

submitted to Optica (2018)

- Main contribution to all presented results, except for the simulation of the supercontinuum generation by the silicon nitride waveguide.
- Development, design, processing, construction, and testing of the SESAM-modelocked VECSEL.
- Building of the setup to couple into the silicon nitride waveguide and characterization of the silicon nitride waveguide.
- Rebuilding and optimizing of the f-to-2f interferometer and characterization of the carrier envelope-offset frequency.
- Building of the stabilization setup for the pulse repetition rate and the carrier envelope-offset frequency.
- Stabilization of the pulse repetition rate and the carrier envelope-offset frequency and measurement and analyzation of the corresponding noise.

Multipulse instabilities of a femtosecond SESAM- modelocked VECSEL

D. Waldburger, C. G. E. Alfieri, S. M. Link, S. Meinecke, L. C. Jaurigue, K. Lüdge, U. Keller

Optics Express (2018)

- Main contribution to all presented results, except for the coupled multi-delay differential equations results.
- Development, design, processing, construction, and testing of the SESAM-modelocked VECSEL.
- The full modelocking characterization.
- Full characterization of the VECSEL and the SESAM and the modeling of the saturation of the VECSEL roundtrip reflectivity.
- The rate equation model including the kinetic hole filling effect to describe the side pulse operation.

High-power 100 fs semiconductor disk lasers

D. Waldburger, S. M. Link, M. Mangold, C. G. E. Alfieri, E. Gini, M. Golling, B. W. Tilma, U. Keller

Optica (2016)

- Main contribution to all presented results.
- Development, design, processing, construction, and testing of the SESAM-modelocked VECSEL.
- Characterization of the modelocking result.
- Gain characterization of the VECSEL chip.
- Simulation of the modelocking performance depending on the cavity dispersion.

Sub-150-fs pulses from a broadband MIXSEL

C. G. E. Alfieri, D. Waldburger, J. Nürnberg, M. Golling, U. Keller

submitted to Optics Letters (2018)

- Support in development, design, construction, and modelocking of the MIXSEL presented in this paper.
- Construction of thermal surface image setup and thermal characterization of the VECSEL chips.

Wavelength calibration of high performance spectrometers using a fully stabilized semiconductor disk laser comb

A. Jallageas, J. Nürnberg, C. G. E. Alfieri, D. Waldburger, S. M. Link, F. Emaury, J. Morel, U. Keller

in preparation (2018)

- Development, design, processing, construction, and testing of the SESAM-modelocked VECSEL used in the preliminary experiment of the presented result in this paper.
- Support in development, design, construction, and modelocking of the MIXSEL used in the experiment presented in this paper.

An unstabilized femtosecond semiconductor laser for dual-comb spectroscopy of acetylene

J. Nürnberg, C. G. E. Alfieri, Z. Chen, D. Waldburger, N. Picqué, U. Keller

submitted to Optics Express (2018)

- Support in development, design, construction, and modelocking of the MIXSEL presented in this paper.
- Support in optimization of the spectroscopy measurement.

Mode-locking Instabilities for High-Gain Semiconductor Disk Lasers Based on Active Submonolayer Quantum Dots

C. G. E. Alfieri, D. Waldburger, J. Nürnberg, M. Golling, L. C. Jaurigue, K. Lüdge, U. Keller

Physical Review Applied (2018)

- Support in the development and characterization of the used QDs.
- Support in the epitaxial growth, processing, modelocking of the QD VECSEL
- Simulations of the modelocking instabilities.

High-power Sub-300- Femtosecond Quantum Dot Semiconductor Disk Lasers

C. G. E. Alfieri, D. Waldburger, M. Golling, U. Keller

IEEE Photonics Technology Letters (2018)

- Initial development and characterization of the used QDs.
- Support in the epitaxial growth, processing, modelocking of the QD VECSEL.

Coherent beam combining and noise analysis of a colliding pulse modelocked VECSEL

S. M. Link, D. Waldburger, C. G. E. Alfieri, M. Golling, U. Keller

Optics Express (2017)

- Development, design, processing, construction, and testing of the SESAM-modelocked VECSEL used in the experiment presented in this paper.
- Support in the noise characterization (method and measurement).
- Support in the coherent beam combining.

Optical efficiency and gain dynamics of modelocked semiconductor disk lasers

C. G. E. Alfieri, D. Waldburger, S. M. Link, E. Gini, M. Golling, G. Eisenstein, U. Keller

Optics Express (2017)

- Design inputs to the epitaxial layer design of MIXSEL.
- Development, implementation and refinement of the presented rate equation model.

Dual-comb spectroscopy of water vapor with a free-running semiconductor disk laser

S. M. Link, D. J. H. C. Maas, D. Waldburger, U. Keller

Science (2017)

- Support in finding the best spectroscopy measurement method.
- Support in debugging of the measurement setup.
- Support in optimization of the spectroscopy measurement.

Multiphoton in vivo imaging with a femtosec- ond semiconductor disk laser

F. F. Voigt, F. Emaury, P. Bethge, D. Waldburger, S. M. Link, S. Carta, A. van der Bourg, F. Helmchen, U. Keller

Biomedical Optics Express (2017)

- Development, design, processing, construction, and testing of the SESAM-modelocked VECSEL used in the experiment presented in this paper.

Carrier-envelope offset frequency stabilization of a gigahertz semiconductor disk laser

N. Jornod, K. Gürel, V. J. Wittwer, P. Brochard, S. Hakobyan, S. Schilt, D. Waldburger, U. Keller, T. Südmeyer

Optica (2017)

- Development, design, processing, construction, and testing of the SESAM-modelocked VECSEL used in the experiment presented in this paper.

High-power amplification of a femtosecond vertical external- cavity surface-emitting laser in an Yb:YAG waveguide

N. Jornod, V. J. Wittwer, C. Kränkel, D. Waldburger, U. Keller, T. Südmeyer, T. Calmano

Optics Express (2017)

- Development, design, processing, construction, and testing of the SESAM-modelocked VECSEL used in the experiment presented in this paper.

First investigation of the noise and modulation properties of the carrier-envelope offset in a modelocked semiconductor laser

P. Brochard, N. Jornod, S. Schilt, V. J. Wittwer, S. Hakobyan, D. Waldburger, S. M. Link, C. G. E. Alfieri, M. Golling, L. Devenoges, J. Morel, U. Keller, T. Südmeyer

Optics Letters (2016)

- Development, design, processing, construction, and testing of the SESAM-modelocked VECSEL used in the experiment presented in this paper.

Recent advances in ultrafast semiconductor disk lasers

B. W. Tilma, M. Mangold, C. A. Zaugg, S. M. Link, D. Waldburger, A. Klenner, A. S. Mayer, E. Gini, M. Golling, U. Keller

Light: Science & Applications (2015)

- Minor contributions.

Literature

[1] T. H. Maiman, “Stimulated Optical Radiation in Ruby”, Nature 187 (1960), 493–494

[2] B. P. Abbott, *et al.* (full author list online), “Observation of Gravitational Waves from a Binary Black Hole Merger”, Phys. Rev. Lett. 116 (2016), 061102

[3] L. Gallmann, C. Cirelli, U. Keller, “Attosecond Science: Recent Highlights and Future Trends”, Annu. Rev. Phys. Chem. 63 (2012), 447–469

[4] T. A. Klar, S. W. Hell, “Subdiffraction resolution in far-field fluorescence microscopy”, Opt. Lett. 24 (1999), 954–956

[5] J. P. Grotzinger, “Habitability, Taphonomy, and the Search for Organic Carbon on Mars”, Science 343 (2014), 386–387

[6] A. H. Zewail, “Femtochemistry: Atomic-Scale Dynamics of the Chemical Bond Using Ultrafast Lasers (Nobel Lecture)”, Angew. Chem. Int. Ed. 39 (2000), 2586–2631

[7] T. W. Hänsch, “Nobel Lecture: Passion for precision”, Rev. Mod. Phys. 78 (2006), 1297–1309

[8] H. S. W., “Nanoscopy with Focused Light (Nobel Lecture)”, Angew. Chem. Int. Ed. 54 (2014), 8054–8066

[9] R. N. Hall, G. E. Fenner, J. D. Kingsley, T. J. Soltys, R. O. Carlson, “Coherent Light Emission From GaAs Junctions”, Phys. Rev. Lett. 9 (1962), 366

[10] H. Soda, K. Iga, C. Kitahara, Y. Suematsu, “GaInAsP-InP Surface Emitting Injection-Lasers”, Jpn. J. Appl. Phys. 18 (1979), 2329–2330

[11] M. A. Hadley, G. C. Wilson, K. Y. Lau, J. S. Smith, “High single-transverse-mode output from external-cavity surface-emitting laser diodes”, Appl. Phys. Lett. 63 (1993), 1607–1609

[12] M. Kuznetsov, F. Hakimi, R. Sprague, A. Mooradian, “High-Power (>0.5-W CW) Diode-Pumped Vertical-External-Cavity Surface-Emitting Semiconductor Lasers with Circular TEM00 Beams”, IEEE Photon. Technol. Lett. 9 (1997), 1063–65

[13] A. Giesen, H. Hügel, A. Voss, K. Wittig, U. Brauch, H. Opower, "Scalable Concept for Diode-Pumped High-Power Solid-State Lasers", Appl. Phys. B 58 (1994), 365–372

[14] B. Heinen, T. L. Wang, M. Sparenberg, A. Weber, B. Kunert, J. Hader, S. W. Koch, J. V. Moloney, M. Koch, W. Stolz, "106 W continuous-wave output power from vertical-external-cavity surface-emitting laser", Electron. Lett. 48 (2012), 516–U102

[15] M. Guina, A. Rantamäki, A. Härkönen, "Optically pumped VECSELs: review of technology and progress", J. Phys. D: Appl. Phys. 50 (2017), 383001

[16] U. Keller, K. J. Weingarten, F. X. Kärtner, D. Kopf, B. Braun, I. D. Jung, R. Fluck, C. Hönninger, N. Matuschek, J. Aus der Au, "Semiconductor saturable absorber mirrors (SESAMs) for femtosecond to nanosecond pulse generation in solid-state lasers", IEEE J. Sel. Top. Quantum Electron. 2 (1996), 435–453

[17] A. Klenner, U. Keller, "All-optical Q-switching limiter for high-power gigahertz modelocked diode-pumped solid-state lasers", Opt. Express 23 (2015), 8532–8544

[18] A. S. Mayer, C. R. Phillips, U. Keller, "Watt-level 10-gigahertz solid-state laser enabled by self-defocusing nonlinearities in an aperiodically poled crystal", Nat. Commun. 8 (2017), 1673

[19] C. G. E. Alfieri, D. Waldburger, S. M. Link, E. Gini, M. Golling, G. Eisenstein, U. Keller, "Optical efficiency and gain dynamics of modelocked semiconductor disk lasers", Opt. Express 25 (2017), 6402–6420

[20] C. Hönninger, R. Paschotta, F. Morier-Genoud, M. Moser, U. Keller, "Q-switching stability limits of continuous-wave passive mode locking", J. Opt. Soc. Am. B 16 (1999), 46–56

[21] S. Hoogland, S. Dhanjal, A. C. Tropper, S. J. Roberts, R. Häring, R. Paschotta, U. Keller, "Passively mode-locked diode-pumped surface-emitting semiconductor laser", IEEE Photon. Technol. Lett. 12 (2000), 1135–1138

[22] P. Klopp, U. Griebner, M. Zorn, M. Weyers, "Pulse repetition rate up to 92 GHz or pulse duration shorter than 110 fs from a mode-locked semiconductor disk laser", Appl. Phys. Lett. 98 (2011)

[23] D. Waldburger, S. M. Link, M. Mangold, C. G. E. Alfieri, E. Gini, M. Golling, B. W. Tilma, U. Keller, "High-power 100 fs semiconductor disk lasers", Optica 3 (2016), 844–852

[24] C. W. Baker, M. Scheller, A. Laurain, A. Ruiz-Perez, W. Stolz, S. Addamane, G. Balakrishnan, S. W. Koch, R. J. Jones, J. V. Moloney, "Multi-Angle VECSEL Cavities for Dispersion Control and Peak-Power Scaling", IEEE Photon. Technol. Lett. 29 (2017), 326–329

[25] U. Keller, A. C. Tropper, "Passively modelocked surface-emitting semiconductor lasers", Phys. Rep. 429 (2006), 67–120

[26] B. W. Tilma, M. Mangold, C. A. Zaugg, S. M. Link, D. Waldburger, A. Klenner, A. S. Mayer, E. Gini, M. Golling, U. Keller, "Recent advances in ultrafast semiconductor disk lasers", Light Sci. Appl. 4 (2015), e310

[27] M. A. Gaafar, A. Rahimi-Iman, K. A. Fedorova, W. Stolz, E. U. Rafailov, M. Koch, "Mode-locked semiconductor disk lasers", Adv. Opt. Photonics 8 (2016), 370–400

[28] A. Rahimi-Iman, "Recent advances in VECSELs", J. Opt. 18 (2016)

[29] D. J. H. C. Maas, A.-R. Bellancourt, B. Rudin, M. Golling, H. J. Unold, T. Südmeyer, U. Keller, "Vertical integration of ultrafast semiconductor lasers", Appl. Phys. B 88 (2007), 493–497

[30] A.-R. Bellancourt, D. J. H. C. Maas, B. Rudin, M. Golling, T. Südmeyer, U. Keller, "Modelocked Integrated External-Cavity Surface Emitting Laser (MIXSEL)", IET Optoelectronics Vol. 3 (2009), pp. 61–72

[31] M. Mangold, C. A. Zaugg, S. M. Link, M. Golling, B. W. Tilma, U. Keller, "Pulse repetition rate scaling from 5 to 100 GHz with a high-power semiconductor disk laser", Opt. Express 22 (2014), 6099–6107

[32] B. Rudin, V. J. Wittwer, D. J. H. C. Maas, M. Hoffmann, O. D. Sieber, Y. Barbarin, M. Golling, T. Südmeyer, U. Keller, "High-power MIXSEL: an integrated ultrafast semiconductor laser with 6.4 W average power", Opt. Express 18 (2010), 27582–27588

[33] S. M. Link, A. Klenner, M. Mangold, C. A. Zaugg, M. Golling, B. W. Tilma, U. Keller, "Dual-comb modelocked laser", Opt. Express 23 (2015), 5521–5531

[34] S. M. Link, A. Klenner, U. Keller, "Dual-comb modelocked lasers: semiconductor saturable absorber mirror decouples noise stabilization", Opt. Express 24 (2016), 1889–1902

[35] S. M. Link, D. J. H. C. Maas, D. Waldburger, U. Keller, "Dual-comb spectroscopy of water vapor with a free-running semiconductor disk laser", Science 356 (2017), 1164–1168

[36] H. R. Telle, G. Steinmeyer, A. E. Dunlop, J. Stenger, D. H. Sutter, U. Keller, "Carrier-envelope offset phase control: A novel concept for absolute optical frequency measurement and ultrashort pulse generation", Appl. Phys. B 69 (1999), 327–332

[37] J. M. Dudley, G. Genty, S. Coen, "Supercontinuum generation in photonic crystal fiber", Rev. Mod. Phys. 78 (2006), 1135–1184

[38] D. Waldburger, C. G. E. Alfieri, S. M. Link, S. Meinecke, L. C. Jaurigue, K. Lüdge, U. Keller, "Multipulse instabilities of a femtosecond SESAM-modelocked VECSEL", Opt. Express 26 (2018), 21872–21886

[39] S. M. Link, D. Waldburger, C. G. E. Alfieri, M. Golling, U. Keller, "Coherent beam combining and noise analysis of a colliding pulse modelocked VECSEL", Opt. Express 25 (2017), 19281–19290

[40] C. G. E. Alfieri, D. Waldburger, M. Golling, U. Keller, "High-power Sub-300-Femtosecond Quantum Dot Semiconductor Disk Lasers", IEEE Photon. Technol. Lett. 30 (2018), 525–528

[41] M. Mangold, M. Golling, E. Gini, B. W. Tilma, U. Keller, "Sub-300-femtosecond operation from a MIXSEL", Opt. Express 23 (2015), 22043–22059

[42] X. Zhao, G. Hu, B. Zhao, C. Li, Y. Pan, Y. Liu, T. Yasui, Z. Zheng, "Picometer-resolution dual-comb spectroscopy with a free-running fiber laser", Opt. Express 24 (2016), 21833–21845

[43] S. Mehravar, R. A. Norwood, N. Peyghambarian, K. Kieu, "Real-time dual-comb spectroscopy with a free-running bidirectionally mode-locked fiber laser", Appl. Phys. Lett. 108 (2016), 231104

[44] T. Ideguchi, T. Nakamura, Y. Kobayashi, K. Goda, "Kerr-lens mode-locked bidirectional dual-comb ring laser for broadband dual-comb spectroscopy", Optica 3 (2016), 748–753

[45] Q.-F. Yang, X. Yi, K. Y. Yang, K. Vahala, "Counter-propagating solitons in microresonators", Nat. Photonics 11 (2017), 560

[46] R. Liao, Y. Song, W. Liu, H. Shi, L. Chai, M. Hu, "Dual-comb spectroscopy with a single free-running thulium-doped fiber laser", Opt. Express 26 (2018), 11046–11054

[47] J. Guo, Y. Ding, X. Xiao, L. Kong, C. Yang, "Multiplexed static FBG strain sensors by dual-comb spectroscopy with a free running fiber laser", Opt. Express 26 (2018), 16147–16154

[48] K. Gbele, A. Laurain, J. Hader, W. Stolz, J. V. Moloney, "Design and Fabrication of Hybrid Metal Semiconductor Mirror for High-Power VECSEL", IEEE Photon. Technol. Lett. 28 (2016), 732–735

[49] H. Kahle, C. M. N. Mateo, U. Brauch, P. Tatar-Mathes, R. Bek, M. Jetter, T. Graf, P. Michler, "Semiconductor membrane external-cavity surface-emitting laser (MECSEL)", Optica 3 (2016), 1506–1512

[50] I. Kilen, S. W. Koch, J. Hader, J. V. Moloney, "Non-equilibrium ultrashort pulse generation strategies in VECSELs", Optica 4 (2017), 412–417

[51] I. Kilen, S. W. Koch, J. Hader, J. V. Moloney, "VECSEL design for high peak power ultrashort mode-locked operation", Appl. Phys. Lett. 112 (2018), 262105

Acknowledgments

I want to use this chapter to thank and acknowledge all the people who supported me during my doctoral studies but fortunately also distracted me from work such that I did not get lost in it. Looking back, the last four years have been a pleasant time and passed by rather fast.

I want to thank Prof. Ursula Keller, who offered me this doctoral student position in the probably shortest job interview of my life. She provided me an unique opportunity with a lot of freedom, excellent equipped laboratories, and the possibility to present our research in international conferences.

I would also like to thank Prof. Mircea Guina for taking over the external co-examination of my doctoral thesis. I always enjoyed our discussions and was fascinated by his knowledge about semiconductor growth.

During my doctoral studies, I could benefit from several successive collaborations:

The group of Prof. Lipson and Prof. Alexander Gaeta at Colombia University provided us with silicon nitride waveguides which enabled the self-referenced carrier envelope-offset frequency of SDLs. My special thanks go to Adrea Johnson, Xingchen Ji, Alexander Klenner and Yoshitomo Okawachi for designing and fabricating the waveguide.

The group of Prof. Kathy Lüdge at the Technische Universität Berlin supported us with their theoretical simulations. I want to thank Lina Jaurigue and Stefan Meinecke for their endurance explaining me their model and bifurcation diagramms.

The group of Prof. Thomas Südmeyer at the Université de Neuchâtel is in close collaboration with our group. I want to thank Piere Brochard and Nayara Jornod for their work on the carrier envelope-offset frequency detection, Dr. Valentin Wittwer for useful discussion and the on-demand supply of IBS coatings, Dr. Stéphane Schilt for sharing his deep knowl-

edge about frequency stabilization, and Dr. Kutan Gürel and Norbert Modsching for some nice conference evenings.

The team of Dr. Jacques Morel of at METAS, particularly Dr. Antoine Jallageas and Dr. Laurent Devenoges, who worked on the calibration of high-precision spectrometers with SDLs.

The group of Prof. Helmchen at University of Zürich opened us the door to multiphoton microscopy. My special thanks go to Fabian Voigt for his work and knowledge about microscopy, lasers and everything.

The countless semiconductor structures fabricated during my doctoral studies were grown by Dr. Matthias Golling and Dr. Emilio Gini. I want to thank them for their time and effort spend to fulfill my specific growth requests. They gave their best to troubleshoot and maintain the epitaxial machines.

No SDL chip could be processed without the help of Sandro Tiegermann and Martin Klöckner from the Laboratory Support Group who supported us with metallization and relaxing afternoon discussions.

I would like to thank the current and former VECSEL team. Dr. Bauke Tilma, Dr. Mario Mangold, and Dr. Sandro Link provided me a smooth start and I learn everything I need from them. Cesare Alfieri started shortly after me and we worked together on nearly all projects ever since. I really liked the atmosphere and spirit of our self-organized team. My best wishes got to future team Jacob Nürnberg und Léonard Krüger. Not forgetting Dr. Aline Mayer who previously was scheduled for my position but then decided to continue her work in the HighRep team. She teached me her knowledge about waveguides and CEO frequency stabilization.

My office time was cheered up by my office mates Nicolas Bigler, Dr. Florian Emaury and Dr. Mario Mangold.

The entire ultrafast laser physic group deserves my acknowledgement for the wonderful time during and after work. Keep the spirit up with the 9 and 4 o'clock meetings, after work beers, parties, and outdoor activities. My thanks goes to all current and former group members: Dr. Alexander Klenner, Dr. André Ludwig, Dr. Andreas Diebold, Dr. Benedikt Mayer, Benjamin Willenberg, Dr. Christian Zaugg, Dr. Christopher Phillips, Dr. Cinia Schriber, Dr. Clara Saraceno, Dr. Cornelia Hofmann, Fabian Brunner, Fabian Schläpfer, Dr. Florian Emaury, Francesco Saltarelli, Ivan Graumann, Jaco Fuchs, Jacob Nürnberg, Jannie Vos, Dr. Jens Herrmann, Dr. Jochen Maurer, Justinas Pupeikis, Dr. Lamia Kasmi, Dr. Laura Cattaneo, Luca Pedrelli, Dr. Lukas Gallmann, Dr. Matteo Lucchini, Mikhail Volkov, Nadja Hartmann, Dr. Robert Boge, Dr. Sebastian Heuser, Stefan Hrisafov, and Dr. Zeno Schumacher.

Many thanks also to Sandra Schmid, our office manager, without her the group would not work.

I am deeply grateful to my parents Beatrix and Urs Waldburger and to my sister Fabienne for their unrestricted support and care.

My biggest gratitude belongs to my soulmate Carmen Wälchli for her love and patience with me. I feel very lucky to have you by my side.

Dominik Waldburger
Zürich, August 2018